Strength and Durability of Ultra-High Performance Concrete Materials and Structures

By

Mouhamed Alkaysi

A dissertation submitted in partial fulfillment
of the requirements for the degree of
Doctor of Philosophy
(Civil Engineering)
in the University of Michigan
2016

Dissertation Committee:
Professor Sherif El-Tawil, Chair
Associate Professor Jason P. McCormick
Professor Jwo Pan
Professor James K. Wight

Dedication

For my wife,

Sarah

Acknowledgements

The completion of my doctorate represents a long journey pursuing my passion for learning and my endless quest for knowledge. This would not have been possible if not for the help of several people along the way. First and foremost, I would like to thank my advisor Professor Sherif El-Tawil. His unlimited support, time and guidance was pivotal in shaping my work and showed me what it means to be an amazing mentor. His enthusiasm for civil engineering is electric, and inspires me to achieve excellence in all that I do.

I would also like to thank my committee members Professor Jason P. McCormick, Professor James K. Wight and Professor Pan Jwo, for their support, advice and mentoring in the completion of this work. In particular, I would like to thank Professor McCormick who has been a mentor both inside and outside of my academic pursuits and who has on numerous occasions gone out of his way to support my efforts. Additionally, I would like to acknowledge the support of the Michigan Department of Transportation as well as their belief and guidance in this research.

Finally, I would like to thank my wife, Sarah and my family (Mom, Dad, Nadine and Rowan) for their endless love and unconditional support. For the past few years they have been a constant sounding board for my ideas, have listened and encouraged me when I was stressed and pushed me to become the person I am today. Without them I could never hoped to accomplish this dream and for that, I am eternally grateful.

Table of Contents

Dedication ii

Acknowledgements iii

List of Figures x

List of Tables xvi

List of Appendices xvii

Abstract xviii

Chapter 1 1

Introduction 1

- 1.1. Ultra-High Performance Concrete (UHPC) 1
  - 1.1.1. Short Term Mechanical Properties of UHPC 2
  - 1.1.2. Durability Characteristics of UHPC 3
  - 1.1.3. Bond between Steel Reinforcement and UHPC 3
  - 1.1.4. Structural Performance of UHPC 3
- 1.2. Objectives 4
- 1.3. Organization of this Dissertation 4
- 1.4. Publications from this Dissertation 5

Chapter 2 7

Background and Literature Review 7

2.1. Strength of UHPC 7

2.1.1. Compressive and Tensile Behavior of UHPC 7
2.1.2. Effect of Silica Fume 8
2.1.3. Effect of Silica Powder 9
2.1.4. Effect of Cement 9
2.1.5. Effect of Fiber Type and Quantity 10
2.2. DURABILITY OF UHPCs 10

2.2.1. Freeze-Thaw Resistance 10
2.2.2. Chloride Ion Penetration Resistance: 11
2.3. Bond Development in UHPCs 12

2.3.1. Bond Development of Steel Bars Embedded in UHPC 12
2.3.2. Lap Splice & Component Tests with UHPC 13
Chapter 3 15

Effects of Variations in the Mix Constituents of UHPC on Cost and Performance 15

3.1. OVERVIEW 15

3.2. EXPERIMENTAL PARAMETERS AND PROCEDURE 16

3.2.1. UHPC Material Properties and Cost 16
3.2.2. Steel Fibers 20
3.2.3. Mixing Procedure 21
3.2.4. Tensile Strength Testing: 23
3.2.5. Compression Testing: 24
3.3. RESULTS AND DISCUSSION 25

3.3.1. Analysis of Data 25

3.3.2. Overview of Results 27
3.3.3. Cement Type 28
3.3.4 - Silica Powder 29
3.3.4. Silica Fume 32
3.3.5. Fiber Content 34
3.3.6. Cost Analysis 39
3.4. CONCLUSION 40

Chapter 4 42

Effects of Silica Powder Content and Cement Type on the Durability of UHPC 42

4.1. OVERVIEW 42

4.2. EXPERIMENTAL PARAMETERS 42

4.2.1. UHPC Mix Designs 42
4.2.2. Experimental Procedure 44
4.2.3. Air Void Analysis 47
4.2.4. Rapid Chloride Penetration Test 48
4.2.5. Compressive Strength Testing 49
4.3. EXPERIMENTAL RESULTS 49

4.3.1. Freeze-Thaw Resistance 49
4.3.2. Air Void Analysis 53
4.3.3. Rapid Chloride Permeability 57
4.4. DISCUSSION OF EXPERIMENTAL RESULTS 60

4.5. CONCLUSION 63

Chapter 5 66

Factors Effect Bond Development between UHPC and Steel Bar Reinforcement 66

5.1. OVERVIEW 66

5.2. EXPERIMENTAL PARAMETERS AND PROCEDURE: 67

5.2.1. Bar Pull Out Testing Program and Test Set Up 67
5.2.2. Lap Splice Joint Testing Program 72
5.2.3. Material Properties 74
5.3. RESULTS AND ANALYSIS 75

5.3.1. Bar Pull Out Results 75
5.3.2. Effect of Embedment Length 79
5.3.3. Effect UHPC Cast Orientation on Bond 84
5.3.4. Effects of Fiber Volume Content 85
5.3.5. Early Age Testing of UHPC on Bond 86
5.3.6. Bar Pull Out vs. Lap Splice Beam Results 88
5.3.7. Evaluation of Content Bond Data Available on UHPC 90
5.4. CONCLUSION 93

Chapter 6 95

Simplified UHPC Joints for Bridge Construction 95

6.1. OVERVIEW 95

6.2. DESIGN OF THE EXPERIMENTAL PROGRAM 96

6.2.1. Pure Flexure vs. Combined Shear and Flexure Testing 96
6.2.2. Joint Details & Selection 97
6.2.3. Specimen Design 98
6.2.4. Specimens Tested and Material Parameters 100
6.3. EXPERIMENTAL PROCEDURE 102

6.3.1. Test Set Up 102
6.3.2. Instrumentation 103
6.4. MATERIALS 104

6.5. CONSTRUCTION OF THE PRECAST CONCRETE SPECIMENS 105

6.6. RESULTS AND DISCUSSION 107

6.6.1. Comparison of Calculated Bar Stress versus Measured Bar Stress 107
6.6.2. F-100 Specimen Tests 108
6.6.3. F-150 and F-200 Specimens 109
6.6.4. Effect of Fiber Content in Pure Flexure 112
6.6.5. Effect of Joint Size 112
6.6.6. Combined Shear and Flexure Testing 113
6.6.7. Effect of Fiber Content in Combined Shear and Flexure 114
6.7. Evaluation of the Current Design Code 116

6.8. FINITE ELEMENT MODEL AND PARAMETRIC STUDY 117

6.8.1. Model Setup 117
6.8.2. UHPC and Concrete Material Models 118
6.8.3. Parametric Study 119
6.8.4. Model Validation 120
6.8.5. Results of Parametric Study 121
6.9. CONCLUSION 123

Chapter 7 125

Summary and Conclusions …………125

7.1. Short Term Mechanical and Durability of Ultra High Performance Concrete 125

7.2. Structural Evaluation of UHPC through Bar Pull Out Testing and Full Scale Beam Tests 126

7.3. Conclusions 127

7.4. The Promise of UHPC 128

7.5. Future Research Needs 129

7.5.1. Material Level 129

7.5.2. Structural Level 129
Appendix A 130

Appendix B 137

Appendix C 140

Appendix D 172

References 189

List of Figures

Figure 2-1 Typical Tensile Strain Response in UHPC 8

Figure 3-1 Grain Size Analysis for Sand 17

Figure 3-2: Example of the Steel Fibers Used in this Study 21

Figure 3-3 Mixing process (photos courtesy of Prof. Kay Wille) 22

Figure 3-4 (a) Tensile test set up, (b) Instrumentation, (c) Specimen dimensions 23

Figure 3-5: Tensile and Compression Specimens Post Test 25

Figure 3-6: Effects of Different Cements on UHPC for Mixes with 1.5% Volume Fiber Content 30

Figure 3-7: Effects of Silica Powder Content on UHPC for Mixes with 1.5% Volume Fiber Content 31

Figure 3-8: Effect of Silica Fume Contents on UHPC for Mixes with 1.5% Volume Fiber Content 33

Figure 3-9: Effects of Lower Steel Fiber Volume Contents on UHPC 35

Figure 3-10: Strain Response for UHPC Specimens in Tension 38

Figure 3-11: Strain (%) Capacity as function of Steel Fiber Content... 38

Figure 3-12: Compressive Strength as a function of Cost Index 39

Figure 4-1: Freeze Thaw Test Close-Up (17) 45

Figure 4-2: Specimen with Test Surface Facing the Bottom under Frozen Condition................ 46

Figure 4-3: Temperature Profile of Freeze-Thaw Test 46

Figure 4-4: (a) Polished surface for point count measurement and (b) coated surface for linear traverse measurement... 48

Figure 4-5: Mass Loss of UHPC Mixes after at Least 60 Cycles 51

Figure 4-6: a. Effect of Silica Powder on Mass Loss; b. Average Mass Loss as a Function of Silica Powder Quantity 52

Figure 4-7: Average Mass Loss as a Function of Cement Type 53

Figure 4-8: Air Content by LTM and PCM 54

Figure 4-9: Air Content as a Function of Power's Spacing Factor 55

Figure 4-10: a. Air Content as a Function of Silica Powder Percent, b. Average Air Content as a function of Silica Powder.. 56

Figure 4-11: Average Air Content as a Function of Cement Type 56

Figure 4-12: Total Charge Passed for UHP C and RC Mix... 57

Figure 4-13: a. Total Coulombs passed as a function of Silica Powder Percent; b. Average Coulombs passed as a function of Silica Powder 59

Figure 4-14: Average Coulombs passed as a function of Cement Type 59

Figure 4-15: Particle Size Distributions for UHPC Mixes and Regular Concrete 62

Figure 4-16: Moisture Uptake and RDM% for UHPCs (27) 63

Figure 5-1: (a) Test Set Up for Bar Pull Out (b) and Instrumentation and Load Path for Specimen 68

Figure 5-2: (a) Fibers Aligned Parallel to Bar (b) Fibers Aligned Transversely to Bar 70

Figure 5-3: Construction and Reinforcement Details for Precast Decks with UHPC Joint 73

Figure 5-4: Four Point Bending Test Set Up for Flexure Test for Specimens F-100-1P-1, F-100-1P-2, F-100-2P-1 and F-100-2P-2 73

Figure 5-5: (a) Bar Fracture, (b) Bar Slip, and (c) Conical Concrete Failure 77

Figure 5-6: (a) Force-Displacement for 6 d_b embedment and (b) 4 d_b embedment, (c) Nominal Peak Bond Stress vs. Embedment Length in mm and (d) in d_b for 13 mm bars 80

Figure 5-7: (a) Force-Displacement for 6.4 d_b embedment, (b) 4.8 d_b embedment, (c) 3.2 d_b embedment, (d) Nominal Peak Bond Stress vs. Embedment Length in mm and (e) in d_b for 16 mm bars 82

Figure 5-8: (a) Force-Displacement for 5.3 d_b embedment, (b) 4.0 d_b embedment, (c) 2.6 d_b embedment, (d) Nominal Peak Bond Stress vs. Embedment Length in mm and (e) in d_b for 19 mm bars 83

Figure 5-9: (a) Nominal Peak Bond Stress Achieved vs. Embedded Length and (b) Peak Bar Stress vs. Embedded Length, 2% fiber vol., Parallel Fiber Orientation, 28 days cured 84

Figure 5-10: Peak Bond Stress Comparison (Dark Gray- 19 mm bars at 4.0 d_b, Light Gray – 16 mm bars at 6.4 d_b) 85

Figure 5-11: (a) Nominal Peak Bond Stress Achieved and (b) Normalized Nominal Peak Bond Stress at 1% and 2% Fibers by volume: 19 mm bars, Embedded 4.0 d_b (Dark Grey) and 16 mm bars, Embedded 6.0 d_b (Light Grey) 86

Figure 5-12: (a) Force-Slip Curve, (b) Bond Stress – Relative Slip 87

Figure 5-13: (a) τ_{bond} as a Function of Curing Time, (b) Compressive Strength vs. Curing Time, (c) τ_{bond} vs. Square Root of Compression Strength of Concrete, $\sqrt{f'c}$, over time 88

Figure 5-14: Average Bond Stresses in lap splices vs. bar pull out specimens. 90

Figure 5-15: Scatter of the current data available for 13 mm, 16 mm, and 19 mm bars (Graybeal 2006, 2014, Fehling 2012, Holschemacher 2004, Jungwirth 2004) 91

Figure 5-16: τ_{bond} for 16 mm Bars (Graybeal, 2014) 92

Figure 6-1: Shear and Moment forces in beams under (a) pure flexure loading and (b) combined shear and flexure testing 97

Figure 6-2: Joint Dimensions and Reinforcement Details 100

Figure 6-3 Joint Shape Details for the 4 in (a), 6 in (b) 8 in (c) joint, Lap Splice Connection Detail (d) 102

Figure 6-4: Instrumentation of the Precast Bridge Deck Beams 104

Figure 6-5: Deformed #5 (16 mm) Epoxy Reinforcement Bar 104

Figure 6-6: Forms and Placed Bars (a), Lap Splice (b), Poured UHPC Joint (c), and Set up with DIC (d) 106

Figure 6-7: Comparison of Calculated and Measured Bar Stresses 108

Figure 6-8: (a) DIC of 100 mm joint specimens, (b) Splitting Failure in deformed specimen, (c) Load-Deflection Curves for 100 mm specimens with 2% fibers and (d) 100 mm specimens with 1% fibers. 109

Figure 6-9: (a) DIC of 150 mm joint specimens, (b) Splitting Failure in deformed specimen, (c) Load-Deflection Curves for 150 mm specimens and (d) 200 mm specimens. 111

Figure 6-10: Maximum Force in F-100 Decks at a Function of Fiber Volume Content 112

Figure 6-11: Moment at Joint as a function of Joint Width 113

Figure 6-12: (a) DIC of 100 mm joint, SF specimens, (b) Splitting Failure in deformed specimen, (c) Load-Deflection Curves for 100 mm specimens, 1% fiber by vol. and (d) 100 mm specimens, 2% fiber by vol. 115

Figure 6-13: Peak Average Bond Stress in UHPC lap splices (Dark Gray) vs. bar pull out specimens (Light Gray, Alkaysi & El-Tawil (2016)) 117

Figure 6-14: (a) Finite Element Model and (b) Mesh for F-150-2P Specimens 118

Figure 6-15: Typical UHPC Tensile Response for Joint Fill Material (a) tension and (b) compression 119

Figure 6-16: (a) Original Joint Design for FEA, (b) non-tapered joint design, and (c) flat joint design. 120

Figure 6-17: Experimental FEA Load-Deflection for (a) 150 mm joints and (b) 200 mm joints 122

Figure 6-18: (a) Un-deformed shape, (b) deformed shape and (c) von Mises Strain for 150 mm, (d) Plot of the cracks developed and (e) and Damaged Beam after Testing, Actual joint.......... 123

Figure A.1. – White Cement Mixes ...…………………………………………………… 132

Figure A.2. – Portland V Mixes ………..……………………………………………… 134

Figure A.3. – GGBS Mixes …...…………………………………………………..………136

Figure B.1. – Durability for White Cem. ...…………………………………………..………138

Figure B.2. – Durability for PV Cem. ...……..……………………………………..………139

Figure B.3. – Durability for GGBS Cem. ...……………………………………...…..………140

Figure C.1. – Details from Bar Pull Out ....………………………………………….………142

Figure D.1. – Details from Beam Testing ..……………………………………………..………174

List of Tables

Table 3-1: Chemical and Physical Properties of Materials 17

Table 3-2: Mixture Proportions by Weight with Cost Index 19

Table 3-3: Cement Properties 20

Table 3-4: Cost and Performance Summary 28

Table 3-5: UHPC Mix Design and Ratios 40

Table 4-1: Mix Proportions for tested UHPCs 44

Table 4-2: Summary of Test Results 50

Table 4-3: Chloride Permeability Rating 58

Table 5-1: Experimental Parameters and Number of Tests 71

Table 5-2: Steel Strength Properties Provided Steel Reinforcement Bars 75

Table 5-3: Test Results for Simple Bar Pull Out 78

Table 5-4: Test Results Beam Lap Splice Tests 89

Table 6-1: Main Variable of Beam Specimens 101

Table 6-2: Summary of Results from Experimental Testing 107

Table 6-3: Material Parameters for FEM 119

Table 6-4: Summary of Simulated Beams 120

List of Appendices

Appendix A - Stress-Strain Plots for All UHPC Mixes ……………………...…….……… 130

Appendix B - Results of Freeze-Thaw Testing – Rilem ……………………………………… 137

Appendix C - Details from Bar Pull-Out Testing …….………………………………………… 140

Appendix D - Details of Beam Testing …….………………………………………………… 172

Abstract

Ultra-high performance concrete (UHPC) is a cementitious material that achieves a compressive strength of at least 22 ksi (150 MPa) and has self-consolidation properties. It is comprised of component materials with particle sizes and distributions carefully selected to maximize packing density. The high packing density, which means that constituent particles are arranged as compactly as possible, is the reason for the extremely high mechanical and durability properties of the material.

Some of the component materials of UHPC are substantially more expensive than those used in regular concrete. To optimize cost, research was conducted to investigate the relationship between material performance and the type or amount of the most expensive components, i.e. cement, silica fume and silica powder. Short-term material performance was assessed via tensile and compressive tests and durability properties were evaluated based on freeze-thaw and chloride ion penetration testing as well as quantification of the presence and distribution of air voids. The test results were used to optimize cost versus performance characteristics of the UHPC blends considered.

A low cost UHPC material with excellent characteristics in compression and tension, as well as exceptional resistance to freeze-thaw and chloride ion penetration was developed. The proposed mix deviates from traditional UHPC mixtures in that it uses a 50:50 mix of Portland Type I and Ground Granulated Blast Furnace Slag (GGBS) as a binder, lacks any Silica Powder (inert filler) and requires no post-placing treatment. The cost of the cementitious material ingredients was reduced by half compared to available non-proprietary UHPCs available at the onset of this research. The use of GGBS improves the material's 'greenness' making it a more sustainable cementitious product.

At the structural level, a comprehensive study investigating the bonding between UHPC and deformed bars was carried out to investigate the effect on bond of bar size, type, embedded length, fiber content, fiber orientation and curing age. The developed UHPC blend was then used to conduct a comprehensive study on bond between UHPC and deformed steel bars to facilitate and enable future structural applications. Bond pull out tests showed the developed UHPC requires significantly reduced development lengths in order to attain steel bar yield compared to traditional concrete. Using this data, new joints making use of UHPCs superior bond characteristics were constructed and tested in order to prove a quick and simple method for the assembly of precast bridge elements. Models to characterize the bond strength were proposed and a UHPC joint consisting of two pre-cast bridge deck elements was developed and tested. It was shown that a 150 mm (6 inch) joint was sufficient to successfully transfer loading between the decks.

Chapter 1

Introduction

Infrastructure in the United States is consistently rated poor by the American Society of Civil Engineers (ASCE, 2013). Our roads, bridges, highways, buildings and water resources have largely outlived their design life span and are in need of replacement or rehabilitation. This is especially true for the majority of our reinforced concrete bridges, roadways and buildings. Traditional concretes lack significant tensile resistance. They therefore easily crack under service loads allowing for the ingress of water and chlorides, which in turn can lead to corrosion of the steel reinforcement. Corrosion of bar reinforcement leads to additional spalling of the concrete cover leading to further structural degradation, resulting in a vicious cycle of deterioration. Ultra-high performance concrete has the potential to address many of the flaws of regular concrete. Using it as a replacement to traditional concretes presents a unique opportunity for future engineers to design new reinforced concrete structures which would be longer lasting, more sustainable, and require lower maintenance.

1.1. Ultra-High Performance Concrete (UHPC)

Ultra-high performance concrete is a new class of cementitious materials that achieve a compressive strength of at least 22 ksi (150 MPa) (Wille et al. 2014, Graybeal 2014, Wille et al. 2012, Wille et al. 2011). When properly reinforced with steel fibers, UHPCs can achieve strain hardening behavior and display compressive and direct tensile strengths as high as 35 ksi (242

MPa) and 2 ksi (14 MPa), respectively (Graybeal, 2003). Changes in the type and quantity of steel fibers directly affect the ductility, durability and strength of the material (Wille et al. 2011; Kim et al. 2011, 2010a, 2010b, 2010c, 2008a, 2008b, 2008c, 2008d, 2007). UHPC also exhibits exceptional energy absorption prior to crack localization (Pyo et al. 2015a, 2015b, 2013a, 2013b, 2013c) and self-consolidation properties (Graybeal, 2006).

Recent developments in UHPC at the University of Michigan have led to new, non-proprietary formulations that are cheaper than the patented versions (Wille et al, 2011). The new formulation described in Wille et al. (2011) is made up of components readily available on the US open market, does not require any special mixing or placing equipment and has a higher ductility than other commercially available products (Rigaud et al., 2012). Relative to traditional concretes, the price of the non-proprietary UHPC in Wille et al. (2011) remains high, but still it is substantially less than its patented commercial equivalent. Further, there is little information regarding the behaviors of non-proprietary UHPCs at the structural level.

1.1.1. Short Term Mechanical Properties of UHPC

Previous works on UHPC have focused largely focused on achieving certain mechanical properties. Specifically, the goal had been to maximize the compressive and tensile performance, with little consideration to cost. Acknowledging that the majority of reinforced concrete structures will not need extremely high mechanical performance, the focus of this work was on understanding the underlying mechanisms effecting mechanical properties of UHPC with the goal of identifying a mixture that provides excellent mechanical properties while also minimizing the overall cost. This also includes an investigation into the effects of steel fiber reinforcement at the lower limits of fiber volume content.

1.1.2. Durability Characteristics of UHPC

Ultra-high performance concrete exhibits not only exception mechanical performance, but also resistance to the environmental damages typically associated with reinforced concrete structures. Previous works have investigated proprietary UHPCs' resistance through freeze-thaw tests and chloride ion penetration resistance testing (Holschemacher, 2005), but none have studied the effects of individual material components on the overall durability of UHPCs. Specifically, works investigating the effect of cement type and silica powder on UHPCs' resistance to freeze-thaw and chloride ion damage needs to be investigated.

1.1.3. Bond between Steel Reinforcement and UHPC

Data on bond between ultra-high performance concrete and steel reinforcement bars is needed in order for ultra-high performance concrete to see a proliferation in its use for structural applications. Previous works on bond have (Graybeal, 2014, Holschemacher, 2005) have shown that UHPCs ability to bond with steel reinforcement is much greater than traditional concretes Still, this work is only available for proprietary materials, and of that data, there is no clear trend for bond development to assist in future reinforced UHPC design.

1.1.4. Structural Performance of UHPC

The use of UHPC in full scale structural applications needs to be developed and shown to be possible outside of the proprietary materials. Currently, the majority of UHPC scale testing has involved live, on-site installations and demonstrations. Not only do there need to be UHPC components tested a larger scale, the structural building codes also need to be evaluated for their applicability for UHPC structures (ACI, AASHTO).

1.2. Objectives

With strengths in compression approaching that of mild steel, finding new uses for UHPCs is intriguing many practitioners, who want to use the material in their projects. However, broad usage is hindered by the high cost of the material and lack of test results, and understanding in general, of UHPCs behavior at the structural level. With these issues in mind, along with the gaps in knowledge identified in Section 1 above, the objectives of this research project are:

- Investigate whether a family of new UHPC materials can be made using locally available components and optimize the cost by tailoring of the mix, while still maintaining ultra-high performance characteristics.
- Characterize the properties of the new family of UHPCs, focusing on tensile strength, compressive strength, modulus of elasticity, and durability (resistance to environmental factors) by laboratory testing.
- Conduct pullout tests of steel reinforcing bars from UHPC to investigate the bond strength between steel bars with various coatings and the surrounding UHPC matrix.
- Investigate using computational and experimental methods the behavior of UHPC field joints (closure pours).

1.3. Organization of this Dissertation

- *Chapter 1: Introduction.* A general overview of the motivation and objectives of the research is presented.
- *Chapter 2: Background and Literature Review.* An outline of the previous works involving UHPC that are of interest to the topics covered in this dissertation.

- *Chapter 3: Effects of the Variations in the Mix Constituents of UHPC on Cost and Performance.* An investigation into how material properties change as a result of variations in the amount and/or type of individual components. The chapter aims to optimize the cost of UHPC with respect to its strength.
- *Chapter 4: Effects of Silica Powder and Cement Type on the Durability of UHPC.* Investigates the durability of select UHPC mixes identified in chapter 3 through freeze-thaw testing, rapid chloride penetration testing and air void characterization.
- *Chapter 5: Factors Effecting Bond Development Between UHPC and Steel Bar Reinforcement.* This chapter provides an in depth study into the factors affecting bond between UHPC and reinforcing steel.
- *Chapter 6: Simplified non-proprietary UHPC Joints for Pre-Cast Bridge Deck Connections.* A study on the use of UHPC in precast bridge constructions via experimental testing and finite element analysis. A model is proposed and analyzed for future FE analysis of UHPC structures.
- *Chapter 7: Summary and Conclusions.* A summary of the research, the most important conclusions and future work.

1.4. Publications from this Dissertation

The material in Chapters 3 and 4 has already been published as two different journal papers. Chapter 5 is currently under review and chapter 6 is in preparation.

- **Alkaysi, M.,** Sherif El-Tawil. (2015). “Effects of Variations in the Mix Constituents of Ultra High Performance Concrete (UHPC) on Cost and Performance." *Materials and Structures* **(Chapter 3)**

- **Alkaysi, M.**, Sherif El-Tawil. (2016). "Effects of Silica Powder and Cement Type on Durability of Ultra High Performance Concrete (UHPC)." *Cement and Concrete Composites* **(Chapter 4)**
- **Alkaysi, M.**, S. El-Tawil. (2016). “Factors Effecting Bar Bond Development Between Ultra-High Performance Concrete (UHPC) and Steel Bar Reinforcement,” *ASCE Journal of Structural Engineering,* In Review (**Chapter 5)**
- **Alkaysi, M.**, S. El-Tawil. “Simplified Ultra-High Performance Concrete (UHPC) Joints for Accelerated Bridge Constructions” In Preparation. **(Chapter 6)**

Chapter 2

Background and Literature Review

2.1. Strength of UHPC

2.1.1. Compressive and Tensile Behavior of UHPC

The high compressive strength of UHPC is well known and established (Graybeal, 2014). Larrard and Sedran (1994) produced a concrete mortar with a compressive strength of 35 ksi (236 MPa). Wille, Naaman and El-Tawil (2011) were able to prepare UHPCs with 28-day compressive strengths in excess of 30 ksi (200 MPa) without requiring the use of expensive post treatment techniques. Graybeal (2006) has shown that UHPC reaches a peak stress of around 22 ksi at 0.003 strains (0.3%). Wille and Namaan (2011) showed that when reinforced with steel fibers, UHPC mixes were able to achieve 0.6% strain capacity in tension prior to strain softening. More information regarding the tensile and compressive behavior of UHPCs can be found in the works by Wille (2011) and Graybeal (2003, 2006, and 2014).

UHPC not only has a higher tensile strength than conventional concrete, it can also exhibit strain hardening response after initial cracking when properly reinforced with steel fibers. The typical stress strain curve for ultra-high performance concrete is shown in Figure 2-1. Following the definitions set forth by Naaman (Naaman & Reinhardt, 2007), the first part of the material's tensile behavior is elastic, which continues up until the specimen develops an initial crack at what is known as the first cracking strength point (σ_{cc}, ε_{cc}) in Figure 2-1. Following this, the material then exhibits strain hardening up until its peak point (σ_{pc}, ε_{pc}). The strain hardening behavior of segment II is typically characterized by multiple crack development in the gauge length of the specimen. Following the strain-hardening region, the material then begins to exhibit crack localization (segment III). This segment of the curve is best represented by a stress versus crack opening response but many researchers continue to describe the region as a stress versus strain relationship, based on the nominal gage length of the specimen, as is done herein.

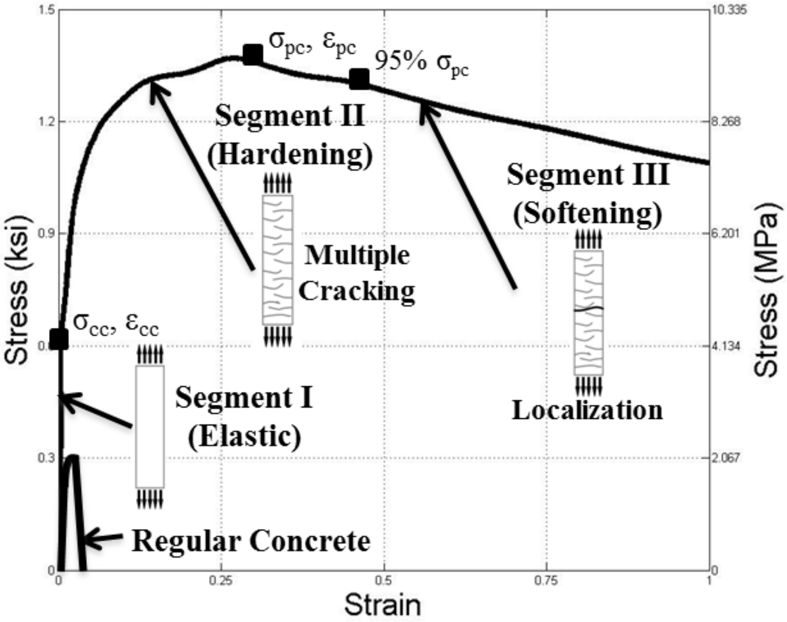

Figure 2-1 Typical Tensile Strain Response in UHPC

2.1.2. Effect of Silica Fume

Most UHPCs contain silica fume and silica powder. Silica fume is a reactive powder with pozzolonic properties. Silica powder is an inert powder, used primarily to increase the density of the cementitious matrix. Several research studies have investigated the effects of silica fume (SF) on the behavior of UHPCs. Rong, Xiao and Wang (2014) investigated the effects of SF on the hydration and microstructure of UHPCs, concluding that SF dominated the hydration process at lower water-binder ratios. Rong et al. (2015) also partially replaced cement with SF in UHPCs and determined the flexural and compressive strengths were highest when the content of SF was approximately 3% to binder, and decreased at higher contents due to the agglomeration of SF particles. Brouwers et al. (2014) similarly investigated the effect of SF on the UHPC hydration process and material behavior, concluding that an optimal ratio of 3.74% SF to binder yields the highest mechanical properties of UHPC. Oertel et al. (2013) reported that the nearer the dispersion of silica particle sizes match to those in the primary mixture particle sizes, the further the compressive strengths increase in UHPCs. Wille (2015) studied the effects of various SFs on the compressive behavior in UHPCs, and reported compressive strengths ranging from 20 ksi to 26 ksi. To the authors' knowledge, no work has been done on the effect of silica fume on the direct tensile properties of UHPCs.

2.1.3. Effect of Silica Powder

To date, little work has been done to investigate the effects of Silica Powder (SP) on the tensile and compressive performance of UHPCs. Wille (2011) researched the effects of SP on UHPCs ranging from 0 SP-binder to 0.5 SP-binder ratios, finding a ratio of 0.3 SP to cement yielded the highest compressive strength. As with silica fume, to the knowledge of the authors, no work has been done evaluating the effect of different silica powder quantities in UHPCs under direct tension.

2.1.4. Effect of Cement

Additionally, little work has been done to investigate the effects of various cements on the material behavior of UHPC. Yu and Brouwers (2015) used fly ash (FA), ground granulated blast-furnace slag (GGBS) and limestone powder (LP) to replace cement in UHPC mixes, determining UHPCs with the GGBS has higher mechanical properties at 28 and 91 days than with other cements they considered. Wille (2015) investigated the compressive strengths for UHPCs substituting several different cements, yielding strengths between 19 ksi (130 MPa) and 32 ksi (221 MPa). To date, no work quantifies the effects of cement type on the tensile response of UHPCs.

2.1.5. Effect of Fiber Type and Quantity

Several papers currently discuss the effects of fiber content, shape, size and topology on ultra-high performance concretes. The addition of steel fibers into the ultra-high performance concrete matrix leads to enhanced material performance such as a high tensile capacity, ductility, reduced crack spacing, and high energy dissipation capability. The magnitude of these effects is a direct result of the fiber material strength, cementitious matrix – fiber bond ability, fiber aspect ratio (length: diameter), fiber volume content and fiber surface topology. Pyo (2015) investigated the strain rate dependent tensile properties of UHPCs with different fibers and fiber volume contents. Wille (2011) investigated the tensile performance of UHPCs with fiber contents as low as 1%. Yu and Brouwers (2015) investigated hybrid fiber UHPCs containing a combination of hooked, short and long straight fibers, at 2% volume contents. They concluded that the combination of several fiber types yields ultra-high performance while using fewer fibers. To date, no work has been done investigating the effect of low fiber contents (<1%) on the compressive and tensile performance of UHPC.

2.2. DURABILITY OF UHPCs

2.2.1. Freeze-Thaw Resistance

Tests investigating UHPCs resistance to freeze-thaw have been limited. Ahlborn et al. performed freeze-thaw cycling tests in accordance to ASTM C 666 (2008), procedure B, showing that after

32 freeze-thaw cycles, ultra-high performance concrete specimens showed no degradation. Acker and Behloul (2004) similarly reported that after 300 freeze-thaw cycles, UHPC showed no degradation. Pierard et al. (2012) reported that specimens achieving strength between 20.3 ksi (140 MPa) and 23.2 ksi (160 MPa) also showed no degradation after 112 cycles. Graybeal (2006) performed air void analyses on Ductal©, finding UHPC void numbers to be between 0.2 and 7.5 voids/in (0.008 and 0.30 voids/mm), corresponding to an air content of 5.7% to 7.3% with no vibration.

To date, no research has been done to investigate the durability parameters for a non-proprietary blend of UHPC. Further, no testing has been done to investigate the effects of various material parameters on the durability of UHPC. Yazici (2008) looked into the effect of silica fume and high-volume Class C fly ash on the durability of self-compacting concretes, determining that a 10% by volume inclusion of silica fume resulted in enhanced freeze-thaw resistance, accompanied by increased compressive strengths. Work by Alexander and Magee (1999) evaluated the durability of concretes containing condensed silica fumes and ground granulated blast furnace slag (GGBS), determining blends containing these materials outperformed regular concretes in durability testing of water absorption.

2.2.2. Chloride Ion Penetration Resistance:

Performing rapid chloride permeability tests, Ahlborn (2008) showed that UHPC was capable of achieving permeability values less than 100 coulombs for both air-cured and steam-cured specimens. Materials with coulomb values less than 100 are generally considered to have negligible chloride ion penetration. Testing two different types of reactive powder concretes, Bonneau (1997) showed that specimens were able to achieve 6 to 9 coulombs. Graybeal (2006) reported that untreated specimens achieved coulomb values of 360 and 76 at 28 days and 56 days respectively. Most of the existing chloride permeability studies pertain to proprietary materials and data for non-proprietary blends is lacking at present.

2.3. Bond Development in UHPCs

2.3.1. Bond Development of Steel Bars Embedded in UHPC

There is limited published data on the bonding behavior between UHPCs and steel reinforcement bars. Graybeal (2010, 2014) performed pull out tests for #4, #5, and #6 bars embedded 3, 4 and 5 inches (75, 100 and 125 mm) respectively into UHPC cylinders, with all of the steel bars fracturing before bond failure. Graybeal (2014) recently has shown that under static conditions, UHPC specimens are capable of developing a bond stresses of approximately 2.9 - 5 ksi (20 – 35 MPa) in bar pull out specimens and are largely dependent on bar spacing, concrete cover, and development length and bar size. In a different study, Swenty and Graybeal (2012) performed pull out tests on #4 bars embedded into 6 in (150 mm) concrete cubes. Two different UHPC mixes were used, one achieving bar fracture and the other achieving bar yield. Performing pull out tests on 12 mm diameter bars, varying concrete cover and embedment lengths, Fehling et al. (2012) determined that increasing cover widths and embedment lengths increased the bond stress, reaching those sufficient for bar yield. Holschemacher et al. (2004) reported achieving bond stresses up to 8.7 ksi (60 MPa) using 12 mm bars in UHPC cylinders. Saleem et al. (2013) investigated the development length requirements for high strength steel bars in UHPC, concluding that 10 mm and 22 mm (#3 and #7 U.S. sizes) bars require 12 d_b and 18 d_b to develop adequately. Jungworth et al. (2004) performed tests on 20 mm and 12 mm diameter bars, reaching bond stresses of 5.5 ksi (38 MPa) and 9.5 ksi (66 MPa). Of the literature currently available on bond, data only exists on testing performed using Ductal® or Ceracem®, both proprietary concretes No published data currently exists for non-proprietary UHPCs. As discussed later on, there is much discrepancy in existing data regarding the maximum achieved bond stress during the pull out tests, with some studies reporting values as high as 9.5 ksi (66 MPa), or as a low as 1.4 ksi (9.8 MPa) (Graybeal, 2010).

2.3.2. Lap Splice & Component Tests with UHPC

Component level testing with UHPC remains largely confined to highway infrastructure projects. The Federal Highway Administration has released several reports on test installations on existing structures. UHPC was used in concrete waffle slab decks in an accelerated bridge construction in Wapello County, Iowa showing that UHPC is a viable material for infrastructure redesign (Wipf et al, 2011). New York D.O.T. also tested a live installation of a UHPC joint using hooked bars and a small joint width, also concluding exceptional joint performance for the UHPC (FHWA, 2014).

Steinberg et. al. (2010) investigated the structural reliability of pre-stressed UHPC flexure models for bridge girders showing that acceptable levels of reliability can be obtained using typical AASHTO procedures. Graybeal (2014) released a series of tests evaluating the joint force transfer capacity of UHPC under various parameters, including type of bars, size of bars etc. He concluded that UHPC was able to act as a closure pour joint between two precast decks more efficiently than traditional grouts and concretes at splice lengths as little as 6 inches (150 mm). Of these tests performed so far, all of them have made use of Ductal.

Few studies have investigated the splice length requirements for UHPC joints. Graybeal recently investigated the splice length of pre-stressing strands in field cast UHPC connections, concluding that 12 mm and 15 mm diameter strands require 20 inches (510 mm) and 24 inches (610 mm) to fully develop (Graybeal, 2015). Hoonhee and Park (2014) investigated the lower limits of contact splice lengths in precast, steam-cured UHPC beams under flexure, determining a lap splice length greater than 6 in. (150 mm) was required to cause yield in the bars. Both of these studies were performed using Ductal, i.e. no studies currently exist for non-proprietary UHPCs, as provided herein. Furthermore, to the author’s knowledge no studies exist investigating the UHPC’s performance in non-contact lap splices between two precast beam elements, as done herein.

Chapter 3

Effects of Variations in the Mix Constituents of UHPC on Cost and Performance

3.1. OVERVIEW

This chapter investigates the performance of several new UHPC mix designs with a focus on minimizing cost. Performance parameters include compressive strength and full tensile stress-strain characterization. The experimental variables are four different quantities of silica fume, three different quantities of silica powder, three different cement types (white cement Type I, Portland cement Type V, GGBS/Portland cement Type I blend) and three different fiber volume contents (0.5%, 1.0%, and 1.5%) of straight, smooth, high strength steel fibers. Experimental results showed minor differences in mechanical behavior due to variations in the quantity of silica fume. Silica powder changes led to little difference in material behavior, suggesting that silica powder can be removed due to its high cost. UHPCs containing white cement Type I exhibited the best performance in almost all aspects of behavior including load carrying capacity, energy absorption capacity and multiple cracking behaviors, but carried the highest cost. Specimens containing the GGBS/Portland cement Type I binder showed lower performance, but at decreased cost. UHPC specimens containing 0.5% fibers exhibited some strain hardening behavior, which became more pronounced as the fiber volume fraction increased. The results suggest that fiber volume contents of 1.0% or 1.5% could significantly reduce the chance for crack localization under dead load or working conditions, respectively, in structural applications.

3.2. EXPERIMENTAL PARAMETERS AND PROCEDURE

3.2.1. UHPC Material Properties and Cost

UHPC, depending on the types and quantity of reinforcing fibers added to the cementitious mixture, carries a high cost. Currently, commercially available proprietary blends cost \$2,000/yd^3 (\$2615/m^3) and includes 2% steel fibers by volume (Ahlborn, 2008). This is 15 - 20 times higher than the cost of conventional concrete. Using current prices, the UHPC recently developed at the University of Michigan (Wille, 2011) carries a lower cost of materials (\$516/yd^3 without fibers, \$1,029/yd^3 with 2% fibers).

The cement used in the initial development of the UHPC in Wille et al. (2011) was a Portland Type I white cement. This cement has a high C_3S content (74%), and a moderate fineness (3930 cm^2/g Blaine Value) as well as a low C_3A content (less than 5%). The particle sizes and costs for each UHPC constituent is listed in Figure 3-1 shows the grain size distributions for the two types of sands, F12 and F100 used in this research. The materials are obtained from reputable suppliers and the costs specified are valid for 2013 when the bulk of the research was conducted.

In Wille et al. (2011), the optimal cement to silica fume to silica powder ratio was determined to be 1 C: 0.25 SF: 0.25 SP, with a w/c ratio of 0.22 and a compressive strength of 27.8 ksi (192 MPa). Maintaining the w/c ratio established in the previous work, Table 3-2 lists the mix proportions and associated costs (without fibers) for all of the mixes considered in this work. Cost is listed as a cost index in order to simplify the discussion later on. The cost index is simply the ratio of the mix's cost compared to the starting mixture published in Wille (2011), based on current prices in the US. The index is a relative indicator of cost, since actual costs will vary in time and by location. The first entry, W-25-25, represents the original mix ratio in (Wille, 2011).

`	Median	10% of Particles	90% of Particles
Cement	10 – 20 µm	3 µm	40 µm
Silica Fume	0.1 – 1 µm	0.1 µm	10 µm
Silica Powder	10 – 20 µm	1 µm	40 µm
F12 Sand	500 µm	Larger than 300 µm	Smaller than 1000 µm
F100 Sand	100 µm	Larger than 50 µm	Smaller than 300 µm
Silica Fume		Silica Powder	
SiO_2	Minimum 85%	SiO_2	Maximum 90%
H_2O	Maximum 3%	H_2O	Maximum 1%
Pozzolonic Activity	Minimum 105%	Pozzolonic Activity	N/A

Table 3-1: Chemical and Physical Properties of Materials

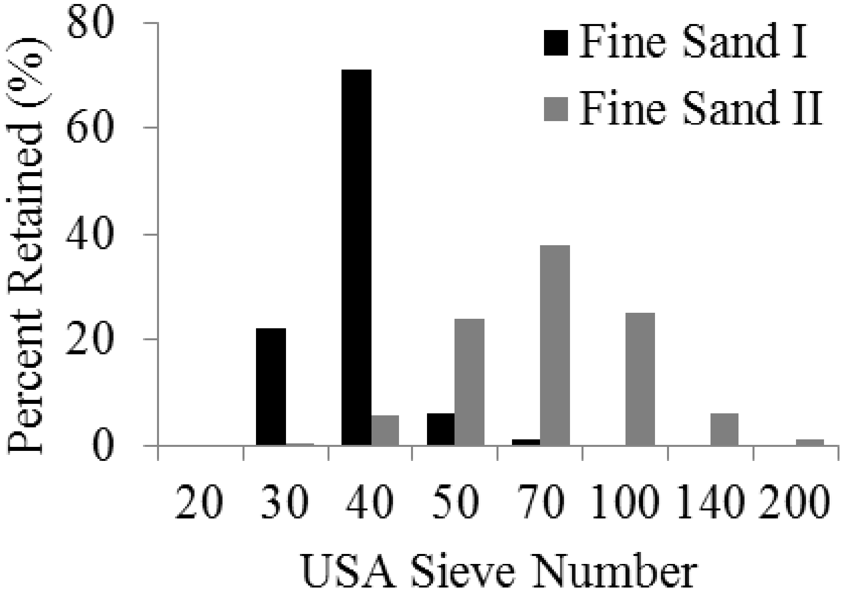

Figure 3-1 Grain Size Analysis for Sand

Cement quantity was held constant at 1306 lbs/yd^3 throughout all mixes. Additionally, the admixture Advacast 575 high range water reducer was again used at a ratio of 1.35% to cement for all mixes. All mixes use the same, low w/c ratio of 0.22. Cement, silica powder, and silica fume carried the highest costs per cubic meter. In order to lower this cost, 2 additional types of cement were identified for their reduced cost, Portland Type V and a Ground Granulated Blast Furnace Slag (GGBS) / Portland I cement blend. Table 3-3 lists the properties for the three cements used in this study. The Type I / GGBS cement blend was identified as a candidate for its exceptional long-term performance (Cheng et al., 2005).

Name	White Cement Type I	Silica Fume	Silica Powder	Cost ($\$/\text{yd}^3$)	Cost Index*
W-25-25	1.00	0.25	0.25	513	1.0
W-30-20	1.00	0.30	0.20	502	0.98
W-35-15	1.00	0.35	0.15	492	0.96
W-25-20	1.00	0.25	0.20	487	0.95
W-25-15	1.00	0.25	0.15	461	0.90
W-25-00	1.00	0.25	0.00	369	0.72
	Portland Type V				
PV-25-15	1.00	0.25	0.15	364	0.71
PV-25-10	1.00	0.25	0.10	338	0.66
PV-25-05	1.00	0.25	0.05	307	0.60
PV-30-05	1.00	0.30	0.05	338	0.66
PV-35-05	1.00	0.35	0.05	348	0.68
PV-25-00	1.00	0.25	0.00	282	0.55
PV-25-25	1.00	0.25	0.25	420	0.82
	Portland Type I / GGBS Cement				
GG-25-00	1.00	0.25	0.00	266	0.52
GG-25-15	1.00	0.25	0.15	353	0.69
GG-25-25	1.00	0.25	0.25	405	0.79

*Matrix only, without fibers.

Table 3-2: Mixture Proportions by Weight with Cost Index

Type	C_2S %	C_3S %	$C_2S + C_3S$ %	C_3A %	C_4AF %	Blaine m^2/kg
White Cement Portland Type I	13	74	87	5	1	395
Portland Type V Cement	17	59	76	4	15	430
Type I / Slag Cement Blend	13	58	71	8	10	600

Table 3-3: Cement Properties

The cost for silica powder and silica fume was reduced through reductions in material quantities. Ratios for SF ranged from 0.25 SF: C to 0.35 SF: C. Ratios for SP ranged from 0.00 SP: C to 0.25 SP: C. Reduction in the amount of SP was of particular interest due to its high material cost. In some mix designs, when SP was reduced, the amounts of SF were increased since SF and SP have similar particle sizes along their particle size distribution.

3.2.2. Steel Fibers

Steel fiber reinforced concretes resist post-cracking tensile stress through the composite action between the concrete and fibers, including chemical and mechanical bonding at the interface between the two. In this study, all UHPC mixes contain 1.5% steel fibers by volume of the wet concrete. The steel fibers (Figure 3-2) used are brass coated, smooth fibers. Each fiber is 0.75 in (19 mm) long with a diameter of 0.0078 in (0.2 mm) and has a minimum tensile strength of 285 ksi (1965 MPa).

Figure 3-2: Example of the Steel Fibers Used in this Study

3.2.3. Mixing Procedure

Mixing was done using a large Hobart food-type mixer with a 2.65 gal. (10 liter) capacity (Figure 3-3). First, silica fume and the two silica sands were added into the mixer and were dry mixed for approximately 5 minutes at 136 rpm. Silica powder (if any) and cement were then added into the pan and mixed for an additional 5 minutes at 136 rpm. After this, water and the high range water reducer was gradually dispensed into the pan while the mixer was spinning. The blend was allowed to mix for approximately 1-2 more minutes at 136 rpm. Then the mixing speed was increased to 281 rpm for approximately 5 min, or until the concrete reached an acceptable consistency. Once an adequate mixture consistency was achieved, the high strength steel fibers were added into the mixer and allowed to mix at 136 rpm until the fibers were sufficiently dispersed.

Figure 3-3 Mixing process (photos courtesy of Prof. Kay Wille)

3.2.4. Tensile Strength Testing:

For the purpose of this study, a direct tension test based on AASHTO T 132-87 (2009) was chosen to test the specimens. In this test procedure, precast specimens were made and then tested under direct tension. As shown in Figure 3-4, the specimens are supported by plates ensuring anchored and rotation-capable boundary conditions.

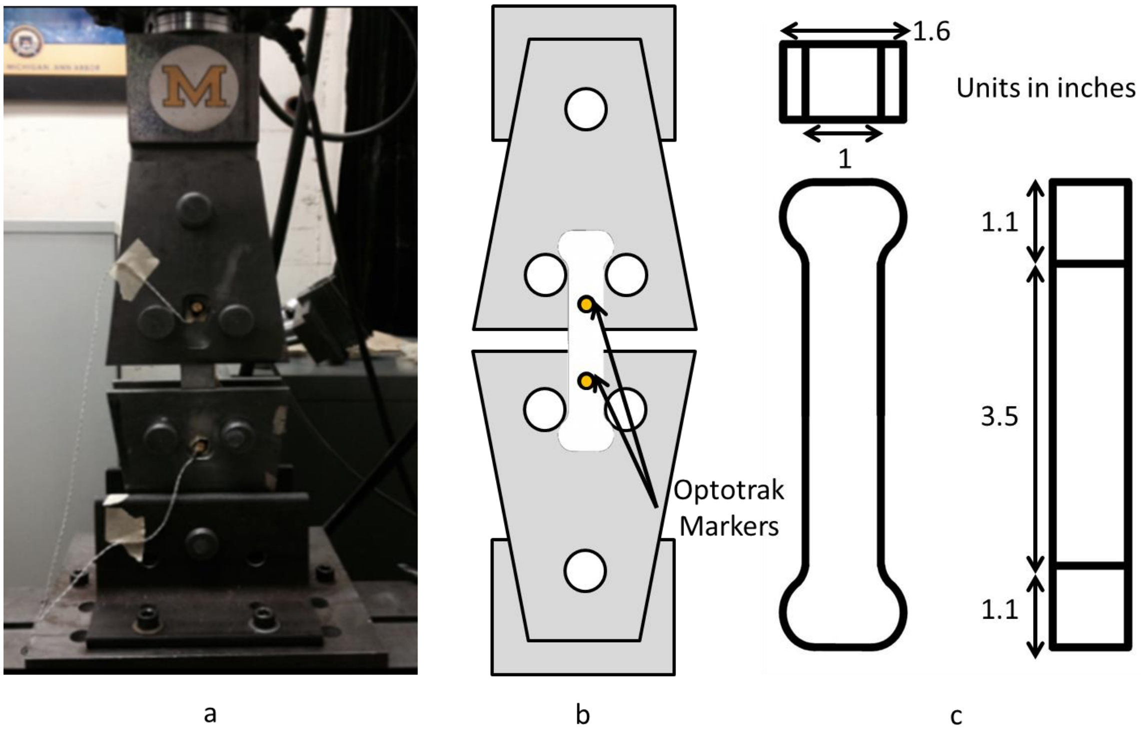

Figure 3-4 (a) Tensile test set up, (b) Instrumentation, (c) Specimen dimensions

Each specimen has a constant cross sectional area of 1 in^2 (25 mm^2) and a gauge length of 3.14 in (80 mm). The long gauge length used enables careful observation for multiple crack development. The UHPC specimens were first mixed in accordance with the procedure prescribed above. They were then poured in layers into dog-bone shaped molds to full capacity. No vibration was used. After initial casting, the specimens were covered and stored at room temperature for 24 hours. Following this, the specimens were removed from the molds and stored in a water tank at 68° F (20° C) for 28 days. Specimens were then given time to dry (approximately 12 hours) and then tested. For each of the mixes, at least 6 dog-bone tensile specimens were tested and the stress and strain data recorded. Figure 3-5a shows a tested specimen.

Each tensile specimen was carefully loaded into the MTS testing machine. A small preload (20% of the matrix cracking strength) was applied to the specimen, which was then manually moved into the best-aligned position to insure uniaxial tension stress. The loading rate was set to 0.003 in/min those results in an estimated strain rate of $\dot{\varepsilon} = 0.0001 \text{ s}^{-1}$. Following the tensile tests, the specimen crack distribution was observed and quantified. Isopropyl alcohol 99.9% was sprayed onto the specimens followed by a blue dye. The contrast in color between the dye and specimen enables a clear visualization of the crack formations.

3.2.5. Compression Testing:

The UHPC specimens were first mixed in accordance with the ratios prescribed above. Compression specimens were poured at once into 2 in. (50 mm) cubed molds. At least 6 compression specimens were tested for each mix and their post cracking strength recorded. The cube specimens were placed into the center of the testing machine and tested in accordance to ASTM C109 (2009). Some specimens were initially precision ground in order to provide a flat surface for testing, however this was later stopped, as it did not yield noticeable differences in strengths between ground and non-ground specimens. Figure 3-5b shows a tested specimen.

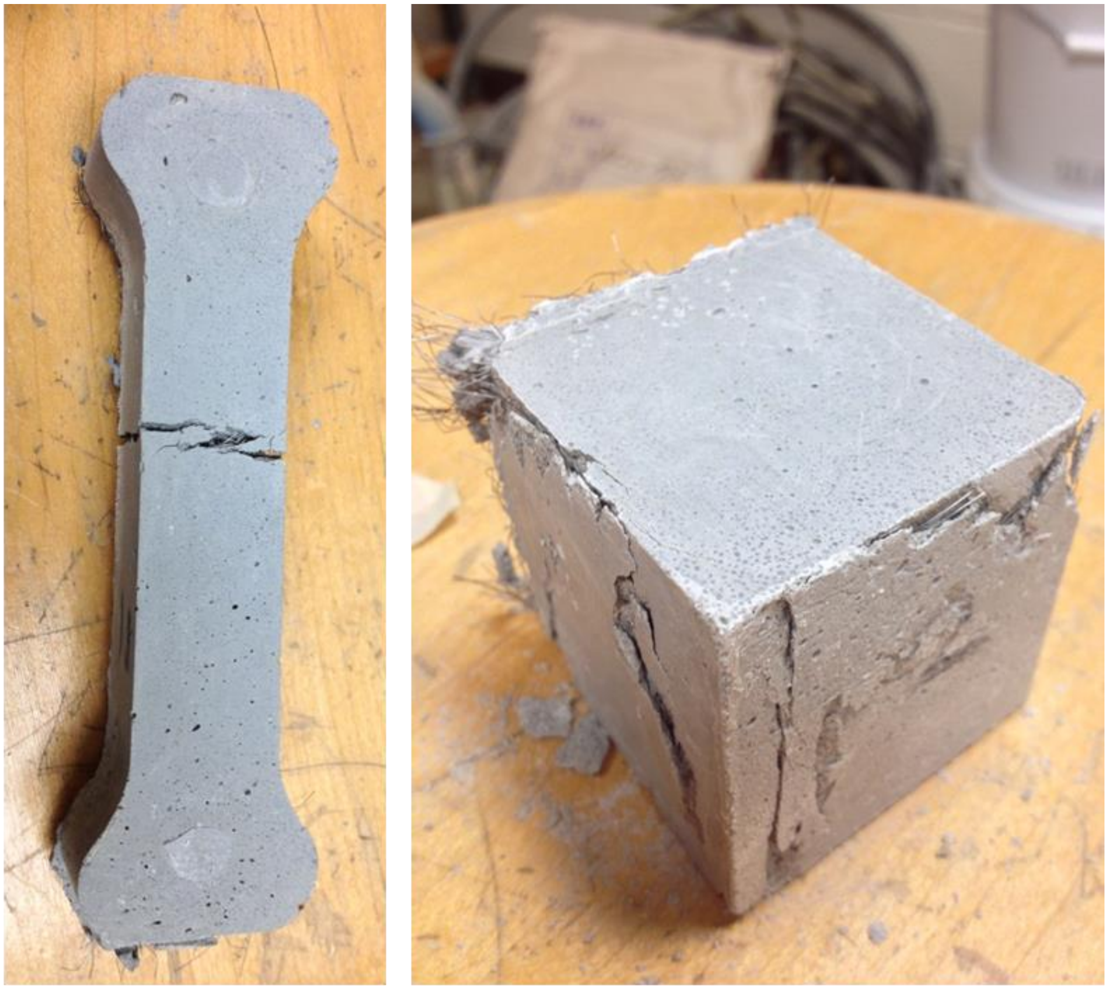

Post Test Tensile Specimen **Post Test Compression Specimen**

Figure 3-5: Tensile and Compression Specimens Post Test

3.3. RESULTS AND DISCUSSION

3.3.1. Analysis of Data

The following naming scheme was used in order to simplify the discussion of the results. The first number corresponds to the cement type used in the mix design as discussed earlier, W for White Cement Type I, PV for the Portland V and GG for the Portland I / GGBS mix. The second letter refers to the quantity of silica fume present in the mix. The third number corresponds to the quantity of silica powder, and the fourth number corresponds to the steel fiber volume fraction of the UHPC mix design. For example, W-25-25-1.5 would indicate white cement, with 25% silica fume and 25% silica powder, containing 1.5% steel fibers by volume.

For compression, only the maximum compressive strength was considered. For the tensile testing, the test curve was broken down into the three distinct regions as discussed earlier. Adopting the characterization scheme from Naaman (1996), the following parameters were determined: first cracking strength, σ_{cc}, post cracking strength, σ_{pc}, strain capacity, ε_{pc}, energy absorption capacity, g, elastic modulus, E_{cc}, and stress in the fibers, σ_{fpc}. Also, the average number of cracks in the gauge length of the specimen was found. The energy absorption capacity, g, represents the energy absorption capacity prior to tension softening. This graphically corresponds to the total area under the curve up until 95% of σ_{pc}. Experience and experimental data showed that consistent softening behavior occurred in samples beyond this point. E_{cc} represents the elastic modulus of the material and is determined by the slope of the tensile curve prior to initial cracking. The value of σ_{fpc} represents the average fiber tensile stress as determined using the equation proposed by Naaman (1996) and is simply the total post cracking strength divided by 90% of the fiber volume content. This 90% factor is recommended to account for the statistical variability in the experimental procedure. For each set of tensile tests, at least 3 specimen tensile plots are averaged in order to produce a single tensile response curve. The plots are averaged at each point along the strain range. The result is then processed through a moving average filter to account for minute changes due to the sensitivity of the equipment. The average number of cracks is observed visually.

3.3.2. Overview of Results

The tensile and compressive test results produced by the experimental procedure are shown in **Table 3-4**. The average values between the six specimens tested per experiment were used.

Test Series	Compressive Strength	Post Cracking Strength σ_{pc}	Energy Absorption Capacity G	Strain Capacity ε_{pc}	Fiber Tensile Stress σ_{fpc}	Average Number of Cracks	Cost Index ($/$ Original Mix)*
	ksi (MPa)	ksi (MPa)	kcal/yd^3 (KJ/m^3)	%	ksi (MPa)	#	
W-25-25-1.5	28.0 (192.7)	1.4 (9.48)	5.5 (30.2)	0.19	101.3 (698)	7.8	1.0
W-30-20-0.5	21.0 (144.7)	0.9 (6.1)	0.6 (3.3)	0.05	196.5 (1354)	1.7	0.98
W-30-20-1.0	23.7 (163.5)	1.2 (8.1)	2.7 (14.9)	0.11	131.2 (904)	5.2	
W-30-20-1.5	28.3 (195.2)	1.4 (9.4)	10.0 (54.7)	0.64	100.9 (695)	8.3	
W-35-15-0.5	20.9 (144.1)	0.8 (5.7)	0.5 (2.6)	0.01	182.7 (1259)	2.2	0.96
W-35-15-1.0	24.0 (165.6)	1.4 (9.7)	3.7 (20.3)	0.16	155.7 (1073)	6.2	
W-35-15-1.5	28.4 (195.4)	1.3 (8.8)	4.3 (23.7)	0.07	94.9 (654)	7.8	
W-25-20-0.5	25.8 (177.6)	0.7 (5.1)	0.7 (4.1)	0.08	164.4 (1133)	2.2	0.95
W-25-20-1.0	27.3 (187.8)	1.0 (7.2)	2.7 (14.9)	0.18	116.5 (803)	4.3	
W-25-20-1.5	28.3 (195.3)	1.6 (10.9)	3.2 (17.5)	0.10	117.3 (808)	7.7	
W-25-15-0.5	26.3 (181.0)	1.1 (7.7)	1.4 (7.6)	0.07	246.9 (1701)	2.3	0.90
W-25-15-1.0	25.8 (177.8)	1.4 (9.6)	5.6 (30.5)	0.10	154.7 (1066)	5.2	
W-25-15-1.5	28.0 (192.7)	1.3 (9.2)	5.3 (29.2)	0.16	99.0 (682)	7.5	
W-25-00-1.5	25.2 (173.8)	1.2 (8.2)	4.0 (21.7)	0.18	88.2 (608)	11.0	0.72
PV-25-15-0.5	20.9 (143.7)	0.9 (6.1)	1.7 (9.4)	0.06	197.7 (1362)	2.5	0.71
PV-25-15-1.0	25.0 (172.1)	1.4 (9.5)	3.2 (17.3)	0.13	152.5 (1051)	6.4	
PV-25-15-1.5	26.6 (183.1)	1.6 (10.7)	6.5 (35.6)	0.11	115.4 (795)	8.3	
PV-25-10-1.5	25.3 (174.4)	1.2 (8.5)	10.5 (57.2)	0.33	91.6 (631)	10.5	0.66
PV-25-05-1.5	26.4 (182.0)	1.2 (8.1)	7.6 (41.6)	0.50	86.5 (596)	10.7	0.60
PV-30-05-1.5	25.0 (172.4)	1.2 (8.2)	7.0 (38.5)	0.27	87.8 (605)	11.0	0.66
PV-35-05-1.5	25.7 (177.2)	1.0 (7.2)	3.7 (20.2)	0.24	77.5 (534)	10.5	0.68
PV-25-00-0.5	22.2 (152.9)	0.6 (4.1)	1.4 (7.4)	0.15	132.8 (915)	2.4	0.55
PV-25-00-1.0	23.5 (161.7)	1.1 (7.6)	6.4 (35.1)	0.11	122.9 (847)	5.6	
PV-25-00-1.5	25.3 (174.0)	1.3 (9.0)	6.4 (35.1)	0.11	96.7 (666)	8.1	
PV-25-25-1.5	27.6 (190.0)	1.3 (8.8)	3.4 (18.7)	0.15	94.5 (651)	10.0	0.82

Test Series	Compressive Strength	Post Cracking Strength σ_{pc}	Energy Absorption Capacity G	Strain Capacity ε_{pc}	Fiber Tensile Stress σ_{fpc}	Average Number of Cracks	Cost Index ($/$ Original Mix)*
	ksi (MPa)	ksi (MPa)	kcal/yd^3 (KJ/m^3)	%	ksi (MPa)	#	
GG-25-00-1.5	25.2 (173.8)	1.2 (8.0)	3.2 (17.6)	0.15	86.4 (595)	9.0	0.52
GG-25-15-1.5	26.2 (180.6)	1.2 (8.6)	4.4 (24.2)	0.21	91.9 (633)	10.5	0.69
GG-25-25-1.5	26.9 (185.5)	1.4 (9.4)	7.4 (40.5)	0.28	101.5 (699)	11.3	0.79

*Matrix only, no fibers.

Table 3-4: Cost and Performance Summary

3.3.3. Cement Type

Three different cements were tested with three different mix ratios. Figure 3-6 shows the effects of cement types on various performance parameters for mixes with 1.5% volume fiber fraction. From Figure 3-6a, it can be seen that the compressive strength of the material varies slightly with differences in cement type. In general, the mixes containing the Portland Type V mixes perform the worst, averaging 25.9 ksi (179 MPa). Slightly better, those containing the GGBS / Portland Type I cement achieved on average 26.1 ksi (180 MPa) in compression. Those containing the White cement performed the best, averaging 27.7 ksi (191 MPa). All three cements performed above the minimum required compressive strength to qualify as UHPC, i.e. 22 ksi (150 MPa).

In tension, the average post cracking strength for each mix was also considered. From Figure 3-6b, White Cement mixes exhibited the highest tensile strength, averaging a max post cracking strength of 1.3 ksi (9.3 MPa). Portland Type V mixes averaged the lowest strengths, 1.2 ksi (8.4 MPa) and those containing GGBS / Portland Type I mixes achieved average post crack strengths of 1.3 ksi (8.9 MPa). All specimens showed at least 8 cracks in the gage length (Figure 3-6c), while specimens containing the GGBS / Portland Type I cement exhibited the most cracking. All specimens exhibited strain hardening and had a strain capacity, ε_{pc}, ranging from 0.21 to 0.24 (Figure 3-5d). Similarly, the energy absorption capacity (Figure 3-6e) and fiber tensile stress (Figure 3-6f) for all three cement types showed little variation and no clear trend between the three cement types. While specimens containing white cement performed the best in compression, all three cements showed good performance under tension and compression indicating they are all suitable for UHPC.

3.3.4 - Silica Powder

Figure 3-7 shows the effects of SP on various performance parameters for all mixes with 1.5% volume fiber fraction. From Figure 3-7a, it's seen that compressive strengths ranged from 25.1 ksi (173 MPa) at 0% SP up to 27.1 ksi (187 MPa) at 25% SP. Compressive strengths increased as SP increased up to 20%, dropping slightly as SP increased further to 25%. In tension, post cracking strengths (Figure 4b) showed little variation, with specimens containing 0% SP achieving 1.2 ksi (8 MPa) up to 1.4 ksi (9.5 MPa) for those containing 25% SP. Similarly, the average number of cracks formed showed little change from 0% SP to 25% SP. Energy absorption capacity decreased slightly from 0% SP to 20% SP, though 25% SP showed the greatest energy absorption capacity. Fiber tensile stresses essentially remained unchanged, indicating SP did not affect the ability of the fibers to transfer load. Figure 3-7 shows that significant changes in SP content resulted in minor changes in all the performance parameters.

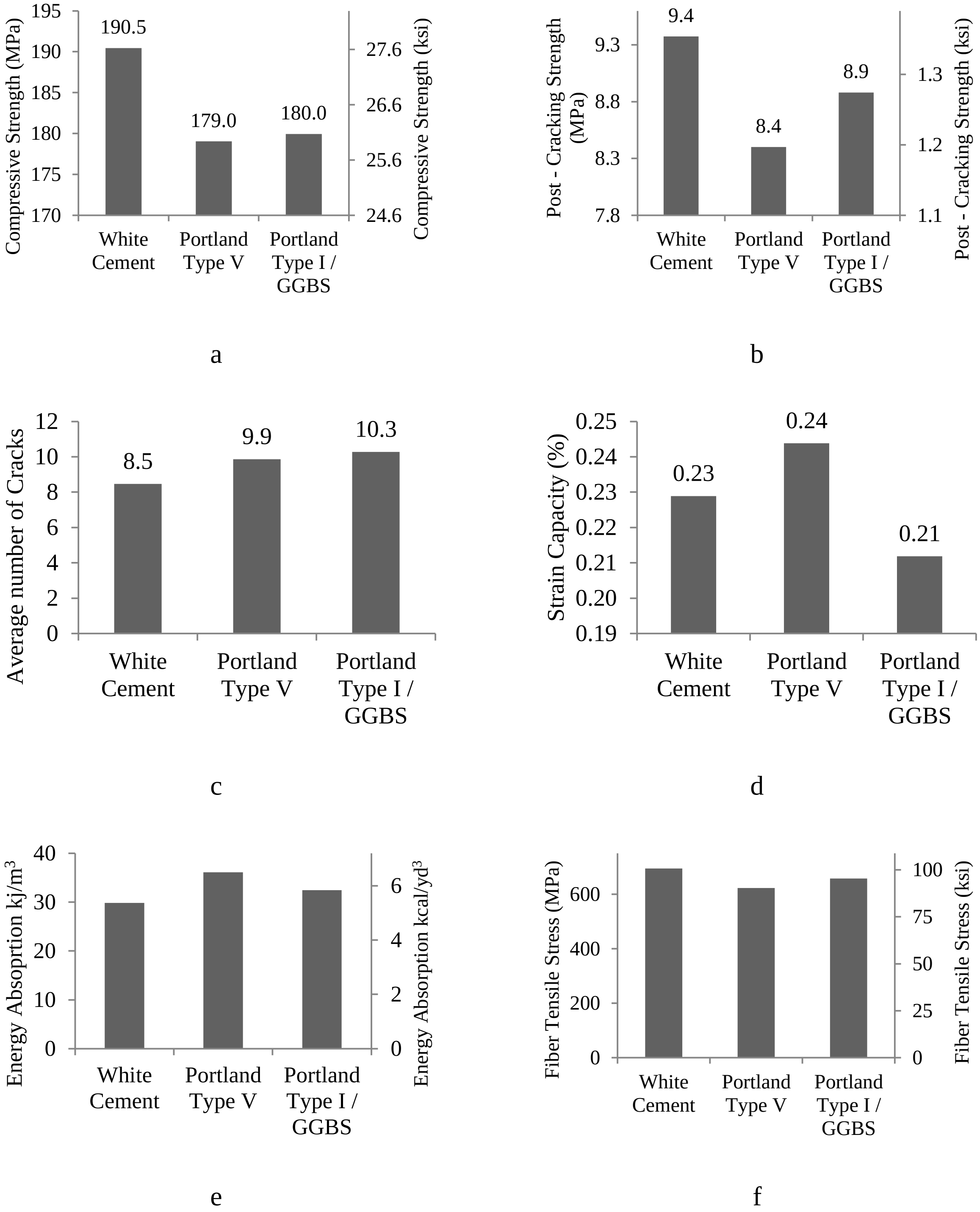

Figure 3-6: Effects of Different Cements on UHPC for Mixes with 1.5% Volume Fiber Content

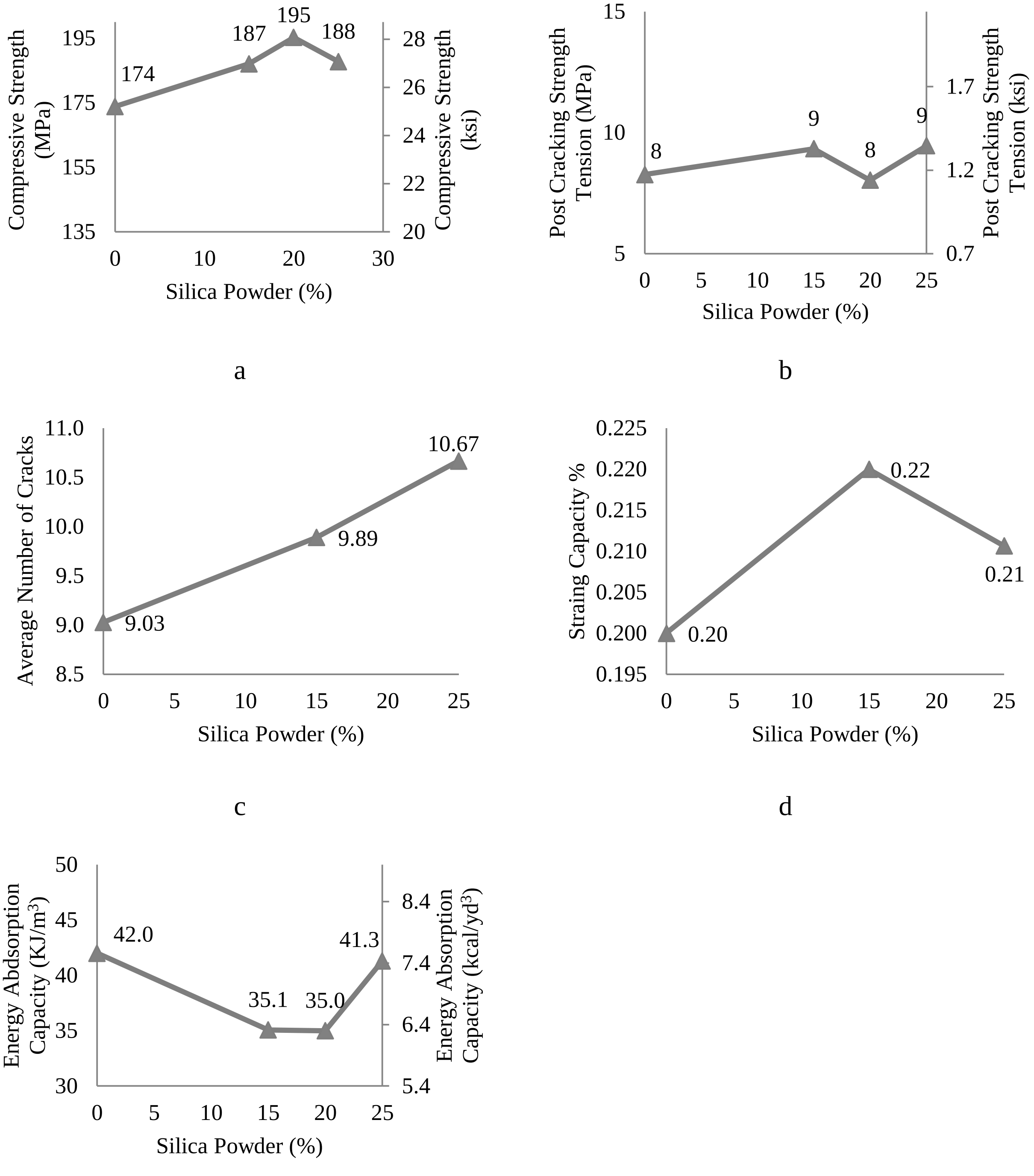

a

b

c

d

e

Figure 3-7: Effects of Silica Powder Content on UHPC for Mixes with 1.5% Volume Fiber Content

3.3.4. Silica Fume

Three different ratios of silica fume were tested. Figure 3-8 shows the effects of silica fume on various performance parameters for all mixes with 1.5% volume fiber fraction. In Figure 3-8a, the compressive strength of the material varies slightly with variation in silica fume. Mixes containing 25% SF averaged 26.7 ksi (184 MPa), increasing up to 27 ksi (186 MPa) for those containing 35% SF. This accounts for less than a 1.5% variation in compressive strength at increases in SF up to 15%.

Similarly, in tension, the results showed slight changes with variations in silica fume. Post cracking strengths (Figure 3-8b) for mixes containing 25% SF averaged 1.3 ksi (9 MPa) decreasing with additional SF; 35% SF averaged 1.2 ksi (8 MPa) in tension. This accounted for an 11% difference in strengths for a 15% increase in SF. The average number of cracks for all mixes was above 8 (Figure 3-8c), again indicating good strain hardening behavior. Strain capacity for all SF percentages ranged from 0.2% to 0.24%. Energy absorption (Figure 3-8e) decreased somewhat as SF content increased. While the changes in compressive strength were minimal, increased SF content led to lower performance under tension, and a reduction in fiber tensile stress indicated a decrease in the ability of the steel fibers to carry tensile forces.

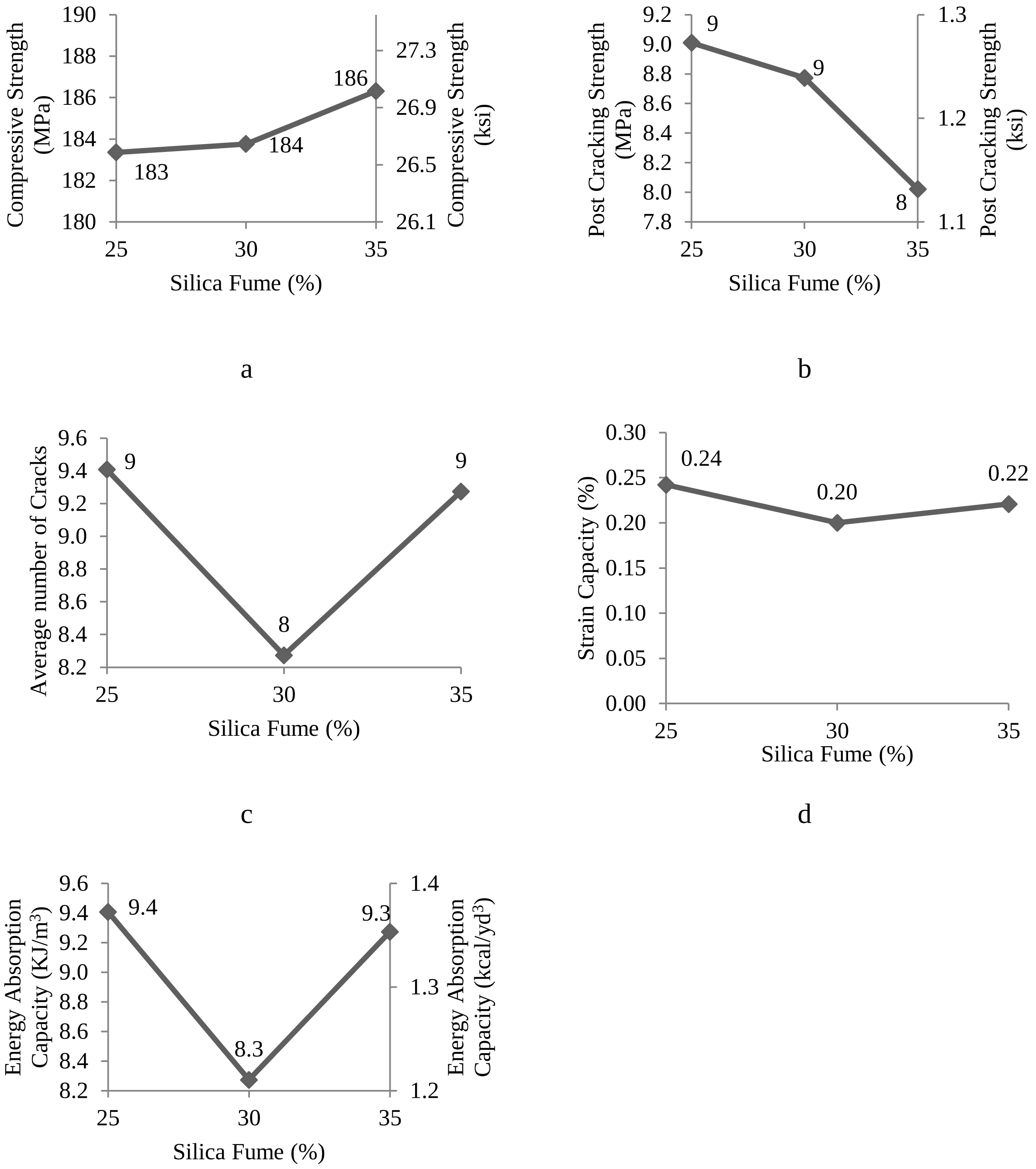

a

b

c

d

e

Figure 3-8: Effect of Silica Fume Contents on UHPC for Mixes with 1.5% Volume Fiber Content

3.3.5. Fiber Content

Figure 3-9 shows the effect of fiber volume fractions averaged across all performance parameters for the various mixes. As seen in Figure 3-9a, compressive strength ranges from 22.7 ksi (157 MPa) at 0.5% fibers by volume to 26.5 ksi (183 MPa) at 1.5% fibers by volume, a difference of 15% in strength capacity. Compressive strength of the specimens increased linearly with increases in fiber content. In tension, specimens containing 1.5% fibers yielded the highest average post cracking strength (Figure 3-9b) averaging 1.3 ksi (9.0 MPa), while those containing 0.5% fibers were the lowest at 0.8 ksi (5.8 MPa). Similarly, the strength increases linearly with respect to increasing fiber content. The remaining tensile properties also increased almost linearly with an increase in the steel fiber content (Figure 3-9c, d, e). The fiber tensile stress decreased with increasing fiber content, as more fibers were available to transfer the load. The decreased stress in the steel fibers is also likely affected by the fiber-group effect, which reduces the matrix's ability to resist the bond. These results are in line with what has been observed in other fiber reinforced concretes (Wille et al, 2012).

Figure 3-10 shows the average tensile stress-strain response for specimens containing 0.5%, 1.0% and 1.5% steel fibers by volume, while Figure 3-11 shows the data in another format for clarity. The average tensile response curve was calculated taking the mean value of the stress for each strain value for each of the tests performed in the series. It is clear that strain hardening is achieved for all fiber contents studied in this work. At 0.5% steel fibers, the strain capacity is 0.07%. This almost doubles to 0.13% as the fiber volume fraction increases to 1%. At 1.5% volume fraction, the strain capacity is 0.23.

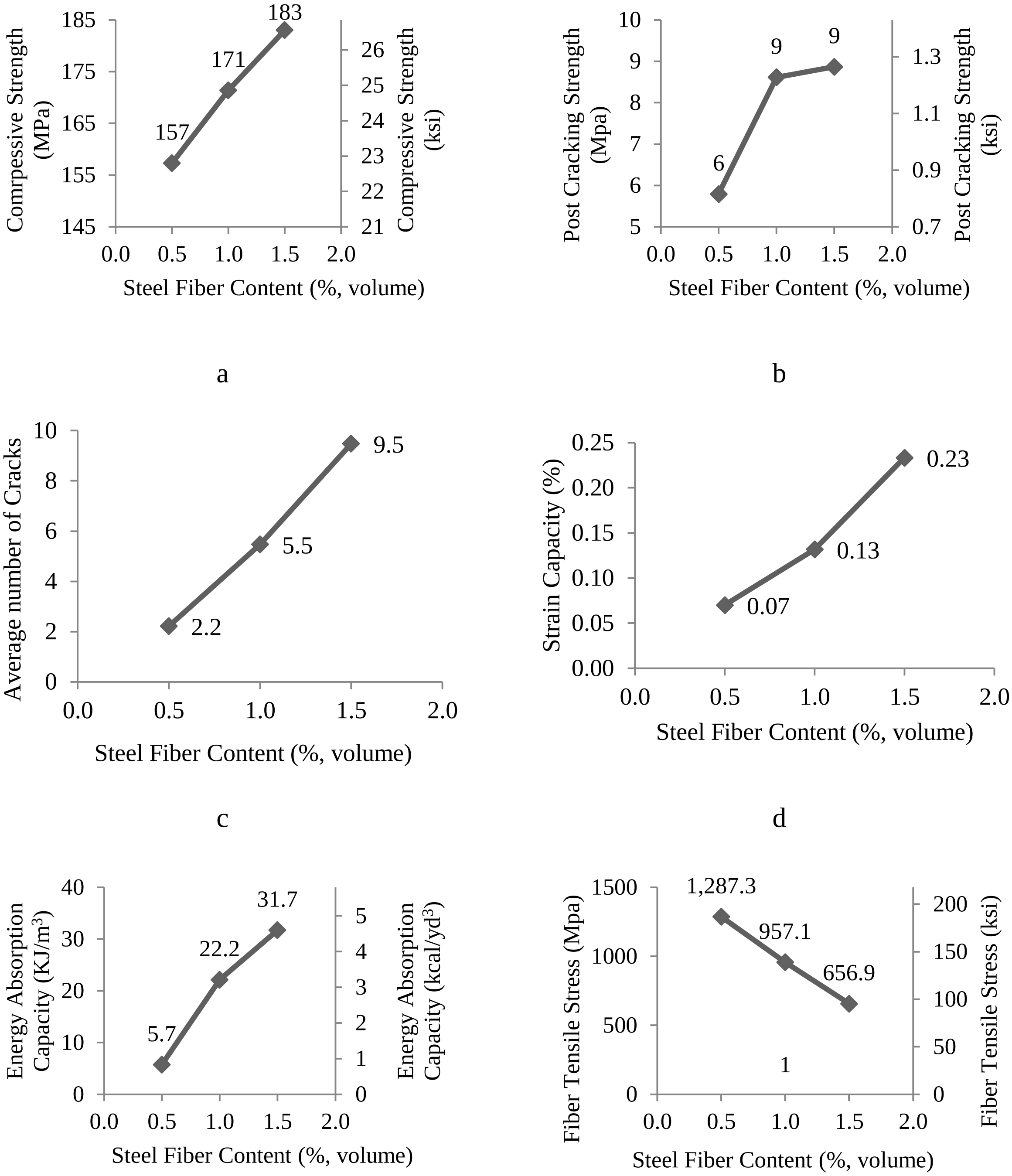

a b

c d

e f

Figure 3-9: Effects of Lower Steel Fiber Volume Contents on UHPC

In most structural applications, construction grade reinforcing steel yields at 0.2% strain. Assuming that the live and dead loads on a structure are equal, load factors for them to be 1.4 and 1.7 according to ASCE7 (2010) respectively, and the only forces on a structure, the strain in steel bars can be estimated to be 0.09% under dead loads alone and 0.13% under working conditions. Using a tensile strain hardening material that has a strain capacity that is at least one of these values will limit crack localization and protect the steel from moisture and ingress of chlorides.

It appears from the test results provided that using UHPC with 0.5% volume fiber content could come close to the lower bound (0.09%). However, the tensile coupons conducted in this work tend to align fibers preferentially along the load direction. In a real structure, the fibers will be randomly oriented, resulting in a lower effective volume fraction in any particular direction. Hence it is unlikely that UHPC with 0.5% volume fraction can provide sufficient strain hardening to eliminate crack localization under dead loads. However, UHPC with 1% fibers likely is able to do so, and with 1.5% fibers, the protection likely extends beyond just dead loading and into working conditions. Clearly, the observations pertaining to structural behavior must be evaluated through full-scale structural tests.

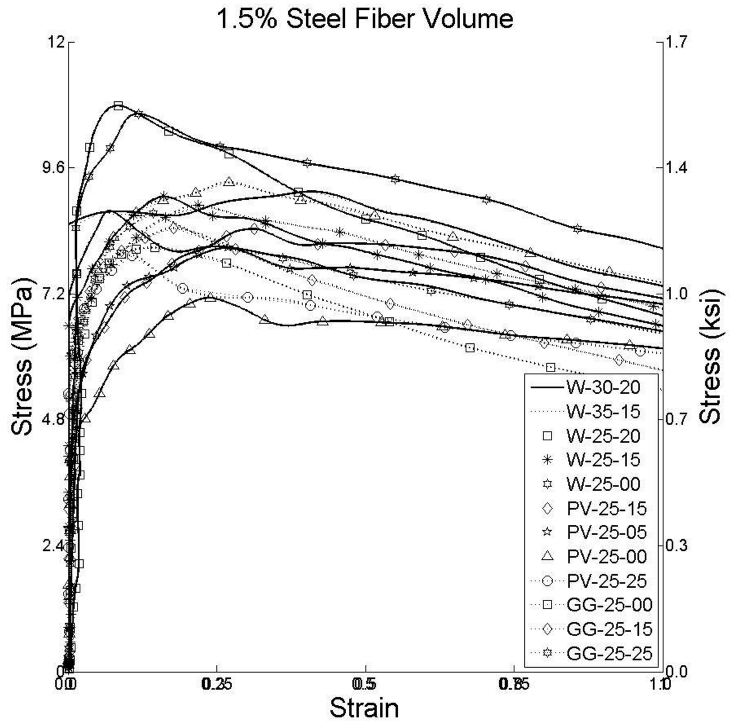
1.5% Steel Fiber Volume
Stress (MPa)
Stress (ksi)
Strain
12
9.6
7.2
4.8
2.4
0
1.7
1.4
1.0
0.7
0.3
0.0
0.0
0.25
0.5
0.75
1.0
W-30-20
W-35-15
W-25-20
W-25-15
W-25-00
PV-25-15
PV-25-05
PV-25-00
PV-25-25
GG-25-00
GG-25-15
GG-25-25

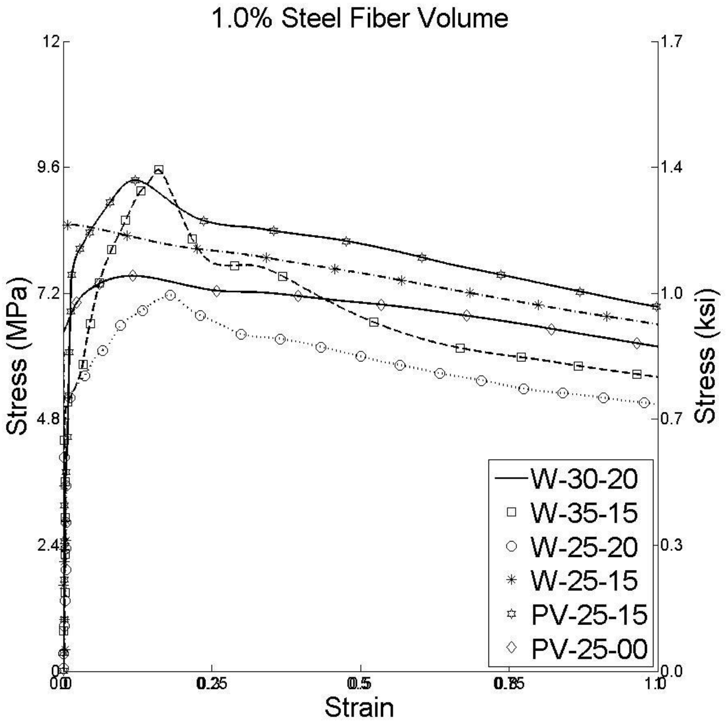
1.0% Steel Fiber Volume
Stress (MPa)
Stress (ksi)
Strain
12
9.6
7.2
4.8
2.4
0
1.7
1.4
1.0
0.7
0.3
0.0
0.0
0.25
0.5
0.75
1.0
W-30-20
W-35-15
W-25-20
W-25-15
PV-25-15
PV-25-00

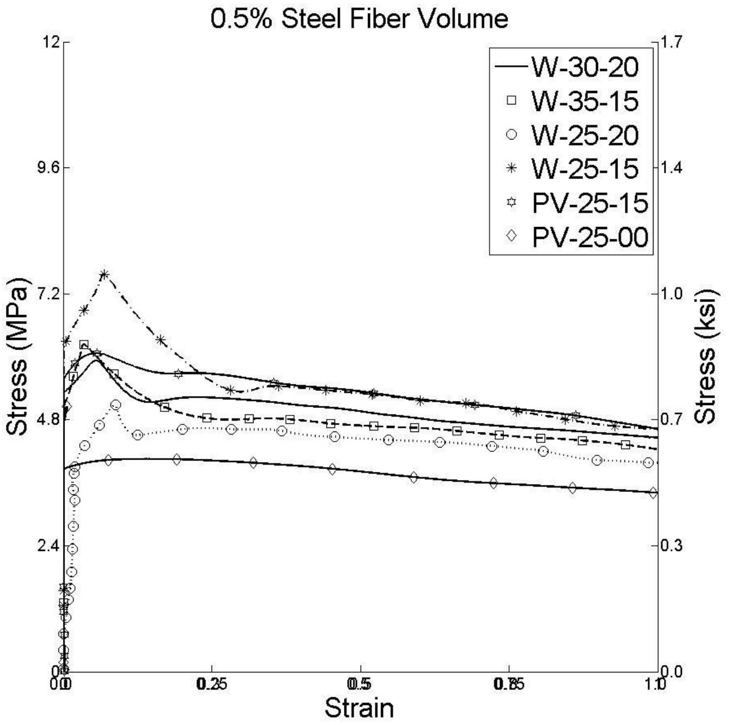

Figure 3-10: Strain Response for UHPC Specimens in Tension

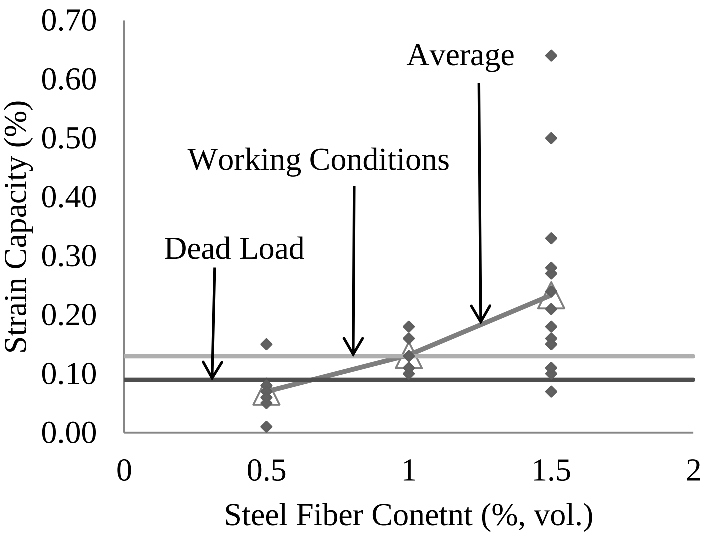

Figure 3-11: Strain (%) Capacity as function of Steel Fiber Content

3.3.6. Cost Analysis

The cost indices for each of the UHPC mixes tested are listed in Table 3-4. All of the costs used to calculate the cost index are for the cementitious materials alone, excluding the cost of steel fibers. Steel fibers, produced and sold in the US, would add an additional cost of approximately \$516/yd^3 for every 1% increase in fiber content by volume, or increase the cost index by 1.0. Figure 3-12 shows the compressive strengths for all the specimens tested vs. cost index. As can be seen, compressive strength increases linearly with increased cost. In general, cost was the highest in specimens containing the white cement, and lowest in those containing the Portland Type I / GGBS mix, as is consistent with their material costs. The least expensive mix, GG-25-00, contained 0% silica powder and used the Portland Type I / GGBS blend. Its cost index of 0.52 represents a 48% reduction in cost compared to the starting mix (5), W-25-25. Considering its lowered cost, and overall good performance, GG-25-00 presents the most optimal performance vs. cost mix of those tested. Details of this mix can be found in Table 3-5.

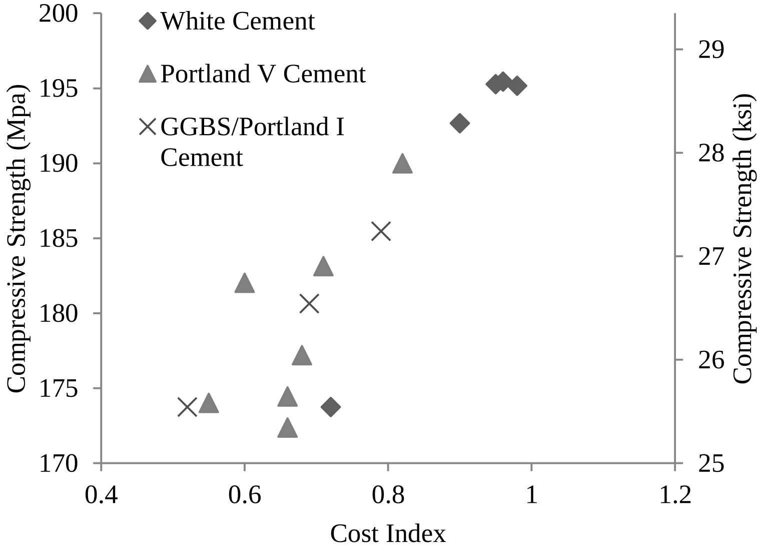

Figure 3-12: Compressive Strength as a function of Cost Index

Type	UHPC Ratio	kg/m^3
Cement	1	775
Silica Fume	0.25	194
Water	0.22	165
High Range Water	0.0054	10
Fine Sand I	0.26	245
Fine Sand II	1.03	975

Table 3-5: UHPC Mix Design and Ratios

3.4. CONCLUSION

The objective of this study was to optimize a UHPC mixture through modification of the material’s constituents. Several parameters were considered, and designs were created and tested. Each design was assigned a cost index value, and ultimately a recommendation was made. The conclusions of this study are as follow:

- All of the mixes tested achieved sufficient strengths in compression for them to be labeled as UHPC.
- All three cements tested performed comparably well in tension and compression. White cement yielded the high compressive strengths, but the Portland Type I / GGBS Cement blend carried the lowest cost, thus making it a good, cost-effective choice for future UHPC mixes.
- Changes in silica powder content yielded little variation in the performance parameters examined. In particular, specimens containing no silica powder were all within 5% of the strength in tension and compression. Due to its high cost and minimal beneficial effects, silica powder could be eliminated from UHPC mixes to reduce cost.

- Changes in silica fume led to minimal changes in compressive strength. Increased SF content led to somewhat lower performance under tension, and a reduction in fiber tensile stress indicating a slight decrease in the ability of the steel fibers to carry tensile forces.
- The results suggest that fiber volume contents of 1.0% or 1.5% could significantly reduce the chance for crack localization under dead load or working conditions, respectively, in structural applications.
- Mix GG-25-00 had the lowest cost index, while still maintaining ultra-high performance, making it the recommended mix from this study. Additionally, the availability of GGBS and Portland Type I cement make it an appealing choice for use in further UHPCs.

Chapter 4

Effects of Silica Powder Content and Cement Type on the Durability of UHPC

4.1. OVERVIEW

The dense matrix of UHPC promotes exceptional durability properties and is arguably the biggest benefit of the material. A durable concrete enables structures to last longer, reduces the cost of maintenance and helps achieve a significantly more sustainable infrastructure. To assess the durability of UHPC, the performances of several non-proprietary blends are investigated by assessing the materials' resistance to freeze-thaw cycles, ingress of chlorides as well as the presence and distribution of air voids. The main experimental variables are cement type and the quantity of silica powder, which varies from 0% to 25% of the cement weight. All mixes display negligible chloride ion penetration and high resistance to freeze-thaw with mass loss well below the limit in over 60 cycles of freeze-thaw. Analysis of the test data indicates that the silica powder content has little influence on performance.

4.2. EXPERIMENTAL PARAMETERS

4.2.1. UHPC Mix Designs

UHPC blends from Chapter 3 identified as potential, lower cost mixes, were selected for durability testing in this chapter. Three different cements are considered, the previously mentioned White Cement, Portland Type V and the Ground Granulated Blast Furnace Slag. The last cement was selected due to its reduced cost and the known high durability of GGBS cements (Cheng, 2005). GGBS also has the added benefit of being a sustainable material as it is currently produced as a byproduct of the iron manufacturing process and therefore its use in concrete is an efficient method of recycling.

The quantity of cement and silica fume was held constant for all of the mixes, but the amount of silica powder was changed from 0% (none) to 25% of the total amount of cement. The water to cement ratio was held constant for all mixes, at 0.22 w/c. The admixture Advacast 575 high range water reducer was again used at a ratio of 1.35% to cement for all mixes. All of the blends tested in this chapter contain 1.5% smooth steel fibers by volume fraction. Particle sizes for each material can be found in Table 3-1. The chemical properties of Silica Fume and Silica Powder used in the testing are presented in Table 3-1. Additionally, the grain size distribution for the silica sand filler can be seen in Figure 3-1. Table 4-1 lists the mix constituents of the 9 mixes highlighted in this study. The naming scheme follows the same convention as in Chapter 3.

Name	White Cement Type I	Silica Fume	Silica Powder	Fiber (%)	F100	F12
W-25-25-1.5	1.00	0.25	0.25	1.50%	0.26	1.06
W-25-15-1.5	1.00	0.25	0.15	1.50%	0.29	1.14
W-25-00-1.5	1.00	0.25	0.00	1.50%	0.31	1.26
	Portland Type V					
PV-25-25-1.5	1.00	0.25	0.25	1.50%	0.26	1.05
PV-25-15-1.5	1.00	0.25	0.15	1.50%	0.28	1.14
PV-25-00-1.5	1.00	0.25	0.00	1.50%	0.31	1.26
	Type I / GGBS					
GG-25-25-1.5	1.00	0.25	0.25	1.50%	0.26	1.06
GG-25-15-1.5	1.00	0.25	0.15	1.50%	0.28	1.14
GG-25-00-1.5	1.00	0.25	0.00	1.50%	0.31	1.26

Table 4-1: Mix Proportions for tested UHPCs

4.2.2. Experimental Procedure

Freeze-Thaw Resistance

The resistance of concrete to the combined attack of de-icing salt and frost is evaluated by a modified CIF (Capillary suction, Internal damage and Freeze-thaw) test, where the surface scaling, moisture uptake and the internal damage were measured simultaneously. Cylindrical specimens of 6 inches (150 mm) in diameter and 12 inches (300 mm) in height were made. After 24±2 hours of curing the specimens were removed from the mold and submerged in tap water at 68 °F (20 °C) for 28 days. After storage in the water, the specimens were cut into rectangular prisms of 4.75 inches (120 mm) by 4.25 inches (107 mm) by 2.75 inches (70 mm). The cut section was away from the two ends of the cylinder to avoid surface in-homogeneity associated with a cast surface and is parallel to the finishing surface. After air drying at 68 °F (20 °C) and

65% relative humidity for 24 hours, the lateral surfaces of the specimens were sealed by the aluminum foil with butyl rubber. The freeze-thaw machine, as shown in Figure 4-1, contains fifteen stainless steel bowls, each containing one specimen. The specimen sits on four spacers so that the bottom test surface is in contact with the test liquid (Figure 4-2).

A freeze-thaw cycle duration is 12 hours. The temperature profile is as follows (Figure 4-3): the start temperature for the freeze-thaw test is 68 °F (20 °C); the temperature of the stainless steel bath with liquid (3% NaCl solution in this case) is lowered at a linear rate of 50 °F (10 °C) /hour for 4 hours; the specimens are kept at -68 °F (-20 °C) for 3 hours, then brought back up to room temperature at the same constant rate of 50 °F (10 °C) /hour as used for cooling; the temperature is maintained for 1 hour at 68 °F (20 °C) before the commencement of the next freeze-thaw cycle. During the one-hour isothermal period at 68 °F (20 °C), the amount of surface scaling, the moisture uptake and the internal damage were measured after a specific number of freeze-thaw cycles. A total of two specimens were tested for each of the material parameters.

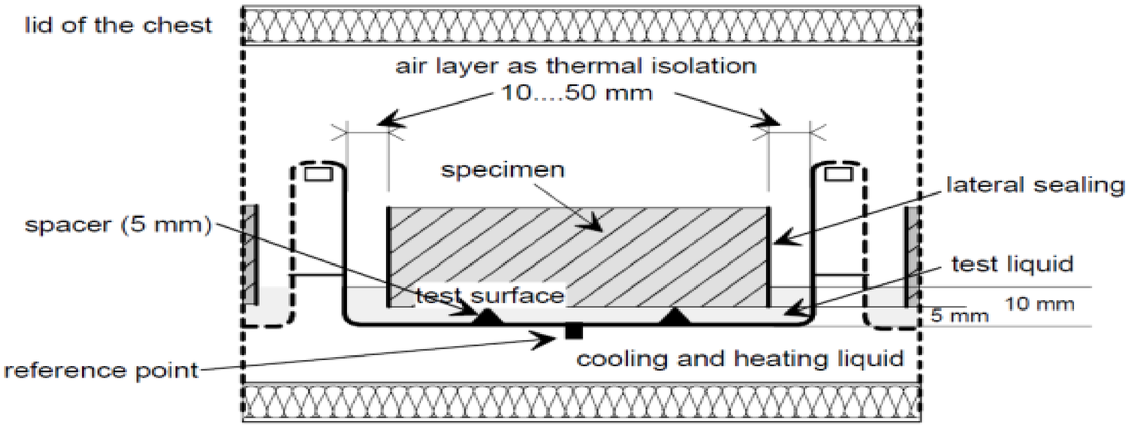

Figure 4-1: Freeze Thaw Test Close-Up (17)

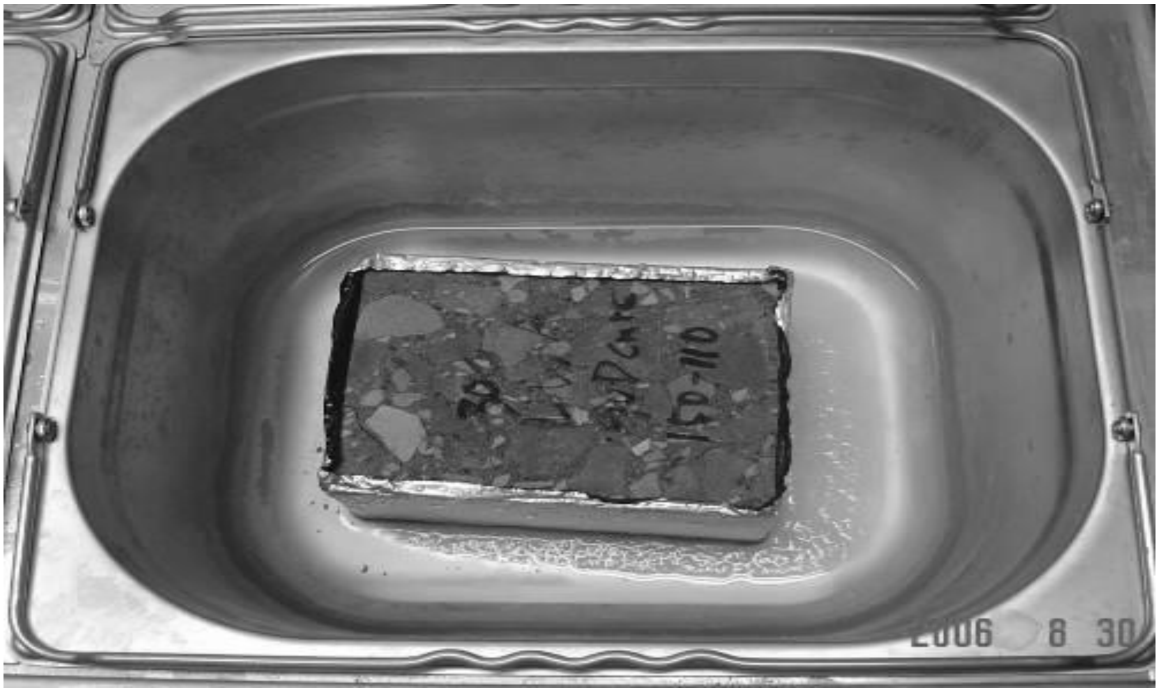

Figure 4-2: Specimen with Test Surface Facing the Bottom under Frozen Condition

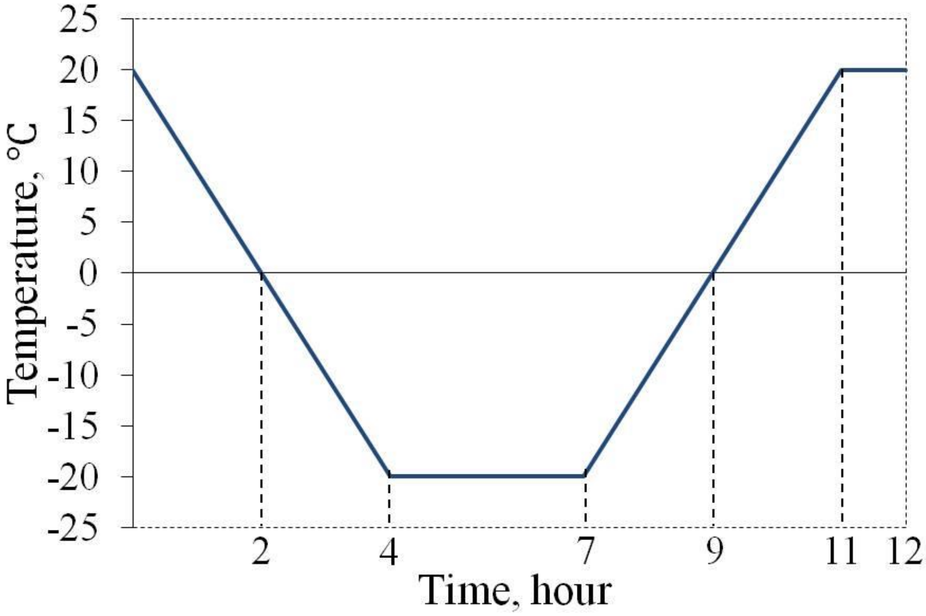

Figure 4-3: Temperature Profile of Freeze-Thaw Test

4.2.3. Air Void Analysis

The air void analysis of the concrete was measured using ASTM C457, “Standard Practice for Microscopical Determination of Parameters of the Air-Void System in Hardened Concrete”. Square specimens of 4 inches (100 mm) by 4 inches (100 mm) were cut from the mid-depth portion of 6 inch (150 mm) diameter cores with the testing surface parallel to the finishing surface. Specimens were carefully polished with silicon carbide abrasives to obtain a smooth surface with undamaged paste and clearly defined air voids. Then the point count method was used to determine the fractions of air void, paste and aggregate and also the percentage of air voids with infillings. This step provides information on the quality of air void and the input to the computation of the spacing factor in the next step. After the point count procedure, the polished surface was pretreated by filling all the air voids with a white powder (barium sulfate) and the rest of the surface was darkened by a permanent marker to produce a sharp contrast (Figure 4-4). Then, the linear traverse method was used to measure the chord length distribution and the total length of the traverse line over air void, based on which, the air void parameters can be calculated. A total of two specimens were tested for each of the material parameters.

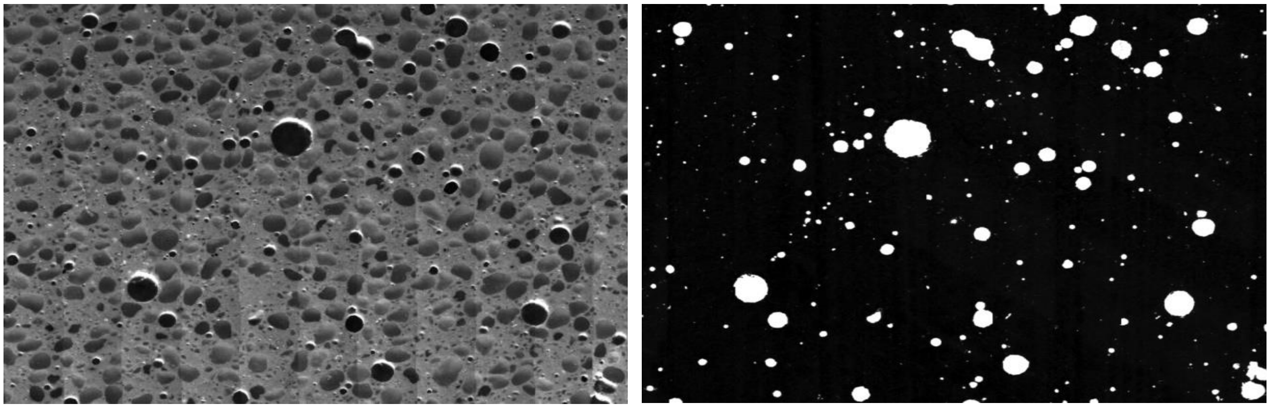

(a) Untreated Surface

(b) Coated Surface

Figure 4-4: (a) Polished surface for point count measurement and (b) coated surface for linear traverse measurement.

4.2.4. Rapid Chloride Penetration Test

Evaluation of chloride ingress resistance was tested according to ASTM C1202-12, “Standard Test Method for Electrical Indication of Concrete’s Ability to Resist Chloride Ion Penetration”. A commercially available device, PROOVE’it, was used in order to complete the testing. Specimens of 4” (100 mm) in diameter and 2” (50 mm) in width were positioned into the measuring cell. Each cell contains a fluid reservoir at each face of the specimen. One reservoir is filled with a sodium chloride solution (3.0% NaCl). The other reservoir is filled with a sodium hydroxide solution (0.3 M NaOH).

The reservoir containing the NaCl is connected to a negatively charged terminal, the NaOH reservoir is connected to the positively charged terminal of the device’s microprocessor-controlled power unit. Once started, the test automatically measures the total electrical current passing through a concrete specimen for a standard period of 6 hours, with a direct current voltage of 60 V. A total of two specimens were tested for each of the investigated parameters.

4.2.5. Compressive Strength Testing

For each of the mixes, at least 6 cube specimens were cast. Each cube measured 2” x 2” x 2” (50 mm x 50 mm x 50 mm) and was placed into the molds without any vibration. Previous research has shown that compression test results using cubes vs. cylinders in UHPC yield 4.6 % to 6.1% higher results in the cubed specimens (Graybeal, 2006). The specimens were tested for each mix and peak compressive strength recorded. Each cube specimen was subjected to a loading rate of 0.25 kip/sec until the specimen began to strain soften in compression.

4.3. EXPERIMENTAL RESULTS

Table 4-2 shows a summary of all the test results, which are discussed in more detail in the following sections.

4.3.1. Freeze-Thaw Resistance

The freeze-thaw resistance of the ultra-high performance concrete specimens was tested in accordance with RILEM TC 176-IDC. The specimens were subjected to at least 60 freeze-thaw cycles and the mass loss of the specimens was recorded. For all of the different mixes tested, it was clear that no internal damage occurred, as evidenced by an almost unchanged relative dynamic modulus (RDM). The RDM provides a reliable measure for evaluating internal frost damage, and is calculated as follows (Equation 4-1):

$$RDM\% = \frac{n_c^2}{n^2} x100$$

Equation 4-1: Relative Dynamic Modulus

where c is the number of cycles of freezing and thawing, n_c is the resonant frequency after c cycles, and n is the initial resonant frequency (at zero cycles). For all 9 specimens, the RDM remained at 100%.

	Rapid Chloride Penetration	Air Void Analysis	Freeze-Thaw Test		Compressive Strength	
UHPC	Total Charge Passed (Coulombs)	Air Content (%)	Total Mass Loss after 28 cycles oz./yd^2 (g/m^2)		ksi (MPa)	
W-25-25-1.5	89	5.8	2.9	(98.8)	28.3	(195.0)
W-25-15-1.5	295	7.9	0.6	(20.7)	27.4	(188.8)
W-25-00-1.5	637	6.6	0.5	(17.7)	25.2	(173.6)
PV-25-25-1.5	939.5	6.1	0.5	(18.2)	25.3	(174.3)
PV-25-15-1.5	488.5	6.5	0.5	(18.0)	27.2	(187.4)
PV-25-00-1.5	57	4.5	1.2	(42.2)	25.8	(177.8)
GG-25-25-1.5	137.5	5.7	0.6	(20.5)	25.1	(172.9)
GG-25-15-1.5	229	4.8	0.7	(24.2)	26.3	(181.2)
GG-25-00-1.5	137.5	5.8	1.3	(44.7)	27.7	(190.9)

Table 4-2: Summary of Test Results

Additionally, as can be seen in Figure 4-5, mass loss for all of the specimens fell significantly below the 44.2 oz./yd^2 (1500 g/m^2) limit defined by the testing standard. This limit for mean scaling after 28 cycles measures surface scaling resistance of the specimens. For all nine specimens, this value remained consistently low, despite changes in cement types used and ratios of silica powder included. For comparison, Figure 4-5 also shows some typical results for regular concretes.

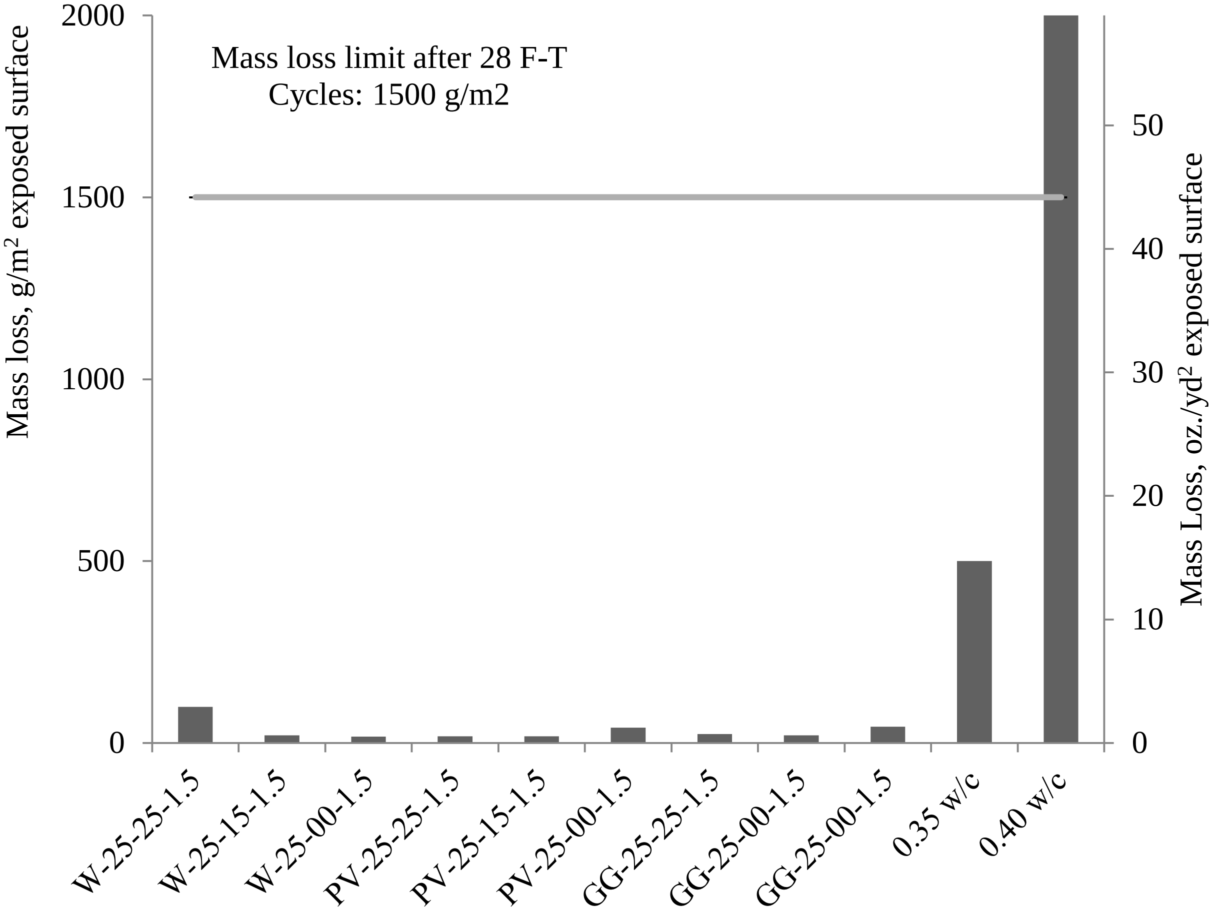

Figure 4-5: Mass Loss of UHPC Mixes after at Least 60 Cycles

From Figure 4-5, the best performing mix in terms of the least total mass loss was W-25-00-1.5, with a total loss of 0.5 oz./yd^2 (17.7 g/m^2). The worst performing mix was W-25-25-1.5, with a total loss of 2.9 oz. /yd^2 (98.8 g/m^2). Generally, there are no distinct differences in the freeze-thaw resistance of UHPCs with 0% SP, 15% SP and 25% SP. The values are all so low compared to the acceptable mass loss limits for concretes that the differences exhibited by W-25-25-1.5 are considered to be within statistical tolerances. Figure 4-5 shows that, with the exception of W-25-25-1.5, all of the mixes are within 15% of each other, and less than 3.3% of the acceptable mass losses limit for concrete, despite varying the level of silica powder and cement type.

As seen in Figure 4-6a, all specimens performed well for freeze-thaw resistance, with those containing Portland Type V performing marginally better than the other two. When averaged across all cement types, (Figure 4-6b), specimens containing 15% silica powder outperformed those containing 25% silica powder by 40% and those containing 0% silica powder by 54%. Figure 4-7 compares the effects of cement type on the total mass loss for the UHPCs averaged for all silica powder contents. Specimens containing Portland V cement experienced 12% less mass loss than its Portland I / GGBS counterpart and 43% less mass loss than those containing white cement. Although the variations may appear large, it should be noted that all the mass loss values are small to start with and well below acceptable mass loss limits.

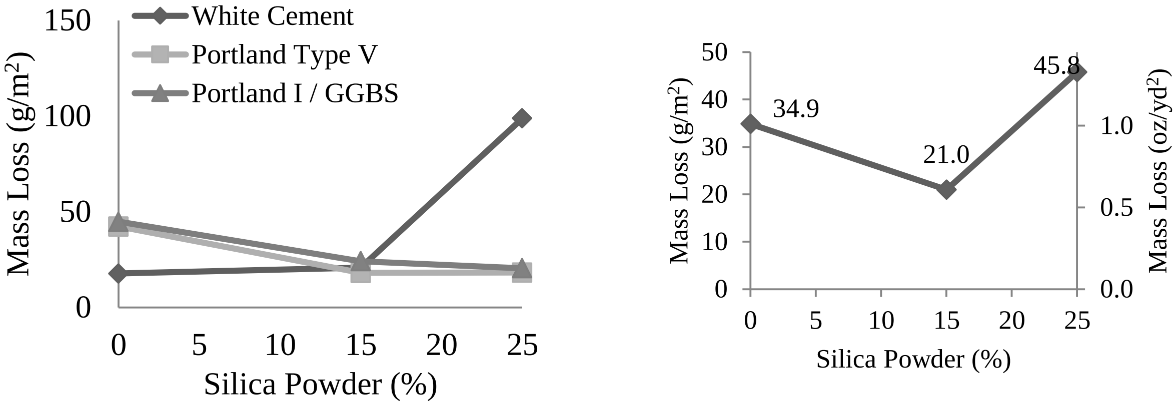

a

b

Figure 4-6: a. Effect of Silica Powder on Mass Loss; b. Average Mass Loss as a Function of Silica Powder Quantity

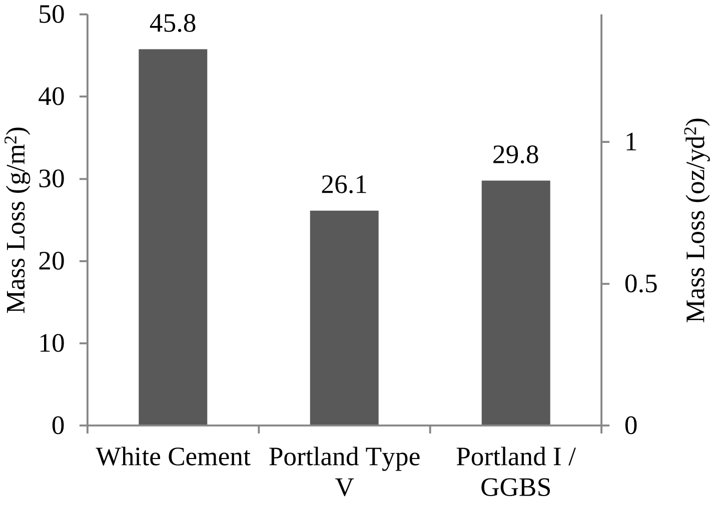

Figure 4-7: Average Mass Loss as a Function of Cement Type

4.3.2. Air Void Analysis

All of the UHPCs tested in this study tested well for freeze thaw resistance using both the linear traverse method and the point count method. The linear traverse method counts the number of voids along a single line, or chord length, while the point count method determines the number of voids within an area. Figure 4-8 shows the measured air contents using the two methods. From the chart, it can be seen that there is good agreement between the two methods.

Figure 4-8 shows that the total hardened air contents for the mixes range between 3.0% - 7.5%. These values correspond to an equivalent air content of 1.8% - 4.0% in normal concrete. Unlike regular concretes, UHPCs have a much large paste content, i.e. approximately 60% versus 30% for regular concretes. For freeze thaw, paste is the frost susceptible component, where the air-voids are embedded. In practice, air content is expressed as the air void volume as a percentage of the concrete volume. In order to accurately compare UHPC and regular concrete, the measured air content in UHPC must therefore be converted to an equivalent for regular concrete, hence the 1.8% - 4.0% range mentioned above.

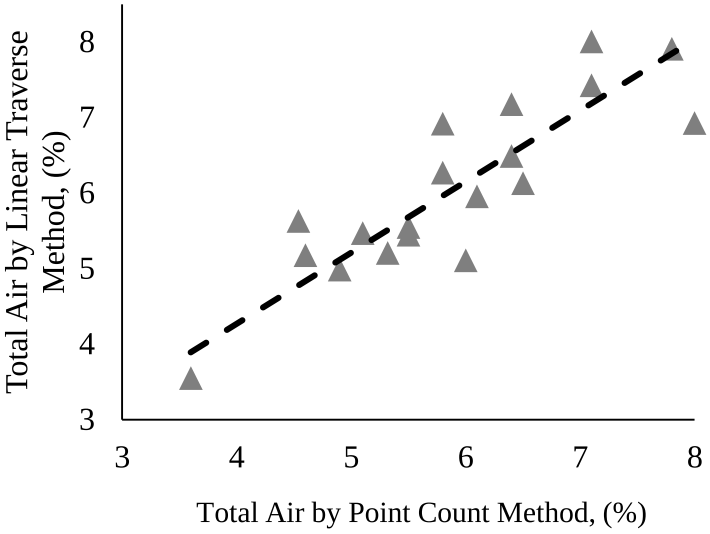

Figure 4-8: Air Content by LTM and PCM

Figure 4-9 shows the total air content as a function of the powers' spacing factor. The spacing factor here refers to the paste-void proximity; the fraction of paste within some distance of an air void. For all of the UHPC specimens tested, both air contents and spacings range from 5.9 E-4 inches to 0.02 inches (0.15 to 0.51 mm), with an average of 0.01" (0.29 mm). For normal concrete (dotted box), air-void systems with a powers spacing factor 0.0078" (0.20 mm) or less depending on conditions and 6% (+/- 1) total air content will typically provide good freeze-thaw protection (Tanesi, 2007). Though the UHPC used in this study had spacing factors higher than those of conventional concrete, it exhibited excellent freeze thaw resistance. These values also fall in line with those reported by other studies (Graybeal, 2006). Thus, the air content and/or powers spacing factor may not be a suitable metrics by which to judge the freeze-thaw resistance in UHPC.

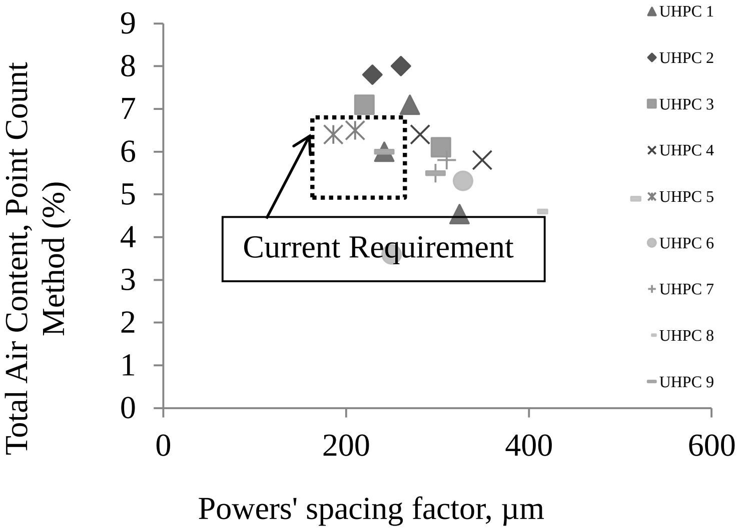

Figure 4-9: Air Content as a Function of Power’s Spacing Factor

Figure 4-10a shows the air content percent as a function of silica powder for the three different cement types. The differences in air content percent between specimens containing 0%, 15% and 25% silica powder are small. When averaged across all cement types (Figure 4-10b), the air content measures are within 13% of the other specimens’ air content. Figure 4-11 shows the average air content for each of the cement type used. From the data, mixes containing the Portland I / GGBS cement mix showed the least total air content percent at 5.4% when averaged across all silica powder contents. Mixes containing White cement showed air content percentages 20% higher (6.8%), and those containing Portland V cement were only 5% higher (5.7%), again when averaged across all silica contents.

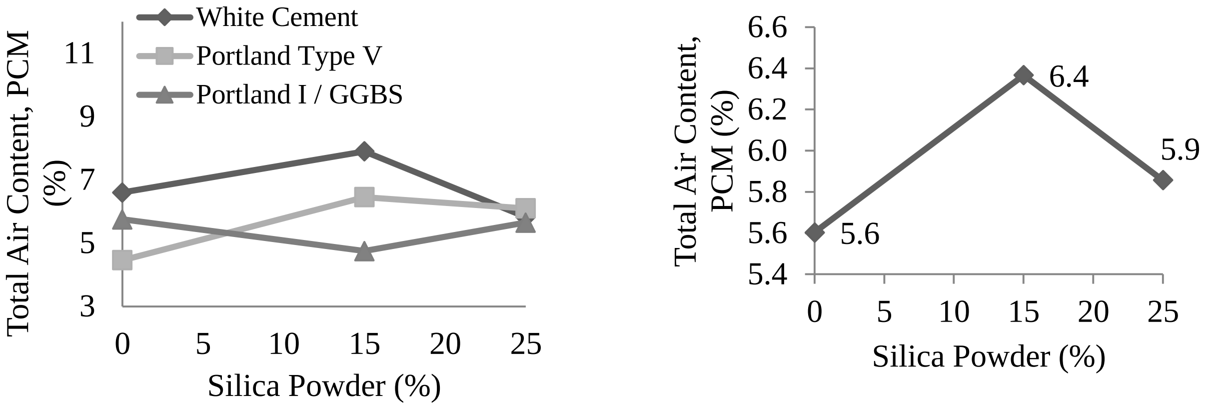

a

b

Figure 4-10: a. Air Content as a Function of Silica Powder Percent, b. Average Air Content as a function of Silica Powder

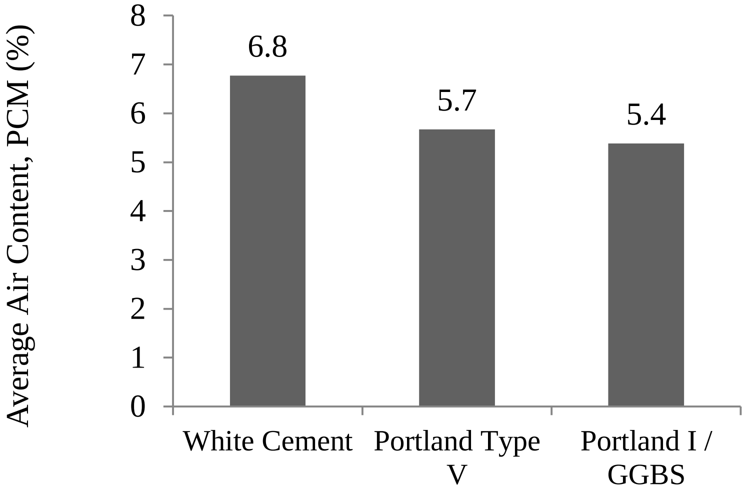

Figure 4-11: Average Air Content as a Function of Cement Type

4.3.3. Rapid Chloride Permeability

A summary of results is shown in Figure 4-12 for the nine mixes. The chloride permeability rating is illustrated based on Table 4-3. Also shown are some typical results for regular concrete.

`

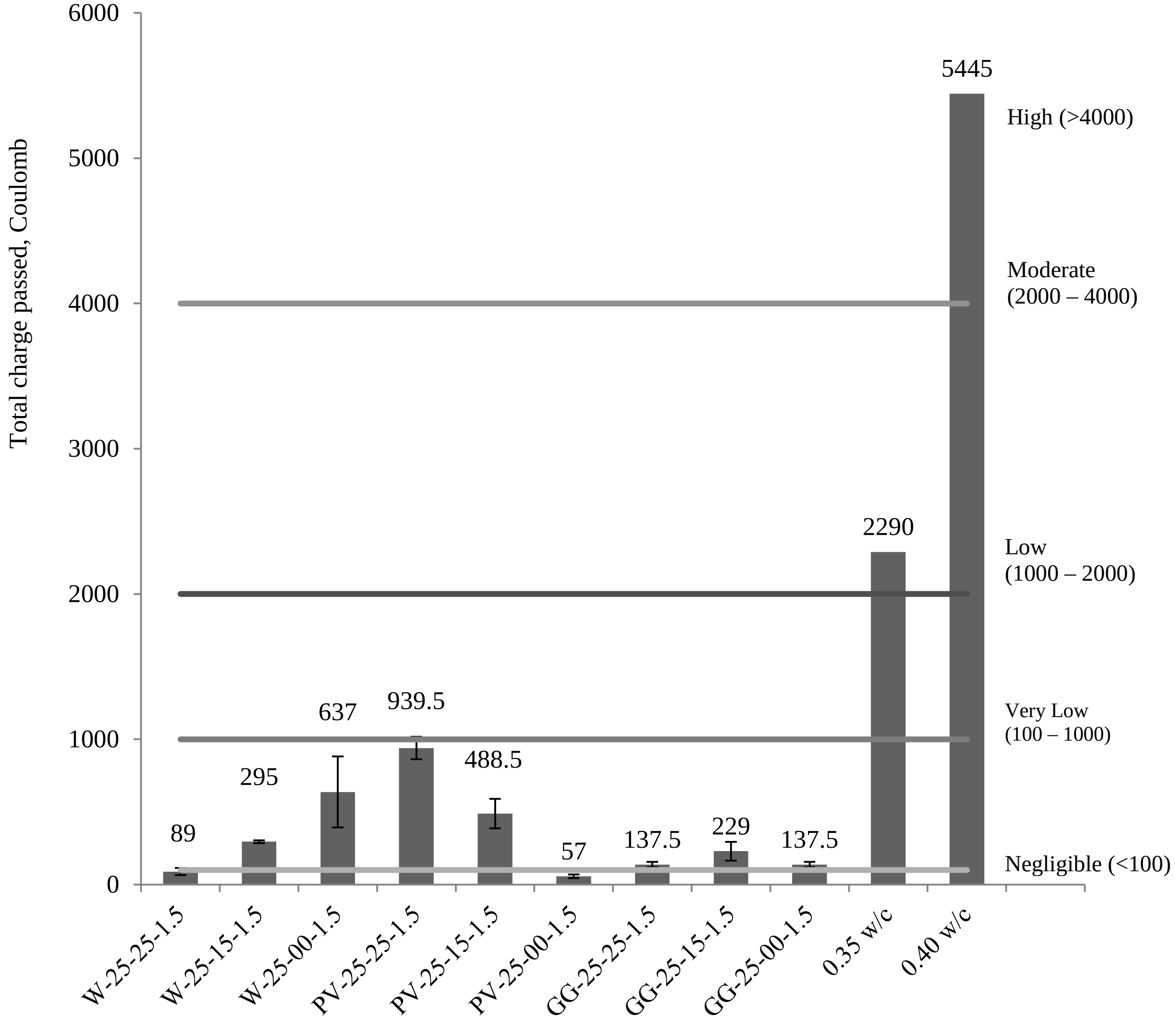

Figure 4-12: Total Charge Passed for UHP C and RC Mix

Chloride permeability	Charge (Coulomb)	Typical concrete
High	> 4000	High w/c ratio (> 0.6)
Moderate	2000 - 4000	Moderate w/c ratio (0.4 - 0.5)
Low	1000 - 2000	Low w/c ratio (< 0.4)
Very low	100 - 1000	Latex-modified concrete, internally sealed concrete
Negligible	< 100	Polymer impregnated concrete, polymer concrete

Table 4-3: Chloride Permeability Rating

From Figure 4-12, all of the UHPC mixes have a rating of “very low” chloride permeability with two mixes falling into the “negligible” category. From Figure 4-13a, it appears that the combined effect of cement type and silica powder content on the chloride ion permeability of UHPC is not clear. When averaged for all cement types, Figure 4-13b shows that the amount of silica powder plays a role: increasing silica powder content leads to higher permeability. Specimens with 0% silica powder perform the best, averaging 277.2 coulombs passed. Those specimens outperformed ones containing 25% silica powder by 40% and those containing 15% silica powder by 17%. For comparison, regular concretes containing 35% and 40% water contents average 2073 and 4000 coulombs passed, or rather 621% and 1343% higher than the mixes containing 0% silica powder. When averaged across all silica powder contents, Figure 4-14 shows that specimens containing Portland Type I / GGBS cement exhibited the best performance on average, with all three mixes averaging 168 Coulombs passed. The mixes containing white cement averaged 340 coulombs passed, a 102% difference compared to Portland I / GGBFS. The mixes containing Portland type V averaged 495 coulombs passed, a 194% percent difference. As noted for mass loss in the freeze-thaw test results, while the variations appear large, the base values are actually small, signifying the good chloride penetration performance of all of the UHPC mixes considered.

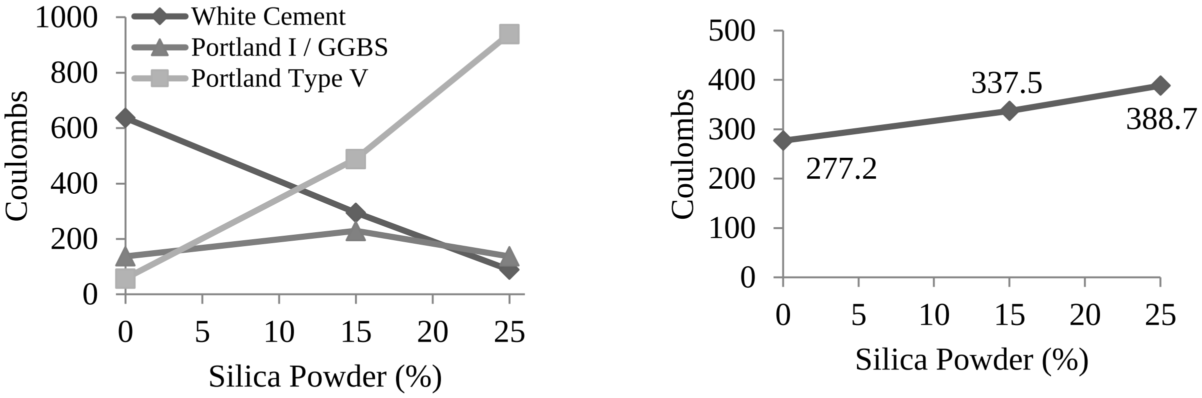

a

b

Figure 4-13: a. Total Coulombs passed as a function of Silica Powder Percent; b. Average Coulombs passed as a function of Silica Powder

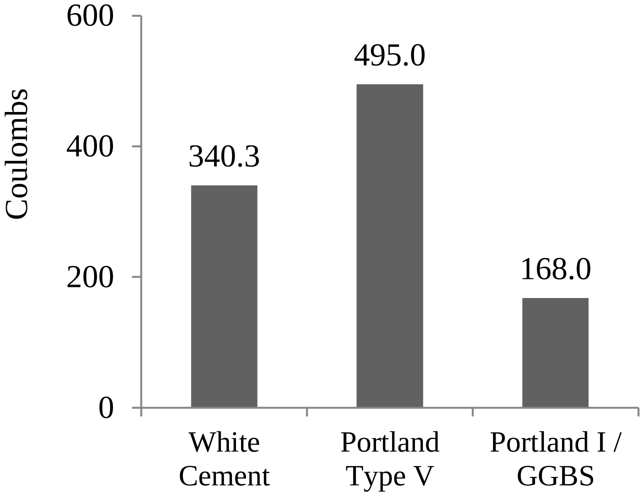

Figure 4-14: Average Coulombs passed as a function of Cement Type

4.4. DISCUSSION OF EXPERIMENTAL RESULTS

The materials tested in this research showed high durability characteristics. It is commonly accepted that the good performance of UHPC is a manifestation of the material's high packing density, which can be characterized through particle packing models. Such models consider the size and quantity of individual particulate components within a material, and show the distribution of those particles for the entire mixture. In order to achieve the densest particle packing, Andreasen and Anderson (1930) developed the Andreasen model. This paper makes use of a modified Andreasen particle packing model, as shown in equation 4-2:

$$CPFT(\%) = 100\left(\frac{d^q - d_m^q}{D^q - d_m^q}\right)$$

Equation 4-2: Modified Andreasen Model

where CPFT is equal to the cumulative percent finer than, d is the particle size for the material, d_m is the minimum particle size, D is the maximum particle size and q is the distribution coefficient. Previous studies have shown that a value of $q = 0.37$ provides higher particle packing densities for self-consolidating concretes which have similar rheology as UHPC (Brouwers, 2013). Therefore, this value was chosen for the analysis.

Figure 4-15 plots the particle size distributions for all the mixes tested in this study and compare them to the modified Andreasen model. Also plotted, for the purpose of comparison, is the distribution for regular concrete (Chia, 2002). Unlike the UHPC mixes, regular concrete deviates significantly from the ideal distribution throughout the entire range of particle sizes, suggesting that the material is sparser than UHPC. Also, regular concrete does not have any particles below 1 micron, suggesting that voids exist at this level.

Figure 4-15 shows that while variations in silica powder content affect the material's packing density differently across the particle size range; the distributions still remain close to the 'optimal' particle packing density. This provides an explanation for why there are little differences between the performances of all mixes, especially for chloride ion penetration. In essence, all the UHPCs tested in this study are so dense that they effectively resist the ingress of chloride ions. The freeze-thaw resistance in UHPCs is due to water being prevented from entering the voids. Figure 4-16 shows that all UHPCs tested had a very low water uptake percent, (<0.3% vs. approximately 1% for regular concrete (Liu, 2014)) and an unchanged RDM% indicating no internal damage.

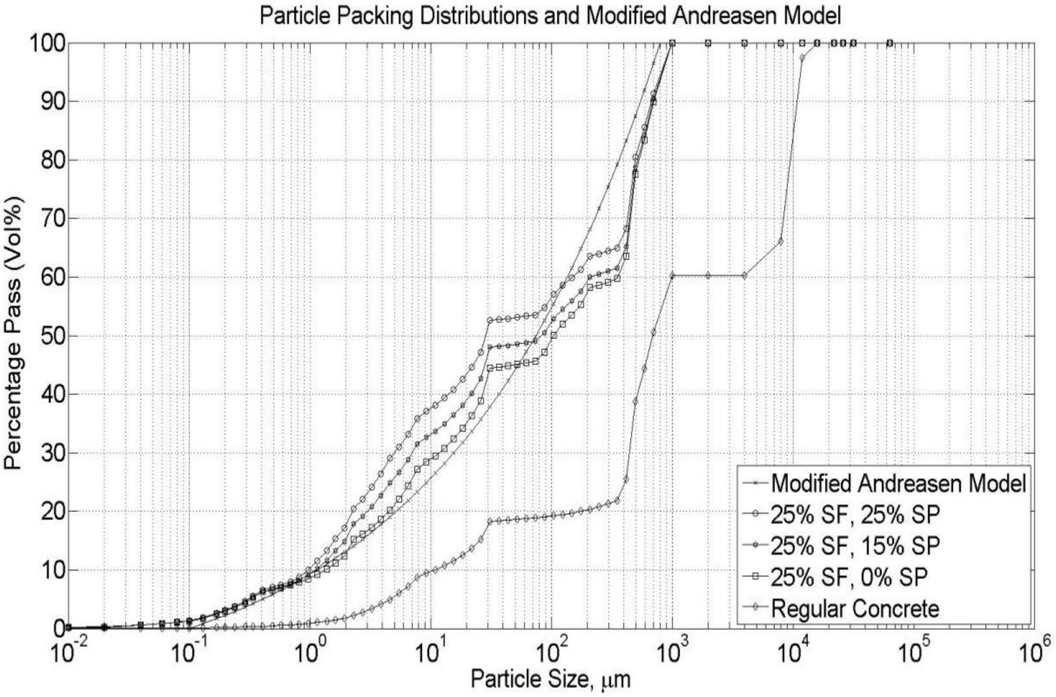

Figure 4-15: Particle Size Distributions for UHPC Mixes and Regular Concrete

One of the most important conclusions from this discussion is that silica powder has little influence on the durability of the tested UHPCs. Figure 4-15 explains why this is the case, i.e. eliminating silica powder does not significantly alter the particle size distribution. This conclusion has commercial implications because eliminating such a component from UHPC will significantly reduce its cost given the high price of silica powder, spurring widespread adoption.

Figure 4-15 also explains why changes in cement type had little effect on durability of the UHPCs tested. Each cement type had very similar particle size distributions. Thus, changes in cement type had no effect on the particle packing density of the UHPC. More work should be performed to determine the effects of cement type on other performance parameters.

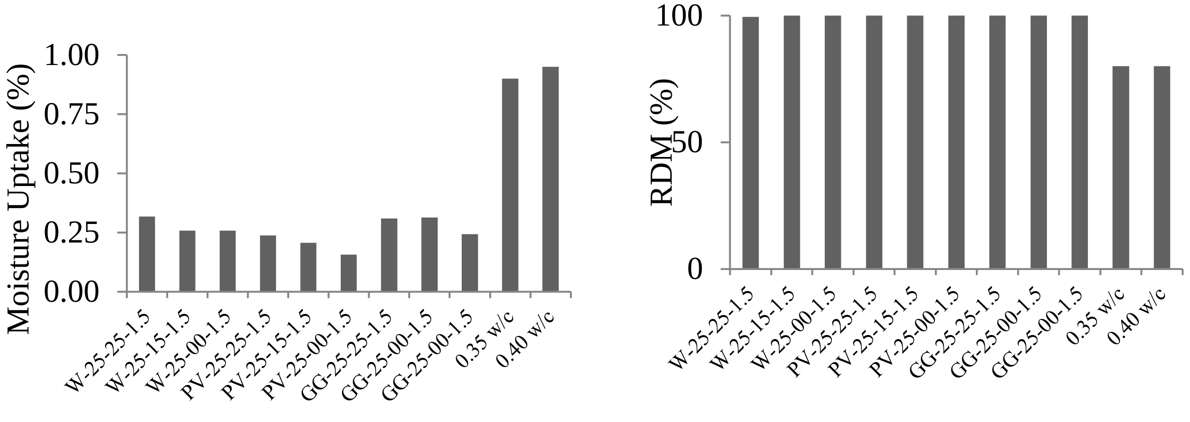

a

b

Figure 4-16: Moisture Uptake and RDM% for UHPCs (27)

4.5. CONCLUSION

This experimental study investigated the durability performance of nine different blends of UHPC, including freeze-thaw resistance, chloride ion penetration resistance, and air void analysis. A modified CIF test and an air void analysis were conducted in order to evaluate freeze-thaw resistance. A rapid chloride permeability test was performed to test the concretes' resistance to the ingress of chlorides and other ions. The RDM percent change, mass loss and total air content were presented in order to gauge the concrete's freeze-thaw resistance. The coulombs passed were presented to gauge the concrete's ion permeability. The observations and findings of this study can be summarized as follows:

- All of the UHPC mixtures tested displayed exceptional resistance to freeze-thaw. All of the specimens tested experienced mass loss that was well below the mass loss limit in over 60 cycles of freeze-thaw.

- Changes in silica powder accounted for differences up to 54% mass loss in concrete's ability to withstand freeze-thaw while changes in cement type showed differences up to 43% in concrete's ability to withstand freeze-thaw. It should be noted that while the variations appear large, the absolute values on which they are based are actually small.
- The average air content for all of the specimens tested in this study ranged from 3.0% - 7.5% (1.8% - 4.0% regular concrete equivalent), below the limit for adequate resistance to freeze-thaw in regular concrete. The use of air content for assessing freeze-thaw resistance may therefore not be applicable for UHPCs. Unlike regular concrete, which relies on having sufficient void space to allow water to expand, the high freeze-thaw resistance in UHPCs is due to water being prevented from entering the material in the first place. Test results showed that all UHPCs tested had a very low water uptake percent and an unchanged RDM%, signifying no internal damage. This corresponds well to other studies of similar materials with dense matrices and shows that this phenomenon also occurs in UHPC.
- All of the UHPC mixtures show high resistance to chloride ion penetration. Concretes made with the Portland Type I / GGBS Cement blend showed the least permeability, followed by specimens made with white cement and Portland type V cement. Concretes containing silica powder at 25% showed slightly higher ion permeability than those with 15% silica powder. The least permeable concrete mixes had 0% silica powder.
- Particle size distribution studies showed that while variations in silica powder content affect the material's packing density differently across the particle size range, the resulting distributions still remain close to the optimal particle packing density. Test results confirm this observation and show that variations in silica powder content had

little effect on the durability performance of the tested UHPC mixes. This signifies that this mix component could potentially be eliminated to reduce cost. Studies in Chapter 3 confirm that that elimination of silica powder, which is a key part of proprietary mixes, does not significantly influence the short term mechanical properties of the material.

Chapter 5

Factors Effect Bond Development between UHPC and Steel Bar Reinforcement

5.1. OVERVIEW

While UHPC's tensile and compression behaviors are relatively well understood, an in-depth analysis of UHPC's behavior at the component level, specifically the bonding ability between UHPC and steel bar reinforcement is lacking and the meager published data is contradictory. In the study presented in this chapter, a series of tests was performed in order to characterize the bond relationship of a non-proprietary UHPC blend with steel bar reinforcement. A series of bar pull out tests were conducted using plain and epoxy-coated grade 60 bars with nominal sizes of #4, #5 and #6 (13 mm, 16 mm, and 19 mm). Other experimental parameters include three development lengths (2", 3" and 4"), two fiber orientations (longitudinal and transverse to the steel bar), two steel fiber volume contents (1% and 2%) and bond strength at early age curing (1, 3 and 7 days). Additionally, the results of four flexure bending tests using UHPC lap spliced joints (discussed in more detail in Chapter 6) were compared to the pull out results in order to determine the bond capacity in a realistic loading scenario. Results from pull out testing show that bonding stress capacity decreases with increased embedment length suggesting a non-uniform distribution of bond stresses. Bond capacity in lap-spliced joints was less than in simple pull out tests, but within current design limits for regular reinforced concrete.

5.2. EXPERIMENTAL PARAMETERS AND PROCEDURE:

5.2.1. Bar Pull Out Testing Program and Test Set Up

The simple bar pull out test is the most widely used measure of bond capacity in concrete due to its simplicity and ease of implementation. It is also considered to be the least accurate testing method as it tends to overestimate the bond capacity as stated in ACI Committee 408's report (2003). In the traditional pull out test, load on the steel bar placed into tension results in compressive forces in the surrounding concrete as it reacts against the rigid support surface holding the specimen. In most reinforced concrete structures, and in contrast to the traditional pull out test method, both the steel reinforcement and concrete are under tension during loading.

In order to minimize the effects of the compressive region during testing, a modified method of supporting the concrete was implemented as shown in Figure 5-1a. This method was proposed by (Chao 2009). Unlike the traditional bar pull out case where the entire surface of the concrete is used as a support, the employed method makes use of the high bearing strength of the UHPC to minimize the surface area needed. The configuration uses 4 small steel plates to support the specimen, distancing the concrete surrounding the bar from any compressive struts which may form during loading. More details regarding this experimental configuration can be found in (Chao 2009).

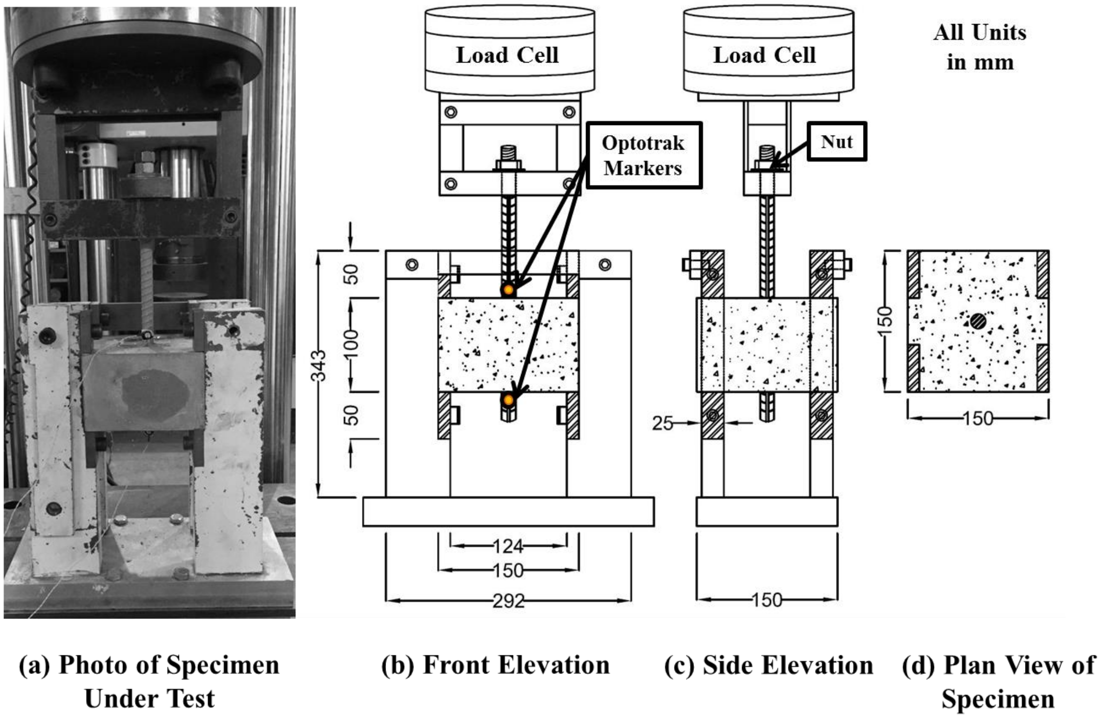

a b

Figure 5-1: (a) Test Set Up for Bar Pull Out (b) and Instrumentation and Load Path for Specimen

Specimens were subjected to a quasi-static displacement controlled load, using a 450 kN kip Instron hydraulic machine, at a rate of 0.025 mm/sec. Force applied on the specimen was recorded using a 450-kN load cell. Pullout displacement of the bar was recorded using the Optotrack displacement tracking system (Figure 5-1b), which is a non-contact measurement system that employs infrared markers.

The experimental program investigated the effects of several parameters on the bonding between the UHPC and embedded steel bars. All deformed bars used in this study were ASTM A615 steel. As shown in Table 1, three different bar diameters were tested at, 13 mm, 16 mm and 19 mm, for both plain and epoxy coated bars. Each of the bars was subjected to embedment lengths of 50, 75 and 100 mm, corresponding to different multiples of the bar diameters, d_b. For each embedded length, great care was taken when preparing the specimens to ensure that the same numbers of deformations (ribs) were embedded during preparation. The total number of deformations (ribs) embedded in each specimen were constant for each bar size and embedded length, with a tolerance of +/- 0.5 ribs (partial embedment of a rib).

Additionally, two different bar sizes (16 mm and 19 mm) were used to investigate the differences caused by fiber alignment during casting. Specimens were cast with fibers preferentially aligned parallel with the bar and transversely to the bar (Figure 5-2). Two different bar sizes (16 mm and 19 mm) were used to evaluate the effect of fiber content at 1% and 2% by volume. Finally, UHPC specimens were cast and tested at 1, 3 and 7 days cured in order to determine the early age bonding ability of the material.

The naming convention for the tests performed is as follows: the first entry represents the bar size and coating (black bars, i.e. not coated, or epoxy coated), followed by the embedded length in d_b (bar diameter), the fiber volume percentage, the casting orientation (P for parallel or T for transverse) and the age of the UHPC (1, 3, 7 or 28 days). For example, 13B-8.0-2%-P-28D represents a 13 mm diameter plain black bar, 8 d_b (100 mm), with 2% fibers by volume, UHPC cast parallel to the steel reinforcement at 28 days.

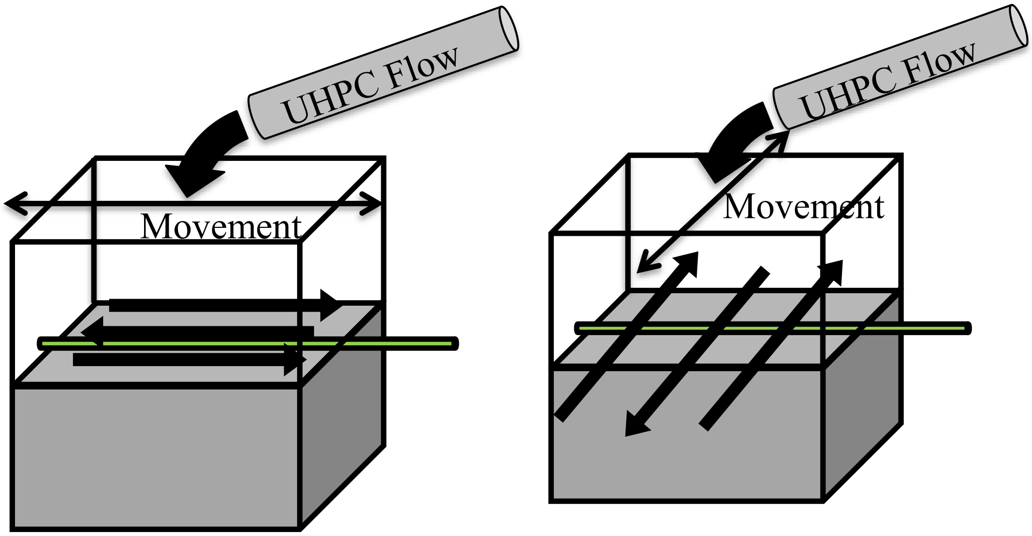

a b

Figure 5-2: (a) Fibers Aligned Parallel to Bar (b) Fibers Aligned Transversely to Bar

Table 5-1: Experimental Parameters and Number of Tests

Name	# of Test	Bar Dia. (mm)	Coating	Embedment Length (mm/D_b)	Fiber Content (% vol.)	Casting Orientation	Curing Age (days)
Effect of Embedded Length & Coating							
13B-8.0-2%-P-28D	2	13	None	100 (8.0)	2.0%	Parallel	28
13E-8.0-2%-P-28D	2	13	Epoxy	100 (8.0)	2.0%	Parallel	28
13B-6.0-2%-P-28D	2	13	None	75 (6.0)	2.0%	Parallel	28
13E-6.0-2%-P-28D	2	13	Epoxy	75 (6.0)	2.0%	Parallel	28
13B-4.0-2%-P-28D	2	13	None	50 (4.0)	2.0%	Parallel	28
13E-4.0-2%-P-28D	2	13	Epoxy	50 (4.0)	2.0%	Parallel	28
16B-6.4-2%-P-28D	3	16	None	100 (6.4)	2.0%	Parallel	28
16E-6.4-2%-P-28D	3	16	Epoxy	100 (6.4)	2.0%	Parallel	28
16B-4.8-2%-P-28D	2	16	None	75 (4.8)	2.0%	Parallel	28
16E-4.8-2%-P-28D	2	16	Epoxy	75 (4.8)	2.0%	Parallel	28
16B-3.2-2%-P-28D	2	16	None	50 (3.2)	2.0%	Parallel	28
16E-3.2-2%-P-28D	2	16	Epoxy	50 (3.2)	2.0%	Parallel	28
19B-5.3-2%-P-28D	2	19	None	100 (5.3)	2.0%	Parallel	28
19E-5.3-2%-P-28D	2	19	Epoxy	100 (5.3)	2.0%	Parallel	28
19B-4.0-2%-P-28D	2	19	None	75 (4.0)	2.0%	Parallel	28
19E-4.0-2%-P-28D	2	19	Epoxy	75 (4.0)	2.0%	Parallel	28
19B-2.6-2%-P-28D	2	19	None	50 (2.6)	2.0%	Parallel	28
19E-2.6-2%-P-28D	2	19	Epoxy	50 (2.6)	2.0%	Parallel	28
Effect of Fiber Orientation							
19E-4.0-2%-T-28D	2	19	Epoxy	75 (4.0)	2.0%	Transverse	28
16B-6.4-2%-T-28D	3	16	None	100 (6.4)	2.0%	Transverse	28

Name	# of Test	Bar Dia. (mm)	Coating	Embedment Length (mm/D_b)	Fiber Content (% vol.)	Casting Orientation	Curing Age (days)
Effect of Curing Age							
16E-6.4-2%-P-1D	2	16	Epoxy	100 (6.4)	2.0%	Parallel	1
16E-6.4-2%-P-3D	2	16	Epoxy	100 (6.4)	2.0%	Parallel	3
16E-6.4-2%-P-7D	2	16	Epoxy	100 (6.4)	2.0%	Parallel	7
Effect of Fiber Volume Content							
16E-6.4-1%-P-28D	3	16	Epoxy	100 (6.4)	1.0%	Parallel	28
16E-6.4-2%-P-28D	3	16	Epoxy	100 (6.4)	2.0%	Parallel	28
19B-4.0-1%-P-28D	2	19	None	75 (4.0)	1.0%	Parallel	28

5.2.2. Lap Splice Joint Testing Program

Beam specimens F-100-1P-1, F-100-1P-2, F-100-2P-1 and F-100-2P-2 described in Chapter 6 represent a more realistic anchorage scenario for UHPC. As discussed later on in Chapter 6, these specimens comprise two regular precast concrete beam elements joined together at the center with a UHPC closure pour. Bottom bars are subjected to pull out in a lap splice configuration when the beams are subjected to flexural loading. The difference between pull out and lap splice testing configurations has been understood for regular concrete for some time. ACI Committee 318-05, Section 12.15.2 (and AASHTO LFRD 5.11.5.3.1) recommends multiplying the required anchorage length by 1.3 l_d when designing a non-contact lap splice vs. simple bar pull out for regular concrete.

Some details from Chapter 6 are repeated here for the sake of readability. Full details are found in Chapter 6. Figure 5-3 shows the construction and reinforcement details for the specimen. Longitudinal bars were spaced at 6.3” (160 mm) and transverse bars were spaced at 8” (200 mm). The lower layer of reinforcement sat at a depth of 3.3" (85 mm) (measured from the top surface) while the upper layer was placed at a depth of 1.4" (36 mm). All reinforcement consisted of epoxy-coated bars with a diameter of 16 mm (#5 bars). The UHPC joint measured 4" (100 mm) wide with a lap splice length of 3.6" (90 mm). All tests were subjected to four-point bending as shown in Figure 5-4. The UHPC joint was cast in order to favor orientation of the steel fibers parallel to the reinforcement bar direction. Force in the steel bars was computed from a cracked section analysis at the joint face.

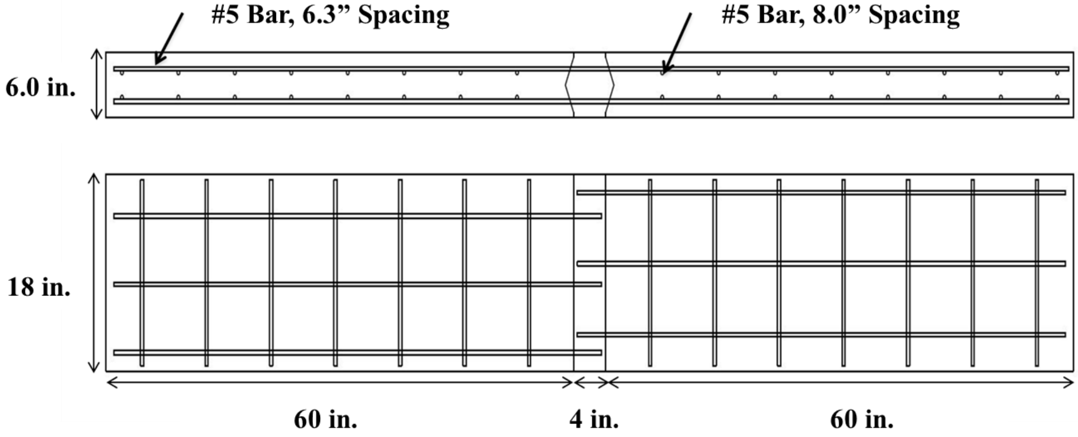

Figure 5-3: Construction and Reinforcement Details for Precast Decks with UHPC Joint

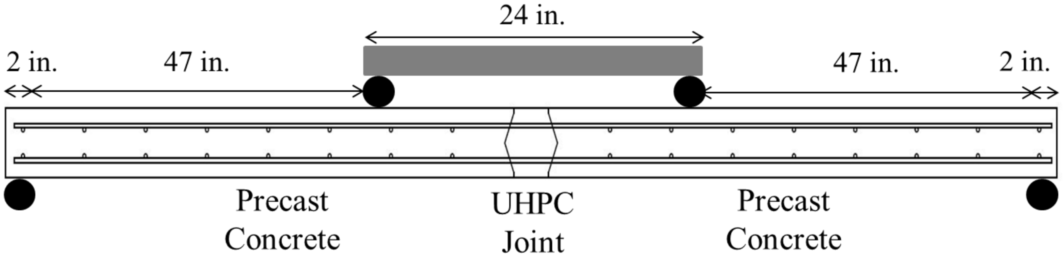

Figure 5-4: Four Point Bending Test Set Up for Flexure Test for Specimens F-100-1P-1, F-100-1P-2, F-100-2P-1 and F-100-2P-2

As discussed in Chapter 6, the beams were subjected to a displacement controlled, quasi-static load at a rate of 0.001 in/sec (0.025 mm/sec), using a 100 kip Instron hydraulic machine. Force on the specimen was recorded using a 100-kip load cell. Deformation in the UHPC joint was recorded using the Optotrack tracking system on one face of the specimen and through Digital Image Correlation on the other face.

5.2.3. Material Properties

The UHPC specimens were constructed using a previously designed low cost, generic form of UHPC. Extensive details regarding the materials strengths in tension and compression as well as other material properties can be found in (Alkaysi 2015, 2016). The design mix ratios and quantities are shown in Table 2. The cement chosen for this mix featured a 50-50 ratio of Portland Type I cement and Ground Granulated Blast Furnace Slag (GGBS). The mix also contains two grades of fine silica sand aggregate, designated as Fine Sand I and II. Bar Pull Out specimens contained 2% steel fibers by volume (unless notes otherwise). The steel fibers are brass coated, smooth fibers. Each fiber is 19 mm long with a diameter of 0.2 mm and minimum tensile strength of 1965 MPa. Table 5-2 lists the yield and ultimate strengths for the 13 mm and 16 mm diameter bars used in this study. Data for 19 mm bar was unavailable and as such, its minimum strengths as required by ASTM A615 are listed instead.

Table 5-2: Steel Strength Properties Provided Steel Reinforcement Bars

Bar Size	F_y kips (KN)	F_u kips (KN)
13 mm	12.3 (54.7)	17.5 (77.84)
16 mm	22.5 (100.1)	32.0 (142.3)
19 mm	26.5 (117.8)*	39.8 (177.0)*

*Per ASTM A615

5.3. RESULTS AND ANALYSIS

5.3.1. Bar Pull Out Results

Table 5-3 below shows the data from the bar pull out testing and lists the type of failure mode for each specimen. Testing revealed three distinct failure modes for bond (Figure 5-5); bar fracture, slip of the bar from the UHPC accompanied by splitting of the UHPC cube, and a conical shaped failure in which the UHPC attached to the bar separates from the UHPC cube. Figure 5-5 shows the different failure modes. Data on peak measured forces and associated nominal bond stresses are listed in Table 5-3. The peak nominal bond stress is computed as the achieved pull out force divided by the initial surface area of the embedded portion of the bar, as follows:

$$\tau_{bond} = \frac{F_{bar,max}}{\pi d_B l_d} \qquad (1)$$

Where $F_{bar,max}$ is the peak force in the bar, taken as failure in the specimen, d_b is the bar diameter (in mm) and l_d is the embedded length (mm).

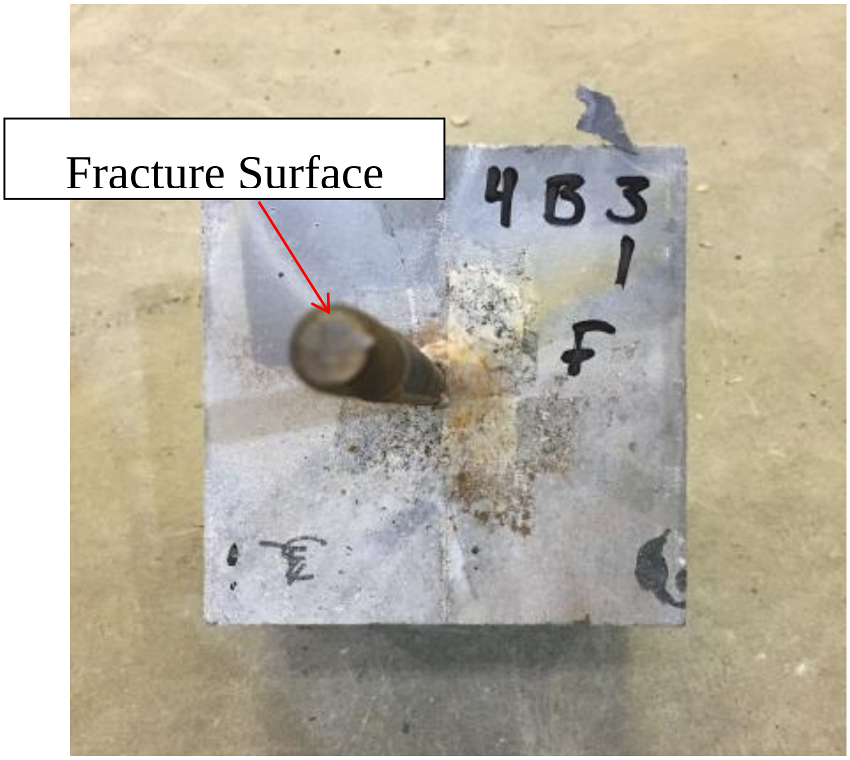

(a)

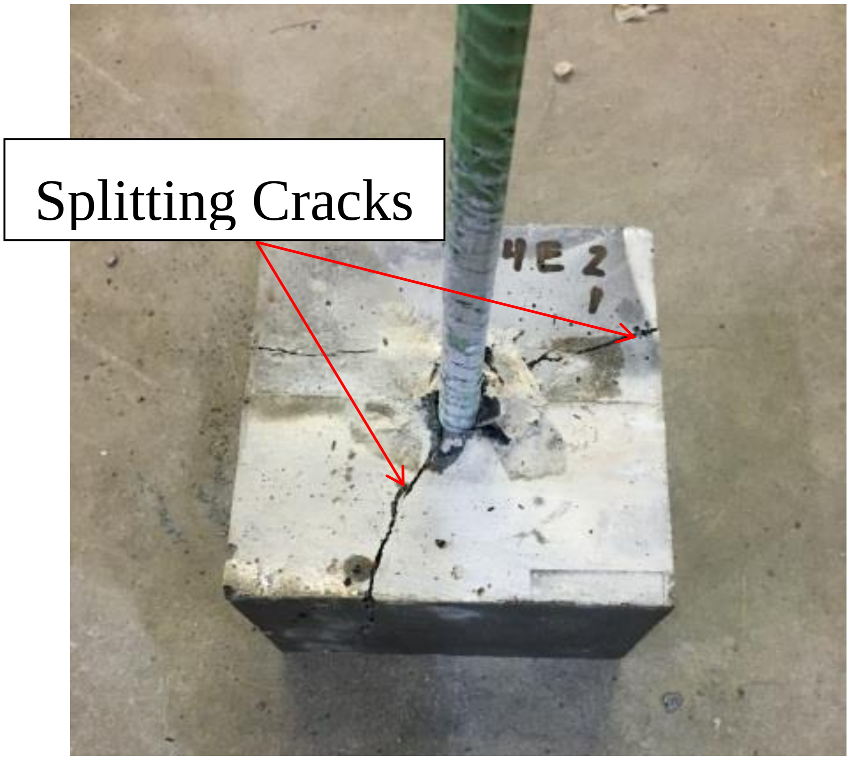

b

c

Figure 5-5: (a) Bar Fracture, (b) Bar Slip, and (c) Conical Concrete Failure

Name	Mode of Failure			τ_{bond}			f’c
	1	2	3	1	2	3	MPa (ksi)
Effect of Embedded Length & Coating							
13B-8.0-2%-P-28D	Fracture	Fracture	-	19.2 (2.8)	19.3 (2.8)	-	189.4 (27.5)
13E-8.0-2%-P-28D	Fracture	Fracture	-	19.2 (2.8)	19.3 (2.8)	-	189.4 (27.5)
13B-6.0-2%-P-28D	Fracture	Yield, Slip	-	22.9 (3.3)	21.7 (3.2)	-	188.9 (27.4)
13E-6.0-2%-P-28D	Fracture	Yield, Slip	-	23.5 (3.4)	22.8 (3.3)	-	188.9 (27.4)
13B-4.0-2%-P-28D	Slip	Yield, Slip	-	32.7 (4.7)	33.5 (4.9)	-	191.0 (27.5)
13E-4.0-2%-P-28D	Slip	Yield, Slip	-	26.2 (3.8)	30.2 (4.4)	-	191.0 (27.5)
16B-6.4-2%-P-28D	Slip	Slip	Slip	16.0 (2.6)	15.3 (2.2)	18.6 (2.7)	189.4 (27.5)
16E-6.4-2%-P-28D	Slip	Slip	Slip	16.2 (2.4)	18.3 (2.7)	19.2 (2.8)	189.4 (27.5)
16B-4.8-2%-P-28D	Slip	Slip	-	18.8 (2.7)	16.7 (2.4)	-	188.9 (27.4)
16E-4.8-2%-P-28D	Slip	Slip	-	18.2 (2.6)	19.9 (2.9)	-	188.9 (27.4)
16B-3.2-2%-P-28D	Slip	Slip	-	30.9 (4.5)	31.0 (4.5)	-	191.0 (27.5)
16E-3.2-2%-P-28D	Slip	Slip	-	30.9 (4.5)	31.5 (4.6)	-	191.0 (27.5)
19B-5.3-2%-P-28D	Slip	Slip	-	14.5 (2.1)	14.3 (2.1)	-	189.4 (27.5)
19E-5.3-2%-P-28D	Slip	Slip	-	14.7 (2.1)	15.2 (2.2)	-	189.4 (27.5)
19B-4.0-2%-P-28D	Slip	Slip	-	18.6 (2.7)	16.5 (2.4)	-	188.9 (27.4)
19E-4.0-2%-P-28D	Slip	Slip	-	21.2 (2.8)	16.9 (2.4)	-	188.9 (27.4)
19B-2.6-2%-P-28D	Cone	Cone	-	20.1 (2.9)	25.8 (3.7)	-	191.0 (27.5)
19E-2.6-2%-P-28D	Cone	Cone	-	26.3 (3.8)	20.1 (2.9)	-	191.0 (27.5)
Effect of Fiber Orientation							
19E-4.0-2%-T-28D	Slip	Slip	-	14.7 (2.1)	15.5 (2.2)	-	188.9 (27.4)
16B-6.4-2%-T-28D	Slip	Slip	Slip	18.0 (2.6)	18.3 (2.7)	18.6 (2.7)	188.9 (27.4)
Effect of Curing Age							
16E-6.4-2%-P-1D	Slip	Slip	-	10.8 (1.6)	9.4 (1.4)	-	52.8 (7.7)
16E-6.4-2%-P-3D	Slip	Slip	-	11.5 (1.7)	10.7 (1.6)	-	88.0 (12.8)
16E-6.4-2%-P-7D	Slip	Slip	-	13.4 (2.2)	15.8 (2.4)	-	124.6 (18.1)
Effect of Fiber Volume Content							
16E-6.4-1%-P-28D	Slip	Slip	Slip	14.0 (2.0)	14.8 (2.1)	15.5 (2.2)	180.1 (26.1)
16E-6.4-2%-P-28D*	Slip	Slip	Slip	15.4 (2.2)	18.5 (2.7)	18.9 (2.7)	188.9 (27.4)
19B-4.0-1%-P-28D	Slip	Slip	-	10.5 (1.5)	11.6 (1.7)	-	180.1 (26.1)

*These specimens are similar to 16E-6.4-2%-P-28D listed earlier in the table. They represent an additional set that was cast at the same time and from the same UHPC batch as 16E-6.4-1%-P-28D to provide more confidence in the experimental data.

Table 5-3: Test Results for Simple Bar Pull Out

5.3.2. Effect of Embedment Length

Figure 5-6 shows the effects of embedment length for a 13 mm dia. bar subjected to simple bar pull out. At 100 mm (8 d_b) embedment, all specimens failed via bar fracture, with no difference between black and epoxy coated bars. For this reason no force-displacement relation has been plotted. At an embedment of 75 mm (6 d_b), the specimens failed in either bar fracture, or bar yielding, followed by slip in the bar. Again, differences between plain and epoxy bars were minor. At 50 mm (4 d_b) embedment, two specimens yielded, followed by bar slip. The remaining specimens all experienced pure slip. At 50 mm, the differences between the black and epoxy bars were more apparent, with black bars achieving a higher peak pull out force, and higher bond stresses.

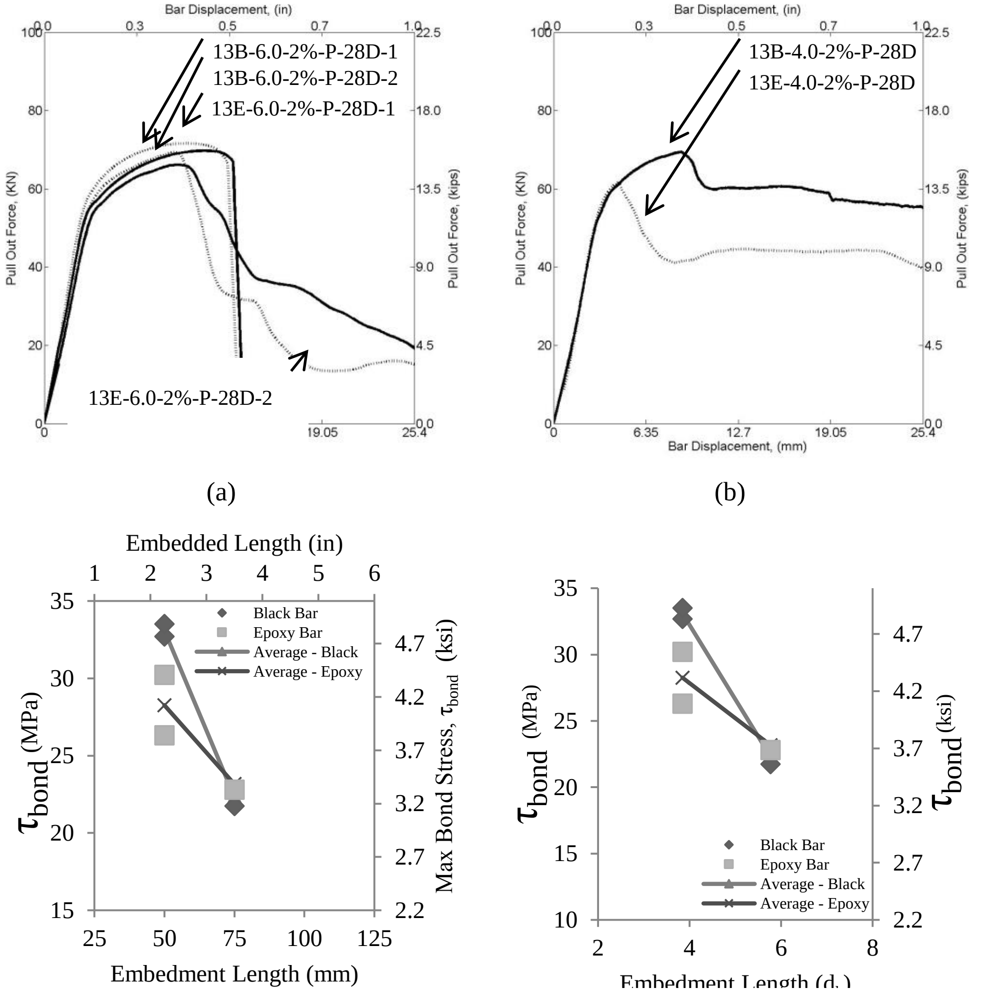

(a) (b)

*Note: Data from 100 mm (8d$_b$) and 75 mm (6 d$_b$) embedded lengths which resulted in bar fracture

(c) (d)

Figure 5-6: (a) Force-Displacement for 6 d$_b$ embedment and (b) 4 d$_b$ embedment, (c) Nominal Peak Bond Stress vs. Embedment Length in mm and (d) in d$_b$ for 13 mm bars

Figure 5-7 shows the results of embedment for 16 mm dia. bars. Unlike the 13 mm dia. bar, no 16 mm dia. bars reached yield or bar fracture (as can be seen in the force-displacement curves). All of the specimens failed via bar slip. At 6.4 d$_b$ (100 mm), black bars were able to reach a slightly higher bond stress vs. their epoxy counter parts. This also occurred at 3.2 d$_b$ (50 mm), though at 4.8 d$_b$ (75 mm). Again, for both bar types, τ_{bond} averaged for all of the tests decreased with increasing embedment, which is again attributed to the uneven force distribution along the length of the bar.

Figure 5-8 shows the data for 19.0 mm dia. bars. At 5.3 d_b (100 mm) and 4.0 d_b (75 mm) embedment, all of the bars experienced slip. At 2.6 d_b (50 mm), all specimens failed due to a conical separation in the concrete. As such, data points at this embedment do not represent bond strength, but merely the peak pullout force achieved prior to concrete cone failure, and are therefore removed from the analysis of the overall test data. In these cases, the UHPC bonded to the bar separated from the UHPC in the cube, leading to a drop in sudden strength. As seen with the previous bar diameters, as embedment increases, τ_{bond} decreases.

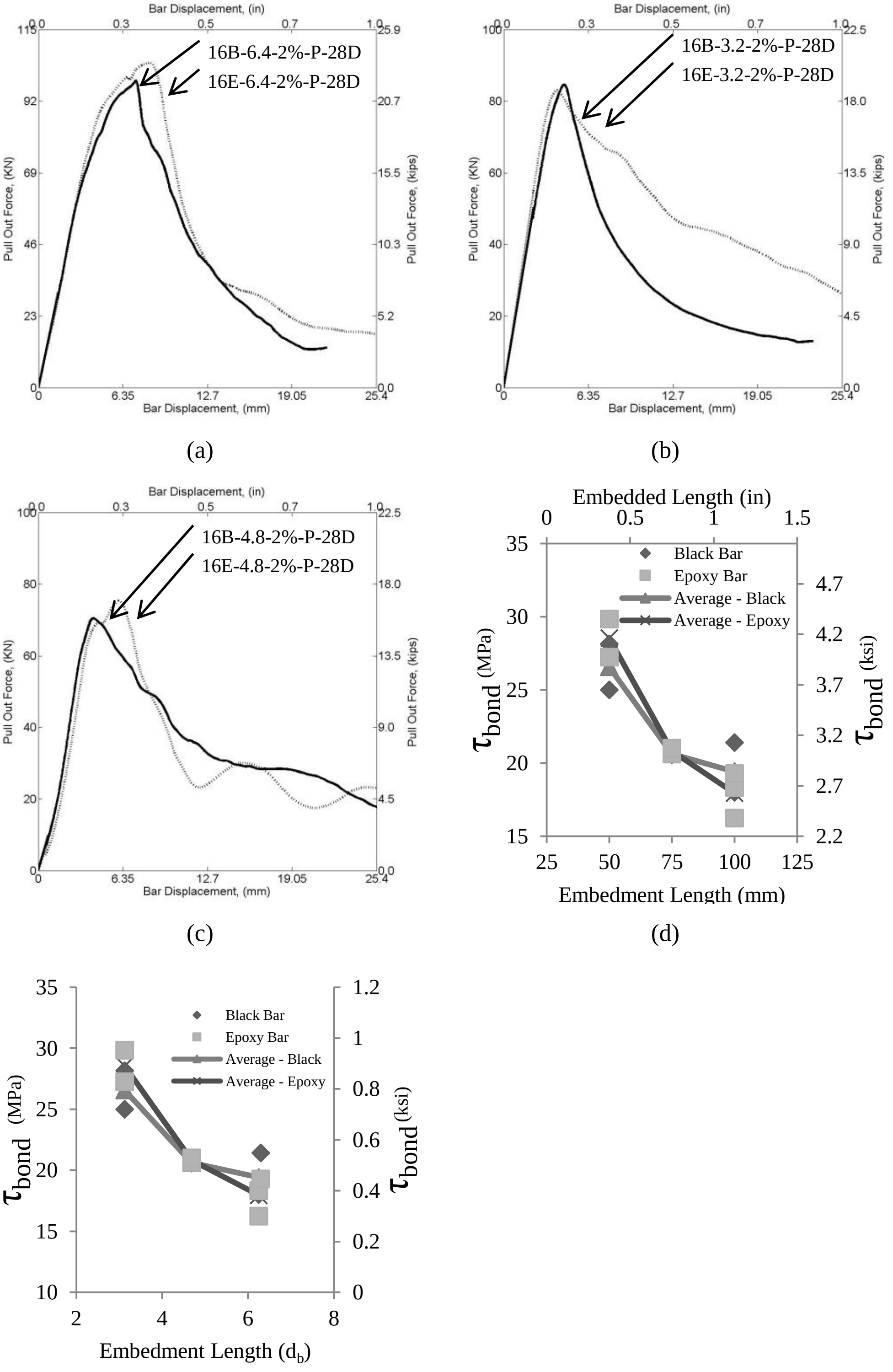

(a)

(b)

(c)

(d)

(e)

Figure 5-7: (a) Force-Displacement for 6.4 d_b embedment, (b) 4.8 d_b embedment, (c) 3.2 d_b embedment, (d) Nominal Peak Bond Stress vs. Embedment Length in mm and (e) in d_b for 16 mm bars

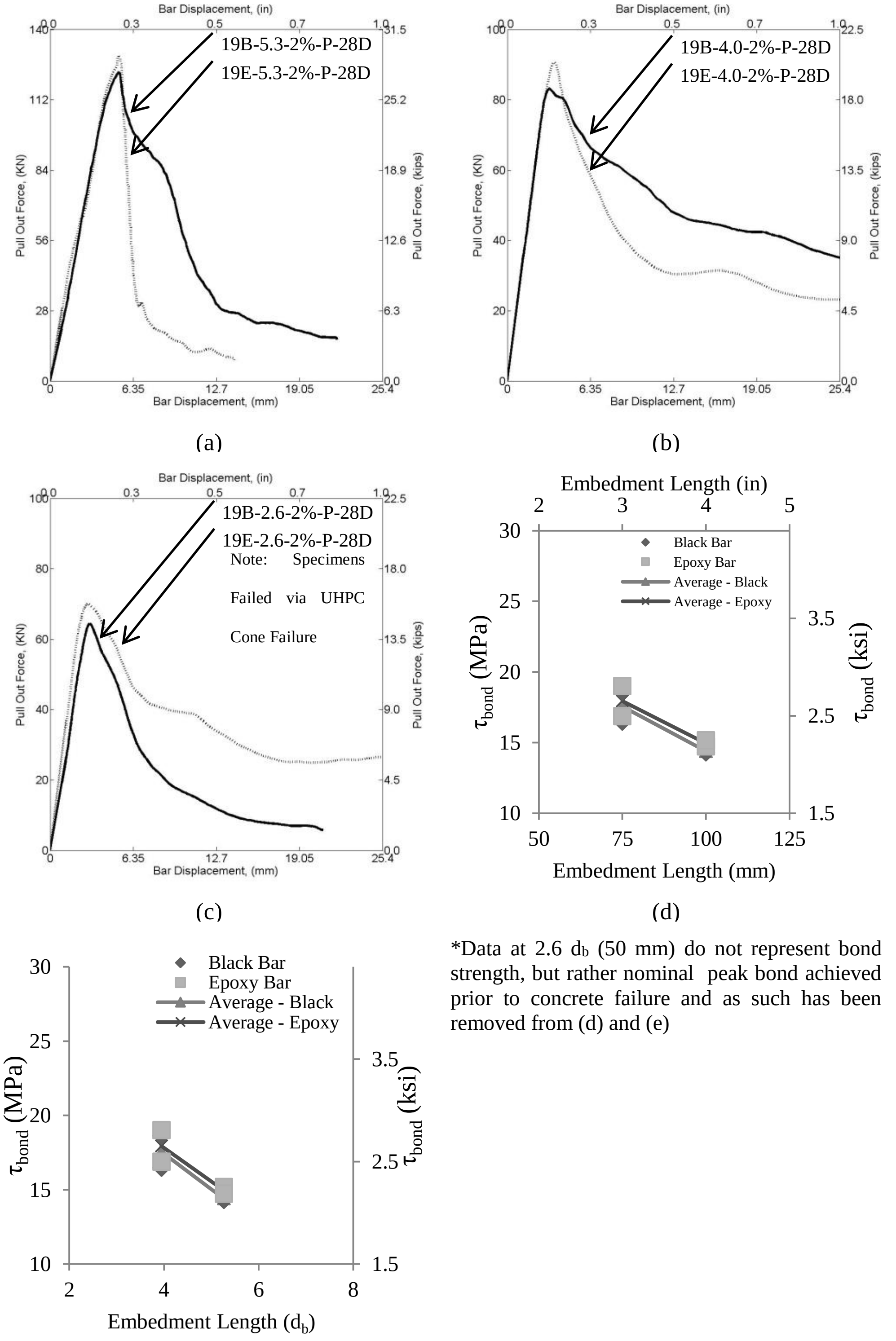

(a)

(b)

(c)

(d)

(e)

*Data at 2.6 d_b (50 mm) do not represent bond strength, but rather nominal peak bond achieved prior to concrete failure and as such has been removed from (d) and (e)

Figure 5-8: (a) Force-Displacement for 5.3 d_b embedment, (b) 4.0 d_b embedment, (c) 2.6 d_b embedment, (d) Nominal Peak Bond Stress vs. Embedment Length in mm and (e) in d_b for 19 mm bars

Figure 5-9a plots τ_{bond} achieved for all of the specimens as a function of the embedment length as a multiple of d_b. The overall downward linear trend observed before is clearly evident here for all bar types and sizes. Figure 5-9b plots the peak bar stress versus embedment length (as a function of d_b) for all specimens with parallel-oriented fibers, at 2% fibers by volume and 28 days cured. As expected the increase in embedment results in an increase in the peak bar stresses.

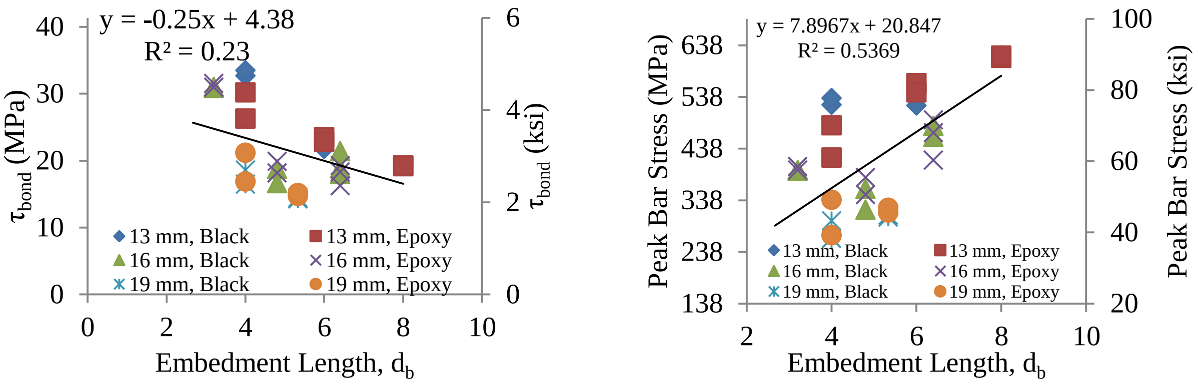

(a) (b)

Figure 5-9: (a) Nominal Peak Bond Stress Achieved vs. Embedded Length and (b) Peak Bar Stress vs. Embedded Length, 2% fiber vol., Parallel Fiber Orientation, 28 days cured

5.3.3. Effect UHPC Cast Orientation on Bond

The effect of casting orientation and fiber alignment on bond was also investigated. Figure 5-10 shows the resulting relation for specimens with UHPC cast parallel and transversely to the steel reinforcement for a 16 mm bar (light grey) and an embedment of 6.4 d_b. As seen, there is little difference in the achieved strengths. For the 19 mm bars (dark grey) with an embedment of 4.0 d_b, fibers aligned parallel with the bar provide a somewhat higher force resistance than those transverse to the steel bar, which leads to a 17% difference in the nominal peak bond stresses reached. A closer examination of Table 5-3 shows that these differences are within the statistical range of variations in the data, and are more likely due to other factors (number of ribs embedded, etc.). Previous studies (Graybeal 2014) have also concluded that the effects of fiber orientation are minimal, though no work has been done on this at embedment less than $3d_b$.

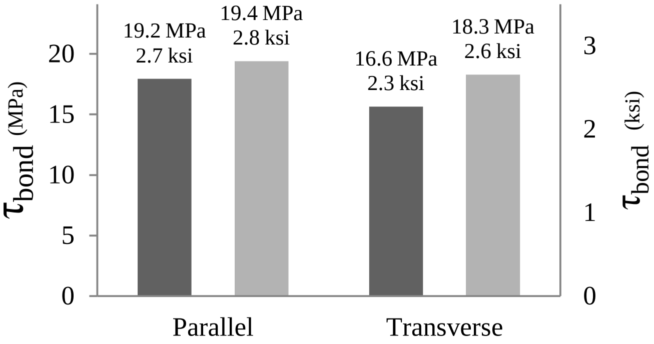

Figure 5-10: Peak Bond Stress Comparison (Dark Gray- 19 mm bars at 4.0 d_b, Light Gray – 16 mm bars at 6.4 d_b)

5.3.4. Effects of Fiber Volume Content

Two series of bar pull out tests were tested containing 1% fibers by volume and compared to those tested containing 2% fibers by volume. Figure 10a shows τ_{bond} compared for the 19 mm and 16 mm bar specimens at 1% and 2% fibers by volume. For the 16 mm bars, τ_{bond} decreased by 18% as the fiber volume dropped from 2% to 1%. For the 19 mm bars, specimens containing only 1% fibers developed 36% less bond strength than those with 2% fibers. The larger drop in strength for the 19 mm bar is likely influenced by differences in the number of ribs embedded from specimen to specimen, since at the lower embedded length the effect of ribs is more pronounced. Figure 5-11b shows τ_{bond} compared for the two fiber contents normalized to the square root of the compressive strength (√f'c). The normalized τ_{bond} showed similar differences; 36% less bond between 2% and 1% fibers for the 19 mm specimens and 15% less bond between 2% and 1% fibers in the 16 mm specimens. This seems to confirm that τ_{bond} is dependent on the quantity of fibers available to bridge any cracks forming under loading, rather than the differences in compressive strength associated with fiber volume quantity.

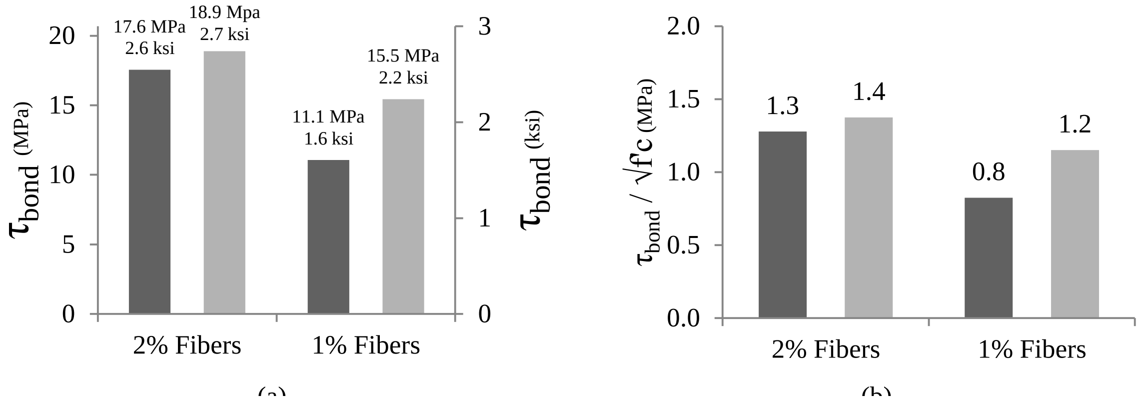

Figure 5-11: (a) Nominal Peak Bond Stress Achieved and (b) Normalized Nominal Peak Bond Stress at 1% and 2% Fibers by volume: 19 mm bars, Embedded 4.0 d_b (Dark Grey) and 16 mm bars, Embedded 6.0 d_b (Light Grey)

5.3.5. Early Age Testing of UHPC on Bond

An investigation into the bonding strength between UHPC and steel reinforcement was performed at 1, 3 and 7 days cure time. From Figure 5-12a, testing at 1 day generally yielded the lowest strength with bond stress increasing at 3, 7 and 28 days respectively. Similar gains in compressive strength are seen in Figure 5-12b. Regular concrete follows a similar trend regarding the increase in early age strength vs. time which results from the pozzolonic reaction of the cement (Elaty 2014). As the UHPC uses ingredients found in regular concrete, a generally comparable increasing trend in strength over time is expected as the reaction requires time to complete. Similarly, as the pozzolonic reaction continues, the bonding between the cementitious material and the steel fibers strengthens. Enhanced fiber-concrete composite behavior increases the total confinement available in the UHPC, which increases the bond strength.

The UHPC composite achieves approximately 75% of its pull-out strength after 7 days. Figure 11c plots τ_{bond} for all tests done with 16 mm epoxy bars, embedded at 6.4 d_b at 1, 3, 7 and 28 days. As seen, τ_{bond} in the specimens increases linearly with increases in the square root of the compressive strength, $\sqrt{f'c}$. Though, as shown later, this correlation diminishes when compared with other bar diameters. Still, this information could be useful for the development of future provisions for UHPC design.

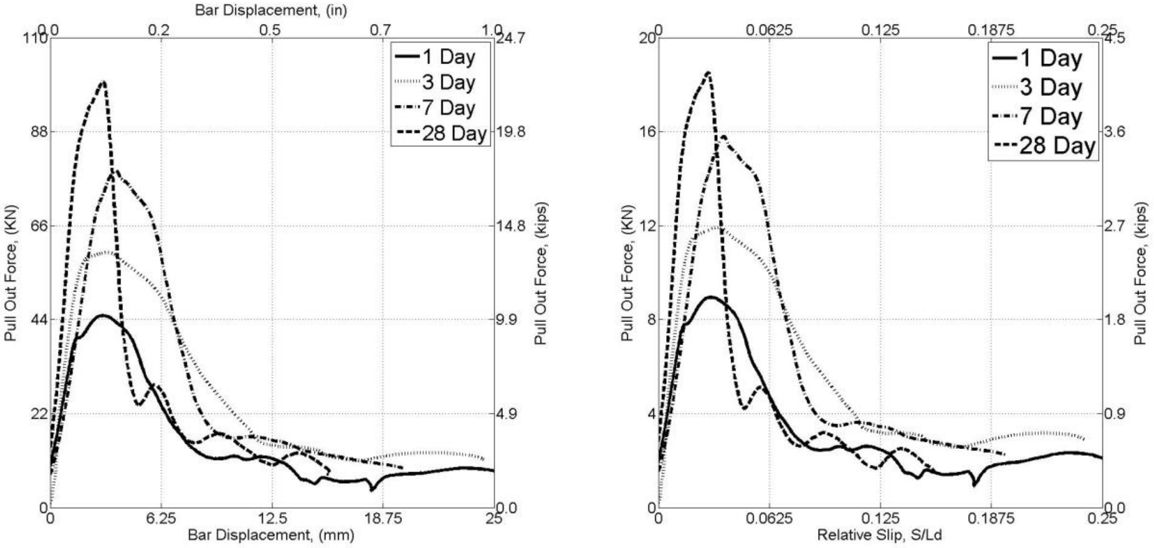

Figure 5-12: (a) Force-Slip Curve, (b) Bond Stress – Relative Slip

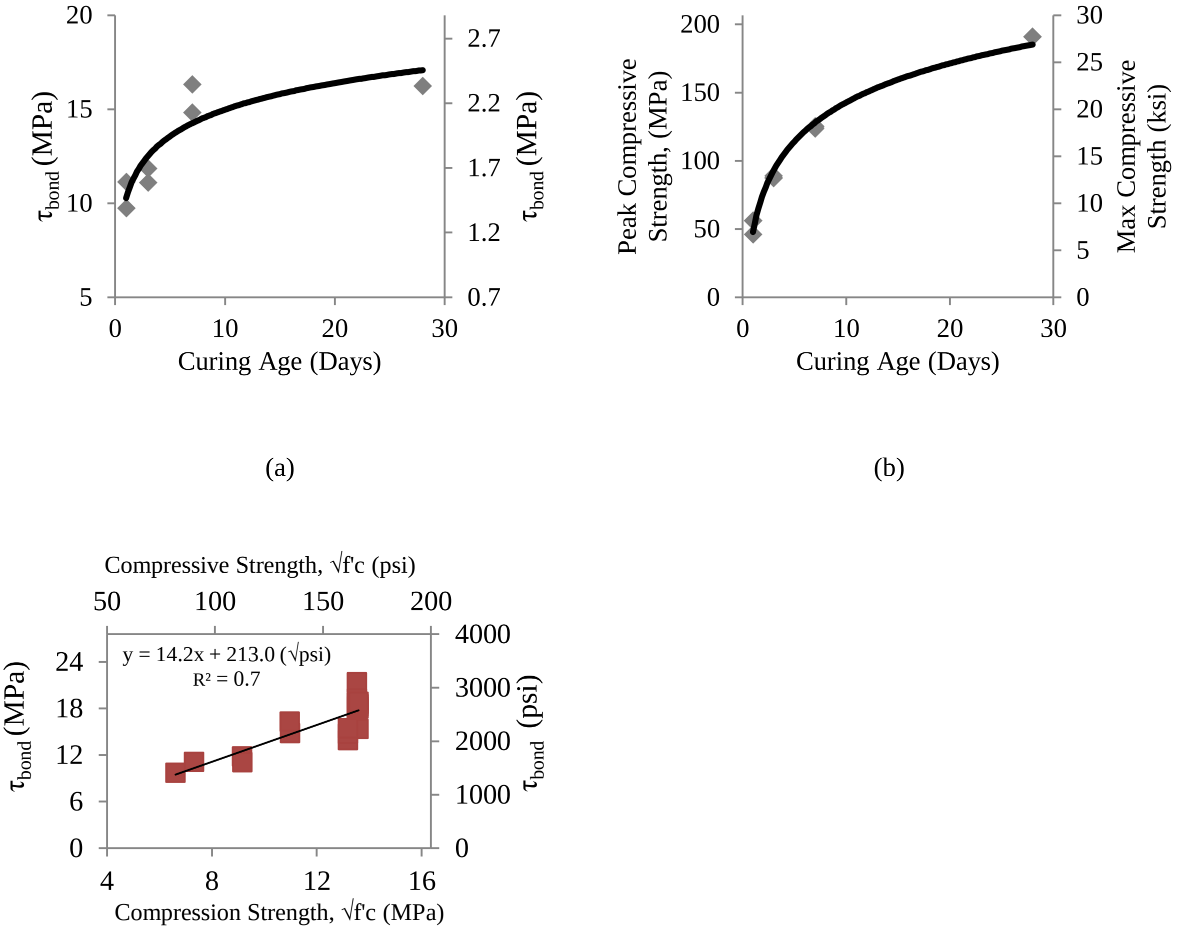

(a)

(b)

(c)

Figure 5-13: (a) τ_{bond} as a Function of Curing Time, (b) Compressive Strength vs. Curing Time, (c) τ_{bond} vs. Square Root of Compression Strength of Concrete, √f’c, over time

5.3.6. Bar Pull Out vs. Lap Splice Beam Results

As discussed previously, the lap spliced specimens were constructed with the intention of comparing the bond data to that gathered from the simple bar pull out testing. All tests in this series contained #5 (16 mm) dia. bars. Pulls out tests in this configuration were embedded 100 mm, and the UHPC joints had an embedment of 4” (100 mm) and splice lengths of 3.6” (90 mm). Both UHPCs were tested at 1% and 2% fibers by volume. More details regarding the specimen details, loading and detailed results can be found in Chapter 6. For brevity, only the results are displayed here (Table 5-4). Figure 5-14 lists the average bond stress achieved between the two series of specimens. At 2% fibers by volume, simple bar bull out specimens averaged bond stresses of 2.6 ksi (18.0 MPa), or about 12% more than the 2.3 ksi (15.7 MPa) achieved by the lap-spliced bars. For specimens containing 1% fibers by volume, specimens developed average bond strength 7% less in the lap splice vs. the pull out case. For both of these fiber volume contents, the decrease in strength sits within the current ACI (and AASHTO) limit of an increase of 1.3 l_d increase for lap spliced anchorages. Therefore, increasing simple bar test bond data by the factor prescribed by ACI (and AASHTO) is deemed acceptable for future designs of reduced UHPC anchorage lengths, albeit on the conservative side.

Test		Embedded Length inches (mm)	Splice Length inches (mm)	Force at Joint kips	Bond Stress ksi
1	Flexure 1%	4” (100)	3.6” (90)	4.3	2.1
2	Flexure 1%	4” (100)	3.6” (90)	4.3	2.1
3	Flexure 2%	4” (100)	3.6” (90)	4.6	2.2
4	Flexure 2%	4” (100)	3.6” (90)	4.8	2.3

Table 5-4: Test Results Beam Lap Splice Tests

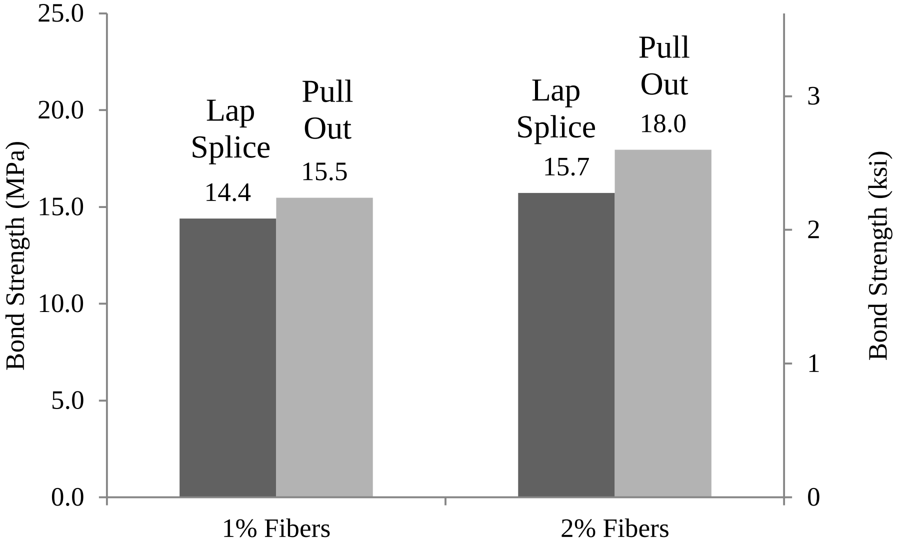

Figure 5-14: Average Bond Stresses in lap splices vs. bar pull out specimens.

5.3.7. Evaluation of Content Bond Data Available on UHPC

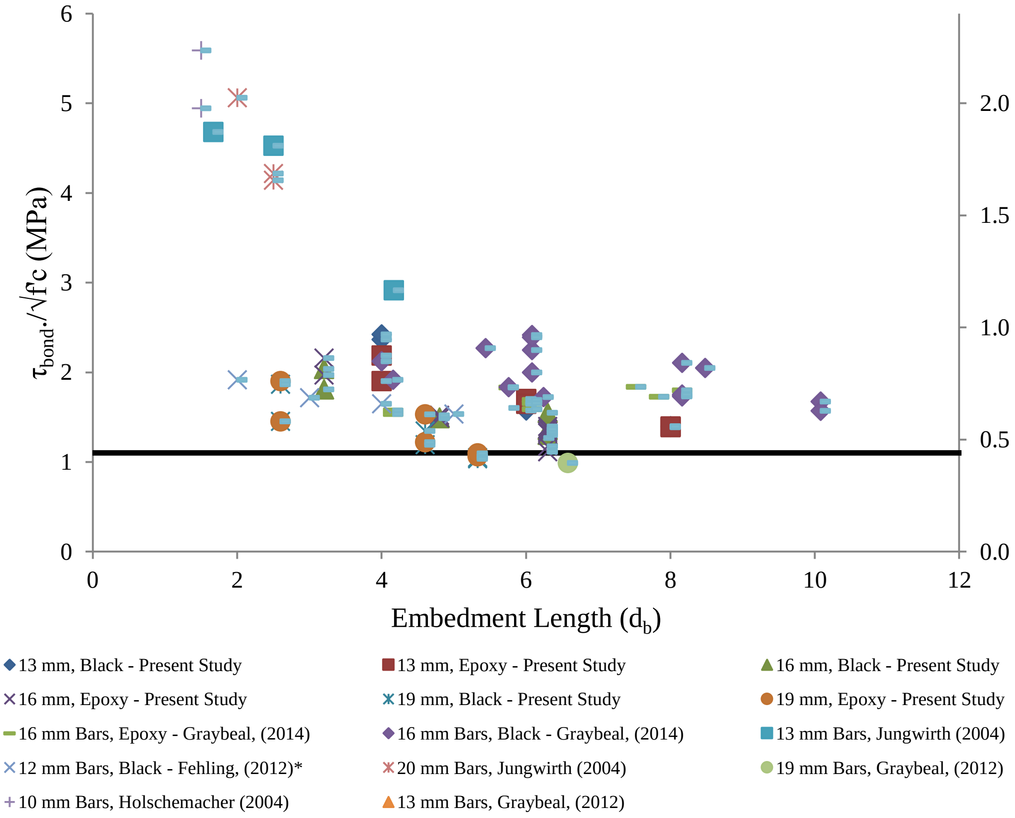

*Data on compressive strength was not provided, so 170 MPa was used to normalize based on data from other works included in the figure.

Figure 5-15: Scatter of the current data available for 13 mm, 16 mm, and 19 mm bars (Graybeal 2006, 2014, Fehling 2012, Holschemacher 2004, Jungwirth 2004)

Figure 5-15 shows the reported bond values normalized to the square root of the compressive strength for the bar sizes tested in this study along with all other published data found by the authors. From the scatter, there appears to be an asymptotically decreasing trend between τ_{bond} and increases in embedment length as a function of d_b. This trend is logical; since the development of bond is non-linear along the length of the bar during loading, it is expected that the relationship between nominal peak bond strength and embedment is also non-linear. The data at the lower limits of embedment (<3 d_b) remains sparse, with bond strengths ranging between1.3$\sqrt{f'c}$ (MPa) and 6$\sqrt{f'c}$ (MPa). More testing is needed to quantify bond in this region.

Further examination of Figure 5-15 shows that τ_{bond} values at embedment lengths greater than 4d_b appear to level off. While τ_{bond} varies across the data range (caused by differences in concrete cover, confinement, material type, fiber content, test set up, etc.) the above trend shows τ_{bond} approaching a value of at least 1.1$\sqrt{f'c}$ (MPa). Focusing more closely on more recent data on UHPC bond, Figure 5-16 shows τ_{bond} developed for 16 mm plain black and epoxy coated bars from the current study and from the Graybeal (2014) study, all normalized by $\sqrt{f'c}$. In general, the data from (Graybeal 2014) shows a slight *increase* in τ_{bond} / $\sqrt{f'c}$ as embedment increases. This is opposite the observed trend from the current study, which shows a *decrease* in τ_{bond} / $\sqrt{f'c}$ with increased embedment. The Graybeal data is recorded at 1 and 7 days curing, unlike this study which is recorded at 28 days. It is not clear why these contradictory (albeit minor) trends occur, but differences in curing time and test method may be contributing factors.

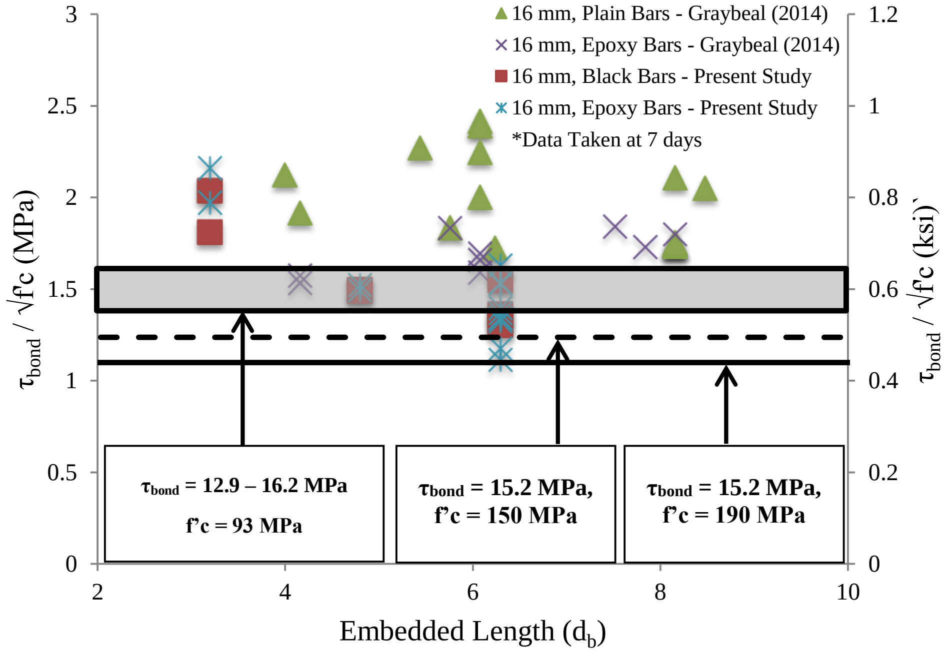

Figure 5-16: τ_{bond} for 16 mm Bars (Graybeal, 2014)

The proposed τ_{bond} limit of 1.1√f'c is represented in figure 13 as a solid line (for f'c = 190 MPa) and a dashed line (assuming f'c = 150 MPa). In the aforementioned Graybeal (2014) study, the following design recommendation was made: for a deformed reinforcing bar embedded in UHPC, bar stress can reach the lesser of the bar yield strength or 75 ksi (517 MPa) for bar sizes between 13 mm and 25 mm, either uncoated or epoxy coated, with a minimum compressive strength of 93 MPa if given a minimum embedment of 8d_b. This corresponds to a τ_{bond} value of 12.9 MPa (1.8 ksi) or 1.3√f'c (MPa) at the recommended lower limit of bar yield of 413.4 MPa (60 ksi) and 16.2 MPa (2.3 ksi) or 1.7√f'c (MPa) at the recommended upper limit of 516.7 (75 ksi). This is represented in the above figure as the shaded gray area.

The limit proposed in the current work is lower than that described in the Graybeal (2014) report. However, it important to note that the proposed limit is lower in order to account for variations in data due to concrete strength, clear spacing, cover, etc., from the scatter of data in the sum of previous works and those collected in the current study. From the previously compiled data, the following recommendation can be made. For bar diameters, ranging between 13 mm and 19 mm, and an embedded length greater than $3d_b$, and a minimum compressive strength of 150 MPa, it is proposed that an assumed maximum bond stress, τ_{bond}, equal to $1.1\sqrt{f'c}$ (MPa) (lower solid black line in Figure 13) can be used in order to predict the required embedment lengths in UHPC.

5.4. CONCLUSION

The objective of this chapter was to investigate the bonding ability between non-proprietary UHPC and steel reinforcement bars. Simple bar pull out tests were performed at 3 different embedment lengths, 2 bar coatings, 3 bar diameters, 2 fiber volume percentages, and 2 UHPC casting orientations. Early age bonding of UHPC was also tested at 1, 3 and 7 days. Additionally, 4 precast beams were joined together with a UHPC lap splice in order to compare the bonding between the simple pull out case and a more realistic anchorage scenario as well as the effect of fiber content.

- At the lower limits of embedment lengths, increasing embedment leads to a reduction in the nominal peak bond stress. This is attributed to an uneven distribution of force along the length of the bar, a fact that is established for high strength concretes. This appears consistent with other studies on UHPC, albeit differing in set up and materials used. Recorded values of bond still vary greatly, especially at lower embedment length, warranting further investigation.
- Casting the UHPC with the alignment of the fibers transverse to the reinforcement steel showed negligible differences in bonding and strength. The tests conducted herein were for small specimens. Further research is needed to ascertain whether this trend holds true at larger scale and other casting conditions.

- Changes in steel fiber content by volume resulted in differences between 21% and 36% in bond strength achieved in the simple pull out test. Similar differences in bond were seen when normalized to √f'c, suggesting that the bond strength is dependent on the quantity of fibers available to bridge any cracks forming under loading, rather than the differences in compressive strength associated with fiber volume quantity.
- Early age characteristics of bond increase over time, with 75% of its bond and compressive strength developed within 7 days of curing. Additionally, the nominal peak bond stress achieved shows a strong linear correlation with the square root of the compressive strength, √f'c.
- An assumed maximum bond stress, τ_{bond}, equal to 1.1√f'c (MPa), can be used for estimating the required embedment length in UHPC. Because of the broadness of the test variables in the data from which it was derived, this value appears reasonably conservative for a wide variety of design conditions. Additional research may refine it for specific design conditions.

Chapter 6

Simplified UHPC Joints for Bridge Construction

6.1. OVERVIEW

This chapter investigates the use of UHPC for bridge joint connections between precast, regular concrete bridge deck elements. The proposed joints make use of UHPC’s superior bond characteristics in order to provide a simple and effective method for the assembly of precast bridge elements. A total of 12 beams with joint widths of 4” (100 mm), 6” (150 mm), and 8” (200 mm) were constructed for physical testing and subsequently modeled. Of the twelve, 8 beams were tested under pure flexure. The four remaining beams were evaluated under combined shear and flexure loading conditions. Findings show that the beams with joint widths of 4” (100 mm) failed to sufficiently transfer load between the precast desks in both pure flexure and combined shear and flexure testing, resulting in splitting failure in the joint. Beams with joints at 6” (150 mm) and 8” (200 mm) were sufficient for achieving the required force transfer between the precast deck elements and were suitable for applications requiring simplified and expedited construction. Finite element simulations used to explore the effect of joint topology on system performance indicate that structural response hardly changes for the three types of joints considered.

6.2. DESIGN OF THE EXPERIMENTAL PROGRAM

As seen in previous research (Alkaysi & El-Tawil, 2016), UHPCs exceptional ability to bond to steel bar reinforcement allows for small bar development lengths under simple bar pull out. This characteristic enables smaller and simpler joints, which promote accelerated bridge construction methods. The objective of the test program in this chapter is to probe the lower limits of joint size, specifically for UHPC lap-spliced connections, in order to gain a better understanding of UHPC joint response.

6.2.1. Pure Flexure vs. Combined Shear and Flexure Testing

Two different testing set ups were implemented in this study. The first, a four-point bending test set up seen in Figure 6-1a places the UHPC joint in pure flexure. The second test type, an offset three-point bending set up (Figure 6-1b), and subjects the UHPC joint to shear forces and moments. The shear and moments that develop along the length of the beam during testing are shown in Figure 6-1. The pure flexure test is intended to study the response of the joined beam under real world loading conditions where the influence of shear force is minimal. The combined shear and flexure test investigates response when a higher shear-moment ratio is present.

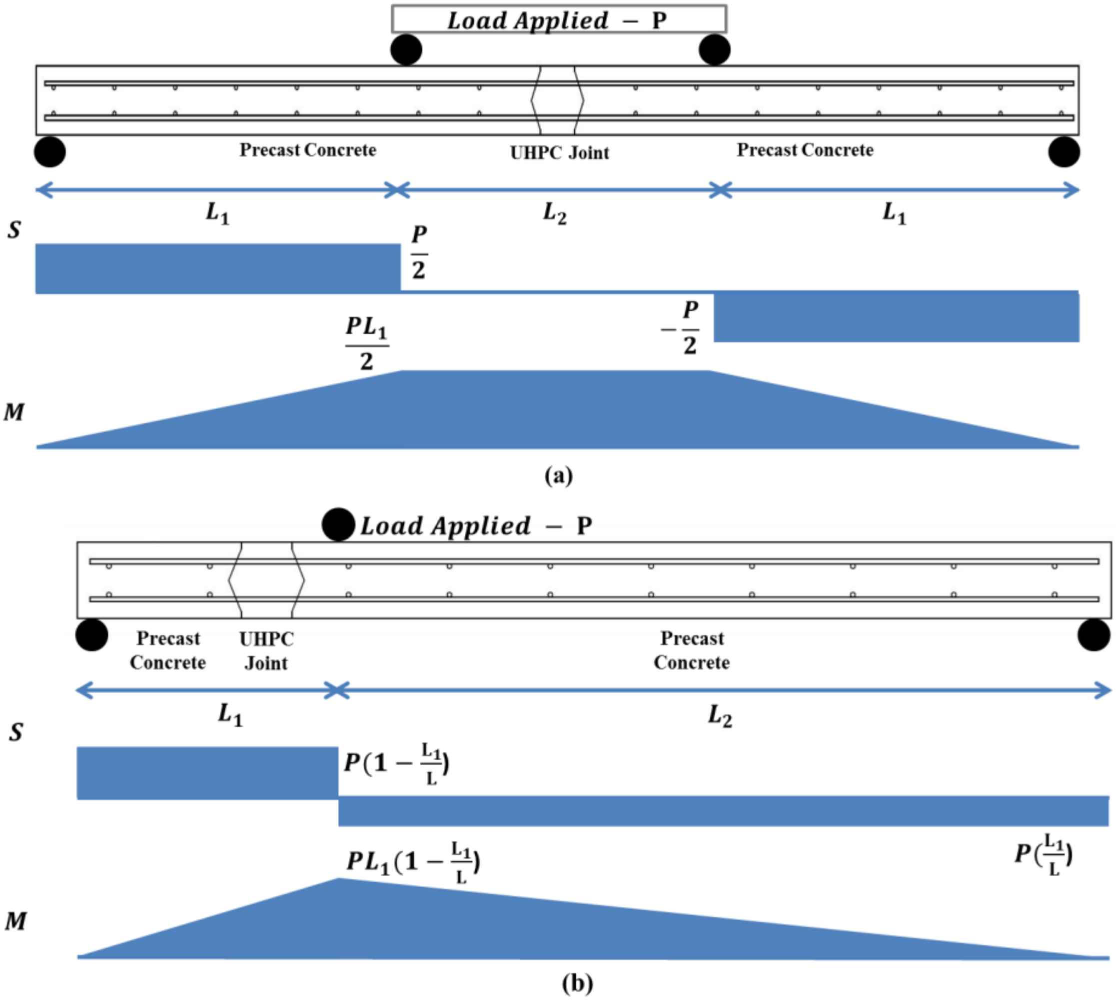

Figure 6-1: Shear and Moment forces in beams under (a) pure flexure loading and (b) combined shear and flexure testing

6.2.2. Joint Details & Selection

Currently the width of a joint for lap splice connection is determined by the lap length which is a function of the development length of the reinforcing bar, and is prescribed by ACI Committee 318 (2014). Equation 1 shows the current method for determining the development length for straight bar reinforcement for #6 (19 mm) bars and smaller.

$$L_d = \frac{f_y \psi_t \psi_e \lambda}{25\sqrt{f_c'}} d_b$$

Equation 6-1: Development Length for Straight Bar Reinforcement (ACI 318)

Where f_y = yield strength of the reinforcement (psi), ψ_t = reinforcement location factor, ψ_e = reinforcement coating factor, λ = lightweight concrete aggregate factor, f_c' = compressive strength of the concrete, and d_b = nominal diameter of the bar reinforcement. Equation 6-1 indicates that the required development length decreases with the square root of the compressive strength of the material. Although not explicitly developed or permitted for use with UHPC, it is interesting to note that the bond required for 25 ksi UHPC versus a regular 5 ksi concrete should be just under half of that required for regular concrete according to Equation 6-1.

Similarly, AASHTO LFRD design requires a development length for No. 11 bars or smaller to equal:

$$L_{d_b} = \frac{1.25 A_b f_y}{\sqrt{f_c'}}$$

Equation 6-2: Development Length for Straight Bar Reinforcement, AASHTO

Where A_b is the area of the bar in in2, f_y is the specified yield strength of the reinforcing bars (ksi) , f'$_c$ is the specified compressive strength of the concrete at 28 days (ksi) and d_b is diameter of the bar in inches.

6.2.3. Specimen Design

For ease of construction, non-contact lap splices are used in this study. Generally, contact lap splices are constructed such that the reinforcing bars are touching and tied together, minimizing displacements during the pouring of concrete. This is not a concern in precast element constructions as the bars are already embedded in the precast concrete and not able to move in relation to each other. While the new low-cost alternative UHPC mix formulations used in this study have lower material costs than previous UHPC mixes, it is important to minimize the joint width as the alternative UHPC used to fill the joint still carries a higher cost as compared to conventional concrete.

Figure 6-2 shows the reinforcement and joint details for the specimens studied. For the pure flexure tests, each precast deck element measures 60” (1500 mm) in length, 18” (457 mm) wide and 6” (150 mm) deep. Joint lengths vary between 4”, 6” and 8” (100, 150 and 200 mm). Longitudinal reinforcement is spaced at 6.3” (160 mm) along the width of the deck. Transverse reinforcement is spaced at 7.8” (200 mm) along the length of the deck. Reinforcement at the lower layer is placed at a depth of 3.5” (89 mm) and 1.5” (39 mm) for the upper layer.

Similarly, for the combined shear and flexure specimens, one of the precast deck element measures 60” (1500 mm) in length, 18” (457 mm) wide and 6” (150 mm) deep. The other precast element measures 13” (330 mm) long, with a width of 18” (457 mm) and depth of 6” (150 mm). Joint width is held constant at 4” (100 mm). Longitudinal reinforcement is spaced at 6.3” (160 mm) along the width of the deck. Transverse reinforcement is spaced at 7.8” (200 mm) along the length of the deck. Reinforcement at the lower layer is placed at a depth of 3.5” (89 mm) and 1.5” (39 mm) for the upper layer.

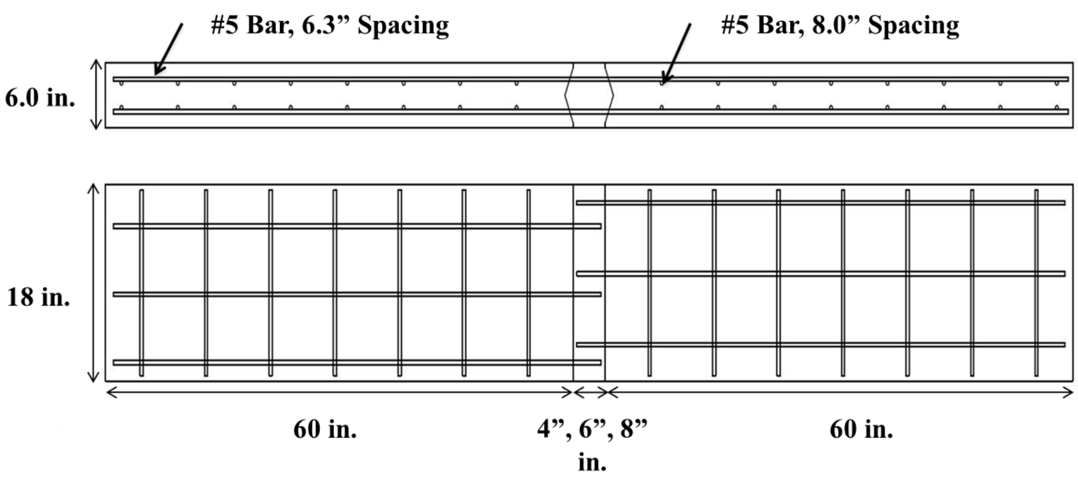

(a) Pure flexure specimens

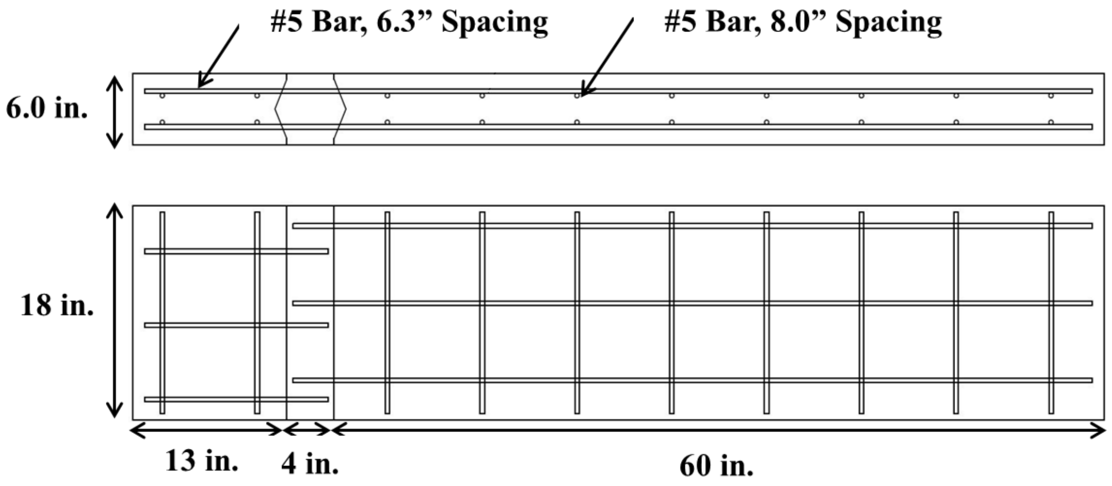

(b) Combined shear/flexure specimens

Figure 6-2: Joint Dimensions and Reinforcement Details

6.2.4. Specimens Tested and Material Parameters

Table 6-1 summarizes the main variables for the specimens tested in this study. The naming convention for the specimens is as follows: test type – joint width – fiber volume content – and test number. For example, an F-100-1P-1 mean the specimen was tested in pure flexure, with a 4” (100 mm) joint, containing 1.0% fiber volume content UHPC and was the first test in the series. All tests were performed after 28 days of concrete curing. Figures 6-2(a and b) provide a more detailed view of the lap spliced joint used for this study. The joint features a shear key design, minimizing the joint at the opening, expanding slightly in the center. This increased width at mid-depth enables an increased splice length while maintaining a small joint opening and minimizing total required volume of UHPC. Figure 6-2c shows the lap splice connection used for all of the specimens tested.

Name	**Test Type**	**Lap Length, inches (mm) (Designed)**	**Lap Length, inches (Constructed)**	**Fiber Volume Content (%)**	**Inter-bar Spacing, inches**	**Fc’ (ksi)**
F-100-1P-1	Flexure	4” (100.0)	3.9	1.0%	6.3	26.1
F-100-1P-2	Flexure	4” (100.0)	3.8	1.0%	6.3	26.1
F-100-2P-1	Flexure	4” (100.0)	3.9	2.0%	6.3	27.7
F-100-2P-2	Flexure	4” (100.0)	3.9	2.0%	6.3	27.7
F-150-2P-1	Flexure	6” (150.0)	6.0	2.0%	6.3	27.7
F-150-2P-2	Flexure	6” (150.0)	5.3	2.0%	6.3	27.7
F-200-2P-1	Flexure	8” (200.0)	7.4	2.0%	6.3	27.7
F-200-2P-2	Flexure	8” (200.0)	7.5	2.0%	6.3	27.7
SF-100-1P-1	Combined	4” (100.0)	3.9	1.0%	6.3	26.1
SF-100-1P-2	Combined	4” (100.0)	3.9	1.0%	6.3	26.1
SF-100-2P-1	Combined	4” (100.0)	3.9	2.0%	6.3	27.7
SF-100-2P-2	Combined	4” (100.0)	3.8	2.0%	6.3	27.7

Table 6-1: Main Variable of Beam Specimens

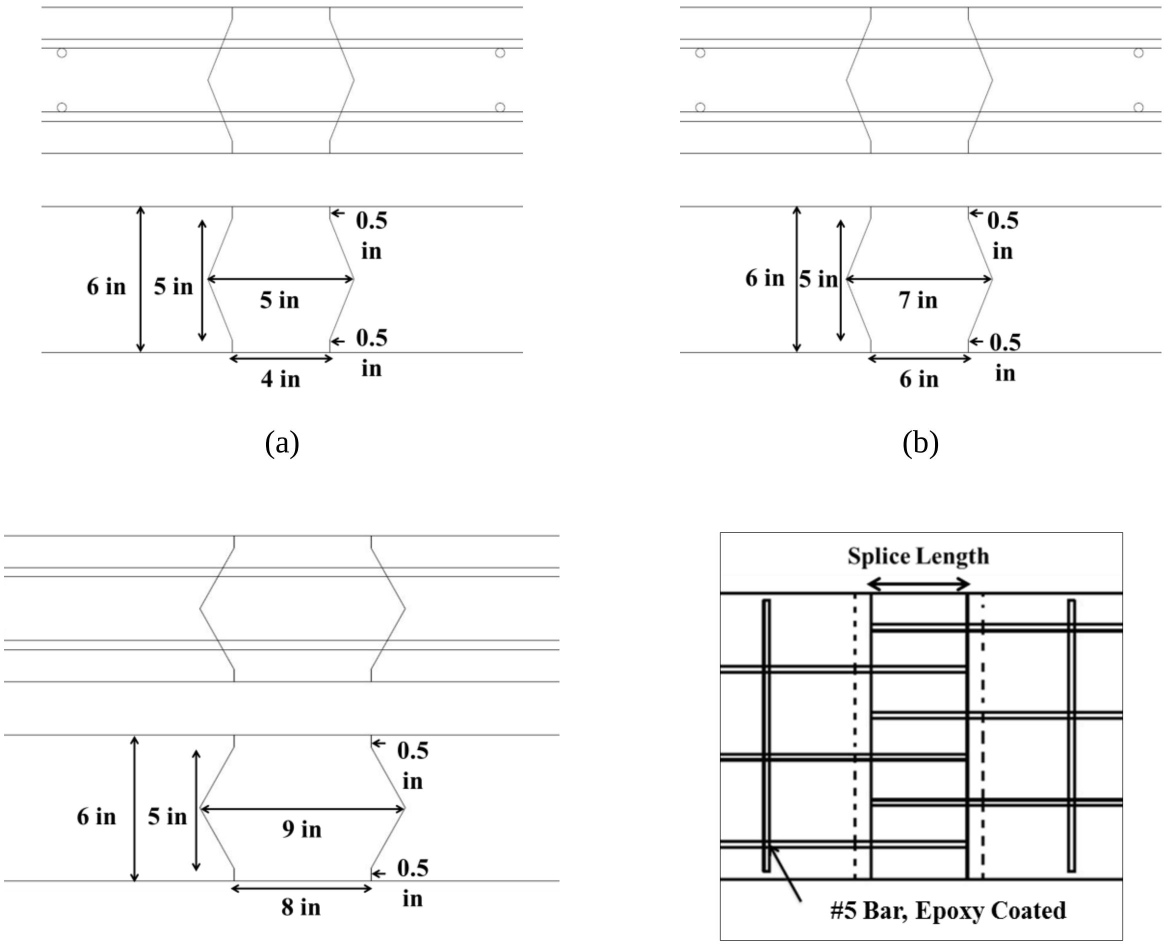

(a) (b)

(c) (d)

Figure 6-3 Joint Shape Details for the 4 in (a), 6 in (b) 8 in (c) joint, Lap Splice Connection Detail (d)

6.3. EXPERIMENTAL PROCEDURE

6.3.1. Test Set Up

All specimens were simply supported. Supports were placed 2” (50 mm) from either edge of the deck. Two rollers applied the load and were placed 12” (300 mm) from either edge of the joint in the pure flexure cases. A single roller was applied 4” (100 mm) from the joint interface in the combined shear and flexure case. Load was applied using a 100 kip INSTRON hydraulic loading machine. A displacement controlled load was applied quasi-statically at 0.001 in/sec (0.0254 mm/sec).

6.3.2. Instrumentation

Load was recorded using a 100 kip load cell integrated with the hydraulic machine. Displacements were measured at the locations shown in Figure 6-4a using the Optotrack measurement system. This system uses a set of cameras to track the relative displacements of the markers shown in three dimensions. Additionally, in each of the precast segments of the beam, for the F-100 and F-200 specimens, strain gauges were placed on the lower layer of reinforcing steel, 1” (25.4 mm) from the edge of the joint interface, Figure 6-4b.

Digital imagine correlation (DIC) was used in order to map the strain developing in the UHPC joint, Figure 6-4c. In DIC, random speckle patterns are applied to the surface of the concrete, being sure to cross the UHPC-Regular concrete joint interface. A high resolution, high frame rate, camera then records the surface of the concrete, specifically the speckles, at a fixed frame rate throughout the test procedure. These images are then uploaded, and the DIC software maps the locations and movements of the speckled pattern. Measuring the relative movements and calculating displacements between the speckles allows for an accurate, 2-D, depiction of the strains occurring in the specimen, clearly highlighting crack patterns.

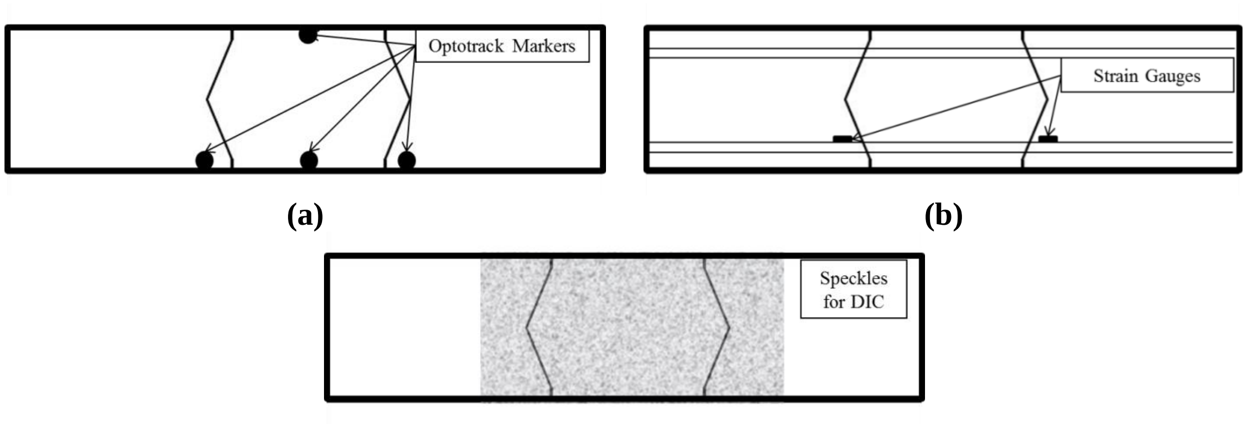

(a) **(b)**

(c)

Figure 6-4: Instrumentation of the Precast Bridge Deck Beams

Data collected from the strain gauges placed on the deformed bars was used to verify the point during the test at which steel yielded. Data from the Optotrack system and DIC were used to measure deflections and strains occurring throughout the joint during testing. Data collected on the load and displacements were then plotted. The resulting curves were then processed through a moving average filter to account for minute changes due to the sensitivity of the equipment.

6.4. MATERIALS

The concrete used to construct the precast bridge deck elements consists of regular 5000 psi (35 MPa) concrete, with a 6” (150 mm) slump and maximum aggregate size of 0.78” (19 mm). The deformed bars all consisted of grade 60, epoxy coated steel and can be seen in Figure 6-5.

Figure 6-5: Deformed #5 (16 mm) Epoxy Reinforcement Bar

The UHPC mix design used to fill the joint and complete the lap splice follows the low-cost mix recommended in Chapter 3 (GG-25-00). The performance parameters for this mix can be found in Table 3-4.

6.5. CONSTRUCTION OF THE PRECAST CONCRETE SPECIMENS

Construction of the specimens for this study was performed in a simple, and easy to replicate process. Wood forms were first constructed with dimensions as designed. Once the rebar was placed, the shape of the joint's interface was created using a high-density foam and cut to the according dimensions (Figure 6-6b). Once the bars were in place and the bars were properly instrumented, the regular concrete was poured into the forms. Vibration was used to ensure proper installation of the regular concrete. After pouring, the surface of the concrete was smoothed and leveled so as to provide an adequate loading surface.

Twenty-four hours after the regular concrete had been cast; the foam was removed, exposing the inner surface of the joint. The two precast sections were brought together, and the splice properly aligned and measured. The bars were cleaned of any dirt and debris that had accumulated during the casting of the decks. The UHPC was then mixed and poured as described in Section 3.2.2. For this study, the UHPC was poured so as to favor fiber orientation in parallel to the deformed bars (Figure 6-6c). The specimens were then allowed to cure at room temperature for 28 days. Following the prescribed curing time, the forms were removed and the speckles were painted onto the joint surface for the DIC measurements (Figure 6-6d).

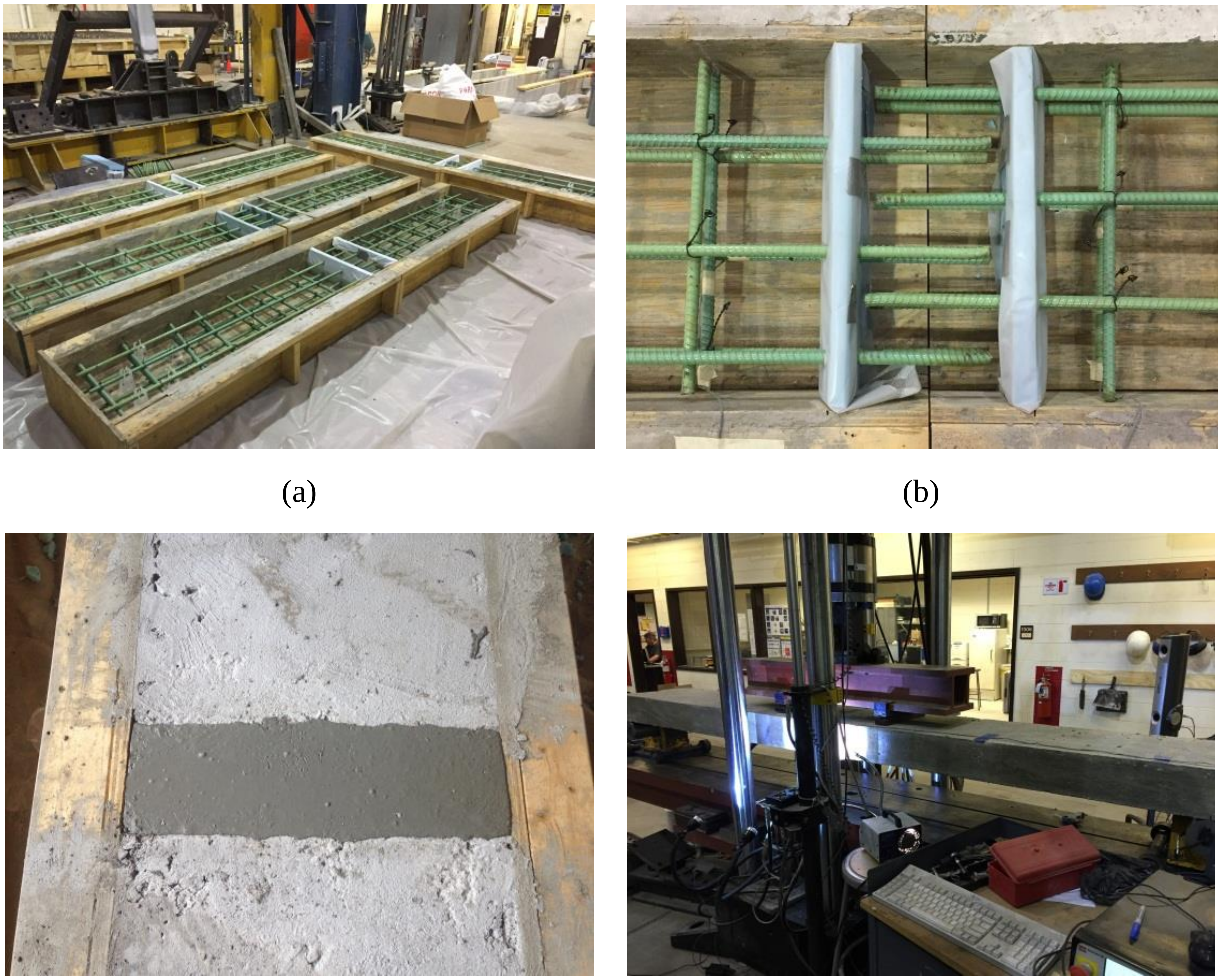

(a) (b)

(c) (d)

Figure 6-6: Forms and Placed Bars (a), Lap Splice (b), Poured UHPC Joint (c), and Set up with DIC (d)

6.6. RESULTS AND DISCUSSION

A summary of the results from the experimental testing for all of the specimens can be seen in Table 6-2.

Name	Embedded Length (mm)	Splice Length (mm)	Failure Mode	Load at Failure, P_{max} (KN)	Peak Bond Stress, τ_{bond} (MPa)	F'c (MPa)
F-100-1P-1	100.0	90	Splitting	19.3	14.5	182.0
F-100-1P-2	100.0	90	Splitting	19.0	14.3	182.0
F-100-2P-1	100.0	90	Splitting	20.6	15.5	182.0
F-100-2P-2	100.0	90	Splitting	21.2	15.9	182.0
F-150-2P-1	150.0	149	Steel Yield	28.7	14.7	185.0
F-150-2P-2	150.0	148	Steel Yield	27.8	16.1	185.0
F-200-2P-1	200.0	198	Steel Yield	28.2	12.4	185.0
F-200-2P-2	200.0	199	Steel Yield	30.2	12.5	185.0
SF-100-1P-1	100.0	95	Splitting	67.7	14.3	182.0
SF-100-1P-2	100.0	98	Splitting	58.1	12.3	182.0
SF-100-2P-1	100.0	97	Splitting	72.4	15.2	182.0
SF-100-2P-2	100.0	97	Splitting	82.3	17.5	182.0

Table 6-2: Summary of Results from Experimental Testing

6.6.1. Comparison of Calculated Bar Stress versus Measured Bar Stress

Figure 6-7 shows the computed bar stresses calculated from the peak load recorded by the load cell compared to the measured strain (converted to stress) from the instrumented deformed bars. From the scatter, the calculated and measured data show no significant variation, though the calculated bar stresses generally measure slightly higher than those measured with the strain gauge. Thus the data is reliable and can be used for evaluation of the test data.

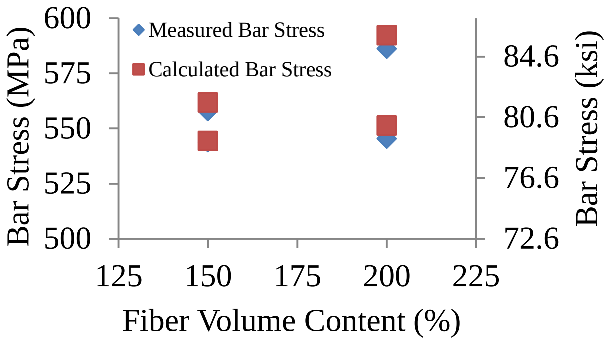

Figure 6-7: Comparison of Calculated and Measured Bar Stresses

6.6.2. F-100 Specimen Tests

Figure 6-8c and Figure 6-8d shows the force-displacement behavior of the four F-100 specimens subjected to flexural loading. For all tests, the load-displacement relation remained linear up to about 80% of the peak load. At this point, the load began to drop, corresponding to initial cracking at the center of the joint as can be seen by the horizontal cracks in Figure 6-8a and Figure 6-8b. The first crack to develop was the horizontal crack spanning the UHPC joint followed by a crack at the interface between the UHPC and regular concrete. For the rest of the loading, all deflections in the beam were localized at this interface. Figure 6-8a also shows the DIC images from the beams. As seen, all of the damage occurred in the joint, and that the corresponding crack pattern shows that a splitting failure occurred, where the reinforcement steel separated from the UHPC. No significant crushing in the regular concrete or UHPC was observed prior to the steel bar yielding. The peak force averaged 8.2 kips (36.5 KN) for specimens with 1% fibers (F-100-1P) by volume and 9.1 kips (40.5 KN) for those with 2% fibers (F-100-2P) by volume.

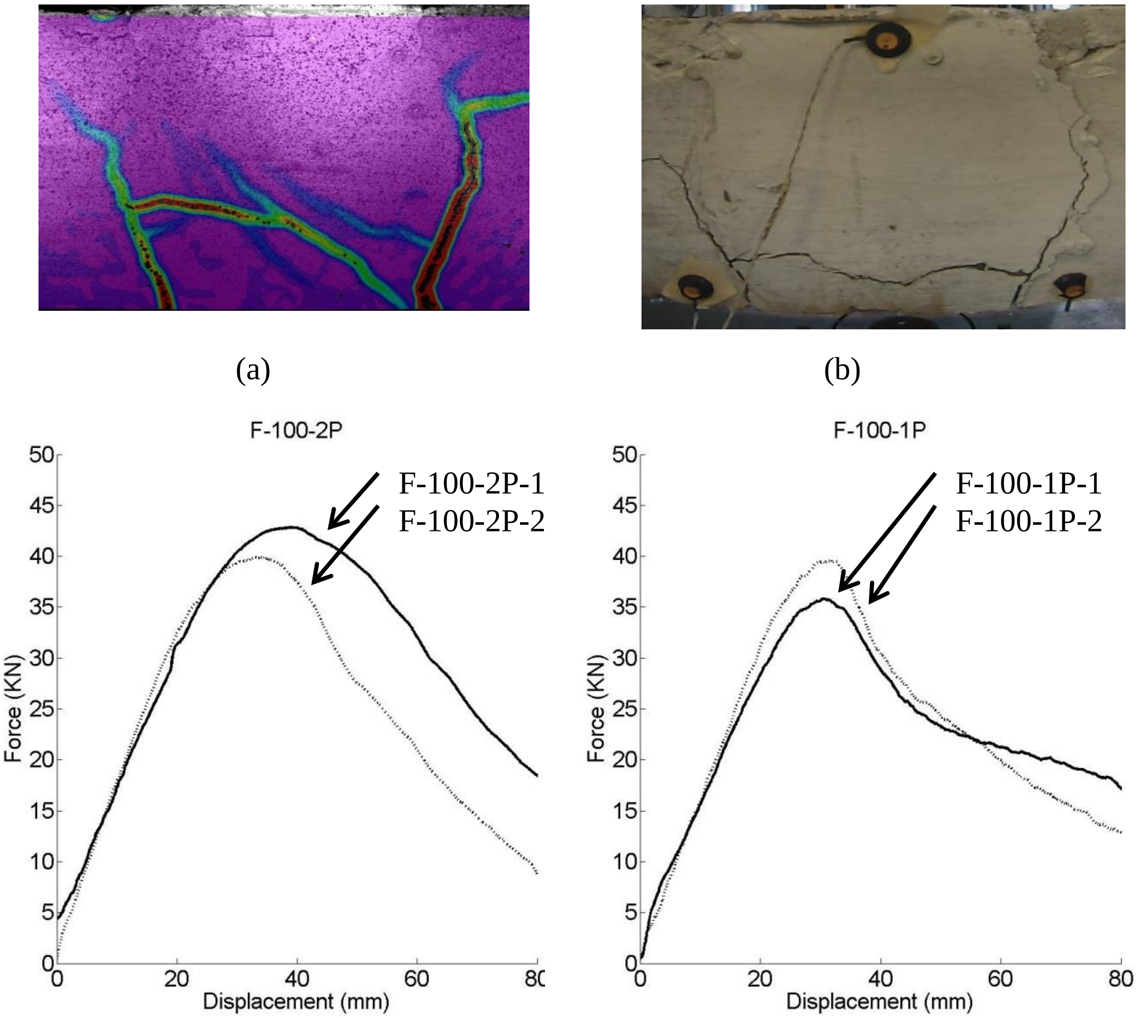

(a) (b)

(c) (d)

Figure 6-8: (a) DIC of 100 mm joint specimens, (b) Splitting Failure in deformed specimen, (c) Load-Deflection Curves for 100 mm specimens with 2% fibers and (d) 100 mm specimens with 1% fibers.

6.6.3. F-150 and F-200 Specimens

Both F-150-2P and F-200-2P specimens were able to complete the joint connection, achieving loads past steel bar yield in the specimens without failure in the UHPC-steel bond. **Figure 6-9**c shows the load-displacement curve for both of the F-150-2P specimens tested. The load-deflection began increasing elastically as load was applied. This was followed by a region of decreased slope in the load-deflection, due to yielding of the steel reinforcement. As steel yielded, flexural cracking was observed in the pre-cast, regular concrete regions of the beam. Load continues to climb until reaching a peak average value of 59.2 KN (moment of 16.9 KN-m). At this point, a sudden crushing of the regular concrete at the UHPC joint interface occurs, observed in the load-deflection curve as the drop off in the load occurring at 65 mm of midspan deflection. At this point the beam was no longer able to carry additional load, and began to gradually drop towards zero. No damage was observed in the UHPC joint.

Figure 6-9d shows the load-displacement curve for both of the F-200-2P specimens tested. Similarly to the F-150-2P specimens, the load-deflection begins with an elastic increase in the response as load was applied. Again, this is followed by a region of decreased slope in the load-deflection, caused by yielding of the steel reinforcement. Flexural cracks in the pre-cast, regular concrete regions of the deck were also observed. Load continued to climb until reaching a peak average value of 56.0 KN (moment of 17.8 KN-m). Again, at the point of maximum load, a sudden crushing of the regular concrete at the UHPC joint interface occurs, observed in the load-deflection curve as the drop off in the load occurring at 65 mm of mid-span deflection for F-200-2P-1 and 80 mm for F-200-2P-2. At this point the beams were no longer able to carry additional load, and began to gradually drop towards zero. As in the F-150-2P tests, no damage was observed in the UHPC joint.

Figure 6-9a shows the results from the DIC at the end of the testing program, typical for both F-150-2P and F-200-2P specimens. From this, it is clear that all of the deformation in the beam is occurring at the UHPC joint – regular concrete interface, and not across the joint itself as observed in the F-100 tests. This confirms that the UHPC and steel reinforcement remained bonded throughout testing, and that opening at this interface is most likely to due to elongation of the steel bar due to yielding. Additionally, **Figure 6-9**b shows that the same lack of damage occurs on both surfaces of the beams.

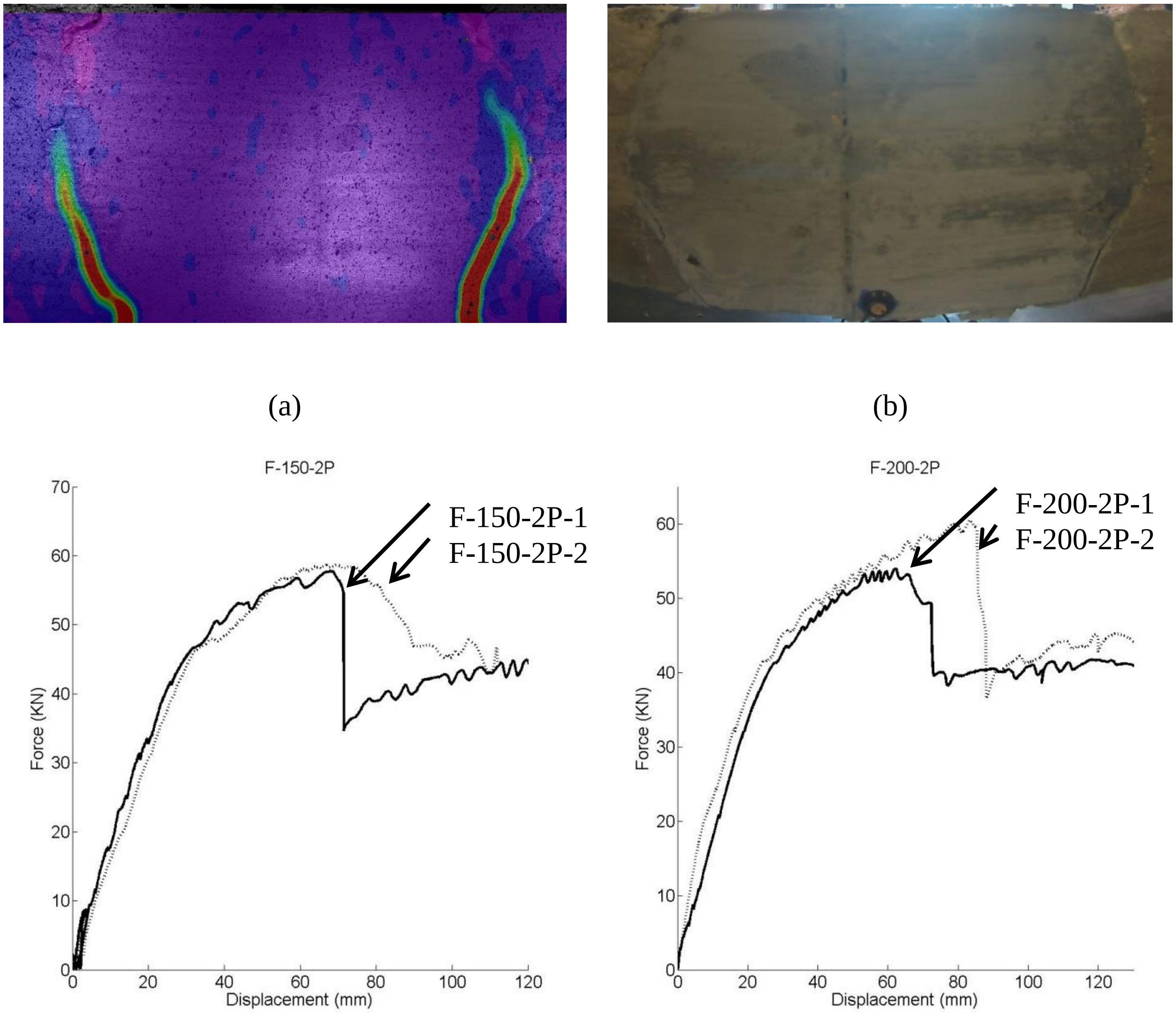

(a) (b)

(c) (d)

Figure 6-9: (a) DIC of 150 mm joint specimens, (b) Splitting Failure in deformed specimen, (c) Load-Deflection Curves for 150 mm specimens and (d) 200 mm specimens.

6.6.4. Effect of Fiber Content in Pure Flexure

As discussed in the previous sections, F-100-1P and F-100-2P specimens were both unable to successfully join the two precast regular concrete deck elements, resulting in a bar pull out failure to occur within the joint. The difference of 1% fibers by volume accounted for an average decrease in maximum force (and bond stress) of 8%. At the point of maximum load, F-100-1P specimens experienced average bar stresses of 47.8 MPa and F-100-2P specimens experienced an average bar stress of 52.75 MPa. Since the force (and bond) increases with the addition of steel fibers in the UHPC, it may be possible to use a 100 mm UHPC joint with a higher fiber volume content to join precast regular concrete sections in future works.

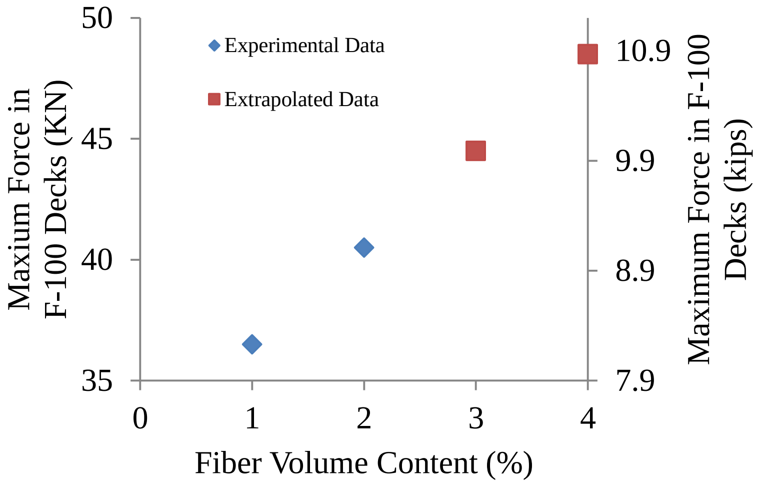

Figure 6-10: Maximum Force in F-100 Decks at a Function of Fiber Volume Content

6.6.5. Effect of Joint Size

Unlike F-100-1P and 2P specimens, both the F-150-2P and F-200-2P specimens were able to complete the joint connection, showing no bond failure in the UHPC joint. Figure 6-11 shows the moment (KN-m) at the joint as a function of the joint width for all tests with UHPC containing 2% fibers by volume. At 100 mm, the maximum average moment achieved, 12.2 KN-m, is the lowest. At 150 mm the average maximum moment achieved is 16.9 KN-m and 17.8 KN-m at 200 mm. The increased width of 50 mm (a 34% increase in width and subsequently, quantity of UHPC needed) between the F-150 and F-200 specimens only achieved an increase in moment capacity of 5.5%. In order to minimize required quantity of UHPC, the F-150-2P joints would provide the best UHPC use – beam strength ratio, despite the marginal gain in moment capacity.

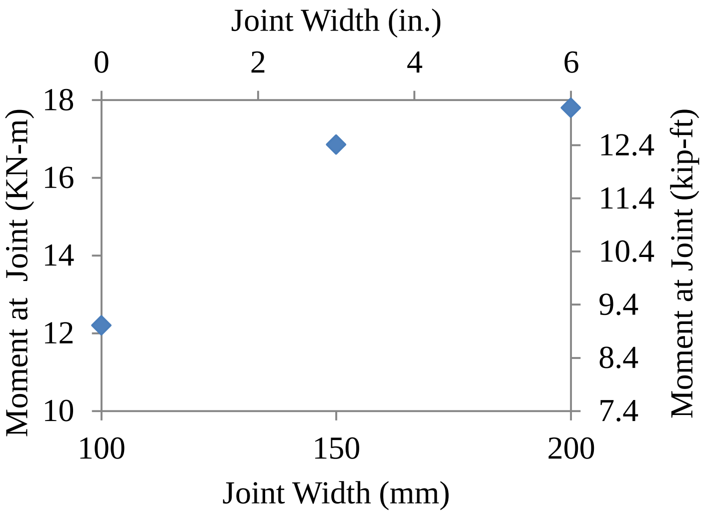

.

Figure 6-11: Moment at Joint as a function of Joint Width

6.6.6. Combined Shear and Flexure Testing

For the SF-100-1P specimens the load-displacement curve remained linear up to about 95% of the peak load. At this point, the load began to drop, corresponding to initial cracking at the center of the joint as can be seen by the horizontal cracks in Figure 6-12a and Figure 6-12b. First, a horizontal crack spanning the UHPC joint developed, followed by a crack at the interface between the UHPC and regular concrete. For the rest of the test program, all deflections in the beam were localized at this interface. Similarly to the F-100-1P and F-100-2P specimens, all of the damage occurred in the joint, and that the corresponding crack pattern indicates a splitting failure, where the reinforcement steel separated from the UHPC. The peak force averaged 61 KN for specimens with 1% fibers (SF-100-1P) by volume and 75.5 KN for those with 2% fibers (SF-100-2P) by volume. Damage showed in Figure 6-12a and Figure 6-12b were representative for SF-100-1P-1, 2 and SF-100-2P-2. For SF-100-2P-1, the concrete between the UHPC joint and the closest support experienced a splitting crack, reducing the overall force achieved in the beam. This can be seen as the sudden drop off in force on the load displacement curve.

event can be seen as the sudden drop off in force on the load displacement curve.

6.6.7. Effect of Fiber Content in Combined Shear and Flexure

On average, SF-100-1P specimens containing 1% fibers by volume achieved 19% less force (and bond) prior to failure than their SF-100-2P counterparts. This result is unsurprising as bonding in UHPC is directly related to the steel fiber contents, as discussed in previous studies (Alkaysi, 2016). SF specimens containing 1% steel fibers by volume averaged 8% less bar force at failure that their pure flexure counterpart with 1% fibers by volume. At 2% fibers by volume, the difference in bar forces achieved between F-100-2P and SF-100-2P specimens was less pronounced, suggesting that the UHPC's capacity in shear increases non-linearly with increases with fiber content. More testing on UHPC specimens in shear should be conducted in order to further clarify these results.

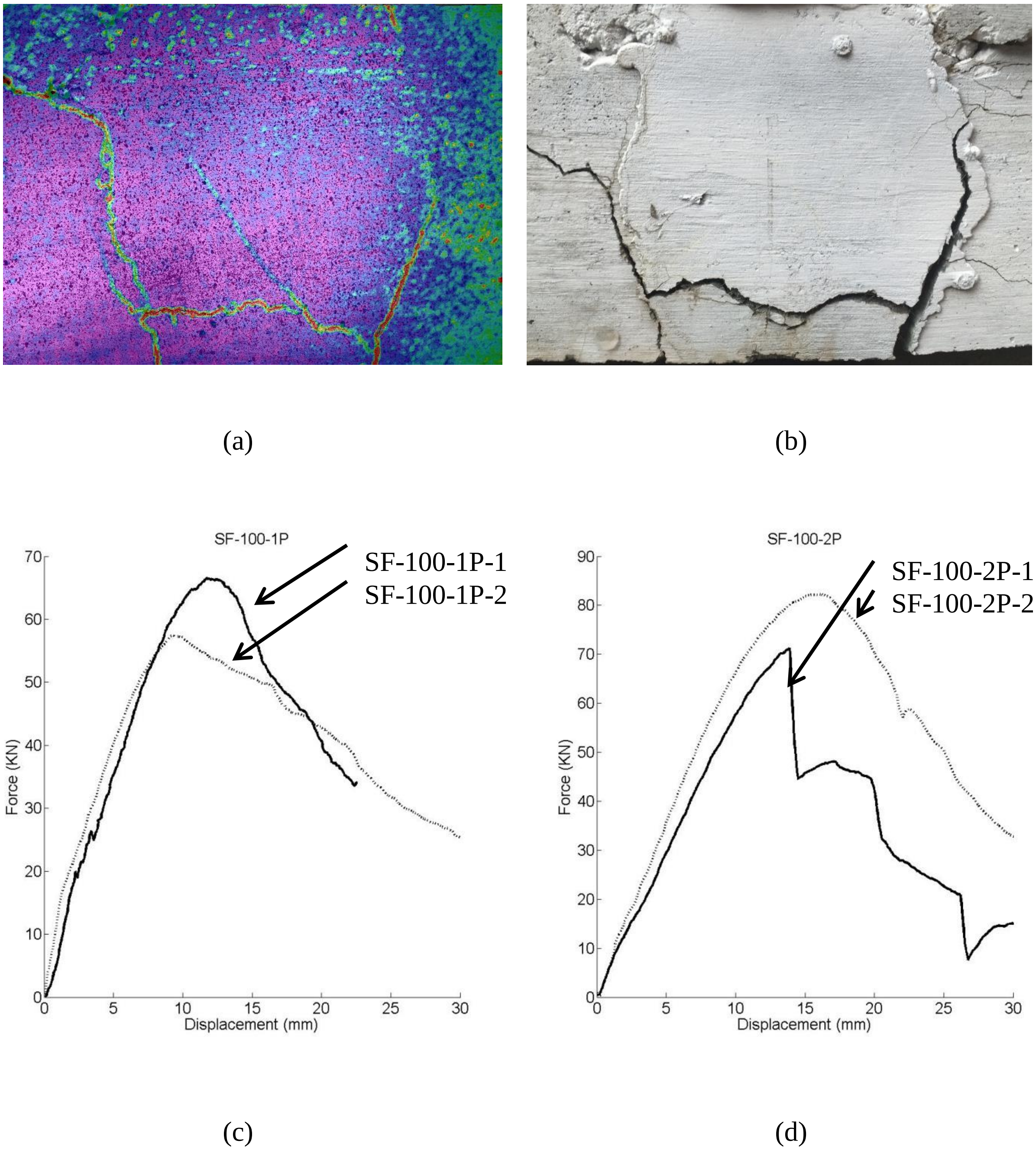

Figure 6-12: (a) DIC of 100 mm joint, SF specimens, (b) Splitting Failure in deformed specimen, (c) Load-Deflection Curves for 100 mm specimens, 1% fiber by vol. and (d) 100 mm specimens, 2% fiber by vol.

6.7. Evaluation of the Current Design Code

As it currently reads, ACI 318-14 cannot be used to design reinforced UHPC structures. Equation 1 shown previously sets a limit on the compressive strength of concrete of $\sqrt{f'c} < 100$ psi (8.3 MPa), rendering essentially all UHPC structures unable to make use of the current design guidelines. Additionally, Section 25.5.2.1of the ACI code requires that all lap splices used be multiplied by a factor of 1.3 l_d when designing joined connections for concrete structures. Figure 18 compares the peak bond stress achieved in the lap spliced UHPC specimens (F-100-1P and F-200-2P) compares to a 16 mm epoxy bar embedded 100 mm into at 1% and 2% fibers by volume subjected to simple bar pull-out (Alkaysi & El-Tawil, 2016). Bar pull out specimens achieve a peak average bond stress equal to 18.9 MPa at 1% fibers by volume and 15.5 MPa at 2% fibers by volume. This accounts for a decrease in bond capacity of 7% at 1% fibers by volume, and a difference of 13% at 2% fibers by volume. Revisiting the ACI, a multiple of 1.3 is overly conservative compared to the experimental values (up to 13%), and rather a lower multiplier could be used in order to fully realize the material benefits of UHPC. Additionally, the limits on f'c should be lifted so as to enable design of UHPC structures.

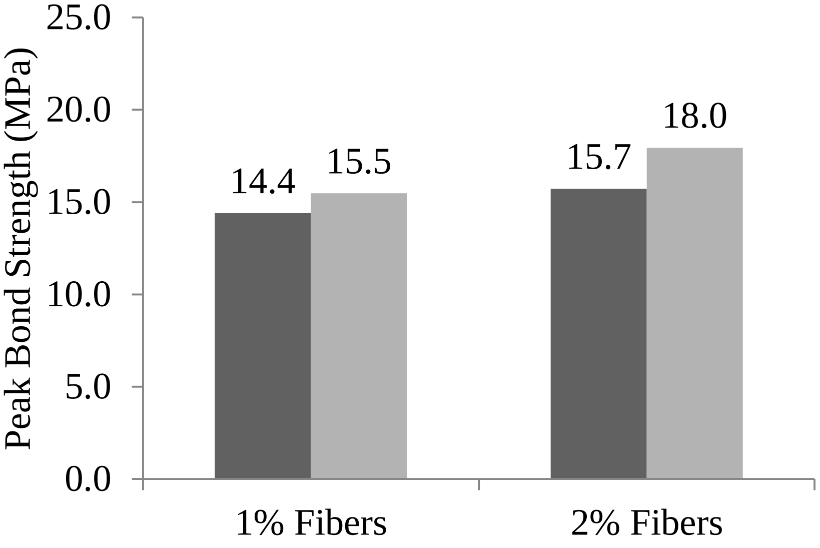

Figure 6-13: Peak Average Bond Stress in UHPC lap splices (Dark Gray) vs. bar pull out specimens (Light Gray, Alkaysi & El-Tawil (2016))

6.8. FINITE ELEMENT MODEL AND PARAMETRIC STUDY

6.8.1. Model Setup

A two dimensional finite element model was developed for the LS-DYNA platform. The model makes use of 3-D fully integrated shell elements (ELFORM = 16) and was discretized using Hypermesh$^{©}$. As shown in Figure 6-14, each model consists of 4 components; 2 precast regular concrete elements, 1 UHPC joint, and steel reinforcement.

All dimensions and reinforcement details follow those prescribed previously for the F-150-2P and F-200-2P specimens, respectively. Reinforcing steel was modeled using one dimensional, linear beam elements. The steel bars and surrounding concrete were assumed to be perfectly bonded. Only F-150-1P and F-200-2P specimens were modeled as part of the parametric study.

Steel material response was modeled using a piecewise linear plasticity model (LS-DYNA card #24). Steel material properties were determined through experimental testing, with the following parameters: yield stress, σ_y = 450 MPa with a young's modulus, E = 200 GPa. After yield, the tangent modulus E_{tan} was set to 1.2 GPa.

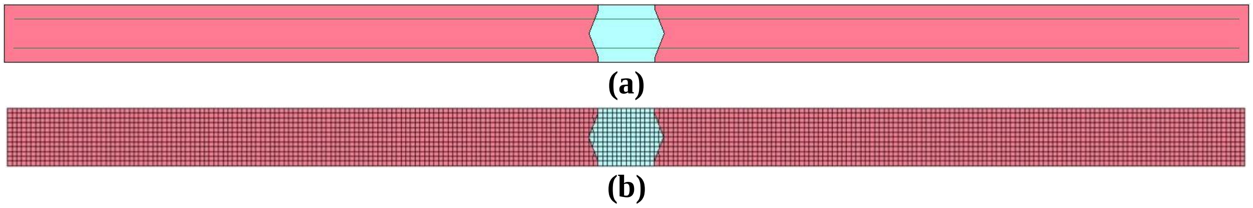
(a)

(b)

Figure 6-14: (a) Finite Element Model and (b) Mesh for F-150-2P Specimens

6.8.2. UHPC and Concrete Material Models

The concrete material model used in this study was previously developed model for high performance fiber reinforced composites (Hung, 2010), and calibrated for use with UHPC based on the experimental results previously reported (Alkaysi, 2015). The model, based upon a hybrid rotating/fixed crack approach, allows perpendicular cracking of the concrete and is capable of modeling the tensile and compressive response for UHPC. The tensile response is characterized by three regions, a linear elastic portion followed by some strain hardening and then a softening of the concrete. Figure 6-15a shows the typical tensile response of uniaxial testing on UHPC specimens as well the material model response used in this study. Figure 6-15b shows the compressive response of UHPC under loading experimentally as well as the model's material response. For the regular concrete material, the same hybrid rotating/fixed crack model was employed, calibrating it with concrete tensile and compressive responses (Gopalaratnam, 1985). Table 6-3 outlines the material properties used. Further details on the development of this model can be found in (Hung, 2010).

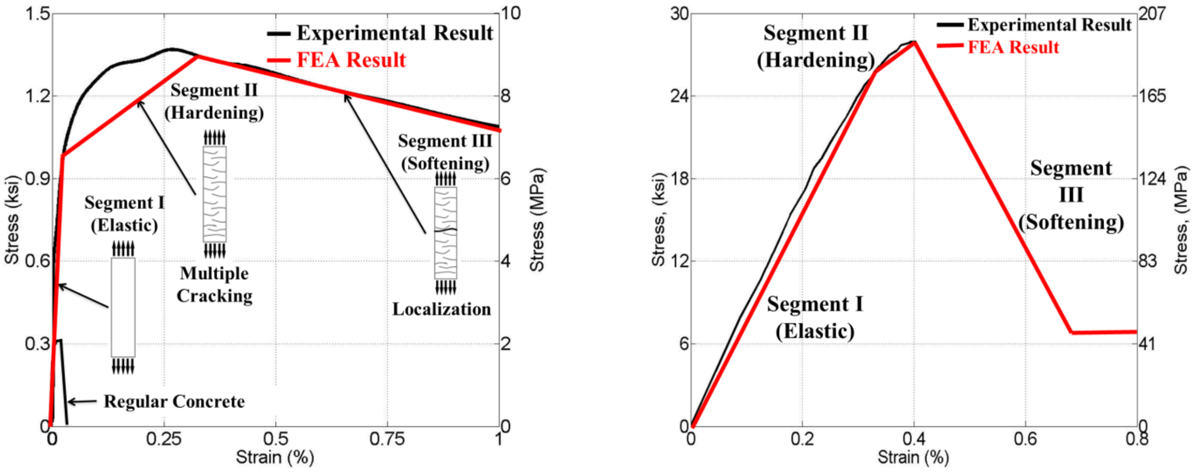

(a) (b)

Figure 6-15: Typical UHPC Tensile Response for Joint Fill Material (a) tension and (b) compression

Name	**Tensile Pre-Cracking Stress (Strain)**	**Tensile Post-Cracking Stress (Strain)**	**Elastic Modulus**	**F'c (ksi)**
UHPC	0.75 ksi (0.0001)	1.2 ksi (0.0002)	751 ksi	26.8
Regular Concrete	0.35 ksi (0.0001)	0.01 ksi (0.0002)	157 ksi	5.0

Table 6-3: Material Parameters for FEM

6.8.3. Parametric Study

The finite element model was validated using the experimental data and from there, a parametric study was performed to determine the effect of the joint's surface topology on the overall performance of the beams. Three different joint designs were modeled and analyzed and can be seen in Figure 6-16. For each joint type, modeling was performed for a 6" (150 mm) joint as well as an 8" (200 mm) joint. Figure 6-15a shows the original joint design tested experimentally and used for the model validation (F-150-2P). Figure 6-15b shows a non-tapered (NT) joint design, and Figure 6-15c shows the flat surface (FS) joint design modeled for the parametric study. The

NT and FS joint designs were selected, as they both are more easily constructed designs. A summary of the simulations performed can be found in Table 6-4.

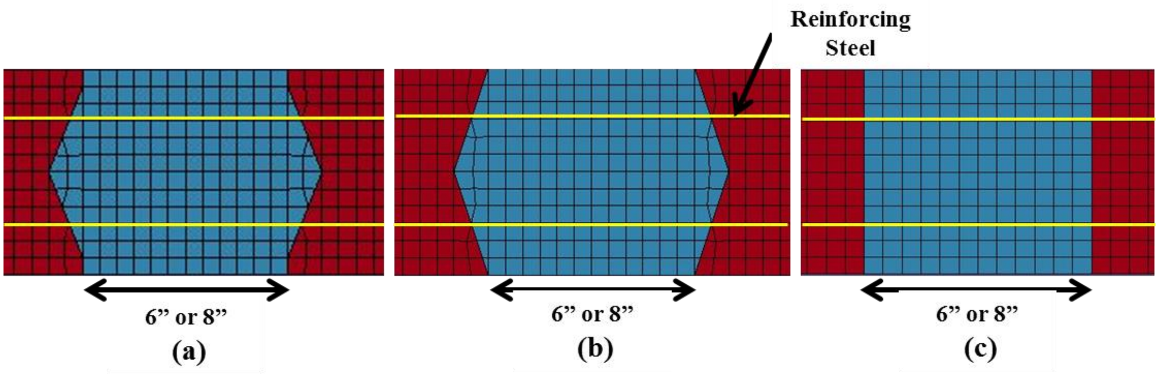

Figure 6-16: (a) Original Joint Design for FEA, (b) non-tapered joint design, and (c) flat joint design.

Name	Joint Type	Joint Size inches (mm)
F-150	Flexure (as F-150-2P)	6” (150)
NT-150	Non-Tapered	6” (150)
FS-150	Flat Surface	6” (150)
F-200	Flexure (as F-200-2P)	8” (200)
NT-200	Non-Tapered	8” (200)
FS-200	Flat Surface	8” (200)

Table 6-4: Summary of Simulated Beams

6.8.4. Model Validation

Results from the experimental testing of beams F-150-2P and F-200-2P were used for model validation. From Figure 6-17a, the numerical results (red line) show good correlation with the results from the experimental testing (black line), including capturing the steel yield, and later on the concrete crushing which occurs for the F-150-2P specimens. Additionally, the deformed shape matches well with the observed experimental deformations (Figure 6-18). While some discrepancies exist, the values from the simulation match reasonably well with the experimental values, and the minor discrepancies between the simulation and experimental data are attributed to experimental scatter. The same conclusion can be reached for the results of the F-200-2P model validation seen in Figure 6-17b.

6.8.5. Results of Parametric Study

For the 150 mm joints, the results from the FEA showed little variation between the F-150, NT-150 and FS-150 joints. All three load-displacement curves began elastically, up until 80% of their max load, at which point the steel reinforcement began to yield. Yielding continued, with the load increasing until approximately 65 mm midpoint deflection. At this point, the concrete at the top of the UHPC-regular concrete interface was crushed, resulting in a drop off in the force capacity of the beam. There was no noticeable difference between the F, NT and FS joints.

Similarly, the F-200, NT-200 and FS-150 joints show little variation. Again, all three load-displacement curves began elastically, up until 80% of their max load, at which point the steel reinforcement began to yield. Yielding continued, with the load increasing until approximately 70 mm midpoint deflection. At this point, the concrete at the top of the UHPC-regular concrete interface was crushed, resulting in a drop off in the force capacity of the beam.

As these simulations were performed under pure flexure for all three joint types, their respective topologies were not fully engaged leading to the primarily flexure failure mechanism. In a more realistic scenario, the shear strength of the UHPC at the joint interface would become important, as more joints are not solely subjected to flexure. Results from the combined shear and flexure testing could not be used for model validation as the primary failure modes in those tests was a bar pull out failure in the joint and thus, a parametric study could not be done for the combined shear and flexure case. UHPC specimens under shear should be further studied to gain more insight into the behavior.

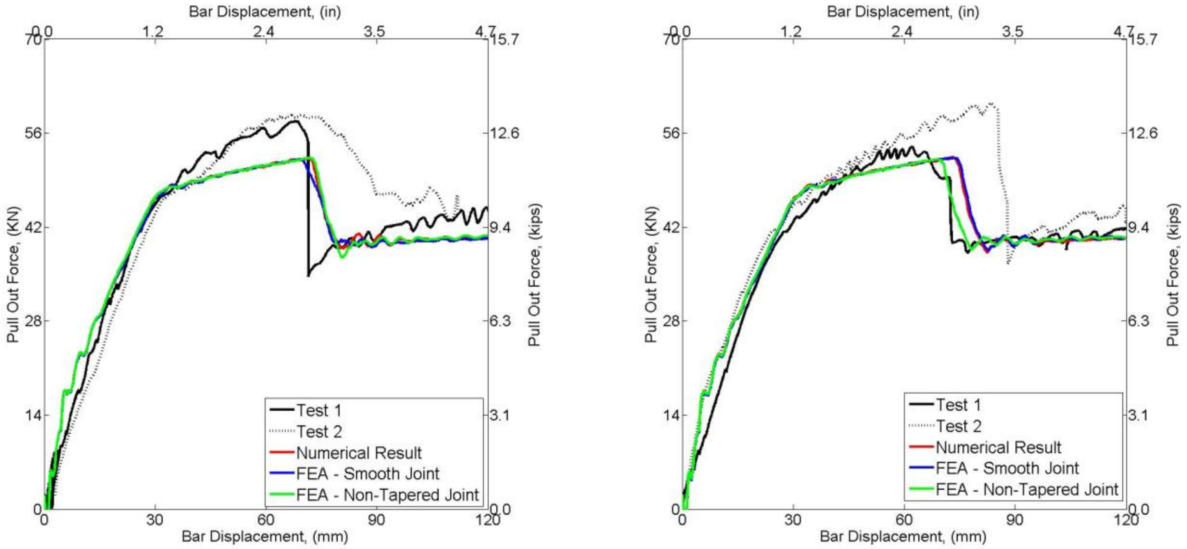

(a) **(b)**

Figure 6-17: Experimental FEA Load-Deflection for (a) 150 mm joints and (b) 200 mm joints

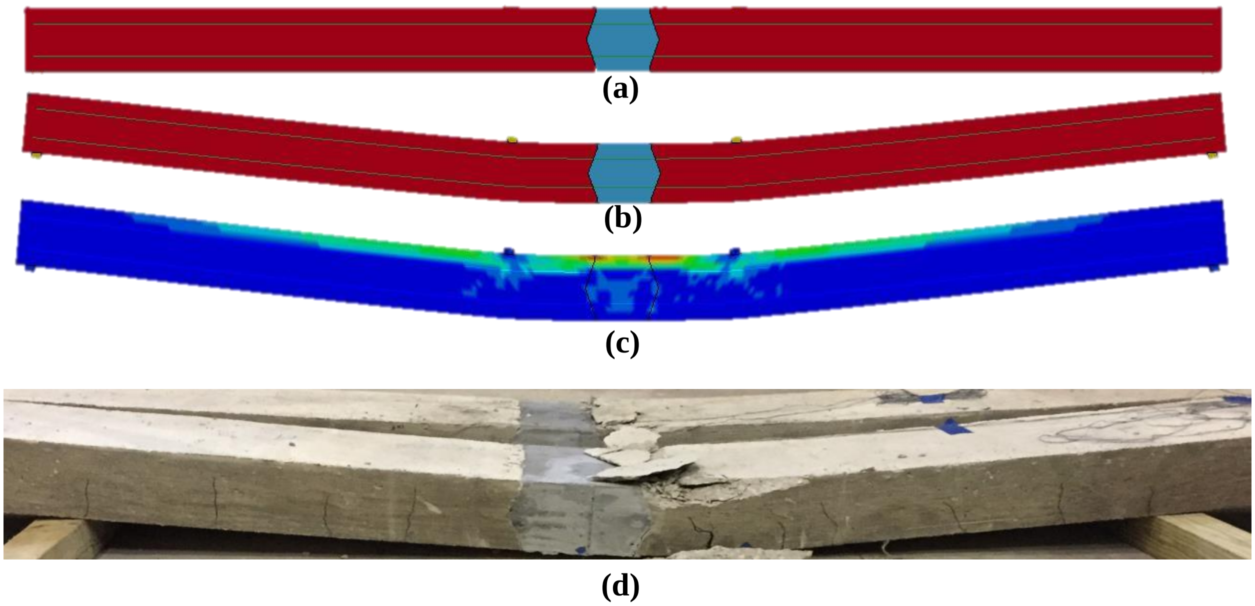

Figure 6-18: (a) Un-deformed shape, (b) deformed shape and (c) von Mises Strain for 150 mm, (d) Plot of the cracks developed and (e) and Damaged Beam after Testing, Actual joint

6.9. CONCLUSION

The objective of the study in this chapter was to evaluate the use of ultra-high performance concrete for simplified joint connections between precast bridge deck elements. The study evaluated three different joint widths, two different fiber volume content UHPCs and two separate loading schemes to simulate real-world loading conditions. The conclusions are as follow:

- All F-100 and SF-100 (4” joint) specimens failed with a splitting failure occurring at the UHPC joints. Bond between the UHPC and deformed bars was insufficient, causing the beams to reach failure prematurely.

- F-150 and F-200 (6” and 8” joints) specimens all failed through steel yield in the deformed bars, followed much later on by crushing in the regular concrete. These specimens were able to carry load through the joints all the way through the desired failure mode.
- F-100 (4” joint) specimens containing 1% fibers by volume achieved an average of 8% lower capacity (and hence bond stress in the joints) than those containing 2% fibers. Extrapolating the test results suggests that a 4” (100 mm) joint may be possible when utilizing a greater steel fiber ratio (~3%). However, increased fiber content leads to greater cost and, possibly, problems with mix workability. Mixes with such high fiber contents were not tested in this work.
- SF-100 (4” joint) beams performed worse than F-100 beams at 1% fibers by volume, though the difference at 2% fibers by volume was non-apparent. This suggests the increase in shear strength in UHPC increases non-linearly with an increase in steel fiber content compared to flexure strength and should be investigated further.
- Changes in the topology of the joint showed no difference in structural performance in the parametric study, under pure flexural loading.

Chapter 7

Summary and Conclusions

This dissertation explores the behavior of ultra-high performance concrete from the materials perspective up to the component performance and behavior at the structural level. The first half of this dissertation analyzed the short term mechanical properties of a series of UHPC mix designs, investigating properties such a tensile performance and compressive strength. This was then followed by a comprehensive analysis of the material's durability, evaluating resistance to freezing and thawing as well as chloride ion penetration. Following the material-level characterization of UHPCs, the structural level performance was investigated. A series of bar pull-out tests were conducted in order to evaluate the bonding between UHPC and structural steel reinforcement. This was then succeeded by the construction of several full-scale bridge deck beams, with a UHPC shear connection joint. More details regarding these specific areas are summarized below.

7.1. Short Term Mechanical and Durability of Ultra High Performance Concrete

To achieve a strong understanding of the mechanical properties of UHPC subject to direct tension and compression, the first phase of the work looked into the material components of non-proprietary UHPC. Mechanical property characterization focused on quantifying tensile properties and compressive strength. This was conducted through direct tensile testing of UHPC “dog-bone” specimens and through the use of 2 in cubes for compression. From the very large data set collection, a series of cost-strength optimized UHPC mixes were selected and durability studies were performed to address the material’s air voids, resistance to freeze-thaw and chloride penetration. All tested mixes had exceptional mechanical and durability properties. Through an analysis of their costs, quantities, and availabilities, a new low-cost alternative UHPC mix formulation was designed. The material cost of this alternative mix is half of the original UHPC mix, while maintaining its ultra-high performance characteristics. The proposed mix deviates from traditional UHPC mixtures in that it uses a 50:50 mix of Portland Type I and Ground Granulated Blast Furnace Slag (GGBS) as a binder, lacks any Silica Powder (inert filler) and requires no post-placing treatment. The use of GGBS improves the material’s ‘greenness’ making it a more sustainable cementitious product.

7.2. Structural Evaluation of UHPC through Bar Pull Out Testing and Full Scale Beam Tests

This phase of the research investigated the bonding performance between steel reinforcement and UHPC. The study spanned several experimental parameters (embedment, bar size & type, UHPC fiber content/orientation, etc.), and ultimately led to a design guideline for achieving specific bar stresses when reinforcement is embedded in UHPC. Additionally, testing showed that UHPC gained half of its bond and compressive strength after just one day of curing, showed a non-linear increase in bond as a function of fiber volume content, and determined little variation in bond performance as a result of UHPC casting orientation. This was then followed by a series of beam tests using two precast regular concrete sections joined together with a UHPC joint. Specimens were heavily instrumented, and tested using a four point flexure method. The results of this testing showed that a 150 mm (6”) UHPC was sufficient for precast bridge construction. Further, results from 100 mm (4”) UHPC joint tests showed that bond decreased

14% in a pure flexural loading scenario as compared to the simple bar pull out testing. This information as direct impact on the current state of reinforced concrete design code. Finally, a finite element material model making use of fully integrated shell elements was developed for UHPC, modified from pre-existing models for HPFRC. The model was shown to be valid for use in evaluating and predicting UHPC structures.

7.3. Conclusions

Major conclusions from this research are as follows.

- The test results suggest that fiber volume contents of 1.0% or 1.5% could significantly reduce the chance for crack localization under dead load or working conditions, respectively, in structural applications. Coupled with the material's inherent resistance to chloride ion penetration, controlling crack localization further limits the ingress of chloride ions and protects steel reinforcement from corrosion.
- UHPC derives its unique properties from its high packing density, which is achieved by carefully controlling the size and distribution of the constituent particles, and incorporating steel fibers. The high freeze-thaw resistance in UHPCs is due to water being prevented from entering the material in the first place.
- At the lower limits of embedment lengths, increasing embedment leads to a reduction in the nominal peak bond stress. This is attributed to an uneven distribution of force along the length of the bar, a fact that is established for high strength concretes. This appears consistent with other studies on UHPC, albeit differing in set up and materials used. Recorded values of bond still vary greatly, especially at lower embedment length, warranting further investigation.

- An assumed maximum bond stress, τ_{bond}, equal to $1.1\sqrt{f'c}$ (MPa), can be used for estimating the required embedment length in UHPC. Because of the broadness of the test variables in the data from which it was derived, this value appears reasonably conservative for a wide variety of design conditions. Additional research may refine it for specific design conditions.
- All beam deck specimens with a joint width of 100 mm (4”) failed with a splitting failure occurring at the UHPC joints. Bond between the UHPC and deformed bars was insufficient, causing the beams to reach failure prematurely. Results showed the bond strength developed in this loading case was 14% lower than in the simple bar pull out case.
- Joint widths of 150 mm and 200 mm (6” and 8” joints) all failed through steel yield in the deformed bars, followed much later on by crushing in the regular concrete. These specimens were able to carry load through the joints all the way through the desired failure mode.
- Bridge deck specimen’s specimens containing 1% fibers by volume achieved an average of 8% lower capacity than those containing 2% fibers. This indicated that the effect of fiber volume content increases is less impactful in the presence of traditional steel reinforcement.

7.4. The Promise of UHPC

The non-proprietary UHPC developed in this work has strong potential for use in structures that will be significantly more durable than currently possible with conventional materials. Therefore, every structure built at the moment using current technology is an opportunity lost to start building a longer lasting infrastructure that is considerably cheaper to maintain in the long run.

For an initial increase in material cost compared to regular concrete the benefits of UHPC can be substantial compared to traditional concrete products. With UHPC’s enhanced strength in tension and compression, thinner and more elegant structures can be built. Not only that, the use of

GGBS in the proposed mix improves the material's 'greenness' making it a more sustainable cementitious product. With durability that boasts no deterioration after 60+ cycles of freeze-thaw and virtually no chloride penetration, UHPC structures will have extremely low maintenance requirements, and therefore costs, for lifespans that are substantially longer than currently possible.

7.5. Future Research Needs

7.5.1. Material Level

To achieve the promise of UHPC as the material for the next generation of infrastructure, research is needed on multiple fronts. Fibers properties need to be optimized and the effect of fiber coatings on UHPC response explored. Commercial production of UHPC remains a challenge. At present, UHPC must be mixed in a paddle mixer and cannot be made and delivered in a ready-mix concrete truck. Research is needed to explore innovative mixing methods that require only small incremental changes to existing mixing technology so that widespread adoption of the material can be facilitated. Research into alternative high range water reducers is also needed so as to ensure that the UHPC described herein is not dependent on a single source.

7.5.2. Structural Level

As new demands on civil engineering infrastructures grows, new innovative materials will have a direct impact on the future of structures. UHPC's unique material characteristics makes it a logical option in designing newer, light-weight structural components. However, research on UHPC structures and structural components is rare in the literature and research efforts are needed to ensure that established design methods apply to UHPC systems and develop new ones, as needed.

Appendix A
Stress-Strain Plots for All UHPC Mixes

This appendix lists the stress-strain plots for all tensile tests conducted on UHPC coupons. For each set of tensile tests, at least 3 specimen tensile plots are averaged in order to produce a single tensile response curve. The plots are averaged at each point along the strain range. The result is then processed through a moving average filter to account for minute changes due to the sensitivity of the equipment. See Section 3.3.1 for further details.

Figure A.1. - White Cement Mixes

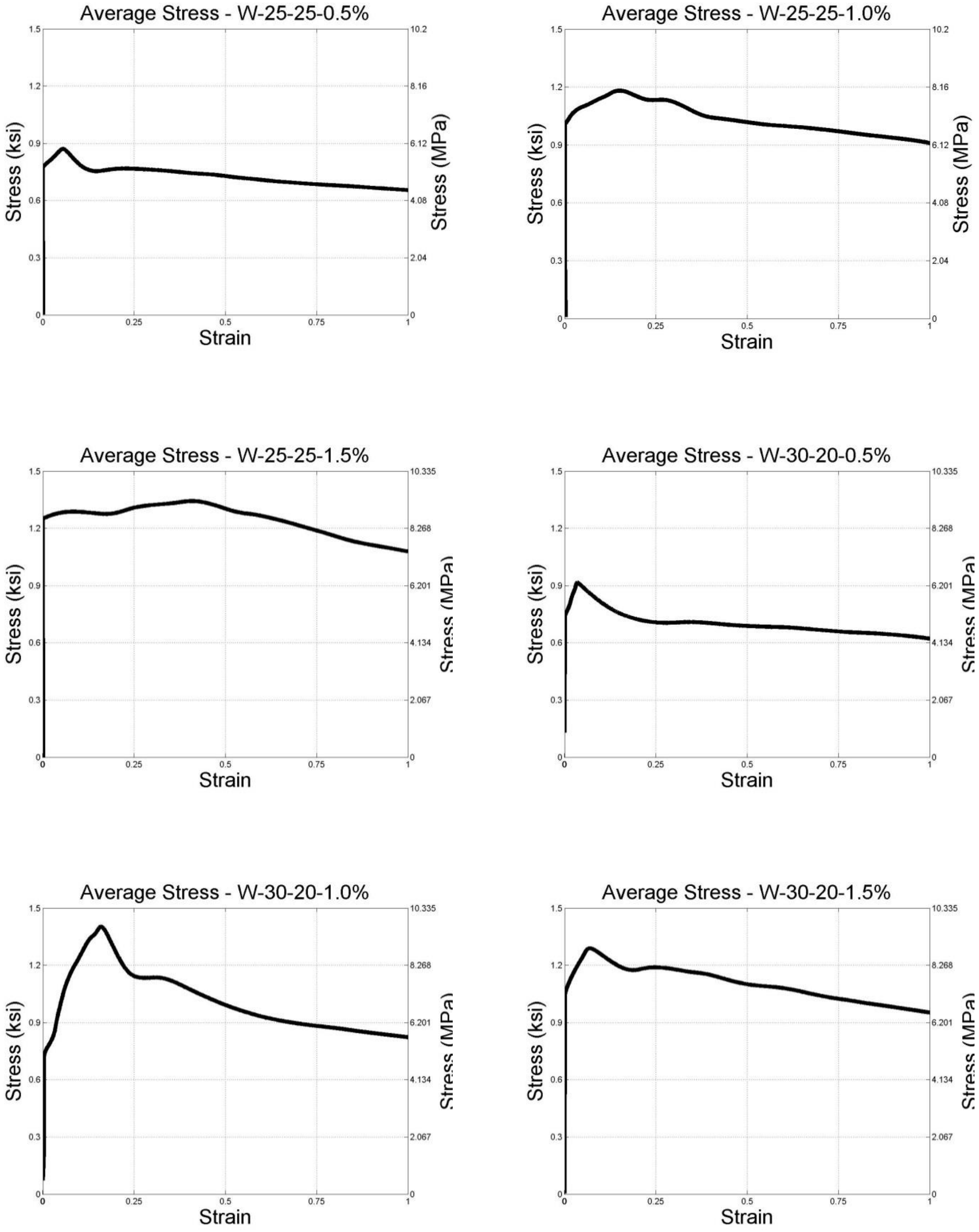

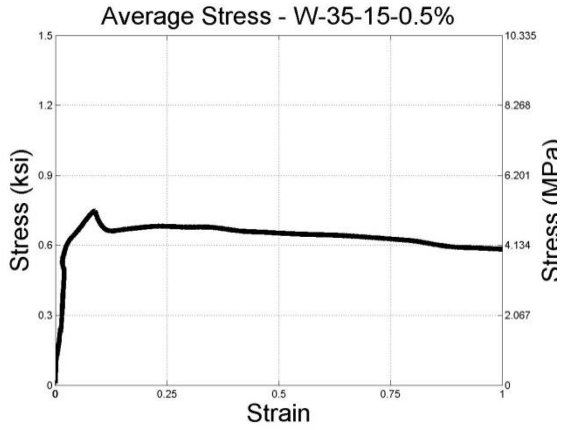
Average Stress - W-35-15-0.5%
Stress (ksi)
Stress (MPa)
Strain
0
0.3
0.6
0.9
1.2
1.5
2.067
4.134
6.201
8.268
10.335
0.25
0.5
0.75
1

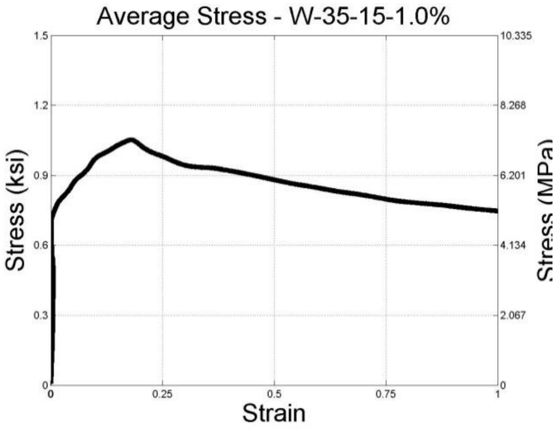
Average Stress - W-35-15-1.0%
Stress (ksi)
Stress (MPa)
Strain
0
0.3
0.6
0.9
1.2
1.5
2.067
4.134
6.201
8.268
10.335
0.25
0.5
0.75
1

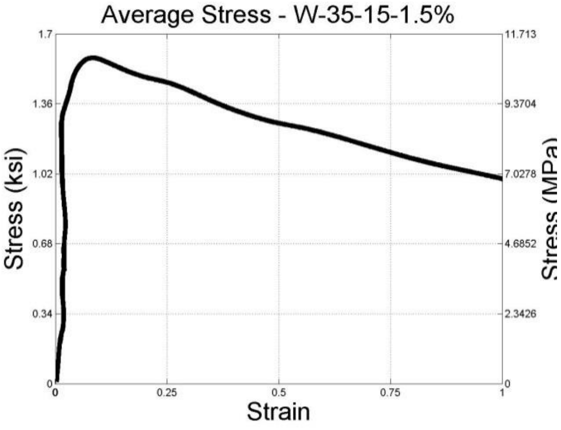
Average Stress - W-35-15-1.5%
Stress (ksi)
Stress (MPa)
Strain
0
0.34
0.68
1.02
1.36
1.7
2.3426
4.6852
7.0278
9.3704
11.713
0.25
0.5
0.75
1

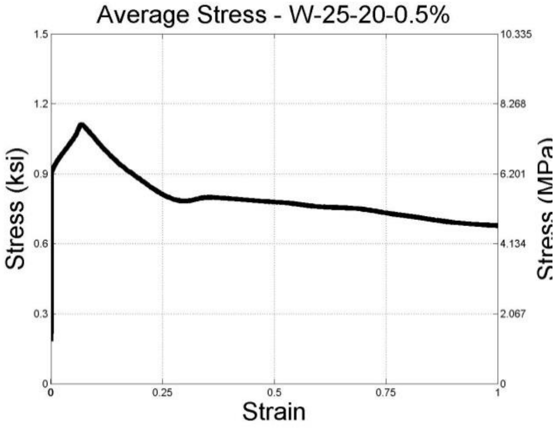
Average Stress - W-25-20-0.5%
Stress (ksi)
Stress (MPa)
Strain
0
0.3
0.6
0.9
1.2
1.5
2.067
4.134
6.201
8.268
10.335
0.25
0.5
0.75
1

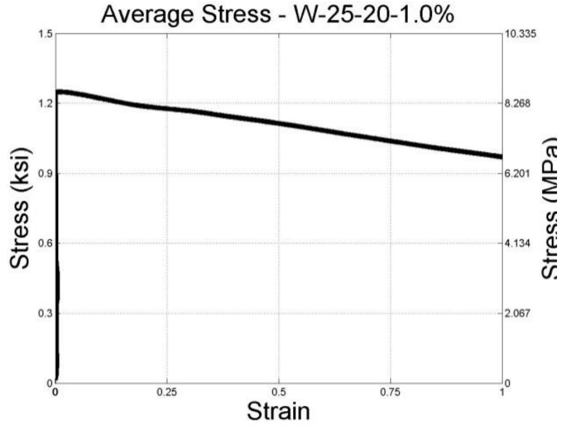
Average Stress - W-25-20-1.0%
Stress (ksi)
Stress (MPa)
Strain
0
0.3
0.6
0.9
1.2
1.5
2.067
4.134
6.201
8.268
10.335
0.25
0.5
0.75
1

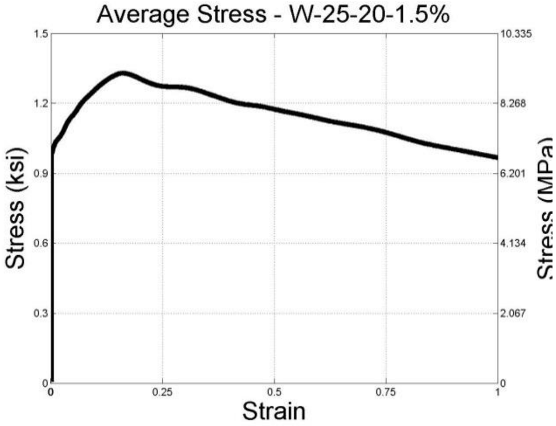
Average Stress - W-25-20-1.5%
Stress (ksi)
Stress (MPa)
Strain
0
0.3
0.6
0.9
1.2
1.5
2.067
4.134
6.201
8.268
10.335
0.25
0.5
0.75
1

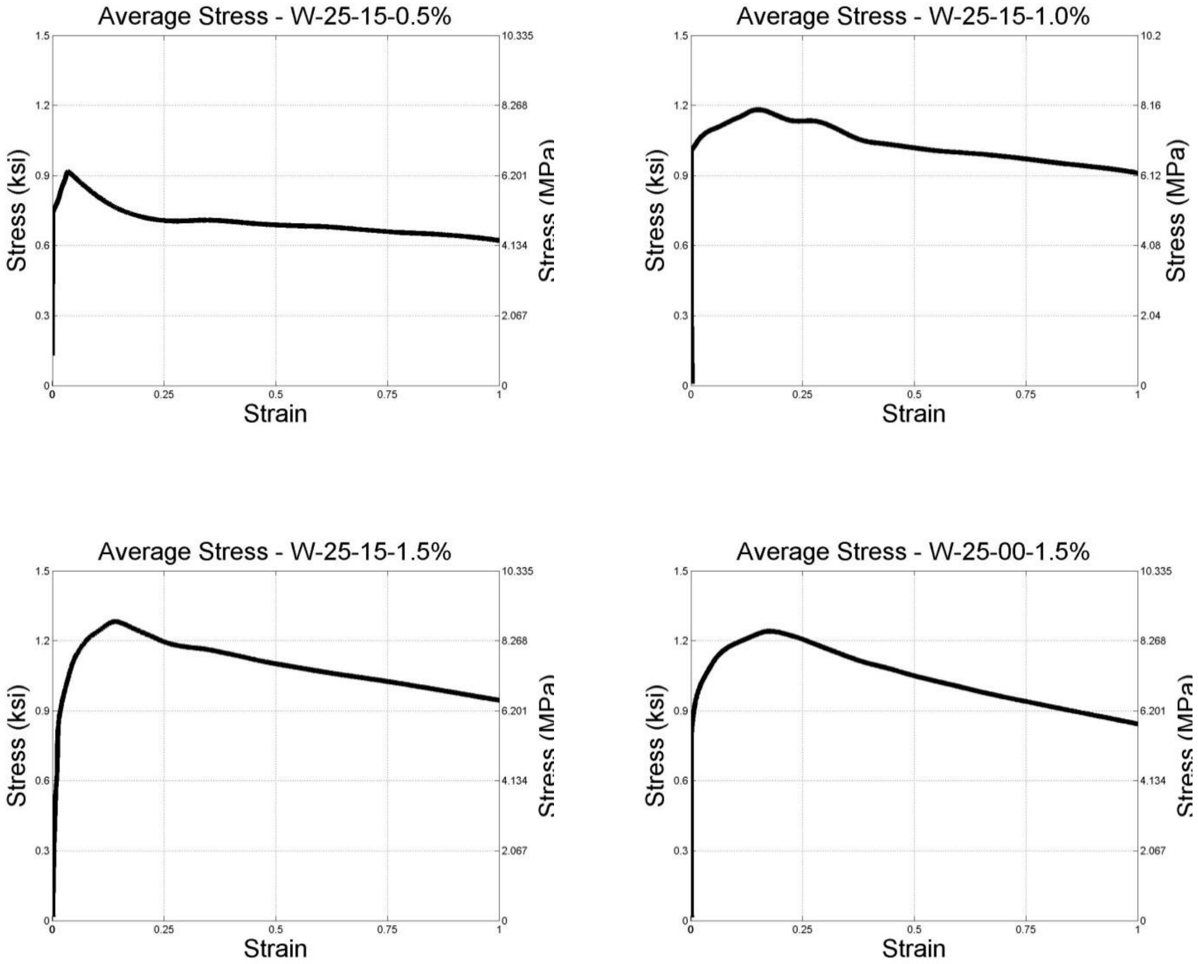

Figure A.2. - Portland V Mixes

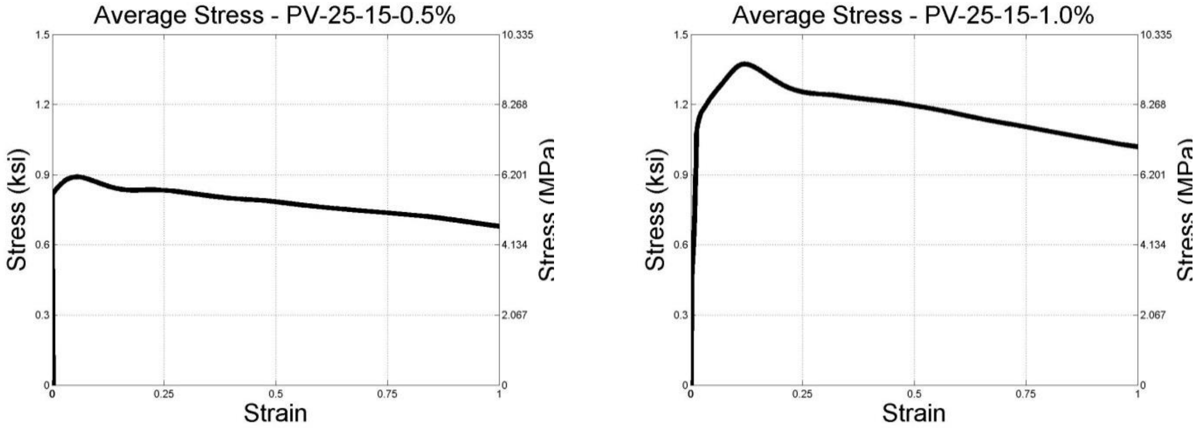

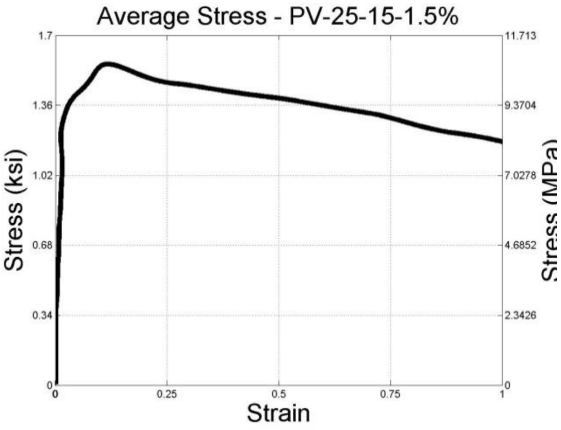
Average Stress - PV-25-15-1.5%

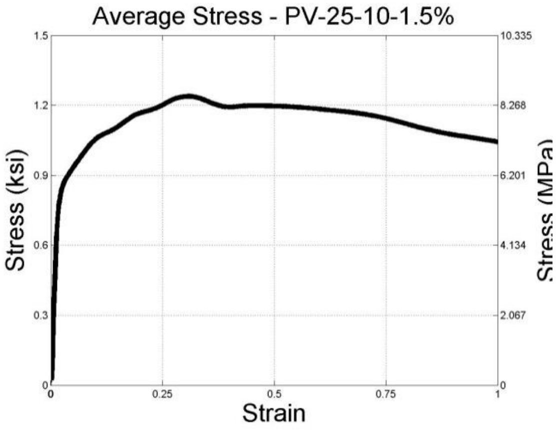
Average Stress - PV-25-10-1.5%

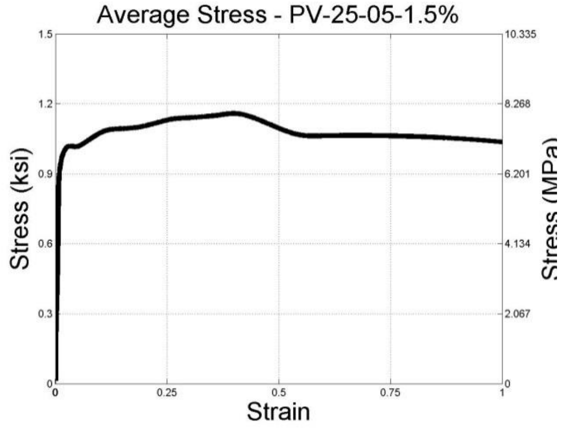
Average Stress - PV-25-05-1.5%

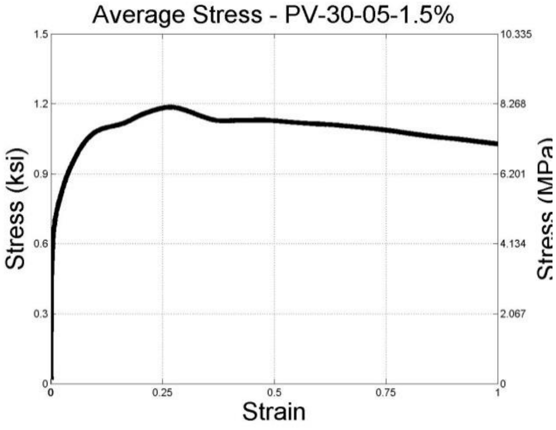
Average Stress - PV-30-05-1.5%

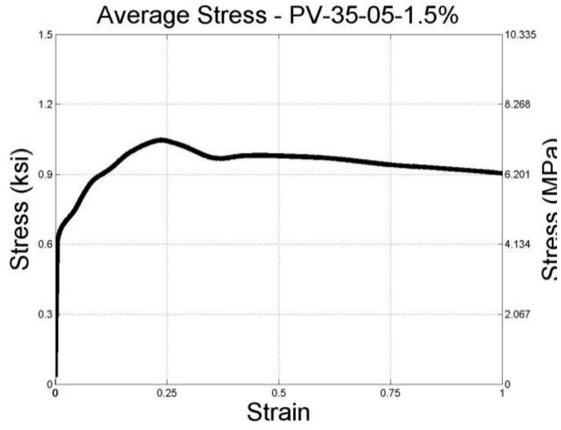
Average Stress - PV-35-05-1.5%

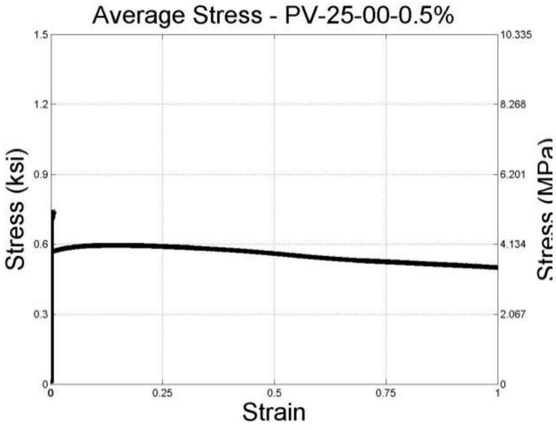
Average Stress - PV-25-00-0.5%

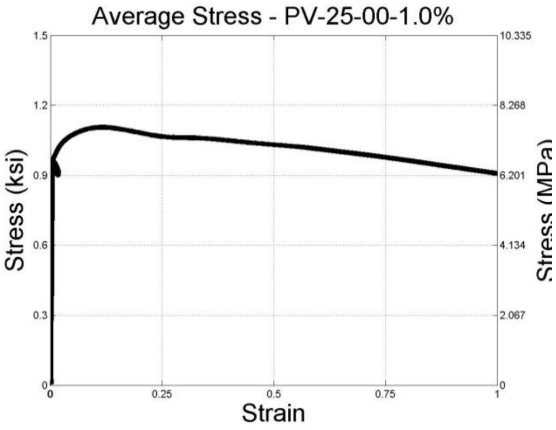
Average Stress - PV-25-00-1.0%

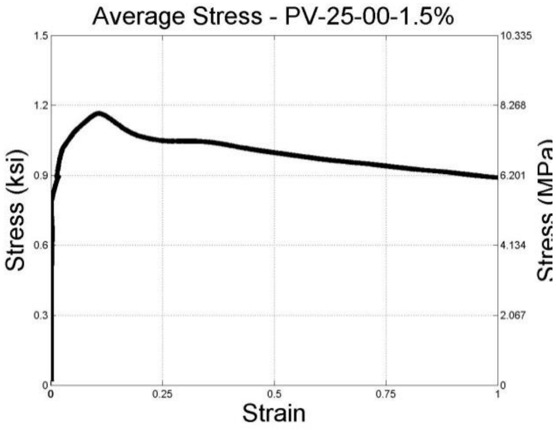
Average Stress - PV-25-00-1.5%

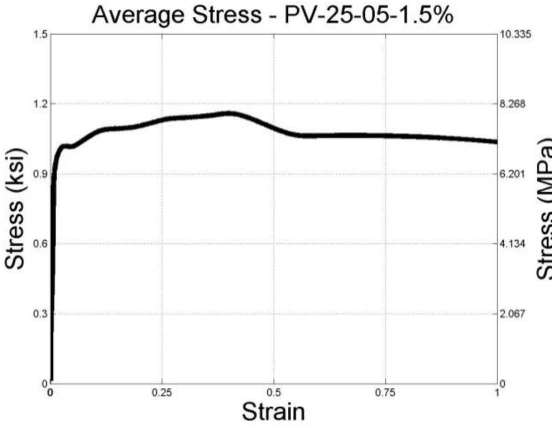
Average Stress - PV-25-05-1.5%

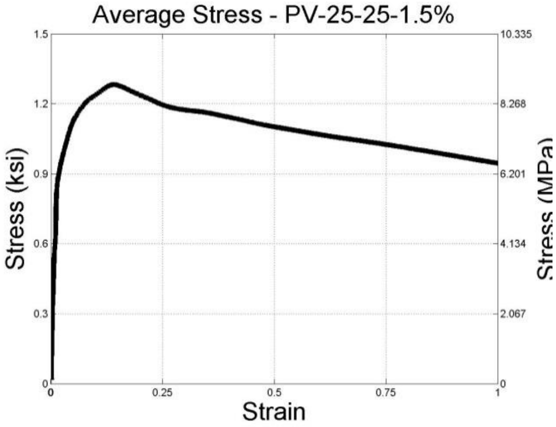
Average Stress - PV-25-25-1.5%

Figure A.3. - GGBS Mixes

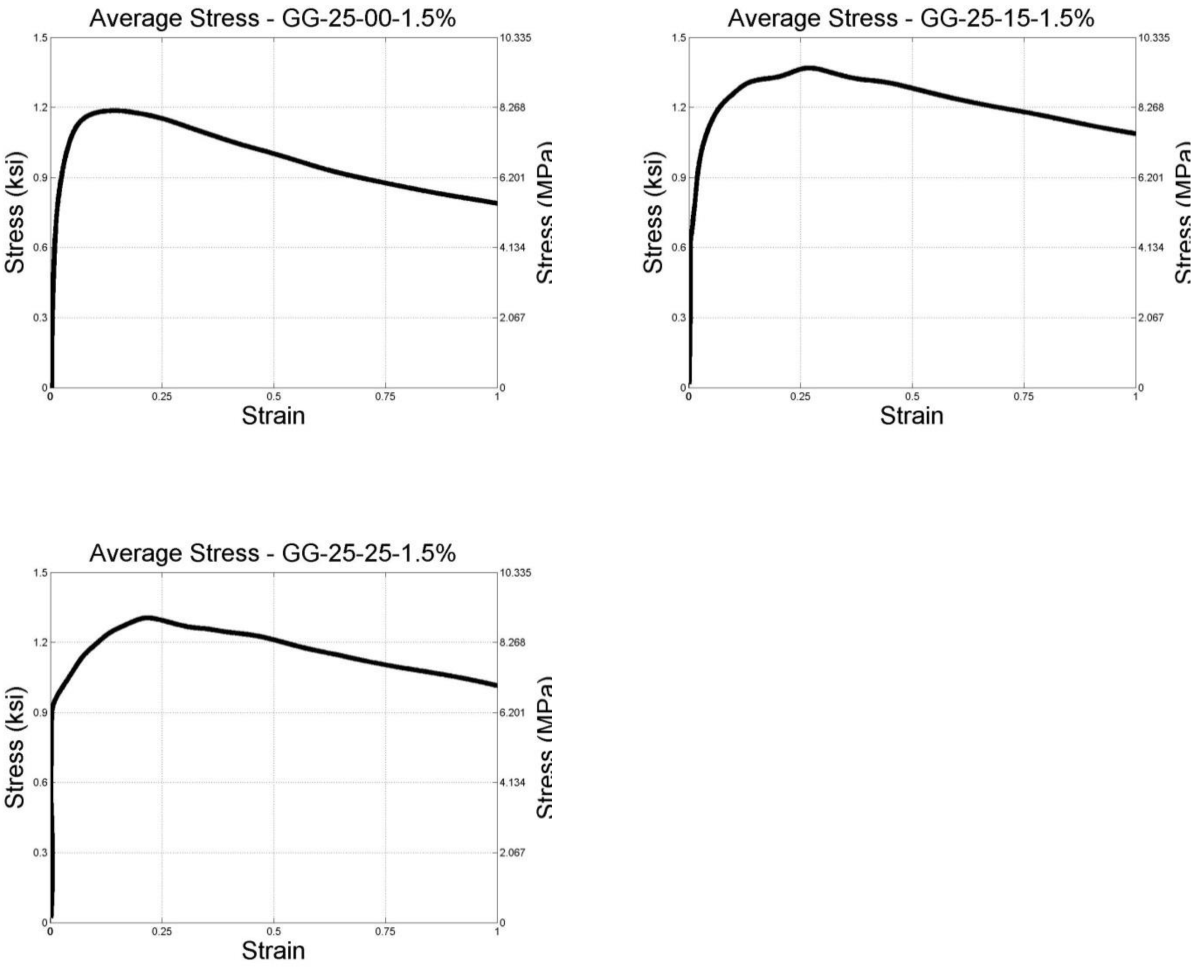

Appendix B
Results of Freeze-Thaw Testing – Rilem

This appendix lists the raw results from the freeze-thaw testing outlined in section 4.3.1. For each specimen, the internal damage as measured by the relative dynamic modulus; moisture uptake and salt scaling are listed.

Figure B.1. - Durability for White Cem.

W-25-25-1.5											
	Salt scaling, g/m^2 concrete				Internal damage by RDM, %				Moisture uptake, %		
F-T cycle	UHPC 1	UHPC 1	UHPC 1		UHPC 1	UHPC 1	UHPC 1		UHPC 1	UHPC 1	UHPC 1
0	0.0	0.0	0.0		100	100	100		0.00	0.00	0.00
10	81.4	67.3	74.4		100	100	100		0.23	0.24	0.23
18	112.3	89.0	100.6		100	100	100		0.25	0.27	0.26
23	161.8	122.6	142.2		100	99	99.5		0.29	0.30	0.30
45	177.3	137.1	157.2		100	99	99.5		0.31	0.30	0.30
61	194.8	157.5	176.2		100	99	99.5		0.32	0.32	0.32

W-25-15-1.5											
	Salt scaling, g/m^2 concrete				Internal damage by RDM, %				Moisture uptake, %		
F-T cycle	UHPC 2	UHPC 2	UHPC 2		UHPC 2	UHPC 2	UHPC 2		UHPC 2	UHPC 2	UHPC 2
0	0.0	0.0	0.0		100	100	100		0.00	0.00	0.00
14	16.4	6.6	11.5		100	100	100		0.18	0.20	0.19
26	24.3	10.7	17.5		100	100	100		0.20	0.23	0.21
40	32.9	24.8	28.8		100	100	100		0.20	0.25	0.22
52	43.1	35.5	39.3		100	100	100		0.24	0.27	0.25
68	49.3	52.1	50.7		100	100	100		0.24	0.27	0.26

W-25-00-1.5											
	Salt scaling, g/m^2 concrete				Internal damage by RDM, %				Moisture uptake, %		
F-T cycle	UHPC 3	UHPC 3	UHPC 3		UHPC 3	UHPC 3	UHPC 3		UHPC 3	UHPC 3	UHPC 3
0	0.0	0.0	0.0		100	100	100		0.00	0.00	0.00
14	9.9	6.0	8.0		100	100	100		0.18	0.18	0.22
26	22.3	9.4	15.9		100	100	100		0.20	0.20	0.23
40	30.6	17.5	24.0		100	100	100		0.20	0.21	0.25
52	42.1	25.5	33.8		100	100	100		0.24	0.25	0.26
68	51.2	35.6	43.4		100	100	100		0.24	0.26	0.28

Figure B.2. - Durability for PV Cem.

PV-25-25-1.5											
	Salt scaling, g/m^2 concrete				Internal damage by RDM, %				Moisture uptake, %		
F-T cycle	UHPC 4	UHPC 4	UHPC 4	UHPC 4	UHPC 4	UHPC 4	UHPC 4		UHPC 4	UHPC 4	UHPC 4
0	0.0	0.0	0.0		100	100	100		0.00	0.00	0.00
14	13.6	10.7	12.2		100	100	100		0.18	0.18	0.17
26	18.7	14.0	16.4		100	100	100		0.20	0.20	0.17
40	27.3	25.6	26.5		100	100	100		0.20	0.21	0.19
52	33.8	32.2	33.0		100	100	100		0.24	0.24	0.22
68	47.4	40.5	43.9		100	100	100		0.24	0.25	0.22

PV-25-15-1.5											
	Salt scaling, g/m^2 concrete				Internal damage by RDM, %				Moisture uptake, %		
F-T cycle	UHPC 5	UHPC 5	UHPC 5		UHPC 5	UHPC 5	UHPC 5		UHPC 5	UHPC 5	UHPC 5
0	0.0	0.0	0.0		100	100	100		0.00	0.00	0.00
14	1.5	6.7	4.1		100	100	100		0.13	0.10	0.12
26	12.3	14.2	13.3		100	100	100		0.16	0.14	0.15
40	22.3	22.5	22.4		100	100	100		0.18	0.15	0.17
52	35.4	32.2	33.8		100	100	100		0.22	0.19	0.20
68	50.8	45.0	47.9		100	100	100		0.22	0.19	0.21

PV-25-00-1.5											
	Salt scaling, g/m^2 concrete				Internal damage by RDM, %				Moisture uptake, %		
F-T cycle	UHPC 6	UHPC 6	UHPC 6		UHPC 6	UHPC 6	UHPC 6		UHPC 6	UHPC 6	UHPC 6
0	0.0	0.0	0.0		100	100	100		0.00	0.00	0.00
14	26.6	20.3	23.4		100	100	100		0.10	0.10	0.10
30	50.6	42.2	46.4		100	100	100		0.13	0.13	0.13
42	75.4	64.9	70.2		100	100	100		0.14	0.15	0.15
56	85.7	70.6	78.2		100	100	100		0.16	0.15	0.16

Figure B.2. - Durability for GGBS Cem.

GG-25-25-1.5

	Salt scaling, g/m^2 concrete				Internal damage by RDM, %				Moisture uptake, %		
F-T cycle	UHPC 8	UHPC 8	UHPC 8		UHPC 8	UHPC 8	UHPC 8		UHPC 8	UHPC 8	UHPC 8
0	0.0	0.0	0.0		100	100	100		0.00	0.00	0.00
14	15.4	4.4	9.9		100	100	100		0.18	0.20	0.19
26	26.3	9.8	18.0		100	100	100		0.23	0.22	0.23
40	40.8	24.0	32.4		100	100	100		0.25	0.25	0.25
52	50.8	36.5	43.6		100	100	100		0.30	0.29	0.29
68	69.8	56.1	63.0		100	100	100		0.32	0.30	0.31

GG-25-15-1.5

	Salt scaling, g/m^2 concrete				Internal damage by RDM, %				Moisture uptake, %		
F-T cycle	UHPC 7	UHPC 7	UHPC 7		UHPC 7	UHPC 7	UHPC 7		UHPC 7	UHPC 7	UHPC 7
0	0.0	0.0	0.0		100	100	100		0.00	0.00	0.00
14	10.8	5.4	8.1		100	100	100		0.18	0.15	0.17
26	24.3	15.4	19.8		100	100	100		0.24	0.19	0.22
40	33.2	23.6	28.4		100	100	100		0.28	0.23	0.26
52	44.0	29.0	36.5		100	100	100		0.34	0.25	0.30
68	61.1	41.7	51.4		100	100	100		0.36	0.27	0.31

GG-25-00-1.5

	Salt scaling, g/m^2 concrete				Internal damage by RDM, %				Moisture uptake, %		
F-T cycle	UHPC 9	UHPC 9	UHPC 9		UHPC 9	UHPC 9	UHPC 9		UHPC 9	UHPC 9	UHPC 9
0	0.0	0.0	0.0		100	100	100		0.00	0.00	0.00
10	23.9	29.9	26.9		100	100	100		0.18	0.16	0.17
24	43.9	46.3	45.1		100	100	100		0.21	0.19	0.20
40	64.6	69.1	66.9		100	100	100		0.24	0.21	0.23
52	83.1	94.0	88.6		100	100	100		0.25	0.23	0.24
66	90.0	100.4	95.2		100	100	100		0.25	0.23	0.24

Appendix C
Details from Bar Pull-Out Testing

This appendix lists the results from the bar pull out testing as outlined in section 5.2.1. For each parameter, at least 2 tests were performed. Below are the images for the damaged specimens taken after testing as well as the material parameters being tested.

Figure C.1. - Details from Bar Pull Out

13B-100-2%-P-28D

Bar Diameter:	#4, Bars (13 mm)
Coating:	Epoxy
Embedded Length:	4 inches (100 mm)
Fiber Content (% vol.)	2%
Casting Orientation:	Parallel
Curing Age:	28 Days
Test 1	
	
Test 2	
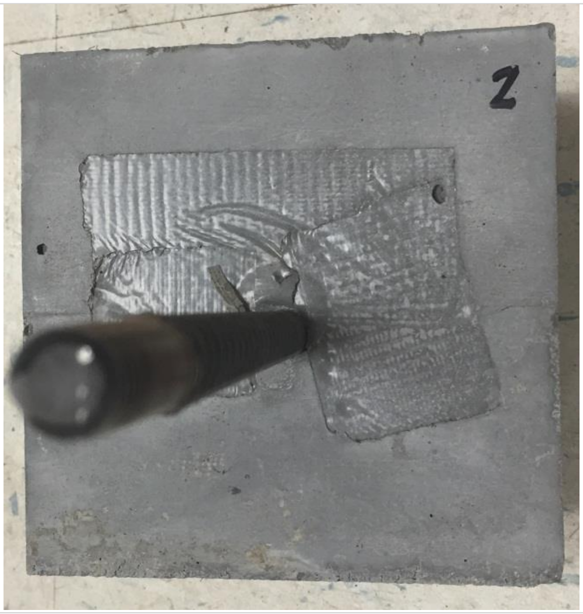	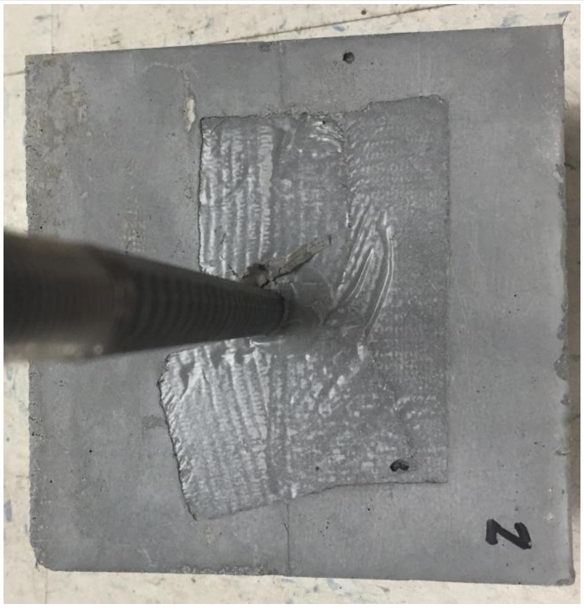

13E-100-2%-P-28D

Bar Diameter:	#4, Bars (13 mm)
Coating:	Epoxy
Embedded Length:	4 inches (100 mm)
Fiber Content (% vol.)	2%
Casting Orientation:	Parallel
Curing Age:	28 Days

Test 1

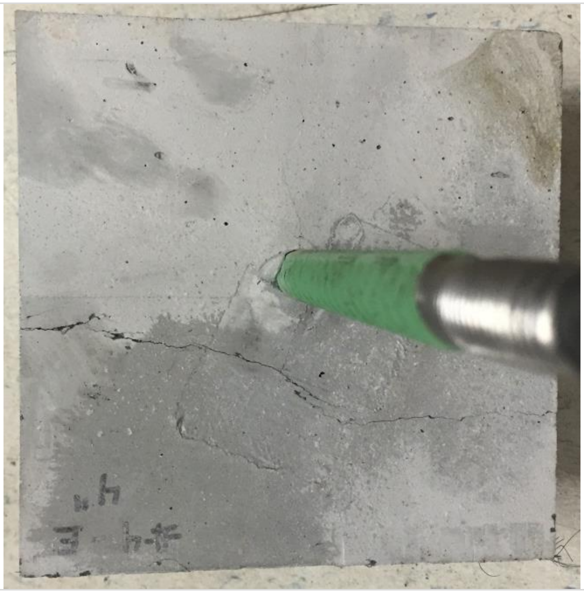

Test 2

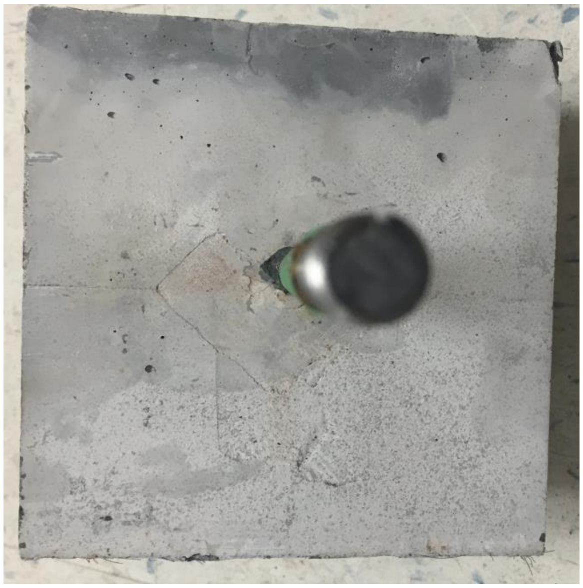

13B-75-2%-P-28D

Bar Diameter:	#4, Bars (13 mm)
Coating:	Plain
Embedded Length:	3 inches (75 mm)
Fiber Content (% vol.)	2%
Casting Orientation:	Parallel
Curing Age:	28 Days

Test 1

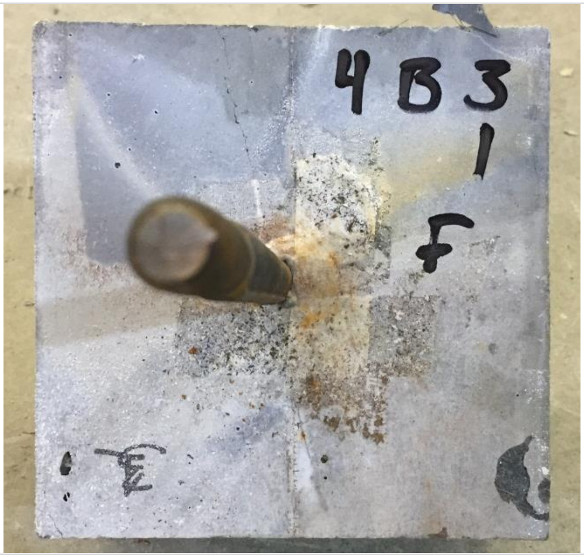

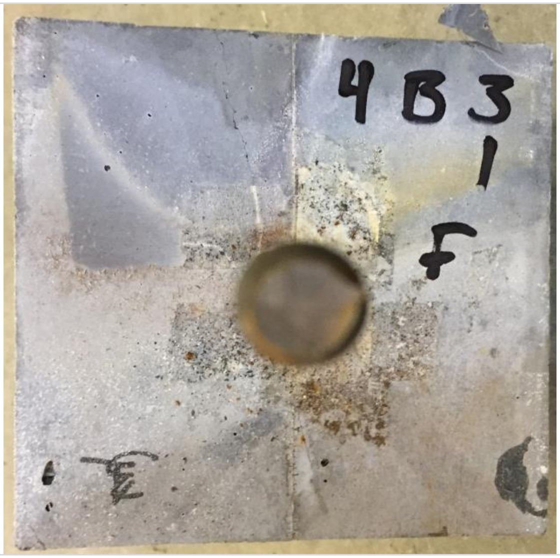

Test 2

13E-75-2%-P-28D

Bar Diameter:	#4, Bars (13 mm)
Coating:	Epoxy
Embedded Length:	3 inches (75 mm)
Fiber Content (% vol.)	2%
Casting Orientation:	Parallel
Curing Age:	28 Days
Test 1	
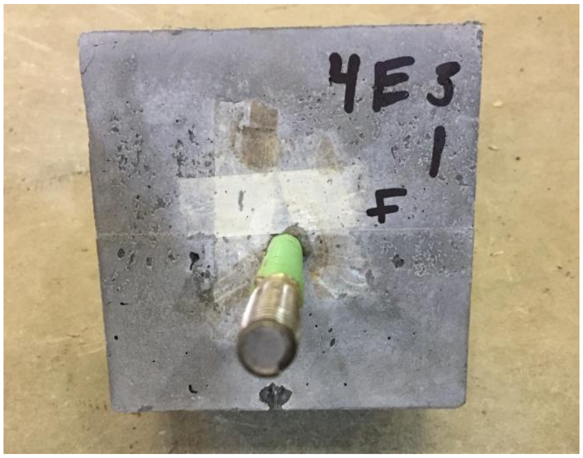	
Test 2	
	

13B-50-2%-P-28D

Bar Diameter:	#4, Bars (13 mm)
Coating:	Plain
Embedded Length:	2 inches (50 mm)
Fiber Content (% vol.)	2%
Casting Orientation:	Parallel
Curing Age:	28 Days

Test 1

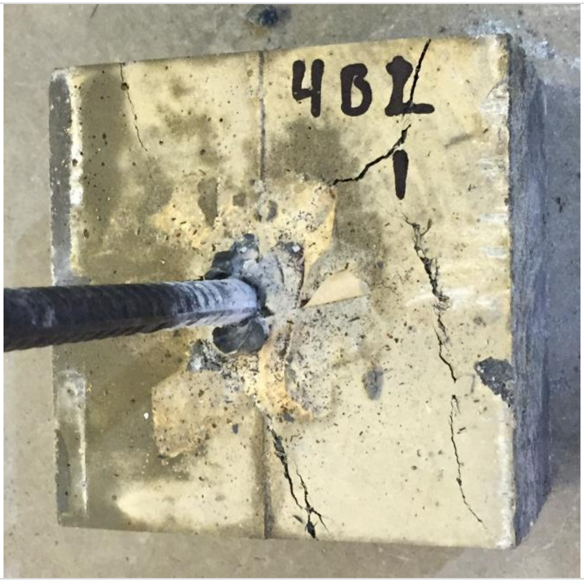

Test 2

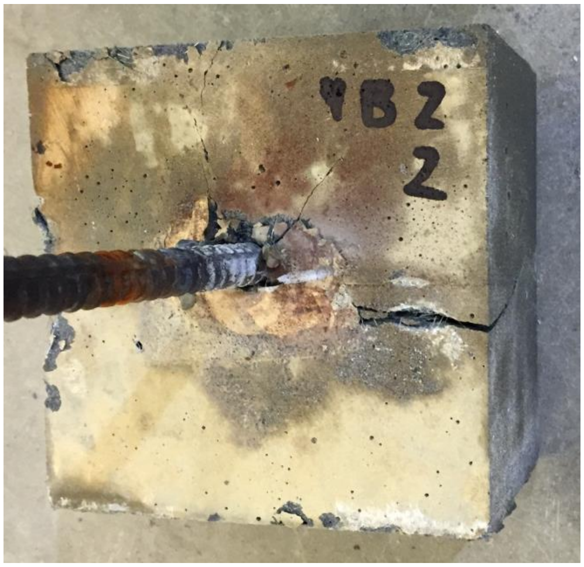

13E-50-2%-P-28D

Bar Diameter:	#4, Bars (13 mm)
Coating:	Epoxy
Embedded Length:	2 inches (50 mm)
Fiber Content (% vol.)	2%
Casting Orientation:	Parallel
Curing Age:	28 Days

Test 1

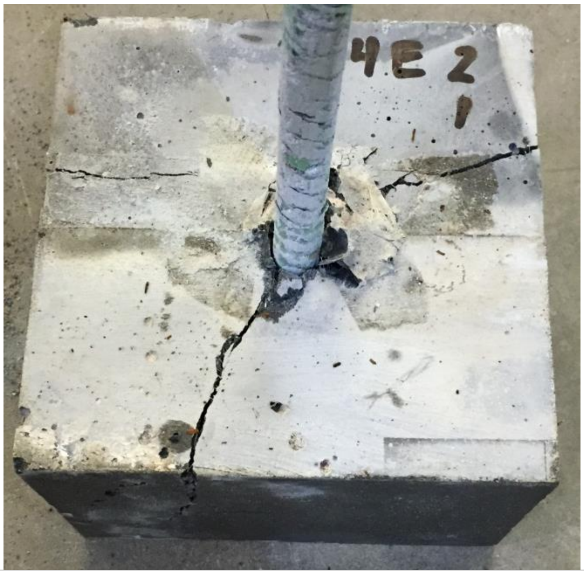	

Test 2

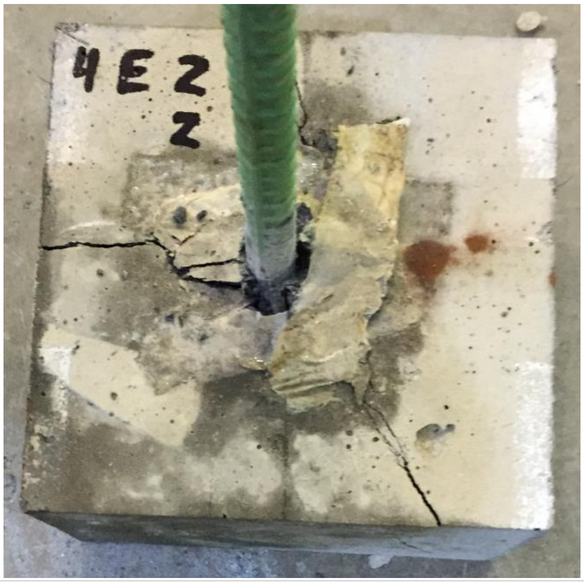	

16B-100-2%-P-28D

Bar Diameter:	#5, Bars (16 mm)
Coating:	Plain
Embedded Length:	4 inches (100 mm)
Fiber Content (% vol.)	2%
Casting Orientation:	Parallel
Curing Age:	28 Days

Test 1

Test 2

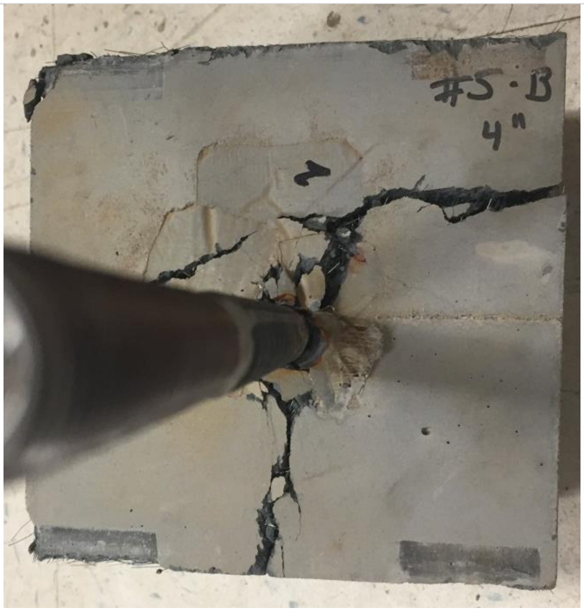

Test 3

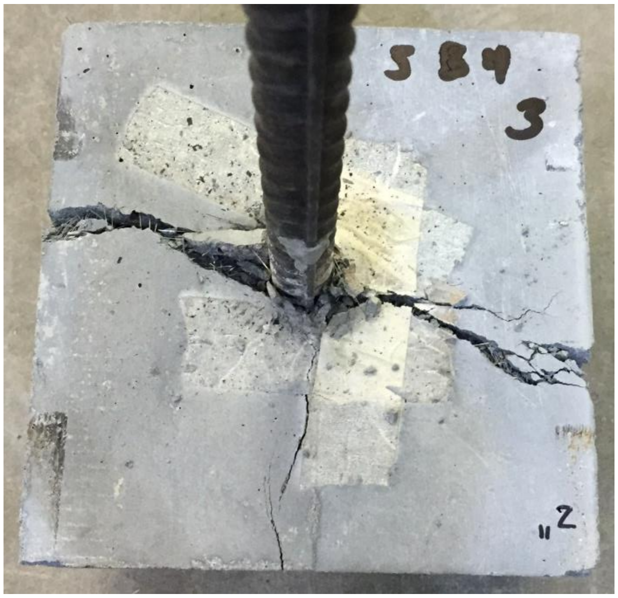
5 B4
3
"2


5 B4
3
"2

16E-100-2%-P-28D	
Bar Diameter:	#5, Bars (16 mm)
Coating:	Epoxy
Embedded Length:	4 inches (100 mm)
Fiber Content (% vol.)	2%
Casting Orientation:	Parallel
Curing Age:	28 Days
Test 1	
	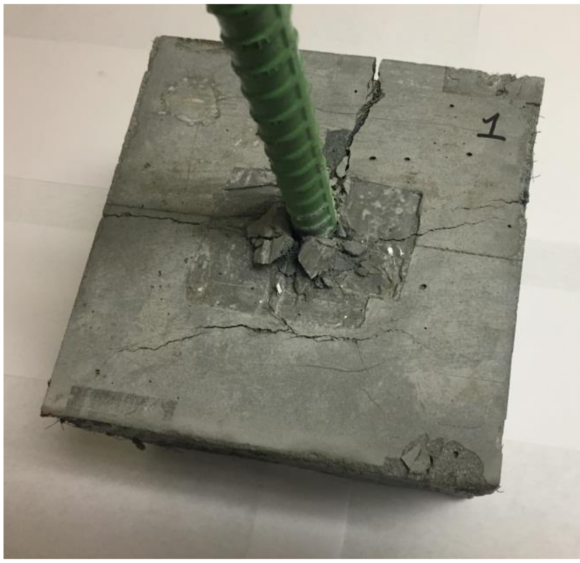
Test 2	
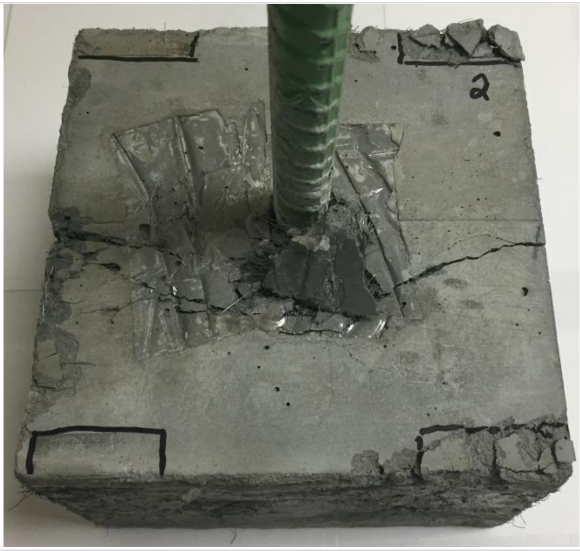	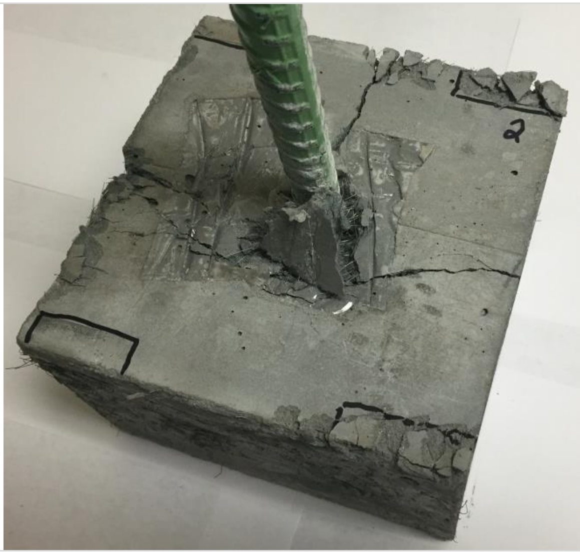

<table>
<tr><th colspan="2">Test 3</th></tr>
<tr><td>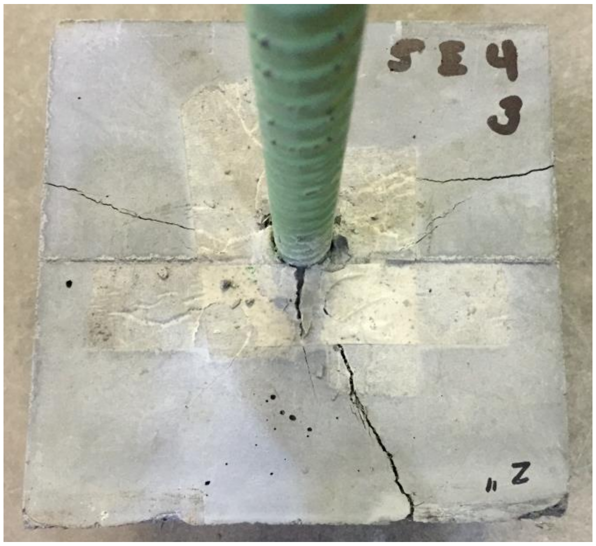 </td><td>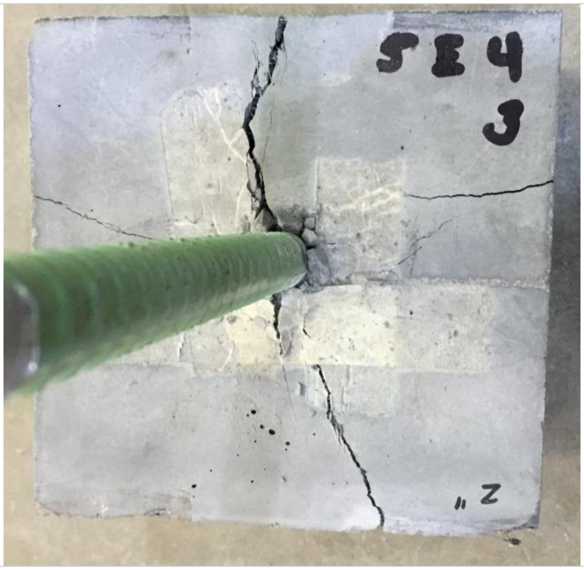 </td></tr>
</table>

16B-75-2%-P-28D

Bar Diameter:	#5, Bars (16 mm)
Coating:	Plain
Embedded Length:	3 inches (75 mm)
Fiber Content (% vol.)	2%
Casting Orientation:	Parallel
Curing Age:	28 Days

Test 1

Test 2

16E-75-2%-P-28D

Bar Diameter:	#5, Bars (16 mm)
Coating:	Epoxy
Embedded Length:	3 inches (75 mm)
Fiber Content (% vol.)	2%
Casting Orientation:	Parallel
Curing Age:	28 Days

Test 1

Test 2

16B-50-2%-P-28D

Bar Diameter:	#5, Bars (16 mm)
Coating:	Plain
Embedded Length:	2 inches (50 mm)
Fiber Content (% vol.)	2%
Casting Orientation:	Parallel
Curing Age:	28 Days

Test 1

Test 2

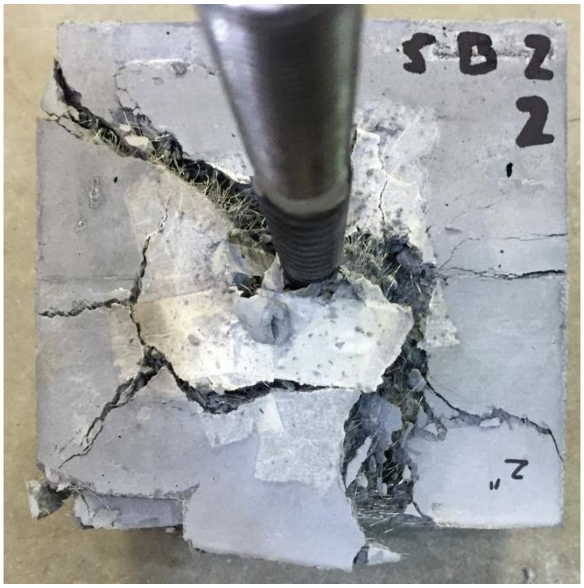

16E-50-2%-P-28D

Bar Diameter:	#5, Bars (16 mm)
Coating:	Epoxy
Embedded Length:	2 inches (50 mm)
Fiber Content (% vol.)	2%
Casting Orientation:	Parallel
Curing Age:	28 Days

Test 1

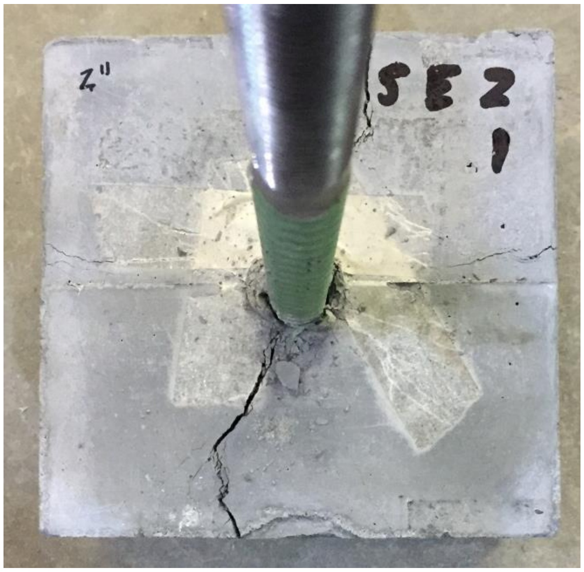

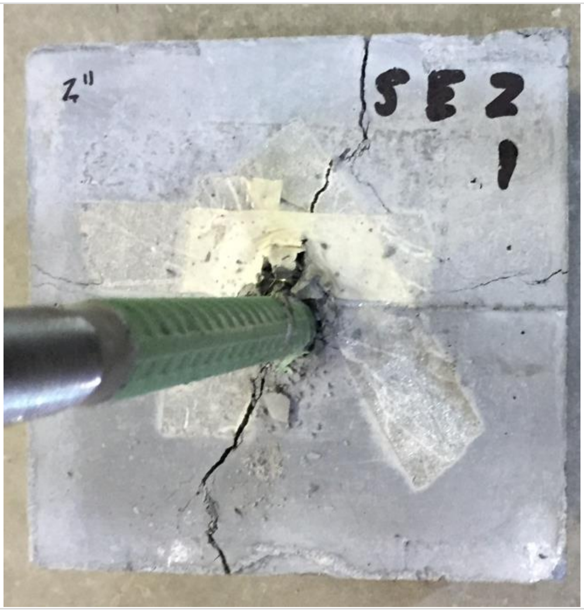

Test 2

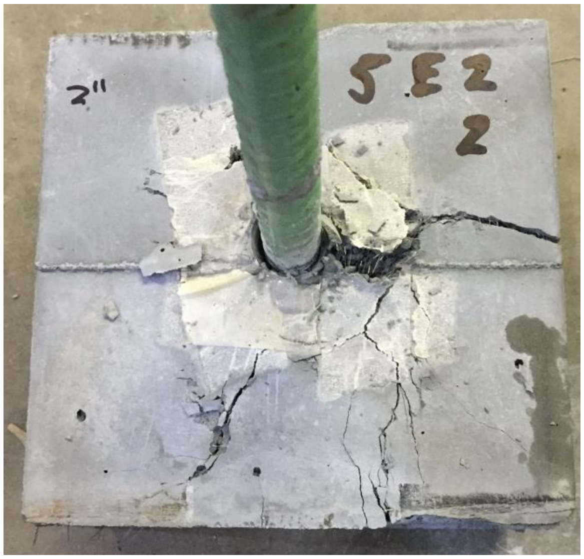

<table>
<tr><td colspan="2">19B-100-2%-P-28D</td></tr>
<tr><td>Bar Diameter:</td><td>#6, Bars (19 mm)</td></tr>
<tr><td>Coating:</td><td>Plain</td></tr>
<tr><td>Embedded Length:</td><td>4 inches (100 mm)</td></tr>
<tr><td>Fiber Content (% vol.)</td><td>2%</td></tr>
<tr><td>Casting Orientation:</td><td>Parallel</td></tr>
<tr><td>Curing Age:</td><td>28 Days</td></tr>
<tr><td></td><td></td></tr>
<tr><td colspan="2">Test 1</td></tr>
<tr><td></td><td></td></tr>
<tr><td colspan="2">Test 2</td></tr>
<tr><td> </td><td>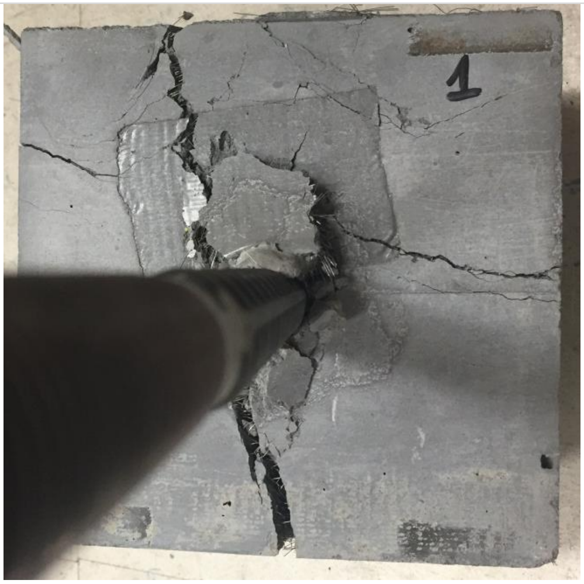 </td></tr>
<tr><td colspan="2"></td></tr>
</table>

19E-100-2%-P-28D

Bar Diameter:	#6, Bars (19 mm)
Coating:	Epoxy
Embedded Length:	4 inches (100 mm)
Fiber Content (% vol.)	2%
Casting Orientation:	Parallel
Curing Age:	28 Days

Test 1

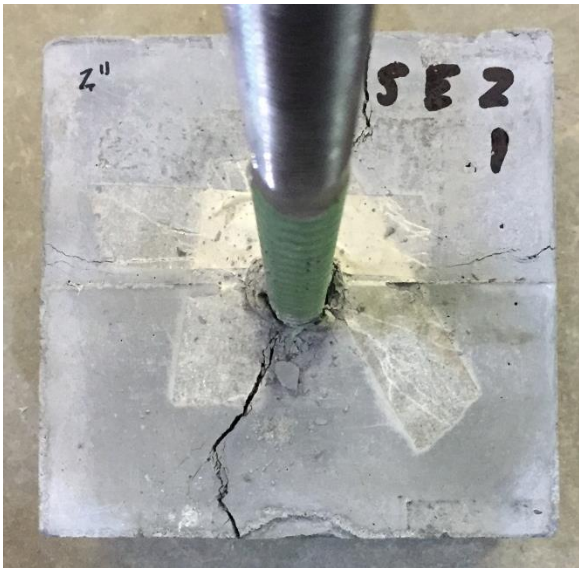

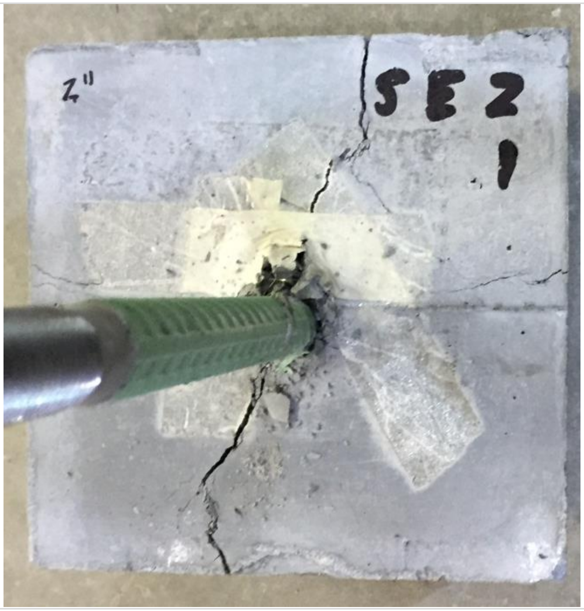

Test 2

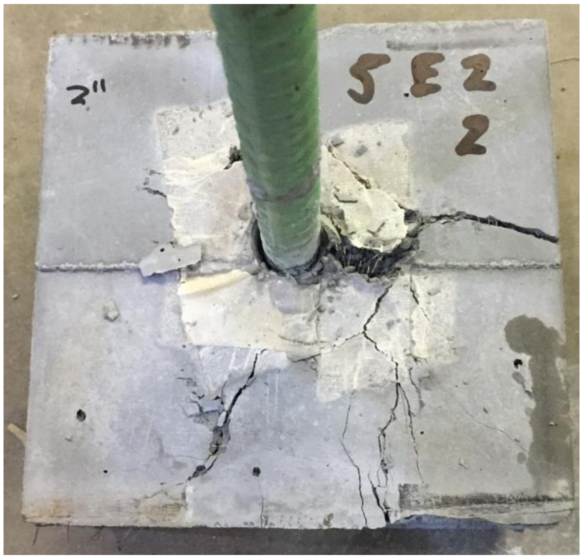

19B-75-2%-P-28D

Bar Diameter:	#6, Bars (19 mm)
Coating:	Plain
Embedded Length:	3 inches (75 mm)
Fiber Content (% vol.)	2%
Casting Orientation:	Parallel
Curing Age:	28 Days

Test 1

Test 2

19E-75-2%-P-28D

Bar Diameter:	#6, Bars (19 mm)
Coating:	Epoxy
Embedded Length:	3 inches (75 mm)
Fiber Content (% vol.)	2%
Casting Orientation:	Parallel
Curing Age:	28 Days

Test 1

Test 2

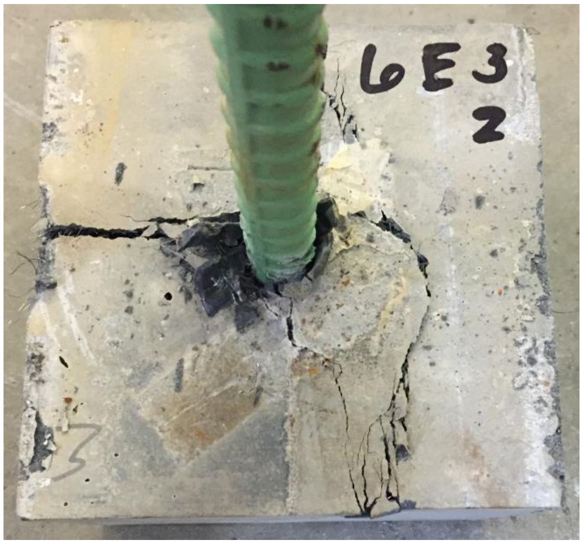

19B-50-2%-P-28D

Bar Diameter:	#6, Bars (19 mm)
Coating:	Plain
Embedded Length:	2 inches (50 mm)
Fiber Content (% vol.)	2%
Casting Orientation:	Parallel
Curing Age:	28 Days

Test 1

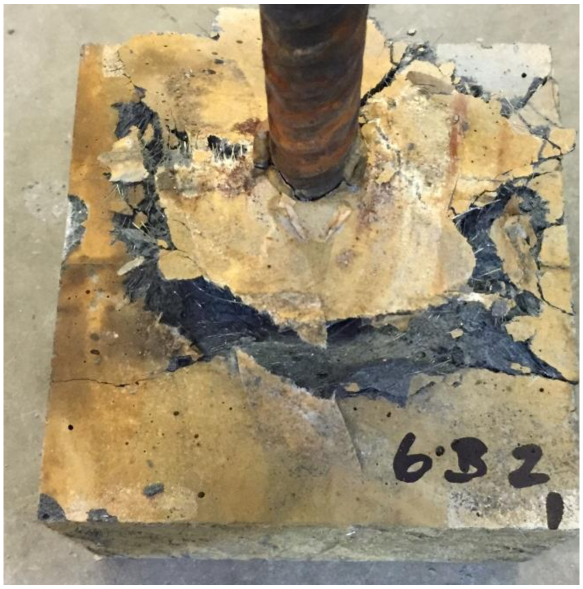

Test 2

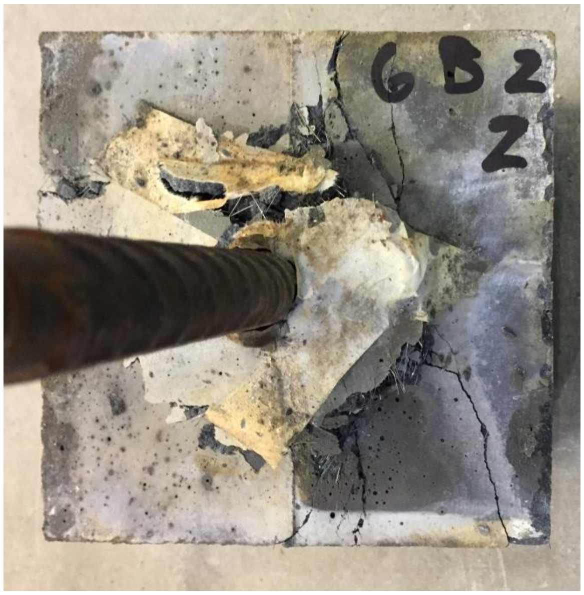

19E-50-2%-P-28D

Bar Diameter:	#6, Bars (19 mm)
Coating:	Epoxy
Embedded Length:	2 inches (50 mm)
Fiber Content (% vol.)	2%
Casting Orientation:	Parallel
Curing Age:	28 Days

Test 1

Test 2

19B-75-1%-P-28D

Bar Diameter:	#6, Bars (19 mm)
Coating:	Plain
Embedded Length:	3 inches (75 mm)
Fiber Content (% vol.)	1%
Casting Orientation:	Parallel
Curing Age:	28 Days

Test 1

Test 2

19E-75-2%-T-28D

Bar Diameter:	#6, Bars (19 mm)
Coating:	Epoxy
Embedded Length:	2 inches (50 mm)
Fiber Content (% vol.)	2%
Casting Orientation:	Transverse
Curing Age:	28 Days

Test 1

Test 2

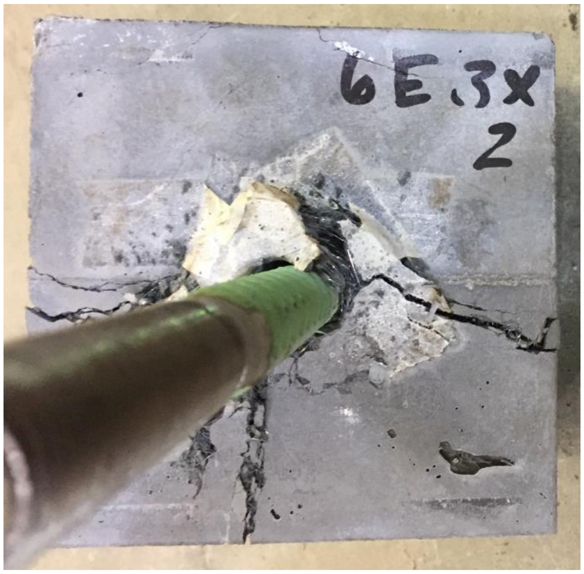

16E-100-2%-P-1D

Bar Diameter:	#5, Bars (16 mm)
Coating:	Epoxy
Embedded Length:	4 inches (100 mm)
Fiber Content (% vol.)	2%
Casting Orientation:	Parallel
Curing Age:	1 Day

Test 1

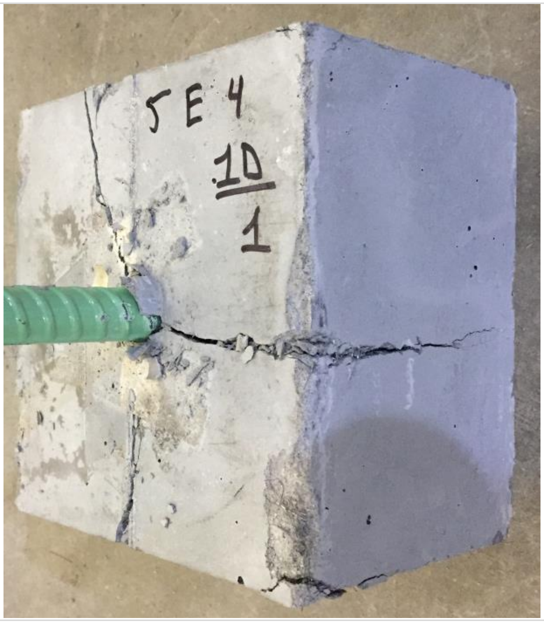

Test 2

16E-100-2%-P-3D

Bar Diameter:	#5, Bars (16 mm)
Coating:	Epoxy
Embedded Length:	4 inches (100 mm)
Fiber Content (% vol.)	2%
Casting Orientation:	Parallel
Curing Age:	3 Days

Test 1

	

Test 2

	

16E-100-2%-P-7D

Bar Diameter:	#5, Bars (16 mm)
Coating:	Epoxy
Embedded Length:	4 inches (100 mm)
Fiber Content (% vol.)	2%
Casting Orientation:	Parallel
Curing Age:	7 Days

Test 1

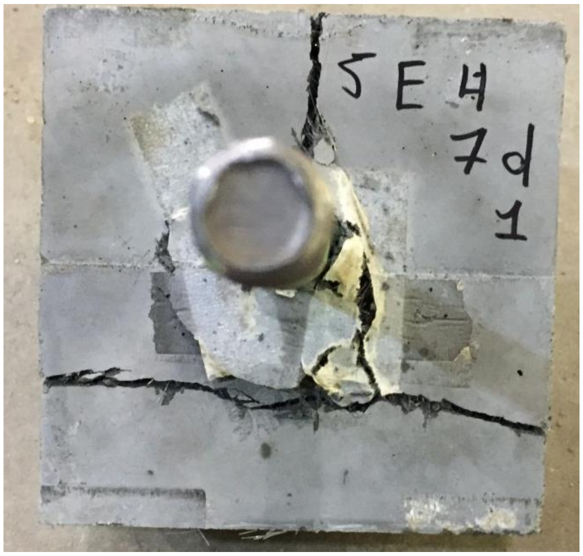

Test 2

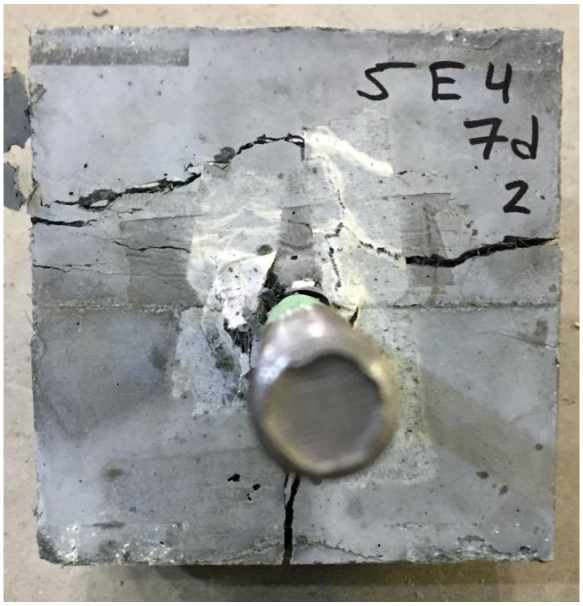

16B-100-2%-T-28D

Bar Diameter:	#5, Bars (16 mm)
Coating:	Plain
Embedded Length:	4 inches (100 mm)
Fiber Content (% vol.)	2%
Casting Orientation:	Transverse
Curing Age:	28 Days

Test 1

Test 2

Test 3	
	

16E-100-1%-P-28D	
Bar Diameter:	#5, Bars (16 mm)
Coating:	Epoxy
Embedded Length:	4 inches (100 mm)
Fiber Content (% vol.)	1%
Casting Orientation:	Parallel
Curing Age:	28 Days
Test 1	
	
Test 2	
	

Test 3	
 	

16E-100-2%-P-28D*

Bar Diameter:	#5, Bars (16 mm)
Coating:	Epoxy
Embedded Length:	4 inches (100 mm)
Fiber Content (% vol.)	2%
Casting Orientation:	Parallel
Curing Age:	28 Days

Test 1

Test 2

Test 3	
	
*Cast & Tested Same Day as 16E-100-1%-P-28D	

Appendix D
Details of Beam Testing

This appendix lists detailed photos from the beam testing series as outlined in Chapter 6. The images are listed as assigned by test name and number. Each set contains an images recorded from the actual test, prior to the loading (shown first) as well as at the peak load (shown second). Additionally, an image as seen through the digital image correlation camera is shown (shown third). For the relevant tests, the strain (%) in the bars vs. load (KN) plots is provided (shown last).

Figure D.1. - Details from Beam Testing

<table>
<tr><th colspan="2">F-100-1P-1</th></tr>
<tr><td>Joint Width:</td><td>4 inches (100 mm)</td></tr>
<tr><td>Fiber Content (% vol.)</td><td>1%</td></tr>
<tr><td>Loading Scheme:</td><td>Pure Flexure</td></tr>
<tr><td colspan="2">Prior to Test</td></tr>
<tr><td colspan="2"></td></tr>
<tr><td colspan="2">At Peak Load</td></tr>
<tr><td colspan="2"></td></tr>
<tr><td colspan="2">Strain Field (DIC)</td></tr>
<tr><td colspan="2">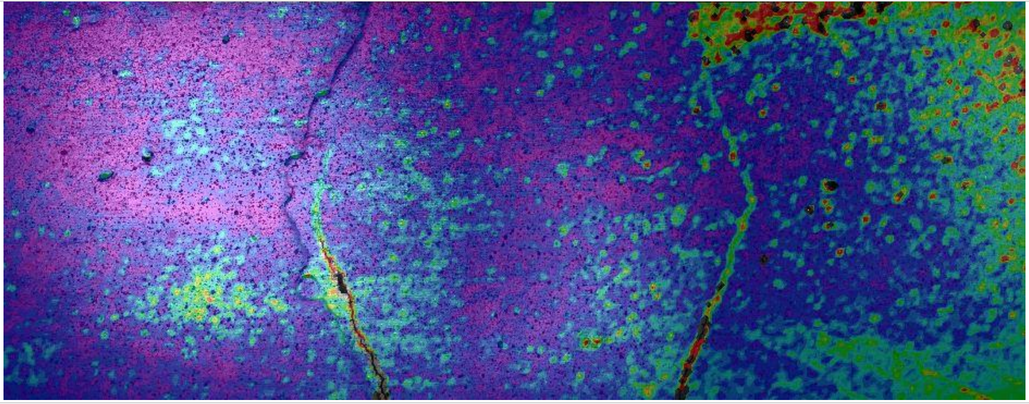</td></tr>
</table>

F-100-1P-2

Joint Width:	4 inches (100 mm)
Fiber Content (% vol.)	1%
Loading Scheme:	Pure Flexure

Prior to Test

At Peak Load

Strain Field (DIC)

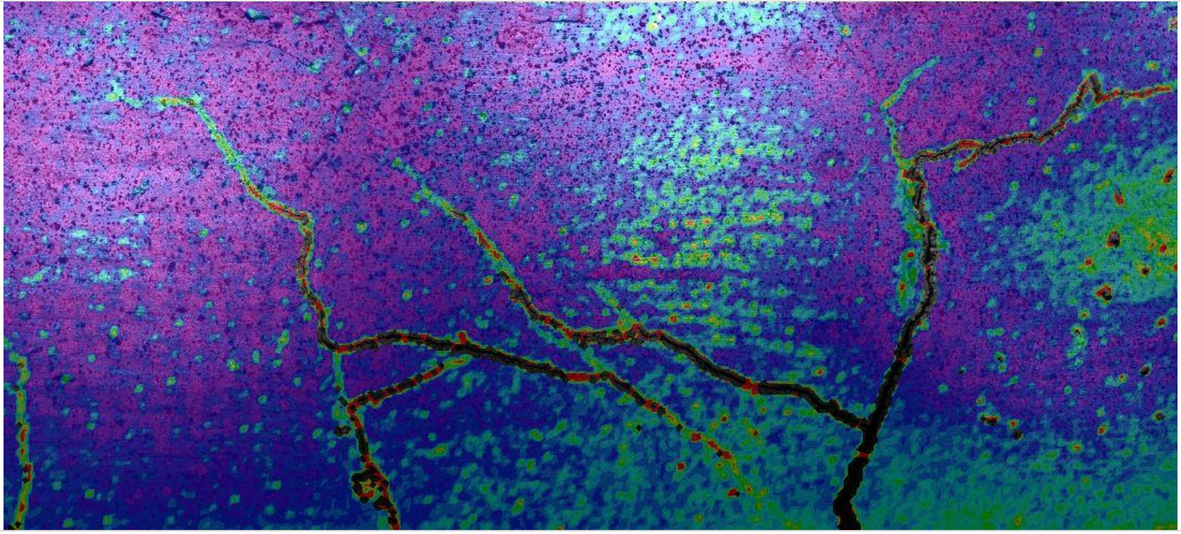

F-100-2P-1

Joint Width:	4 inches (100 mm)
Fiber Content (% vol.)	2%
Loading Scheme:	Pure Flexure

Prior to Load

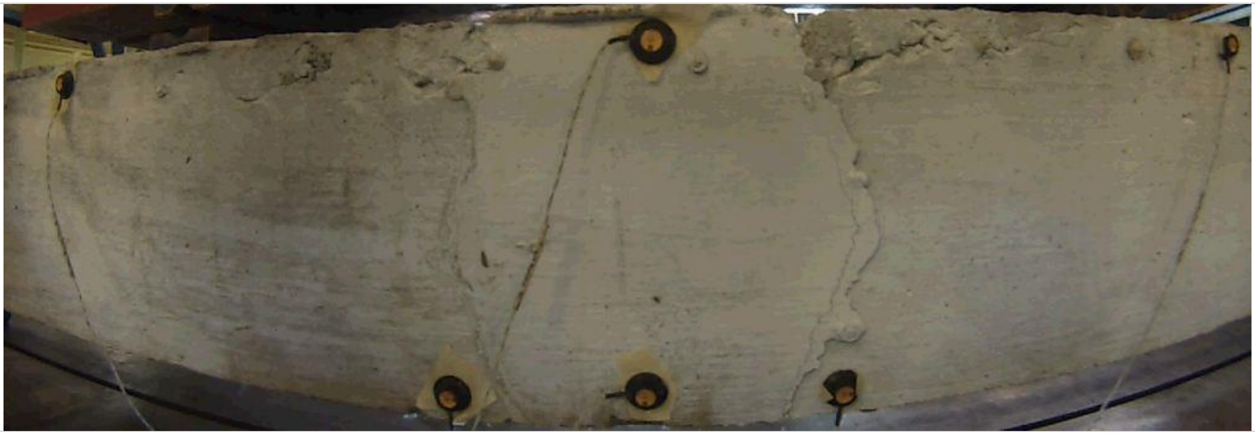

At Peak Load

Strain Field (DIC)

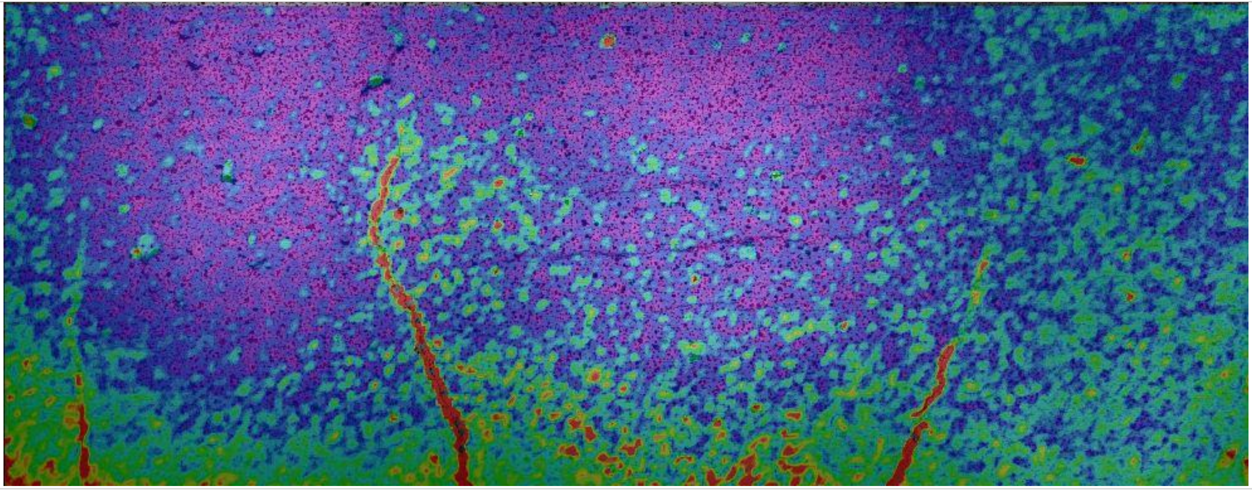

F-100-2P-2

Joint Width:	4 inches (100 mm)
Fiber Content (% vol.)	2%
Loading Scheme:	Pure Flexure

Prior to Load

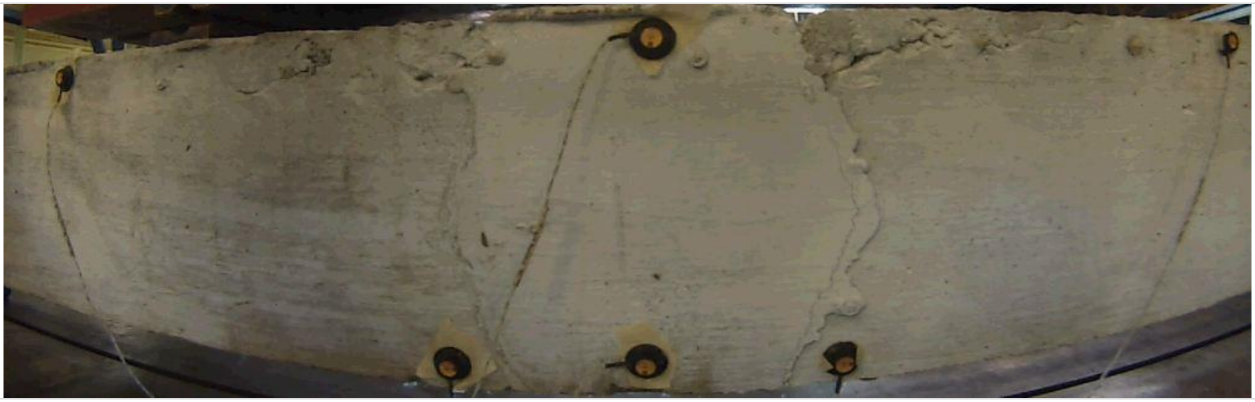

At Peak Load

Strain Field (DIC)

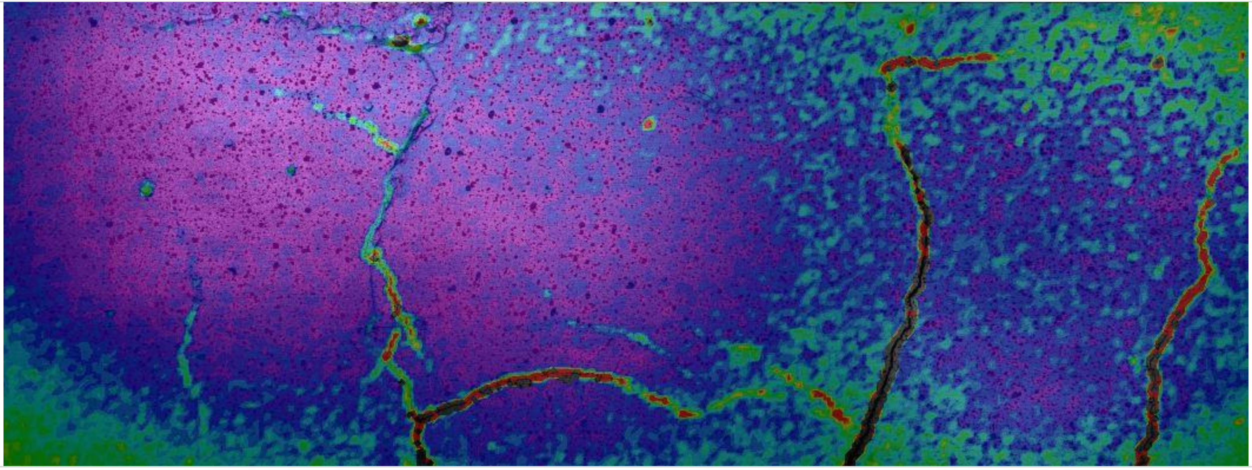

F-150-2P-1

Joint Width:	6 inches (150 mm)
Fiber Content (% vol.)	2%
Loading Scheme:	Pure Flexure

Prior to Load

At Peak Load

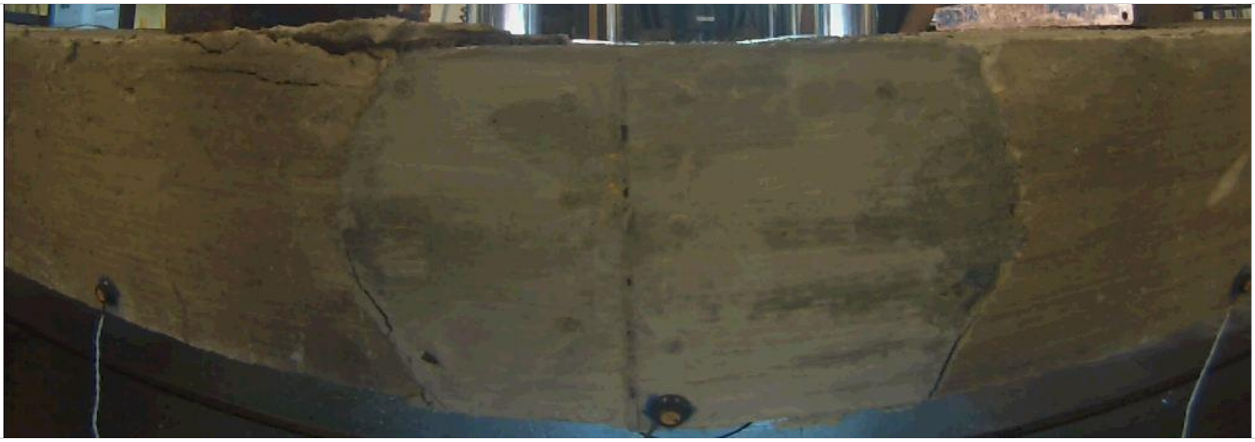

Strain Field (DIC)

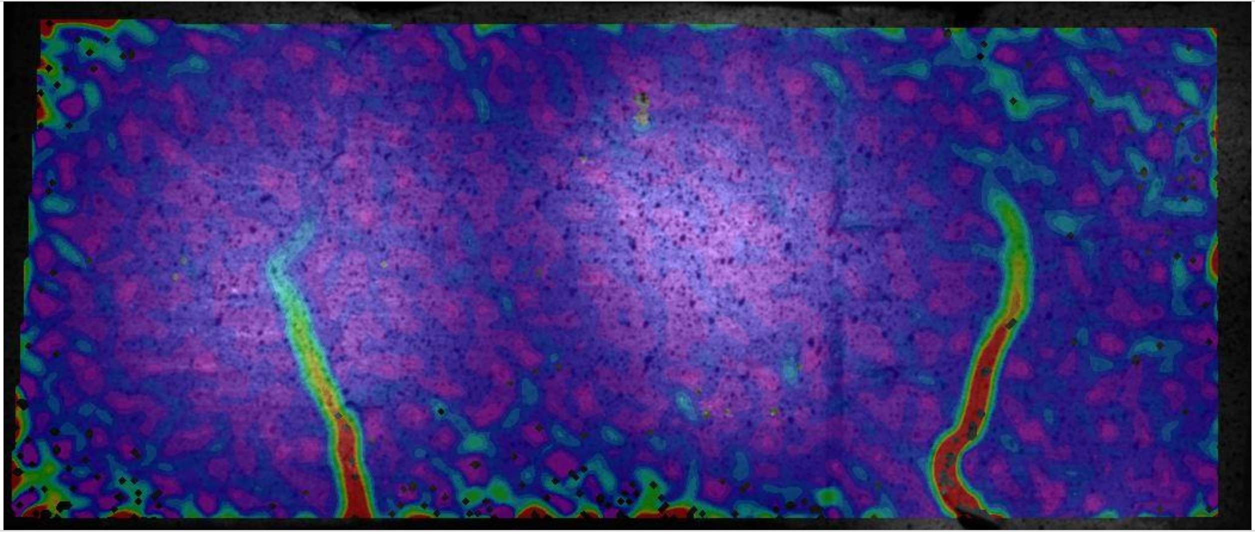

Strain (%) in Bars vs Load (KN)

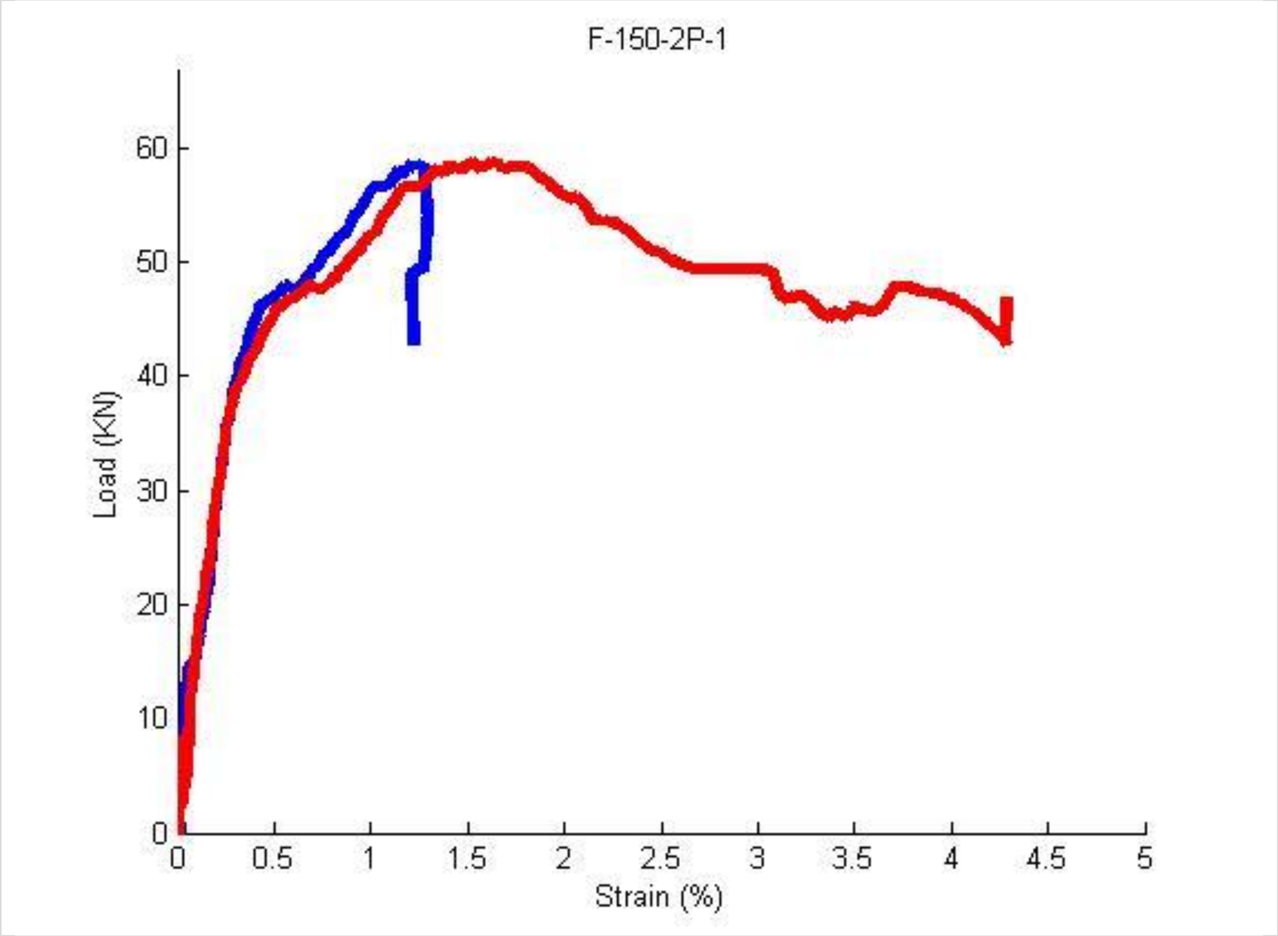
F-150-2P-1
Load (KN)
0
10
20
30
40
50
60
Strain (%)
0
0.5
1
1.5
2
2.5
3
3.5
4
4.5
5

F-150-2P-2	
Joint Width:	6 inches (150 mm)
Fiber Content (% vol.)	2%
Loading Scheme:	Pure Flexure
Prior to Load	
	
At Peak Load	
	
Strain Field (DIC)	
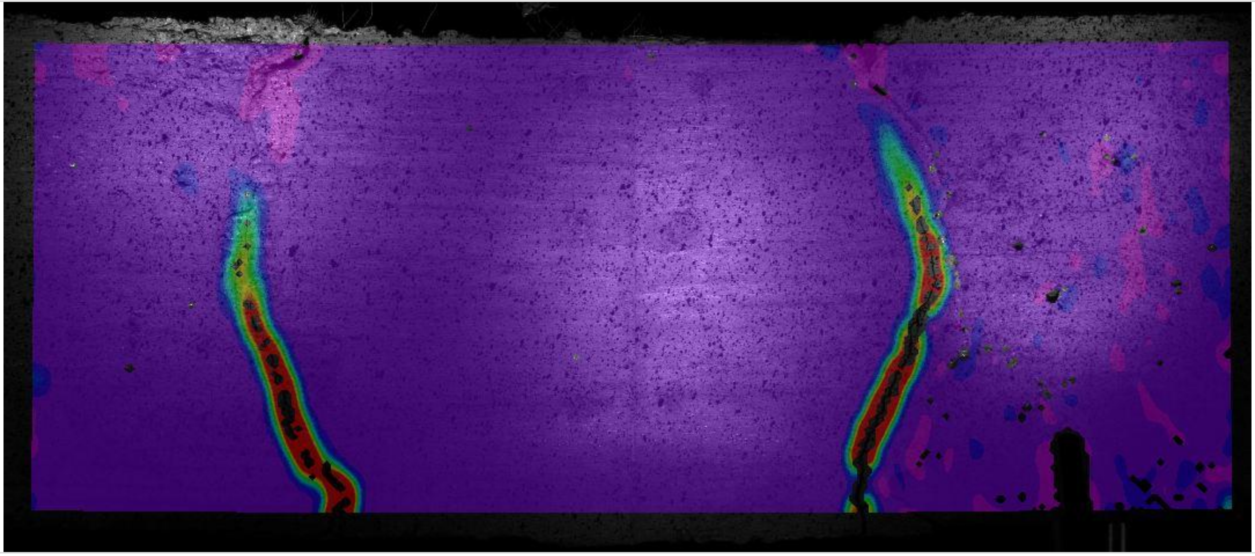	
Strain (%) in Bars vs. Load (KN)	

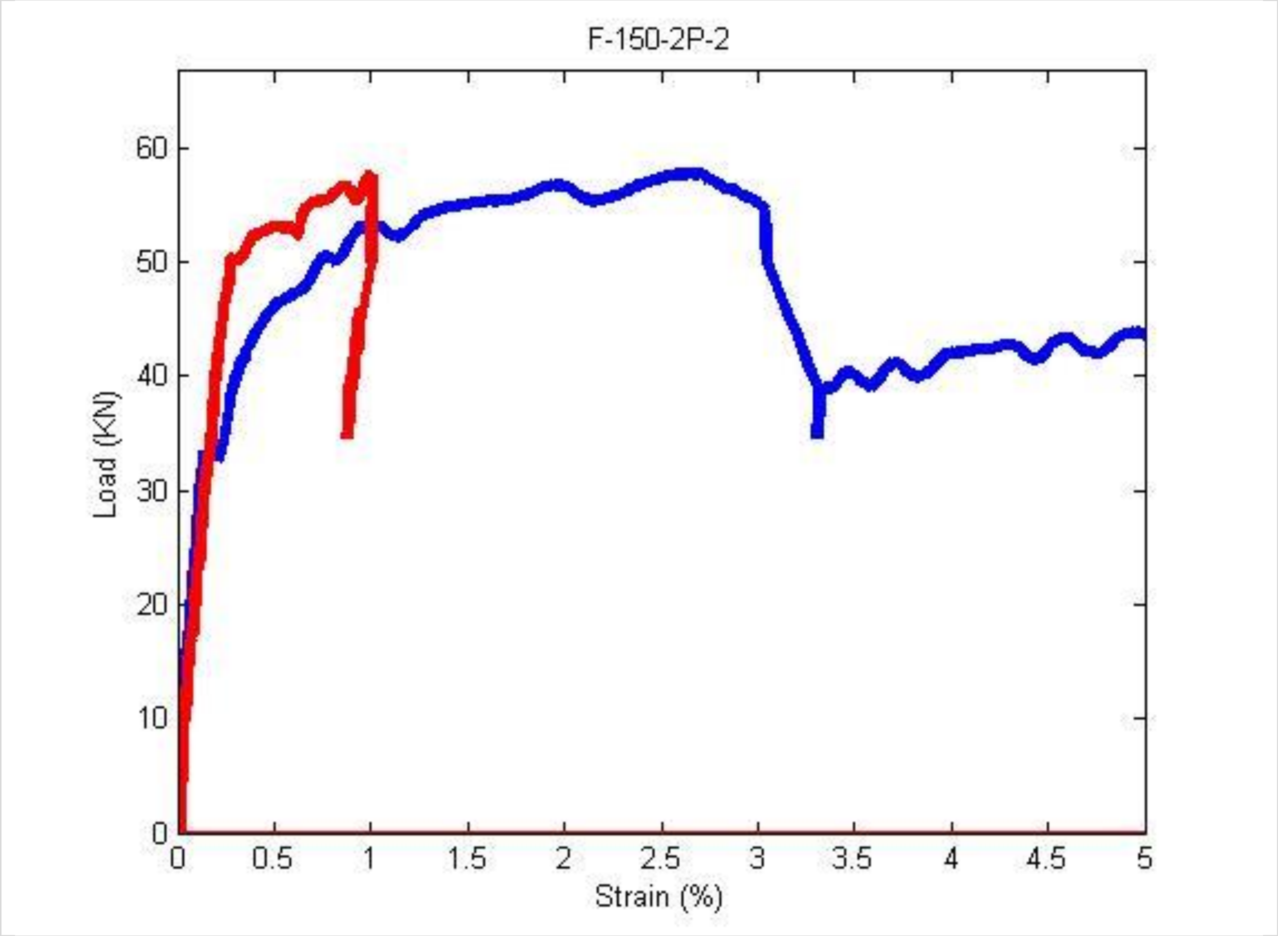
F-150-2P-2
Load (KN)
Strain (%)
0
10
20
30
40
50
60
0
0.5
1
1.5
2
2.5
3
3.5
4
4.5
5

F-200-2P-1

Joint Width:	8 inches (200 mm)
Fiber Content (% vol.)	2%
Loading Scheme:	Pure Flexure

Prior to Load

At Peak Load

Strain Field (DIC)

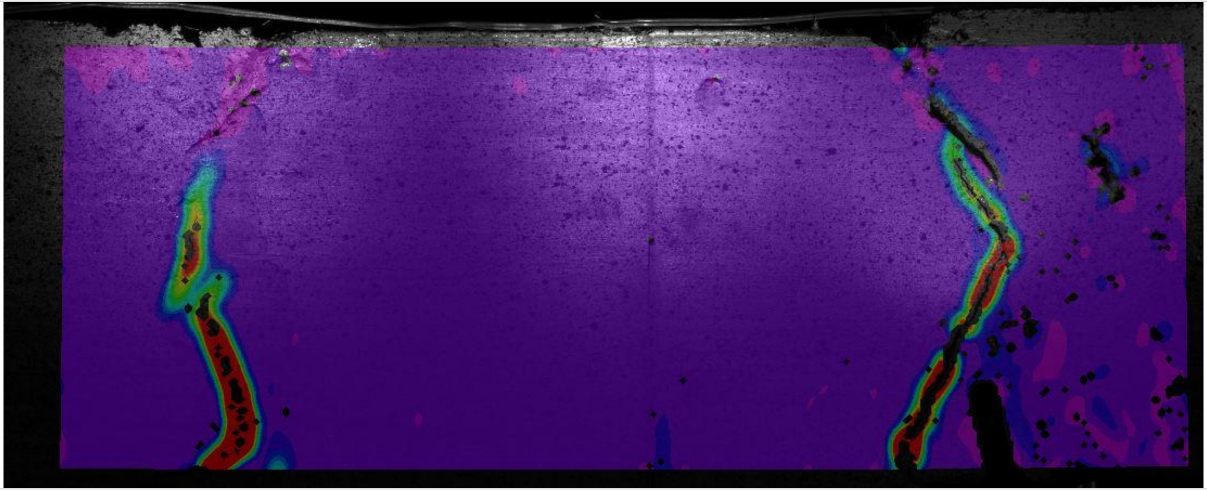

Strain (%) In Bars vs. Load (KN)

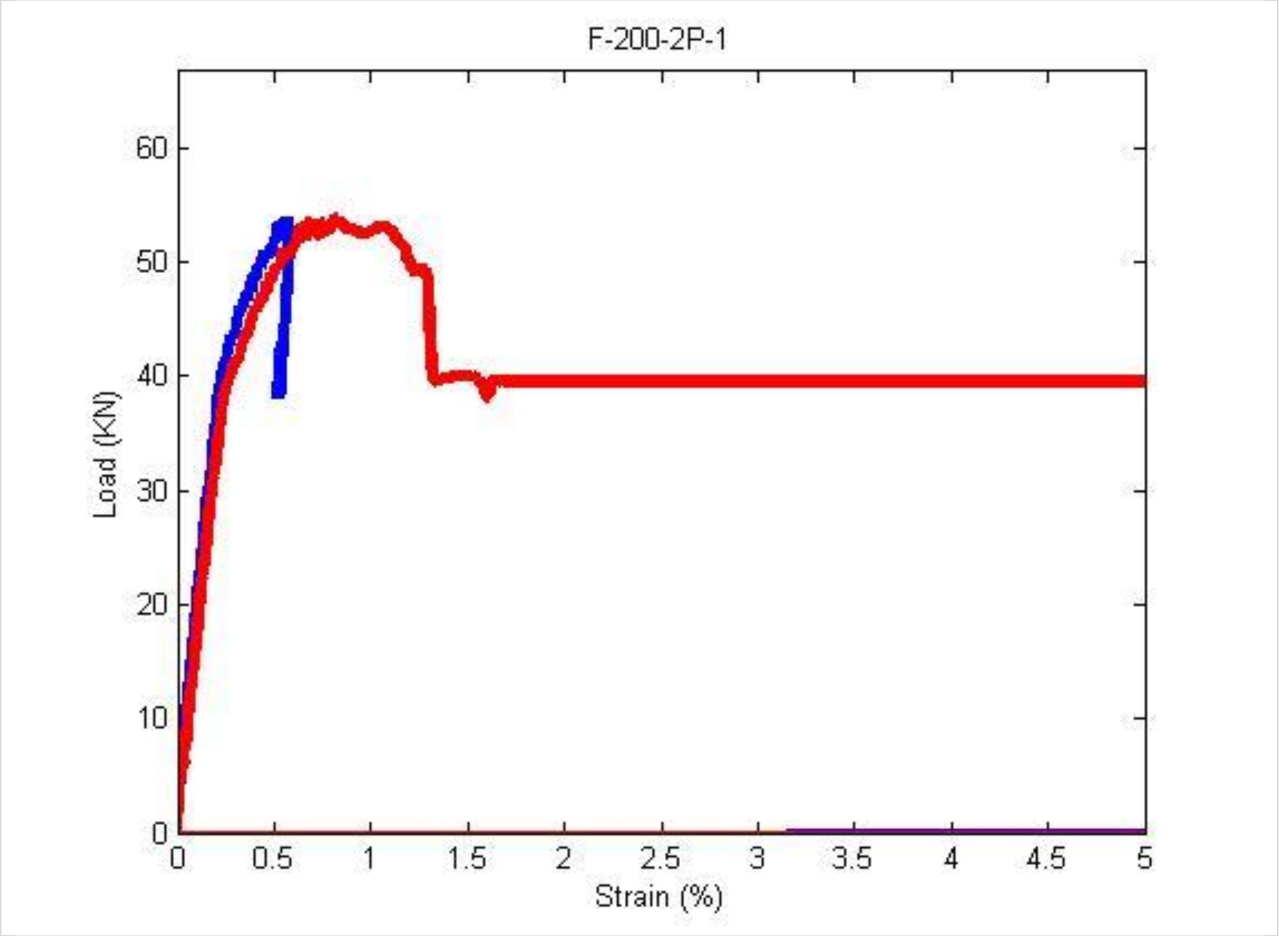
F-200-2P-1
Load (KN)
Strain (%)
0
10
20
30
40
50
60
0
0.5
1
1.5
2
2.5
3
3.5
4
4.5
5

F-200-2P-2

Joint Width:	8 inches (200 mm)
Fiber Content (% vol.)	2%
Loading Scheme:	Pure Flexure

Prior to Load

At Peak Load

Strain Field (DIC)

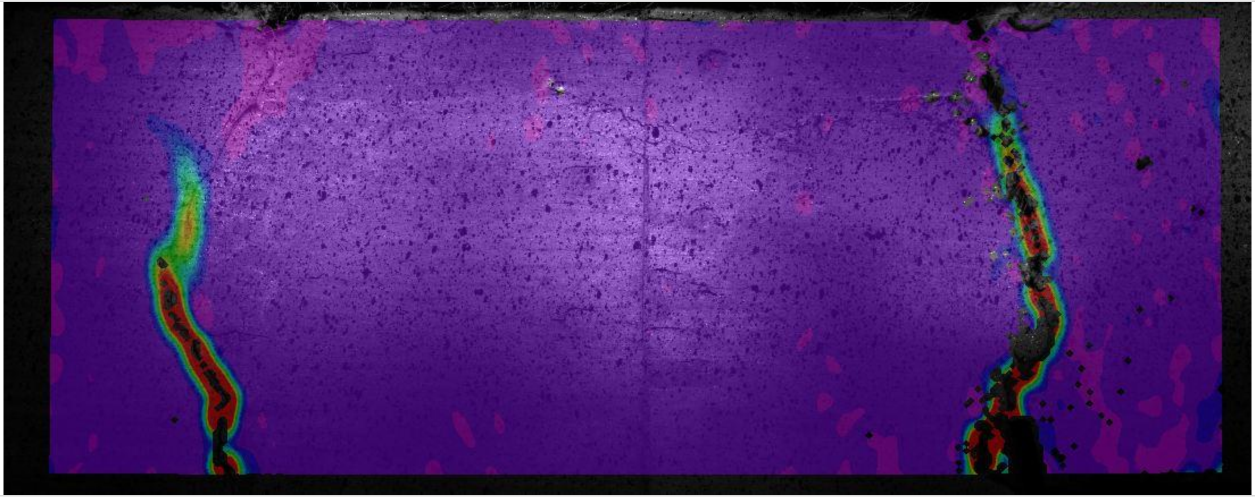

Strain (%) in Bars vs. Load (KN)

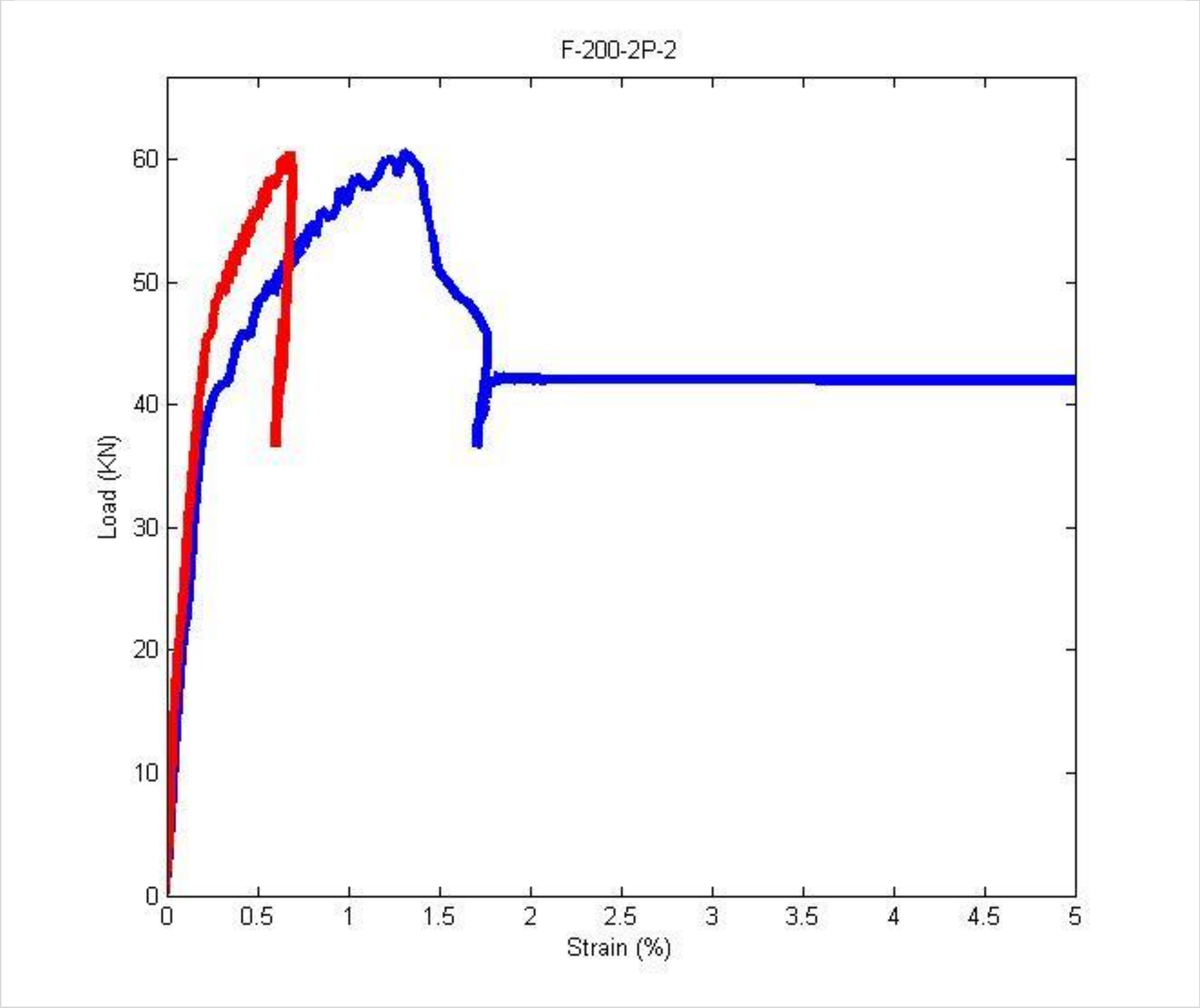
F-200-2P-2
Load (KN)
Strain (%)
0
10
20
30
40
50
60
0
0.5
1
1.5
2
2.5
3
3.5
4
4.5
5

SF-100-1P-1

Joint Width:	4 inches (100 mm)
Fiber Content (% vol.)	1%
Loading Scheme:	Combined Shear and Flexure

At Peak Load

Strain Field (DIC)

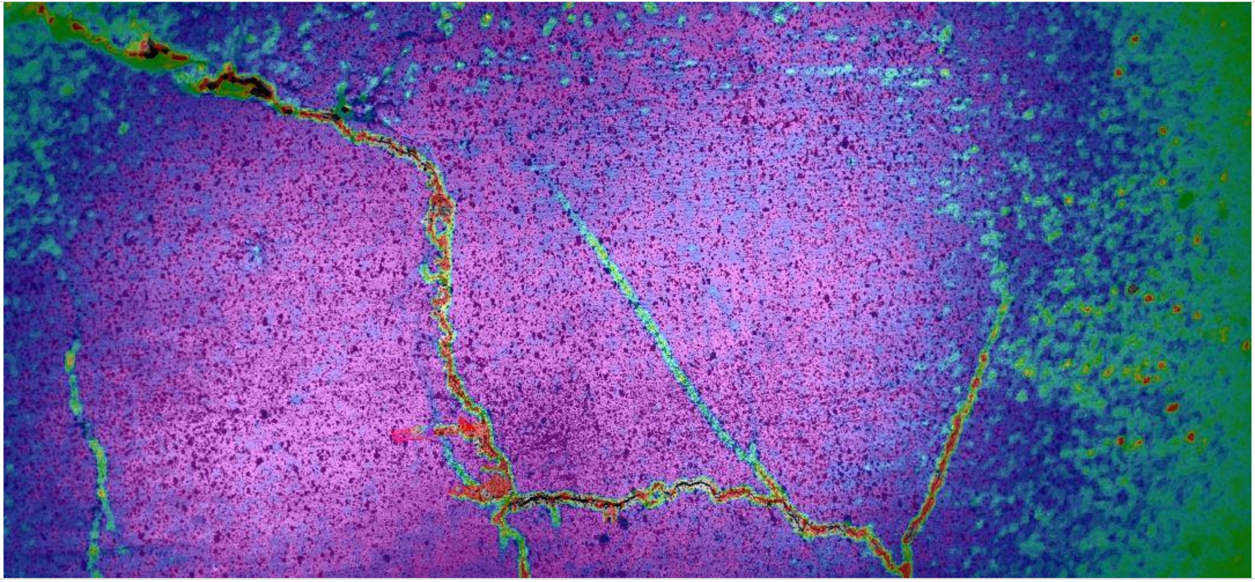

SF-100-1P-2

Joint Width:	4 inches (100 mm)
Fiber Content (% vol.)	1%
Loading Scheme:	Combined Shear and Flexure

At Peak Load

Strain Field (DIC)

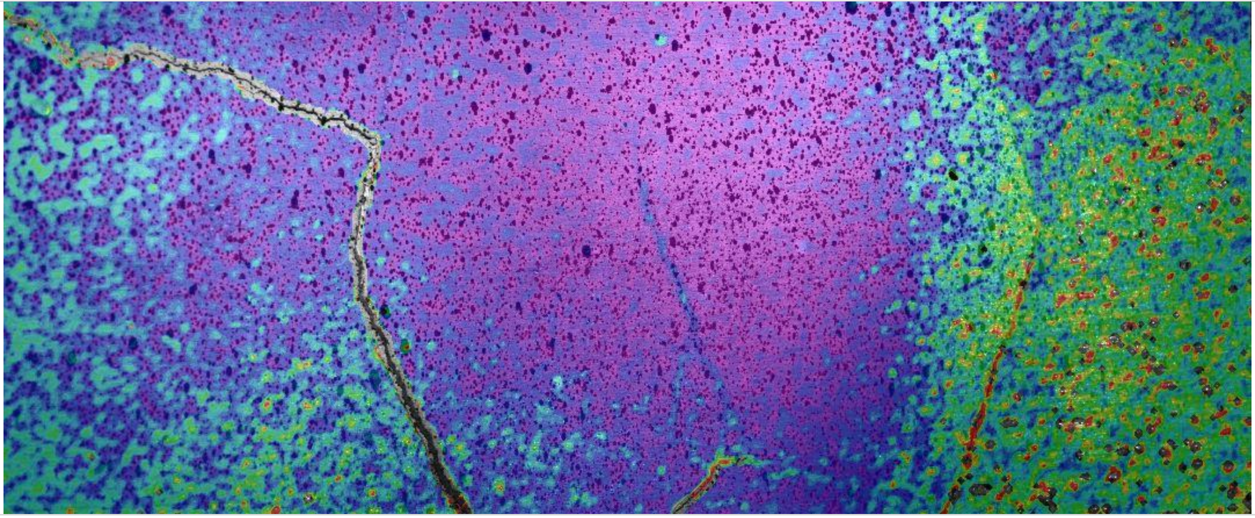

SF-100-2P-1

Joint Width:	4 inches (100 mm)
Fiber Content (% vol.)	2%
Loading Scheme:	Combined Shear and Flexure

At Peak Load

Strain Field (DIC)

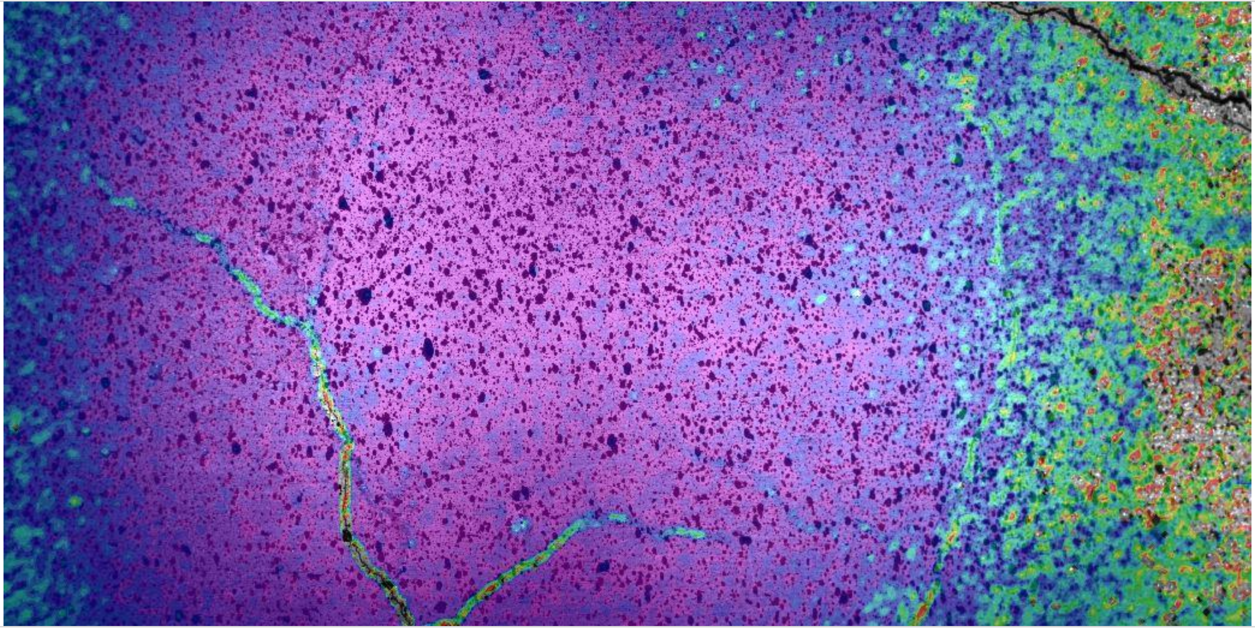

SF-100-2P-2	
Joint Width:	4 inches (100 mm)
Fiber Content (% vol.)	2%
Loading Scheme:	Combined Shear and Flexure
At Peak Load	
	
Strain Field (DIC)	
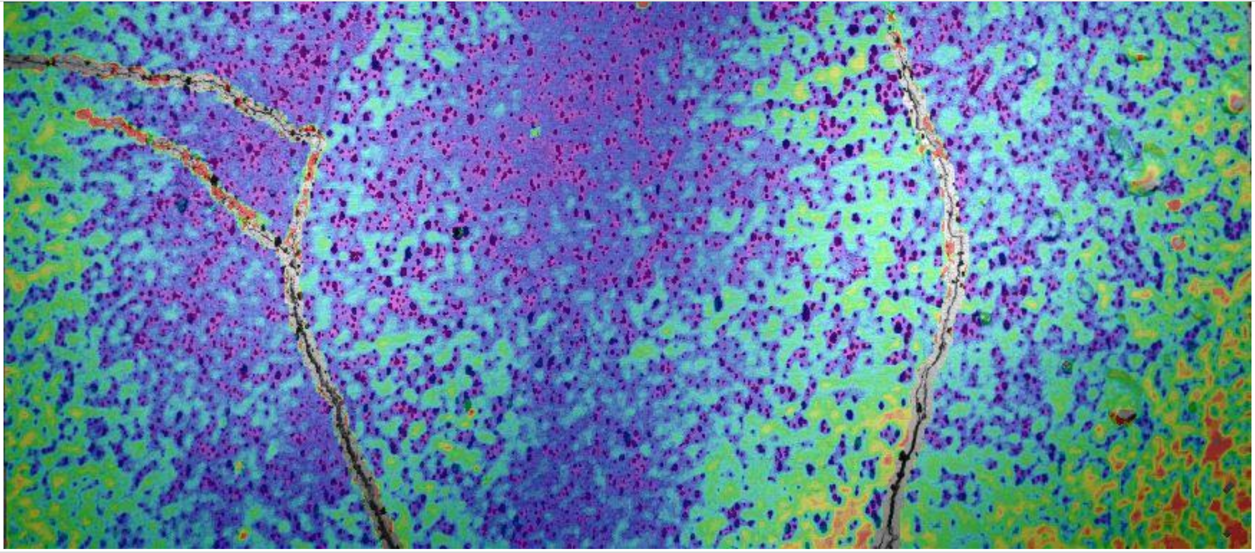	

References

AASHTO T 132-87. Standard Method of Test for Tensile Strength of Hydraulic Cement Mortars. American Association of State and Highway Transportation Officials. 8 pages. 2009.

AASHTO T 277-86, Rapid Determination of the Chloride Permeability of Concrete, American Association of States Highway and Transportation Officials, Standard Specifications - Part II Tests, Washington, D. C., 1990.

ACI Committee 318-05 (2005). Building Code Requirements for Structural Concrete (ACI 318-05) and Commentary (ACI 318R-05), American Concrete Institute Committee 318, Farmington Hills, MI.

ACI Committee 408 (2003). Bond and Development of Straight Reinforcing Bars in Tension. ACI 408R-03, American Concrete Institute Committee 408, Farmington Hills, MI.

Acker, P. and Behloul, M., “Ductal® Technology: A Large Spectrum of Properties, A Wide Range of Applications,” Proceedings of the International Symposium on Ultra High Performance Concrete, Ed., Schmidt, M., Fehling, E., and Geisenhanslüke, C., Kassel University Press, Kassel, Germany, 2004, pp. 11–23.

Ahlborn, T.M. et al., “Durability and Strength Characterization of Ultra-High Performance Concrete Under Variable Curing Regimes,” Proceedings of the Second International Symposium on Ultra High Performance Concrete, Ed., Fehling, E., Schmidt, M., and Stürwald, S., Kassel University Press, Kassel, Germany, 2008, pp. 197–204.

Ahlbourn, Theresa. "ULTRA-HIGH PERFORMANCE CONCRETE FOR MICHIGAN BRIDGES." Final Report, MDOT, Michigan Tech (2008): 1-152. Web.

Alexander, M.g, and B.j Magee. "Durability Performance of Concrete Containing Condensed Silica Fume." Cement and Concrete Research 29.6 (1999): 917-22. Web.

Alkaysi, M., El-Tawil, S., Liu, Z. and Hansen, W. (2016), “Effects of Silica Powder and Cement Type on Long Term Durability of Ultra High Performance Concrete (UHPC),” Accepted for Publication in the ACI Materials Journal.

Andreasen, A.H.M. and Andersen, J., 'Ueber die Beziehung zwischen Kornabstufung und Zwischenraum in Produkten aus losen Körnern (mit einigen Experimenten)', Kolloid-Zeitschrift 50 (1930) 217-228.

Andreassen and J. Andersen: Kolloid Z. 50 (1930) p. 217–228.

ASCE 7: Minimum Design Loads for Buildings and Other Structures. N.p.: ASCE Library, n.d. Print.

ASTM Standard C109, Standard Test Method for Compressive Strength of Hydraulic Cement Mortars (Using 2-in. or (50-mm) Cube Specimens)', ASTM International, West Conshohocken, PA. (2009)

ASTM Standard C1202, “Standard Test Method for Electrical Indication of Concrete's Ability to Resist Chloride Ion Penetration”, ASTM International, West Conshohocken, PA. (2009) 6 pp.

ASTM Standard C457, 'Standard test method for microscopical determination of parameters of the air-void system in hardened concrete', ASTM International, West Conshohocken, PA. (2009) 14 pp

Azizinamini, A., Stark, M., Toller, J.J., and Ghosh, S.K., 1993, “Bond Performance of Reinforcing Bars Embedded in High-Strength Concrete,” ACI Structural Journal, V. 90, No. 5, Sep.-Cot., pp. 554-561.

Bonneau, O. et al., “Mechanical Properties and Durability of Two Industrial Reactive Powder Concretes,” ACI Materials Journal, Vol. 94, No. 4, July–August 1997, pp. 286–290

Borges, Paulo H. R., Lucas F. Fonseca, Vitor A. Nunes, Tulio H. Panzera, and Carolina C Martuscelli. "Andreasen Particle Packing Method on the Development of Geopolymer Concrete for Civil Engineering." Journal of Materials in Civil Engineering (2013): 130413134609008. Web.

Brouwers HJH, Radix HJ, Self-compacting concrete: the role of the particle size distribution. In: The first international symposium on design, performance and use of self-consolidating concrete (SCC’2005) Changsha, Hunan, China; p. 109–18. 200

Castro, A. L., and Pandolfelli, V. C. (2009). “Review: Concepts of particle dispersion and packing for special concretes production.” Cerâmica, 55(333), 18–32

Cheng, An, Ran Huang, Jiann-Kuo Wu, and Cheng-Hsin Chen. "Influence of GGBS on Durability and Corrosion Behavior of Reinforced Concrete." Materials Chemistry and Physics 93.2-3 (2005): 404-11. Web

Cheng, An, Ran Huang, Jiann-Kuo Wu, and Cheng-Hsin Chen. "Influence of GGBS on Durability and Corrosion Behavior of Reinforced Concrete." Materials Chemistry and Physics 93.2-3 (2005): 404-11. Web.

de Larrard, F. and Sedran, T., “Optimization of Ultra-High-Performance Concrete by the Use of a Packing Model,” Cement and Concrete Research, Vol. 24, No. 6, 1994, pp. 997–1,009.

Elaty, Metwally Abd Allah Abd. "Compressive Strength Prediction of Portland Cement Concrete with Age Using a New Model." HBRC Journal 10.2 (2014): 145-55. Web.

Fehling, E., Lorenz, P., and Leutbecher, T., “Experimental Investigations on Anchorage of Rebars in UHPC,” Proceedings of Hipermat 2012 3rd International Symposium on UHPC and Nanotechnology for High Performance Construction Materials, Ed., Schmidt, M.,Fehling, E.

Gilkey, Hj. "Bond with Reinforcing Steel." Significance of Tests and Properties of Concrete and Concrete Aggregates (1956): n. pag. Web.

Glotzbach, C., Fröhlich, S., and Piotrowski, S., Kassel University Press, Kassel,Germany, 2012, pp. 533–540.

Graybeal, B., “Behavior of Field-Cast Ultra-High Performance Concrete Bridge Deck Connections Under Cyclic and Static Structural Loading,” FHWA, U.S. Department of Transportation, Report No. FHWA-HRT-11-023, National Technical Information ServiceAccession No. PB2011-101995, 2010.

Graybeal, B., “Bond Behavior of Reinforcing Steel in Ultra High Performance Concrete,” Federal Highway Administration, FHWA-HRT-14-089, October, 2014, p. 12

Graybeal, B., “Design and Construction of Field-Cast UHPC Connnections,” Federal Highway Administration, FHWA-HRT-14-084, October, 2014, p. 36

Graybeal, B., “Material Property Characterization of Ultra-High Performance Concrete,” FHWA, U.S. Department of Transportation, Report No. FHWA-HRT-06-103, McLean, VA, 2006

Graybeal, B., Perry, V., and Royce, M., “UHPC Ultra-High Performance Concrete,” NHI Innovations Webinar, November 18, 2010. Available at https://connectdot.connectsolutions.com/n134083201011 (Cited April 3, 2012).

Graybeal, B.A. and Hartmann, J.L., “Strength and Durability of Ultra-High Performance Concrete,” Proceedings of the 3rd International Symposium on High Performance Concrete/PCI National Bridge Conference, October 19–22, 2003, Orlando, FL, Compact Disc, Paper 47.

Graybeal, Benjamin A. "Field-Cast UHPC Connections for Modular Bridge Deck Elements." FHWA-HRT-11-022 48.6 (2014): n. pag. FHWA. Web.

Graybeal, Benjamin A. "Splice Length of Prestressing Strands in Field-cast UHPC Connections." Mater Struct Materials and Structures 48.6 (2015): 1831-839. Web.

Graybeal. "Ultra-High Performance Concrete: A State-Of-The-Art Report for The Bridge Community." Chapters 6-7 - , June 2013 - FHWA-HRT-13-060. N.p., n.d. Web. 06 Dec. 2014.

Holschemacher, K. and Weiße, D., “Economic Mix Design Ultra High-Strength Concrete,” Seventh International Symposium on the Utilization of High-Strength/High-Performance Concrete, Vol. II, Publication No. SP-228, Ed., Russell, H.G., American Concrete Institute, Farmington Hills, MI, 2005, pp. 1,133–1,144.

Holschemacher, K., Weiβe, D., and Klotz, S., “Bond of Reinforcement in Ultra High Strength Concrete,” Proceedings of the International Symposium on Ultra High Performance Concrete, Ed., Schmidt, M., Fehling, E., and Geisenhanslüke, C., Kassel University Press, Kassel, Germany, 2004, pp. 375–387.

Hwang, Hoonhee, and Sung Yong Park. "A Study on the Flexural Behavior of Lap-spliced Cast-in-place Joints under Static Loading in Ultra-high Performance Concrete Bridge Deck Slabs." Canadian Journal of Civil Engineering Can. J. Civ. Eng. 41.7 (2014): 615-23. Web.

Innovative Field-Cast Uhpc Joints For Precast Bridge Decks - Highways for LIFE - FHWA."

Jungworth, J., Muttoni, A., "Structural Behavior of Tension Memebers in UHPC,"Proceedings of the International Symposium on Ultra High Performance Concrete, Kassel, Germany, 2004.

Kim, D-J., Wille, K., Naaman, A. E. and El-Tawil, S. (2011), “Strength Dependent Tensile Behavior of Strain Hardening Fiber Reinforced Concrete,” Proceedings of HPFRCC6, H. W. Reinhardt and G. Parra Editors, Ann Arbor, MI.

Kim, D-J, Naaman, A. E. and El-Tawil, S. (2010a), “High Performance Fiber Reinforced Cement Composites With Innovative Slip Hardening Twisted Steel Fibers” International Journal of Concrete Structures and Materials, Korean Concrete Institute, ISSN: 1976-0485, 3(2), pp. 119 – 126; DOI 10.4334/IJCSM.2009.3.2.119.

Kim, D-J, El-Tawil, S., Sirijaroonchai, K. and Naaman, A. E. (2010b), “Numerical Simulation of the Split Hopkinson Pressure Bar Test Technique for Concrete Under Compression,” International Journal of Impact Engineering, 37(2), Pages 141-149.

Kim, D-J., Naaman, A.E. and El-Tawil, S. (2010c), “Correlation between Tensile and Bending Behavior of FRC Composites with Scale Effect,” Proceedings of FraMCoS-7, 7th International Conference on Fracture Mechanics of Concrete and Concrete Structures, May 23-28, 2010, Jeju Island, South Korea

Kim, D-J, Naaman, A. E. and El-Tawil, S. (2008a), “Comparative Flexural Behavior of Four Fiber Reinforced Cementitious Composites,” Journal of Cement and Concrete Composites, Elsevier, Vol. 30, November 2008, pp.917-928.

Kim, D-J, El-Tawil, S. and Naaman, A. E. (2008b), “Rate-Dependent Tensile Behavior of High Performance Fiber Reinforced Cementitious Composites,” Materials and Structures, RILEM, ISSN 1359-5997 (in print), 1871-6873 (online).

Kim, D-J, El-Tawil, S. and Naaman, A. E. (2008c), “Loading Rate Effect on Pullout Behavior of Deformed Fibers,” ACI Materials Journal, 105(6), November-December 2008, pp.576-584

Kim, D-J, Naaman, A. E. and El-Tawil, S. (2008d), “High Tensile Strength Strain-Hardening FRC Composites with Less Than 2% Fiber Content,” Proceedings of the Second International Symposium on Ultra High Performance Concrete, March 05 - 07, 2008, Kassel, Germany.

Kim, D-J, El-Tawil, S. and Naaman, A. E. (2007), “Correlation between Single Fiber Pullout and Tensile Response of FRC Composites with High Strength Steel Fibers,” Proceedings of HPFRCC5, H. W. Reinhardt and A.E. Naaman Editors, July 10-13, Mainz, Germany.

Kok Seng Chia, Min-Hong Zhang, “Water permeability and chloride penetrability of high-strength lightweight aggregate concrete”, Cement and Concrete Research, 32 (2002) 639-645

Liu, Zhichao. FROST DETERIORATION IN CONCRETE DUE TO DEICING SALT EXPOSURE: MECHANISM, MITIGATION AND CONCEPTUAL SURFACE SCALING MODEL. Diss. U of Michigan, 2014. N.p.: n.p., n.d. Print.

Naaman, A. E., and H. W. Reinhardt. "Proposed Classification of HPFRC Composites Based on Their Tensile Response." Materials and Structures 39.5 (2007): 547-55. Web

Naaman, A.E., and Reinhardt, H.W., "Characterization of High Performance Fiber Reinfoced Cement Composites," in "High Performance Fiber Reinforced Cement Composites – HPFRCC 2,' A.E. Naaman and F.W. Reinhardt, Editors, RILEM Pb. 31, E. and FN Spon, England, 1996; pp. 1-24

Oertel, Tina, Frank Hutter, Ricarda Tänzer, Uta Helbig, and Gerhard Sextl. "Primary Particle Size and Agglomerate Size Effects of Amorphous Silica in Ultra-high Performance Concrete." Cement and Concrete Composites 37 (2013): 61-67. Web.

Piérard, J., Dooms, B., and Cauberg, N., “Evaluation of Durability Parameters of UHPC Using Accelerated Lab Tests,” Proceedings of Hipermat 2012 3rd Internationa Symposium on UHPC and Nanotechnology for High Performance Construction Materials, Ed., Schmidt, M., Fehling, E., Glotzbach, C., Fröhlich, S., and Piotrowski, S., Kassel University Press, Kassel, Germany, 2012, pp. 371–376.

Piotrowski, S. and Schmidt, M., “Life Cycle Cost Analysis of a UHPC-Bridge on Example of Two Bridge Refurbishment Designs,” Proceedings of Hipermat 2012 3rd International Symposium on UHPC and Nanotechnology for High Performance Construction Materials, Ed., Schmidt, M., Fehling, E., Glotzbach, C., Fröhlich, S., and Piotrowski, S., Kassel University Press, Kassel, Germany, 2012, pp. 957–964

Pyo, Sukhoon, Kay Wille, Sherif El-Tawil, and Antoine E. Naaman. "Strain Rate Dependent Properties of Ultra High Performance Fiber Reinforced Concrete (UHP-FRC) under Tension." Cement and Concrete Composites 56 (2015a): 15-24. Web.

Pyo, S., El-Tawil, S. (2015b), “Capturing the Strain Hardening and Softening Responses of Cementitious Composites Subjected to Impact Loading,” Journal of Construction and Building Materials, Elsevier, 81(15), April 2015, pp. 276–283, doi:10.1016/j.conbuildmat.2015.02.028.

Pyo, S. and El-Tawil, S. (2013a), “Crack velocity-dependent dynamic tensile behavior of concrete”, International Journal of Impact Engineering, V55, pp. 63-70, http://dx.doi.org/10.1016/ j.ijimpeng.2013.01.003.

Pyo, S. and El-Tawil, S. (2013b), “Dynamic Fracture Mechanics Based DIF Models for Concrete under Tensile Loading,” 2013 Conference of the ASCE Engineering Mechanics Institute, August 4 – 7, 2013, Northwestern University, Evanston, IL

Pyo, S., El-Tawil, S. and Naaman, A.E. (2013c), “Parametric Study of a New Impact Testing System for Ultrahigh Performance Concrete in Tension,” 2013 Conference of the ASCE Engineering Mechanics Institute, August 4 – 7, 2013, Northwestern University, Evanston, IL

Rigaud, Stephane, Phillippe Fonollosa, and Gilles Chanvillard. Concrete Composition. Lafarge, assignee. Patent US8303708 B2. 6 Nov. 2012. Print.

RILEM TC 176-IDC, M.J. Setzer, P. Heine, S. Kasparek, S. Palecki, R. Auberg, V. Feldrappe, E. Siebel, Test methods of frost resistance of concrete: CIF-Test: Capillary suction, internal damage and freeze thaw test)-Reference method and alternative methods A and B, Mater. Struct. 37 (274) (2004) 743-753.

Rong, Z.d., W. Sun, H.j. Xiao, and W. Wang. "Effect of Silica Fume and Fly Ash on Hydration and Microstructure Evolution of Cement Based Composites at Low Water–binder Ratios." Construction and Building Materials 51 (2014): 446-50. Web.

Rong, Zhidan, Wei Sun, Haijun Xiao, and Guang Jiang. "Effects of Nano-SiO2 Particles on the Mechanical and Microstructural Properties of Ultra-high Performance Cementitious Composites." Cement and Concrete Composites 56 (2015): 25-31. Web.

Saleem, Muhammad Azhar, Amir Mirmiran, Jun Xia, and Kevin Mackie. "Development Length of High-Strength Steel Rebar in Ultrahigh Performance Concrete." J. Mater. Civ. Eng. Journal of Materials in Civil Engineering 25.8 (2013): 991-98. Web.

Slater, W.a., F.e. Richart, and G.g. Scofield. "Tests of Bond Resistance between Concrete and Steel." Technologic Papers of the Bureau of Standards (1920): n. pag. Web

Steinberg, Eric. "Structural Reliability of Prestressed UHPC Flexure Models for Bridge Girders." Journal of Bridge Engineering 15 (2010): 65-72. Web.

Sutter, Lawrence L. Evaluation of Methods for Characterizing Air Void Systems in Wisconsin Paving Concrete. Madison, WI: Wisconsin Highway Research Program, 2007. Print

Swenty, M. and Graybeal, B., “Influence of Differential Deflection on Staged Construction Deck-Level Connections,” FHWA, U.S. Department of Transportation, Report No. FHWAHRT-12-057, National Technical Information Service Accession No. PB2012-111528, 2012.

Tanesi, Jussara, and Richard Meininger. "Freeze-Thaw Resistance of Concrete with marginal Air Content." Transportation Research Record 2020.-1 (2007): 61-66. Web.

Wille, K., Kim, D., and Naaman, A.E., “Strain-Hardening UHP-FRC With Low Fiber Contents,” Materials and Structures, Vol. 44, No. 3, 2011, pp. 583–598

Wille, K., Naaman, A.E., and El-Tawil, S., “Optimizing Ultra-High-Performance Fiber Reinforced Concrete,” Concrete International, Vol. 33, No. 9, September 2011, pp. 35–41

Wille, K., Naaman, A.E., and Parra-Montesinos, G.J., “Ultra-High Performance Concrete With Compressive Strength Exceeding 150 MPa (22 ksi): A Simpler Way,” ACI Materials Journal, Vol. 108, No. 1, January–February 2011, pp. 46–54.

Wille, Kay, and Antoinne Naaman. "Pullout Behavior of High-Strength Steel Fibers Embedded in Ultra-High-Performance Concrete." ACI Materials Journal MJ 109.4 (2012): n. pag. Web.

Wille, Kay, and Christopher Boisvert-Cotulio. "Material Efficiency in the Design of Ultra-high Performance Concrete." Construction and Building Materials 86 (2015): 33-43. Web.

Wille, Kay, and Gustavo Parra-Montesinos. "Effect of Beam Size, Casting Method, and Support Conditions on Flexural Behavior of Ultra-High-Performance Fiber-Reinforced Concrete." ACI Materials Journal MJ109.3 (2012): n. pag. Web.

Wille, Kay, Antoine E. Naaman, Sherif El-Tawil, and Gustavo J. Parra-Montesinos. "Ultra-high Performance Concrete and Fiber Reinforced Concrete: Achieving Strength and Ductility without Heat Curing." Mater Struct Materials and Structures 45.3 (2011): 309-24. Web.

Wille, Kay, Dong Joo Kim, and Antoine E. Naaman. "Strain-hardening UHP-FRC with Low Fiber Contents." Materials and Structures 44.3 (2011): 583-98. Web.

Wille, K., Xu, M., El-Tawil, S. and Naaman, A.E. (2015), “Dynamic Impact Factors of Strain Hardening UHP-FRC under Direct Tensile Loading at Low Strain Rates,” Accepted for publication in the RILEM Materials and Structures Journal. DOI: 10.1617/s11527-015-0581-y.

Wille, K., El-Tawil, S. and Naaman, A.E. (2014), “Properties of Strain Hardening Ultra High Performance Fiber Reinforced Concrete (UHP-FRC) under Direct Tensile Loading,” Journal of Cement and Concrete Composites, Elsevier, 48, pp. 53-66, doi:10.1016/j.cemconcomp.2013.12.015

Wille, K., Naaman, A. E. and El-Tawil, S. (2011), “Ultra High Performance Fiber Reinforced Concrete (UHP-FRC) Record Performance under Tensile Loading,” Concrete International, American Concrete Institute, Sept. 2011, pp. 35-41.

Wille, K., El-Tawil, S. and Naaman, A. E. (2011), “Strain Rate Dependent Tensile Behavior of Ultra-High Performance Fiber Reinforced Concrete,” Proceedings of HPFRCC6, H. W. Reinhardt and G. Parra Editors, Ann Arbor, MI.

Wipf, T., Sritharan, Sri,., “Iowa’s UHPC Implementation” Iowa Research, Bureau of Research and Technology, April, 2011

Yazıcı, Halit. "The Effect of Silica Fume and High-volume Class C Fly Ash on Mechanical Properties, Chloride Penetration and Freeze–thaw Resistance of Self-compacting Concrete." Construction and Building Materials 22.4 (2008): 456-62. Web.

Yu, R., P. Spiesz, and H.j.h. Brouwers. "Development of an Eco-friendly Ultra-High Performance Concrete (UHPC) with Efficient Cement and Mineral Admixtures Uses." Cement and Concrete Composites 55 (2015): 383-94. Web.

Yu, R., P. Spiesz, and H.j.h. Brouwers. "Development of Ultra-High Performance Fibre Reinforced Concrete (UHPFRC): Towards an Efficient Utilization of Binders and Fibres." Construction and Building Materials 79 (2015): 273-82. Web.

Yu, R., P. Spiesz, and H.j.h. Brouwers. "Effect of Nano-silica on the Hydration and Microstructure Development of Ultra-High Performance Concrete (UHPC) with a Low Binder Amount." Construction and Building Materials 65 (2014): 140-50. Web.